Clemson University
TigerPrints

All Dissertations | Dissertations

12-2016

Tunable Copper Microstructures in Blanket Films and Trenches Using Pulsed Electrodeposition

James Marro
Clemson University, JMarro@g.clemson.edu

Follow this and additional works at: https://tigerprints.clemson.edu/all_dissertations

Recommended Citation
Marro, James, "Tunable Copper Microstructures in Blanket Films and Trenches Using Pulsed Electrodeposition" (2016). *All Dissertations*. 1831.
https://tigerprints.clemson.edu/all_dissertations/1831

This Dissertation is brought to you for free and open access by the Dissertations at TigerPrints. It has been accepted for inclusion in All Dissertations by an authorized administrator of TigerPrints. For more information, please contact kokeefe@clemson.edu.

TUNABLE COPPER MICROSTRUCTURES IN BLANKET FILMS AND TRENCHES USING PULSED ELECTRODEPOSITION

A Thesis
Presented to
the Graduate School of
Clemson University

In Partial Fulfillment
of the Requirements for the Degree
Doctor of Philosophy
Materials Science and Engineering

---

by
James Marro
December 2016

Accepted by:
Dr. Kathleen Richardson, Committee Co-Chair
Dr. Yaw Obeng, Committee Co-Chair
Dr. Igor Luzinov
Dr. Marian Kennedy
Dr. Fei Peng

ABSTRACT

Copper interconnects in microelectronics have long been plagued with thermo-mechanical reliability issues. Control over the copper deposition process and resulting microstructure can dictate its material properties and reduce stresses as well as defects that form in the copper. In this thesis, pulse electrodeposition processing parameters were evaluated for their impact on the copper microstructure (grain size, texture, and twin density and stress state) through electron backscattering diffraction and wafer curvature measurements. Varying levels of constraint were also investigated for their effect on the copper microstructure to better understand the microstructures of more complex three-dimensional interconnects. Highly texture blanket copper films were deposited with various pulse frequencies and duty cycle, which was found to control grain size, orientation, and twin density. Higher twin densities were also observed in the films with lower residual stress. The findings from blanket film studies were carried over to trench deposited samples, where the influence of organic additives, typically used in the electrolytic bath to produce defect-free filling of advanced geometries, on the copper microstructure was studied. With the addition of organic additives, depositions produced finer grained structures with an increased contribution from the microstructure of the trench sidewall seed layer, especially with increasing trench aspect ratio. In addition, the increased constraint of the copper, resulted in larger stresses within the features and higher twin densities. The core of this dissertation demonstrated the ability to alter the resulting Cu microstructure through variations in pulse electrodeposition parameters.

ACKNOWLEDGMENTS

The author would like to thank all those who supported and aided in the work carried out in this dissertation. First, I would like to thank my family, especially my wife, Emma Marro, for her support and encouragement. I would also like to thank my parents, Jim and Debra Marro, siblings, Justin and Jordan Marro, and in-laws, Roine, Sofie, and Annie Westlund. None of this work would have been possible without the guidance and assistance of my advisors, Dr. Kathleen Richardson and Dr. Yaw Obeng. I would also like to thank my PhD committee members, Dr. Igor Luzinov, Dr. Marian Kennedy, and Dr. Fei Peng, for their advice and support. I am also grateful to Dr. Chukwudi Okoro, who served as a pseudo advisor, for his knowledge in the area of research and assistance in shaping this dissertation. I am thankful to the National Institute of Standards and Technology (NIST) Engineering Physics Division and Research Triangle Nanotechnology Network (RTNN) for the funding this work. Dr. Taghi Darroudi and Dr. Lax Saraf at Clemson University's Electron Microscopy Lab at the Advanced Materials Research Laboratory were also of major help with the electron microscopy work. Likewise, the help from Kirk Scammon, Dr. Mikhail Klimov, and Dr. Matt Schneider at the University of Central Florida's (UCF) Materials Characterization Facility was also greatly appreciated. North Carolina State University's (NCSU) Analytical Instrumentation Facility staff Roberto Garcia, Dr. Phillip Strader, and Dr. Fred Stevie assisted with the electron backscattering diffraction. I would also like to acknowledge Dr. Cheng Li and Amrita Kapat for their assistance conducting some measurements. Lastly, I would like to thank all of the current and past members

of the Glass Processing and Characterization Laboratory, including Dr. Dave Musgraves, Pete Wachtel, Dr. Charmayne Smith, Dr. Jason Lonergan, Dr. Benn Gleason, Dr. Erick Koontz, Dr. Spencer Novak, Andy Buff, Antoine Lepicard, and Laura Sisken.

TABLE OF CONTENTS

ABSTRACT ii

ACKNOWLEDGMENTS iii

LIST OF TABLES viii

LIST OF FIGURES x

LIST OF ACRONYMS xvii

CHAPTER ONE: MOTIVATION AND OBJECTIVES 1

1.1 Motivation 1

1.2 Objectives 4

1.3 Thesis Scope 6

CHAPTER TWO: BACKGROUND 8

2.1 Integrated Circuits (IC) 8

2.1.1 What are integrated circuits? 8
2.1.2 How are 3D-ICs fabricated? (middle of the line) 10

2.2 Thermo-Mechanical Reliability Concerns 11

2.2.1 Void Nucleation 12
2.2.2 Void Growth 15
2.2.3 Void-Induced Material Property Changes 18

2.3 Electrodeposition 19

2.3.1 Electrodeposition Basics 19
2.3.2 Pulsed Electrodeposition 20
2.3.3 Advanced Geometry Filling 21

2.4 Copper Microstructure 26

2.4.1 Desired Microstructure for Microelectronics 26
2.4.2 Electrodeposition Parameters and the Effect on Cu film Microstructure 34
2.4.3 Microstructural Impact from Organic Bath Additives 36

CHAPTER THREE: PULSED ELECTRODEPOSITION OF COPPER FILMS 38

3.1 Motivation and Goals 38

3.2 Experimental Procedure 39

3.2.1 Sample Preparation 39
3.2.2 Pulsed Electrodeposition (PED) 40

TABLE OF CONTENTS (CONT'D)

3.2.3 Microstructural Evaluation 45
3.3 Results and Discussion 48

3.3.1 Grain Morphology of Blanket Cu Films 49
3.3.2 Texture of Cu Films 53
3.3.3 Residual Stress in Cu Films 58
3.4 Conclusions 64

CHAPTER FOUR: ADVANCED GEOMETRY DEPOSITIONS 66
4.1 Motivation and Goals 66

4.2 Experimental Procedure 68

4.2.1 Copper Trench Depositions 68
4.2.2 Physical Property Measurements 70
4.2.3 Cross-Sectioning Protocol 71
4.2.4 Microstructural Evaluation 73
4.3 Results and Discussion 74

4.3.1 Trench Filling 74
4.3.2 Impact of Additives on Resulting Cu Properties 85
4.3.3 Copper Trench Microstructure 92
4.4 Conclusions 103

CHAPTER FIVE: GEOMETRIC CONSTRAINTS OF DEPOSITS 105
5.1 Motivation and Objectives 105

5.2 Results and Discussion 106

5.2.1 Blanket Films vs. Trench Overfill 106
5.2.2 The Influence of Geometric Constraint 111
5.3 Conclusions 119

CHAPTER SIX: CONCLUSIONS AND FUTURE WORK 121
6.1 Summary of Conclusions 122

6.2 Contribution and Impact 125

6.3 Future Work 127

REFERENCES 129

APPENDICES 144

TABLE OF CONTENTS (CONT'D)

Appendix A: Pulse Electrodeposition EBSD Maps 145

Appendix B: Trench Pretreatment and PCD 153

Appendix C: Alternative Organic Additive Impurity Measurements 154

Appendix D: Review on Voids in Copper 156

Appendix E: Review on the Deformation of Copper 170

Appendix F: Review of Copper Twinning 187

Appendix G: Review of Copper Grain Growth 201

Appendix H: List of Publications and Presentations 219

LIST OF TABLES

Table 1.1: The thermo-mechanical properties of silicon, silica, and copper, taken from ref [13]. 3

Table 3.1: The nine pulse parameter conditions used to electrodeposit the Cu films. 43

Table 3.2: The (111), (200), (220), and (311) Cu XRD peak locations and intensities of a randomly oriented Cu sample taken from the International Centre for Diffraction Database (ICDD) code: 03-065-9743. The intensities are used to calculate the texture coefficient for the Cu films. 47

Table 4.1: The organic additive concentrations used in the pulse electrodeposition baths for Cu trench filling. 70

Table 4.2: The widths of the various aspect ratio trenches of interest in this study. All trenches are 500 nm deep. 73

Table 4.3: The void area measurements for 2.78 aspect ratio trenches deposited with various organic additive concentrations. 82

Table 4.4: The void area measurements for the 2.78 aspect ratio trenches deposited with different peak current densities. All trenches were deposited using 200 mg/L PEG, 5 mg/L SPS, and 10 mg/L JGB. 83

Table 4.5: The void area measurements for the 2.78 aspect ratio trenches deposited with after various pretreatments. All trenches were deposited without organic additives. 85

Table 4.6: The relative stress and surface roughness measurements when only one organic additive is used in the electrodeposition bath of Cu. 88

Table 4.7: The relative stress, surface roughness, and void area measurements in Cu deposited with various peak current densities. 92

Table 4.8: The average grain size and percentage of microstructural area consumed by the large grains in the Cu deposited with various organic additive concentrations. The standard deviations are shown for the grain diameter measurements. 98

Table 4.9: The amount of twins in the microstructure of the Cu trenches filled using different organic additive concentrations. 101

Table 5.1: The microstructural characteristics of the blanket films and overfill above the 250 nm and 500 nm wide trenches. 109

LIST OF TABLES (CONT'D)

Table 5.2: The multiple of uniform density inside the 250 nm and 500 nm wide trenches, deposited with various organic additive bath concentrations. 116

Table 5.3: The twin density of the 250 nm and 500 nm trenches and overfill of each, deposited with different organic additive bath concentrations. 119

Table B1: Material properties (stress, roughness, and texture coefficient) with various pretreatments used on trench samples. Stress and surface roughness were measured with the WLI and the (111) texture coefficient was calculated from XRD measurements. 153

Table B2: The (111) texture coefficient, calculated from XRD measurements, for trench samples deposited with various peak current densities. 153

LIST OF FIGURES

Figure 2.1: An illustration of a 3D-IC taken from ref [26]. 9

Figure 2.2: A step by step approach to middle of the line via formation and BEOL fabrication. 11

Figure 2.3: Optical micrograph illustrating triple junctions and grain boundaries in the Cu microstructure are susceptible to void formation due to their higher stress concentrations. Image from ref [15]. 14

Figure 2.4: Depiction of (a) prismatic loop emission and (b) shear loop emission mechanisms of void growth by dislocation emission, taken from [48]. 18

Figure 2.5: A typical PED pulse wave, labelled with the pulse parameters. 21

Figure 2.6: Illustration of voids and seams forming during deposition as well as defect-free bottom-up filling, taken from ref [15]. 23

Figure 2.7: The chemical makeup of PEG (a), SPS (b), and JGB (c). 24

Figure 2.8: The theorized location of the suppressor, accelerator, and leveler organic additives on a Cu cathode containing advanced features. 25

Figure 2.9: Diagram of dislocation pile up creating sources in neighboring grains, taken from [79]. 27

Figure 2.10: An illustration of the difference between coherent twins (a) and incoherent twins (b), taken from [41]. 31

Figure 2.11: A void that formed in a Cu interconnect and is restricting the flow of electrons, taken from [129]. 34

Figure 3.1: An illustration of SKW Associates Inc. blanket wafer cross-section prior to deposition. 40

Figure 3.2: A modified alligator clip used as the cathode in the electrodeposition of the blanket films. It contains an insulated mouth with a single point metal contact. 41

Figure 3.3: An Illustration of the pulse electrodeposition setup and annealing furnace. 42

Figure 3.4: An ion beam image of a film cross-section, prepared using MCF's FEI 200 TEM FIB. 44

Figure 3.5: Radius of curvature measurements were taken along the four directions (x,y,xy1, and xy2) shown here. 45

LIST OF FIGURES (CONT'D)

Figure 3.6: An XRD gonio scan of a Cu film, which contains four Cu peaks and at least one major Si substrate peak. ... 46

Figure 3.7: The types of EBSD maps used to evaluate the cross-sectional microstructure of the Cu films: (a) band contrast map, (b) inverse pole figure map, (c) grain boundary map, and (d) inverse pole figure. ... 48

Figure 3.8: The cross-sectional grain size histogram for the nine deposition pulse conditions. ... 50

Figure 3.9: The area fraction taken up by different sized grains for each pulse deposition condition. ... 51

Figure 3.10: The cross-sectional area occupied by large grains (>2 μm diameter) for the nine deposition pulse parameters. ... 51

Figure 3.11: A graph showing the increase in Cu RMS surface roughness with frequency of the pulse for the three duty cycles used during deposition. ... 53

Figure 3.12: The (a) surface normal and (b)/(c) in-plane inverse pole figure maps for the PED #5 Cu film cross-section. ... 54

Figure 3.13: The XRD chi rocking curve illustrates the preferential (111) orientation normal to the surface of the Cu seed layer prior to deposition. ... 55

Figure 3.14: The change in (111), (200), and (311) texture coefficient with varying deposition pulse on-times. Error bars, which are not visible, are within the size of the data point. ... 56

Figure 3.15: The (111) multiple of uniform density (MUD) for the Cu film cross-sections as the pulse on-time is changed. ... 57

Figure 3.16: An XRD residual stress measurement of a Cu blanket film using the $\sin^2\psi$ method. The points represent individual measurements, thus the error is not shown. ... 58

Figure 3.17: The biaxial residual stress in Cu films with various pulse frequencies and duty cycles. ... 60

Figure 3.18: A graph showing the increase of residual stress in Cu films with longer on-times. ... 61

Figure 3.19: A plot illustrating the lower residual stresses are correlated to increased twin densities in Cu films. Error bars represent standard deviation of the points. ... 63

LIST OF FIGURES (CONT'D)

Figure 3.20: The relationship between twin density and grain area of large grains (> 2 μm) in Cu films deposited at various pulse frequencies. The x's indicate the average twin density for each frequency and are shown with their error (standard deviation). 64

Figure 4.1: The layout of the trench samples provided by SKW Associates Inc. (left) and an illustration of the multi-material cross-section of the wafers (right). 69

Figure 4.2: A liftout of the 250 nm trenches, which will be used for TKD. 74

Figure 4.3: The progression of various aspect ratio trench filling over time of deposition. 76

Figure 4.4: The Cu thickness at the trench base over time of the deposition for different organic additive concentrations used in the bath. 77

Figure 4.5: SEM micrographs of the trench cross-sections after 1 minute of Cu deposition. The four aspect ratios of trenches examined in the matrix are shown by the column heading and the organic additives concentrations (of each, in mg/L) added to the bath, are shown by the row. 78

Figure 4.6: SEM micrographs for the 2.78 aspect ratio trench cross-sections deposited with PEG/SPS/JGB (mg/L) concentrations of (a) 0/0/0, (b) 200/5/0, (c) 200/50/10, (d) 200/20/10, (e) 200/5/5, (f) 200/5/10, (g) 200/5/50, and (h) 200/5/100. The images are in descending order of JGB/SPS ratio. 79

Figure 4.7: The three types of voids found in the Cu trench deposits, exemplified by the SEM cross-sectional image of the trenches deposited with 200/5/100 mg/L (PEG/SPS/JGB). 81

Figure 4.8: SEM images of FIB cross-sectioned 2.78 aspect ratio trenches deposited using a PCD of (a) 5 mA/cm^2, (b) 10 mA/cm^2, (c) 20 mA/cm^2, and (d) 80 mA/cm^2. All trenches were deposited using 200 mg/L PEG, 5 mg/L SPS, and 10 mg/L JGB. 83

Figure 4.9: Cross-sections of the 2.78 aspect ratio trenches, where different pretreatments were used prior to Cu deposition: (a) Standard, (b) w/o NH_4OH, (c) heat treated 300 °C for 30 min, and (d) etched for 5s using a ferric chloride etchant. All trenches were deposited without organic additives. 84

Figure 4.10: A surface map of a typical trench sample after deposition, where the red indicates area of increased height and blue represents depressed areas. This image shows the unsymmetrical nature for the radius of curvature due to the samples' blueprint. 86

LIST OF FIGURES (CONT'D)

Figure 4.11: The relative stress in the four directions for radius of curvature measurements. Although the stress measurements differ with direction, the trends remain the same with changing JGB/SPS ratio. Error bars correspond to standard deviations of the measurements. 87

Figure 4.12: The RMS surface roughness with changing JGB/SPS concentration ratio in the bath and various PEG concentrations. 89

Figure 4.13: The relative stress as a function of JGB/SPS concentration ratio in the bath and various PEG concentrations. A change in y-axis by one arbitrary unit equates to ~10-15 MPa of stress. 91

Figure 4.14: The relative stress and void area per trench plotted side by side with respect to JGB/SPS ratio. A change in y-axis by one arbitrary unit equates to ~10-15 MPa of stress. 92

Figure 4.15: Chi rocking curve of the film and trench sample Cu seed layers prior to deposition illustrating degree of (111) preferential orientation is higher for the trench Cu seed layer over the film Cu seed layer. 94

Figure 4.16: A plot of the Cu (111) texture coefficient as the organic additive concentrations in the electrodeposition bath were changed. 95

Figure 4.17: The change in texture coefficient for the (111) and (311) orientations with various JGB/SPS ratio in the bath used to deposit the Cu. 96

Figure 4.18: The band contrast maps of the 250 nm wide trenches (aspect ratio: 2) for the (a) 0/0/0, (b) 200/20/10, (c) 200/5/10, and (d) 200/5/100 samples. The images are in descending order of JGB/SPS ratio. 97

Figure 4.19: The inverse pole figure maps, normal to the sample surface, of the 250 nm wide trenches (aspect ratio: 2) for the (a) 0/0/0, (b) 200/20/10, (c) 200/5/10, and (d) 200/5/100 samples. The images are in descending order of JGB/SPS ratio. 99

Figure 4.20: The inverse pole figure maps of the 250 nm wide trench cross-sections in the normal, transverse and longitudinal directions for the PEG/SPS/JGB (mg/L) concentrations of 0/0/0 and 200/5/100. 100

Figure 4.21: The SIMS spectra revealing the amount of residual SPS and JGB left in the Cu after deposition. 102

Figure 5.1: A cross-sectional band contrast map of the 250 nm wide trenches, with labelled overfill and trench regions. 107

LIST OF FIGURES (CONT'D)

Figure 5.2: The cross-sectional inverse pole figure maps (normal to the sample surface) of the (a) blanket Cu film, (b) 500 nm trench overfill, and (c) 250 nm trench overfill. All samples shown were deposited without organic additives under the same conditions. 109

Figure 5.3: Comparison of the grain size histogram for the blanket films and overfill above the 250 nm and 500 nm wide trenches. Error bars are not present due to sample limitations. 111

Figure 5.4: Grain size histogram of the 250 nm wide trench microstructure deposited with various bath additive concentrations. 113

Figure 5.5: Grain size histogram of the 500 nm wide trench microstructure deposited with various bath additive concentrations. 114

Figure 5.6: The cross-sectional IPF map normal to the sample surface for the 200/20/10 sample. This map shows the grain sizes at the bottom of trenches compared to other areas. 114

Figure 5.7: The cross-sectional inverse pole figure maps in the direction normal to the sample surface for the regions under various geometric constraint and deposited with different organic additive concentrations in the electrodeposition bath. 116

Figure 5.8: The strain component maps for the 0/0/0 and 200/20/10 deposited trenches (250 nm and 500 nm). Blue indicates smaller strains, while red represents larger strains. 118

Figure A1: The inverse pole figure legend for all figures in Appendix A. 145

Figure A2: The band contrast map (top) and inverse pole figure map (bottom) normal to the sample surface for the cross-section of a Cu blanket film, deposited under the PED #1 conditions (frequency: 1 Hz; duty cycle: 0.05). 145

Figure A3: The band contrast map (top) and inverse pole figure map (bottom) normal to the sample surface for the cross-section of a Cu blanket film, deposited under the PED #2 conditions (frequency: 1 Hz; duty cycle: 0.1). 146

Figure A4: The band contrast map (top) and inverse pole figure map (bottom) normal to the sample surface for the cross-section of a Cu blanket film, deposited under the PED #3 conditions (frequency: 1 Hz; duty cycle: 0.25). 147

LIST OF FIGURES (CONT'D)

Figure A5: The band contrast map (top) and inverse pole figure map (bottom) normal to the sample surface for the cross-section of a Cu blanket film, deposited under the PED #4 conditions (frequency: 50 Hz; duty cycle: 0.05). 148

Figure A6: The band contrast map (top) and inverse pole figure map (bottom) normal to the sample surface for the cross-section of a Cu blanket film, deposited under the PED #5 conditions (frequency: 50 Hz; duty cycle: 0.1). 149

Figure A7: The band contrast map (top) and inverse pole figure map (bottom) normal to the sample surface for the cross-section of a Cu blanket film, deposited under the PED #6 conditions (frequency: 50 Hz; duty cycle: 0.25). 150

Figure A8: The band contrast map (top) and inverse pole figure map (bottom) normal to the sample surface for the cross-section of a Cu blanket film, deposited under the PED #7 conditions (frequency: 100 Hz; duty cycle: 0.05). 150

Figure A9: The band contrast map (top) and inverse pole figure map (bottom) normal to the sample surface for the cross-section of a Cu blanket film, deposited under the PED #8 conditions (frequency: 100 Hz; duty cycle: 0.1). 151

Figure A10: The band contrast map (top) and inverse pole figure map (bottom) normal to the sample surface for the cross-section of a Cu blanket film, deposited under the PED #9 conditions (frequency: 100 Hz; duty cycle: 0.25). 152

Figure C1: The weight loss with temperature measured by thermogravimetric analysis of the individual PEG, SPS, and JGB organic additive powders.. 155

Figure C2: The weight loss from TGA of the 200/5/10 mg/L (PEG/SPS/JGB) to determine if this method was sensitive enough to measure a weight change from the small amount of organics used in the Cu. 155

Figure D1: Illustration of voids and seams forming during deposition as well as defect-free bottom-up filling, taken from [30]. 159

Figure D2: A void that formed in a Cu interconnect and is restricting the flow of electrons, taken from [30]. 160

Figure D3: Depiction of (a) prismatic loop emission and (b) shear loop emission mechanisms of void growth by dislocation emission, taken from [38]........ 163

LIST OF FIGURES (CONT'D)

Figure E1: Stress-strain curve demonstrating the areas of elastic and plastic deformation. ... 170

Figure E2: Plastic deformation occurs through slip (a) and twinning (b), taken from [1]. ... 171

Figure E3: A slip system and its components, taken from [2]. ... 172

Figure E4: An edge dislocation (left) and screw dislocation (right), taken from [2]. ... 173

Figure E5: The three regimes of work hardening, taken from [1]. ... 178

Figure E6: Diagram of dislocation pile up creating sources in neighboring grains, taken from [1]. ... 179

Figure E7: The process of dislocation arrangements creating sub-boundaries, grain boundaries, and new grains, taken from [38]. ... 180

Figure E8: The deformation mechanism map for Cu, taken from [41]. ... 182

Figure F1: An illustration of the difference between coherent twins (a) and incoherent twins (b), taken from [3]. ... 188

Figure F2: Comparison between slip (a) and twinning (b), taken from [6]. ... 189

Figure F3: Proposed annealing twin nucleation process, taken from [6]. ... 190

Figure F4: Example of nano-twinned Cu grains, taken from [25]. ... 192

Figure F5: The formation of a recrystallized grain at a triple junction, taken from [16]. ... 192

Figure G1: An SEM image of a recrystallized grain that formed at a triple junction in copper, taken from [28]. ... 205

Figure G2: The preferred direction of boundary movement due to the number of grain sides. ... 208

Figure G3: Two typical types of film microstructures; grain sizes are smaller than the film thickness (left) and columnar microstructure (right), where grains are large and span the thickness of the entire film, taken from [37]. ... 210

Figure G4: An illustration of a surface groove, taken from [41]. ... 213

LIST OF ACRONYMS

2D: Two-Dimensional

3D: Three-Dimensional

ACD: Average Current Density

Al: Aluminum

AR: Aspect Ratio

BEOL: Back End Of The Line

CEAC: Curvature-Enhanced-Accelerator Coverage

Cl^-: Chloride Ion

CMP: Chemical Mechanical Polishing

CTE: Coefficient of Thermal Expansion

Cu: Copper

$CuSO_4 \bullet 5H_2O$: Copper Sulfate Pentahydrate

CVD: Chemical Vapor Deposition

DC: Direct Current

DRIE: Deep Reactive Ion Etching

EBSD: Electron Backscattering Diffraction

ECD: Electro-Chemical Deposition

EM: Electromigration

FCC: Face Centered Cubic

FEOL: Front End Of The Line

FIB: Focused Ion Beam

H_2SO_4: Sulfuric Acid

LIST OF ACRONYMS (CONT'D)

HCl: Hydrochloric Acid

IC: Integrated Circuit

JGB: Janus Green B

IPF: Inverse Pole Figure

LMIS: Liquid Metal Ion Source

NH_4OH: Ammonium Hydroxide

OA: Organic Additives

PCD: Peak Current Density

PED: Pulse Electrodeposition

PEG: Polyethylene Glycol

PVD: Physical Vapor Deposition

RF: Radio Frequency

SEM: Scanning Electron Microscope

Si: Silicon

SPS: Bis(3-Sulfopropyl) Disulfide

Si_3N_4: Silicon Nitride

Ta: Tantalum

TB: Twin Boundary

TC: Texture Coefficient

TEOS: Tetraethylorthosilicate

Ti: Titanium

TKD: Transmission Kikuchi Diffraction

LIST OF ACRONYMS (CONT'D)

TSV: Through Silicon Via

WLI: White Light Interferometer

XRD: X-Ray Diffraction

CHAPTER ONE:

MOTIVATION AND OBJECTIVES

1.1 Motivation

The use of copper in modern microelectronics is unmatched for its low electrical resistance, high electromigration resistance, and low cost. Copper replaced aluminum as the material of choice for interconnects in the late 1990's [1]. Furthermore, copper can be deposited quickly, over a large area, at low cost, through electroplating techniques. With Moore's Law expected to come to an end in the near future and the *More-than-Moore* era taking over, people are looking to interconnects to provide a pathway for vertically integrated devices [2,3]. These three-dimensional integrated circuits (3D-IC) feature better form factors, heterogeneous integration, and higher performance over traditional ICs. The enhanced performance can be attributed to shortened electrical and communication paths in stacked chips. In 3D-IC global interconnect schemes, high aspect vias (i.e., via depth to width ratio on the order of 15:1), also called 'through silicon vias (TSVs)' are frequently filled with deposited metal (e.g., Cu) and have improved resistance and less signal delay over other interconnects such as wirebonds, due to their shorter path lengths [4,5]. Typical dimensions of TSVs in a state of the art 3D-IC global interconnect level application have a minimum diameter between 2 and 4 μm and a minimum depth between 30 and 50 μm [6]. .

Filling of such high aspect ratio vias with copper can be difficult. Performance limiting defects such as voids, or air pockets, can form in the vias.

The extreme of this condition can prevent current from flowing through the interconnect. To create an optimal via filling profile, three types of organic additives (suppressors, accelerators, and levelers) are typically used by commercial integrated circuit (IC) manufacturers, as they have been found to result in better filling efficiencies. While commercial use and compositional information on additives is largely proprietary, many studies have been conducted to determine the influence of the organic additives on via filling efficiencies [7-12]. Hence, while this information assists in understanding efficiencies, the specific effects of these additives on the copper's more global physical properties and microstructure *within the via* are still largely unreported. Of specific interest in the present dissertation, is the role of these additives on film microstructure and the corresponding defects and stress that are dependent on Cu film processing route. This inter-relationship is something to date which has not been specifically examined in the context of Cu film processing.

Thermo-mechanical reliability issues can also arise in these multi-material systems after via filling has been completed. As shown in Table 1.1, Cu has much different properties than the silicon (Si) and silica (SiO_2) [13] neighboring materials present in IC devices. The coefficient of thermal expansion (CTE) for Cu is ~8 times greater than that of Si. During the later stages of the chip fabrication, heating is necessary to bond stacked chips. Additionally, current passes through the Cu structures during the IC's use, causing Joule heating to occur from the collisions of electrons and Cu atoms. As the system heats up from these various sources of temperature fluctuation, Cu can expand more rapidly than the neighboring Si

leading to within-via stresses. To relieve these stresses, voids can form in the Cu to dissipate the stresses, further adding potential surfaces that lead to signal loss from scattering. Numerous studies have used thermal cycle testing to simulate and predict the reliability of Cu through-silicon vias (TSV), in actual use [14-16]. These studies have found thermal cycling induces void nucleation at device interfaces, which can impact device signal integrity.

Table 1.1: The thermo-mechanical properties of silicon, silica, and copper, taken from ref [13]**.**

Material	Young's Modulus (GPa)	Poisson Ratio	Coefficient of Thermal Expansion (ppm/°C)
Silicon (Si)	169	0.26	2.3
Silica (SiO_2)	75	0.17	0.5
Copper (Cu)	117	0.3	16.7

Understanding the relationship between film processing conditions, bath chemistry and the resulting post-processing properties, defects and film microstructure can assist in defining expectations on device performance. Tuning the copper film's microstructure may be the key to preventing substantial thermo-mechanical stresses and corresponding deleterious void formation. Since Cu is elastically anisotropic, creating preferential crystallographic orientations of Cu within the vias (with respect to the via sidewalls) provides a means by which the deposited material can potentially be made more resistant to thermally-induced stress and accompanying defect formation.

Not all microstructural features are adverse; for example, the presence of twinning in the Cu microstructure has been shown to enhance mechanical strength without sacrificing electrical performance [17,18]. How such microstructural

features are related to processing conditions, the effect of additives and the aspect ratio of features approaching the geometry of vias, is a key theme of this dissertation.

1.2 Objectives

While this study does not explicitly include IC reliability measurements on the structures that were fabricated, it does aim to investigate defect formation due to the deposition process, the impact of feature dimensions, and the role of additives and other deposition parameters to promote specific microstructural attributes. These data are collected with the focus on understanding inter-relationships with the goal of optimization of processing route and resulting microstructure of the Cu, for increased interconnect reliability. Prior work by our team [14,15,19] and others [16,20,21] have evaluated the role of defects IC performance and reliability.

The influence of geometric constraints (specifically, how transitions from blanket films to trenches of varying dimensions) on the Cu microstructure will also be investigated to predict the material's response at much higher constraints, approaching high aspect ratios of through-silicon vias. How additives impact the resulting microstructure, and the application of this knowledge in engineering deposition conditions to reduce via defects and enhance preferential orientation of the Cu, will also be examined.

Pulse electrodeposition (PED) was used as the Cu film deposition method, using a two electrode galvanostatic setup, with a typical acid-based Cu electrolyte.

Specific organic molecules (viz., polyethylene glycol, bis-(sodium sulfopropyl)-disulfide, and janus green-b), that are common in the deposition of Cu, were added to the electrodeposition bath to increase the throwing power (defined as the capability to deposit uniform thicknesses onto complex topographies) of the Cu deposits and reduce the likelihood of creating defective Cu filling into advanced geometries. Coupon samples, 20 mm x 20 mm in size, were fabricated and found to have distinctive post-deposition geometric topographies as a function of the deposition conditions. Blanket films and trenches of varying aspect ratio were chosen for the investigation, and the following objectives formed the primary focus of the effort.

Specifically, this study aimed to:

1. Examine the impact of pulse electrodeposition duty cycle and frequency on the copper microstructure and link these microstructural characteristics to the biaxial residual stress and other physical properties.
2. Analyze the effect of organic additive concentration in the electrodeposition bath on the processes ability to fill 500 nm deep trenches with aspect ratios varying from 0.25 to 2.78.
3. Study the influence of the organic additive concentration on the deposited trench microstructures and stress state.
4. Determine the significance of geometric constraints on the Cu microstructure by investigating trenches of varying size and less confined Cu areas.

Based on the current state of the art in the literature, we hypothesized that the duty cycle and frequency of the Cu film deposition process will have a major impact on the resulting microstructure of the Cu, especially the extent of (desirable) twinning. The organic additives are expected to impede grain growth, resulting in much finer microstructures, an undesirable attribute for electrical resistance, but improves the material's mechanical strength. Furthermore, higher geometrical (i.e., high aspect ratios) constraints in the Cu deposits are expected to produce highly stressed Cu deposits due to the increased interface area between the Cu and surrounding materials. The increased stress in these area is expected to result in larger twin densities. The more confined Cu should also contain much finer grains and the increasing influence of trench sidewalls will result in changes to the Cu grain orientations. How these assumptions and their expected impact on envisioned device performance play out as a result of our experimental investigation are discussed herein.

1.3 Thesis Scope

This thesis is laid out as follows: Chapter Two is a detailed background on the subject-areas pertinent to the present study, and the latest literature in the field. Details of the pulse electrodeposition of blanket Cu films, including pulse plating parameters studied and their impact on the film microstructure are described in Chapter Three. Chapter Four contains a summary on the filling of more advanced geometries (trenches) and studies the influence of organic additives on the depositions and resulting film quality and microstructural attributes. Chapter Five compares the resulting film microstructure of minimally constrained blanket Cu

films to that of the increasingly constrained Cu trenches of higher aspect ratio to give insights into the microstructure that might be expected in the formation of very high aspect ratio features, such as through-silicon vias. Chapter Six summarizes the dissertations' key conclusions and future work.

CHAPTER TWO:

BACKGROUND

This chapter aims to review basic background information on the fabrication and thermo-mechanical reliability issues of interconnects in integrated circuits (ICs). The fundamentals of pulse electrodeposition and filling of advanced features (such as trenches and vias) are also discussed. Moreover, this chapter outlines the key microstructural features which may prove to be beneficial to the reliability of interconnects, as well as state of the art understanding of the impact electrodeposition has on these features.

2.1 Integrated Circuits (IC)

2.1.1 What are integrated circuits?

An integrated circuit (IC) is a semiconductor wafer which contains many electronic circuits. These electronic circuits consist of various components, like resistors, capacitors, and transistors. Transistors were possibly the most significant invention of the 20th century, replacing the vacuum tube in the 1950's. Transistors serve as signal amplifiers and switches within an integrated circuit and a single IC can contain billions of these devices. Modern electronics strive to pack as many transistors into a chip as possible, since a great number transistors equates to better performance of the chips. Moore's Law states that the number of transistors double approximately every 18 months as predicted by an observation of Gordon Moore in 1965 [22]. With the development and

manufacturing of Intel's 14 nm node in 2014, Moore's Law appears to be slowing and many believe is at the risk of ending [23]. Current lithographic techniques used in the 'printing' of the IC structure are reaching their spatial limit (wavelength and thus, smallest feature size) and succeeding 10 nm nodes (expected in 2017) will be difficult to realize with expected quantum effects constraining ultimate feature size goals as we approach the atomic length scale.

Alternatively, more transistors and greater performance can be achieved by stacking chips vertically, in an approach that is commonly referred to as *Moore-Than-Moore*. Such geometries as the three-dimensional integrated circuits (3D-IC),shown in Figure 2.1, not only benefit from improved performance, but also achieve higher levels of heterogeneous integration, reduced power consumption, and better form factors over their traditional IC counterparts [4,24,25]. By vertically integrating chips with different functions, the bottleneck for performance increases is shifted from downscaling of the transistors to the interconnects, which allow current to flow between all the devices on a chip.

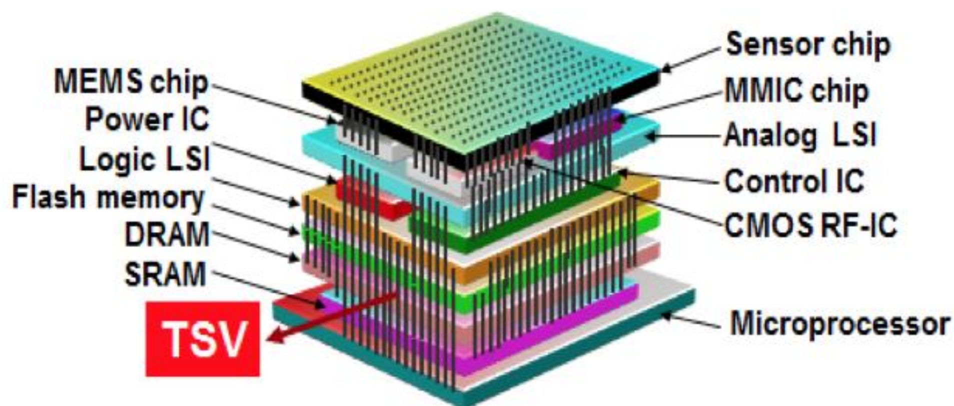

Figure 2.1: An illustration of a 3D-IC taken from ref [26]**.**

2.1.2 How are 3D-ICs fabricated? (middle of the line)

The integrated circuit fabrication process is a very complex process incorporating many individual processing steps and a diverse range of (dissimilar) materials. Figure 2.2 shows a common step by step process for middle of the line IC production. The semiconductor wafer is typically sliced from a silicon single crystal boule grown by the Czochralski process [27]. First, the devices, including the transistors are installed onto the wafer in what is called the front-end-of-the-line (FEOL) processing steps. The through-silicon-via (TSV) holes are created next by dry reactive ion etching (DRIE). This is followed by the deposition of the isolation liner and barrier layer by chemical vapor deposition (CVD) and physical vapor deposition (PVD) respectively. The isolation liner is typically made of tetraethylorthosilicate (TEOS) and serves the role to prevent current from leaving the interconnect. The barrier layer, usually a tantalum (Ta) or tantalum nitride (TaN) film, prevents diffusion of the copper from the interconnects into the silicon substrate. Next, a copper (Cu) seed layer is then applied by PVD and is used as the cathode for the Cu electrodeposition filling process. The excess Cu is removed and the surface is planarized by chemical mechanical polishing (CMP). The TSV process is followed by the application of the back-end-of-the-line (BEOL) components through a damascene process. The BEOL consists of many metallization layers, each containing the necessary interconnects to bridge all the devices from the FEOL. The metallization layers are deposited similarly to the TSV process. A blanket layer of the isolation material (TEOS) is deposited first. This layer is then etched and followed by the barrier and Cu seed layer depositions.

The Cu is electrodeposited into the patterns, planarized through a CMP process and coated with a silicon nitride (Si_3N_4) layer. This process is then repeated until all levels of interconnects are in place and the chips are bonded together and then packaged.

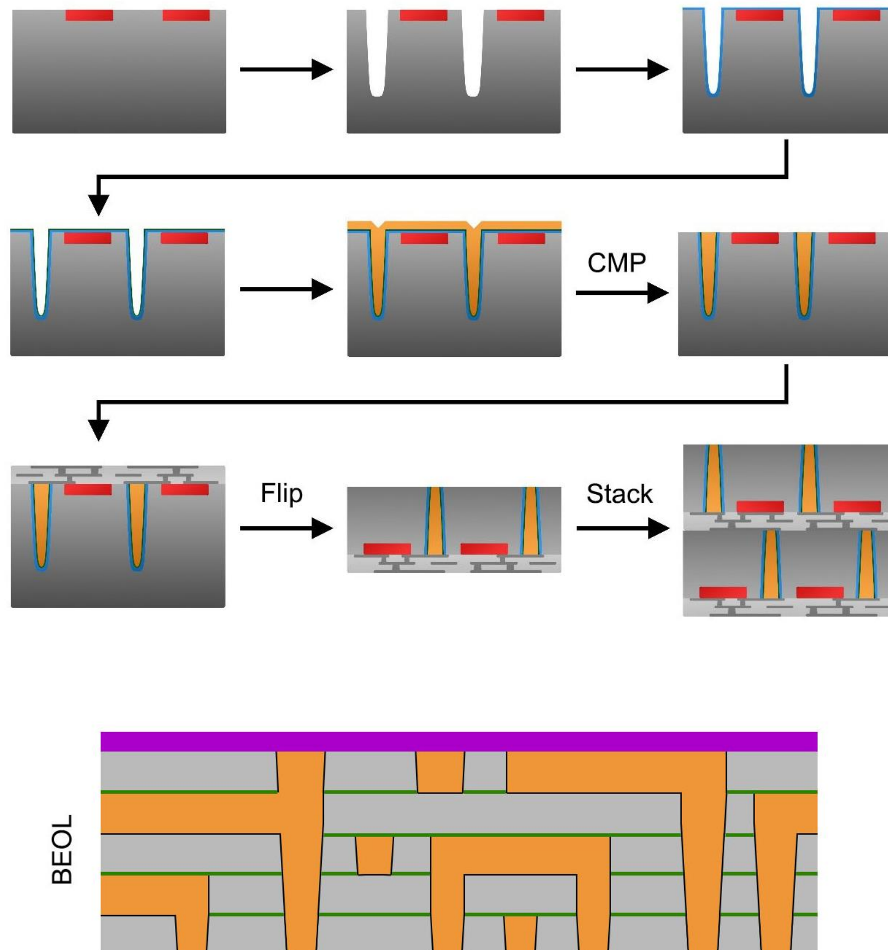

Figure 2.2: A step by step approach to middle of the line via formation and BEOL fabrication.

2.2 Thermo-Mechanical Reliability Concerns

While the benefits of vias was generically discussed in section 2.1.1, there are still thermo-mechanical reliability concerns for the Cu used to fabricate the TSVs. The multi-material systems associated with microelectronics, do not lend

themselves easily to defect-free devices. The mismatch in coefficient of thermal expansion (CTE) between copper (Cu) interconnects and silicon (Si) wafers is 16.7 ppm/°C and 2.3 ppm/°C respectively [13]. The variation of expansion rates between the two materials upon exposure to heat results in the formation of stresses, not only in the Cu, but also the surrounding Si [28-31]. Temperature fluctuations in electronic chips occur during processing, with varying environmental conditions during fabrication, and during use where current flow can produce Joule heating in the Cu interconnects.

The by-product of local stress buildup in a material is typically the formation of voids. Voids are areas or pockets of missing material, which form to relieve stresses by distributing them over a larger area [28,32]. Voids create interfaces which serve as scattering centers for signal transport through the Cu. Furthermore, electromigration (EM), or the mass transport of Cu atoms during current flow, is also a concern for void formation and their subsequent growth which typically occurs by diffusion processes. The phenomena of void nucleation and growth in Cu will be discussed in detail throughout this overview, as well as the affects these voids have on Cu's material properties and their corresponding role in IC device performance. Where applicable, mitigation strategies to avoid voids and how these have impacted processing route choices in the present study, are noted.

2.2.1 Void Nucleation

As mentioned in the opening chapter, voids can form as a mechanism of stress relief [28,32] or simply result from use of a poor filling technique. Thus, post-deposition regions within the Cu film that contain high stress concentrations are

more prone to void nucleation. This occurs most commonly at interfaces, triple junctions, and grain boundaries, as depicted in the schematic of the Cu microstructure in Figure 2.3 [33-38]. Upon heating, the elastic anisotropy of Cu grains result in stress at interfaces, where the crystallographic orientations are significantly different [35]. The elastic anisotropy of copper is discussed in further detail in section 2.4.1.2. Additionally, grain boundaries provide a diffusion path for vacancies to migrate, coalesce, and become voids [36,39,40]. While voids frequently nucleate at twin/grain boundary junctions [35], voids are less likely to form at {111} coherent twin interfaces compared to incoherent twin boundaries, such as {322} textured twins, and at high angle grain boundaries. This can be attributed to the significantly lower interfacial energy and grain boundary diffusivity of coherent twins [36,39]. From an energetic standpoint, coherent twin boundary energy in Cu is estimated at 21 mJ/m^2. This is in contrast to the energy of an incoherent grain boundary (498 mJ/m^2) and 623 mJ/m^2 for the grain boundary energy of high angle (>15°) grain boundaries [41,42]. These findings have been further exemplified by an investigation of Nucci *et al.*, who observed less voids in strongly textured <111> Cu films than in randomly oriented or weakly textured Cu films [43]. Hence, achieving <111> orientation in as-deposited Cu films is desirable and will be a target in this effort.

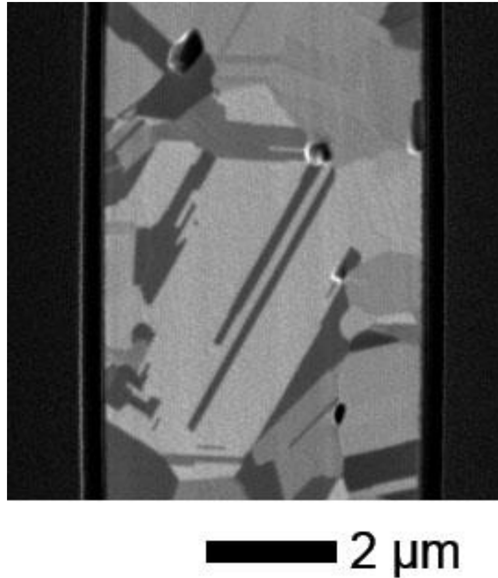

Figure 2.3: Optical micrograph illustrating triple junctions and grain boundaries in the Cu microstructure are susceptible to void formation due to their higher stress concentrations. Image from ref [15]**.**

Creep and fatigue processes can both induce void nucleation in Cu; however, fatigue has been found to produce a much more rapid void nucleation rate [33]. Void nucleation has been found to be strain rate dependent. Thus, larger strain rates have been shown to result in the nucleation of more voids and a decrease in void spacing in Cu [38].

Nucleation of voids in microelectronics differs from that observed in bulk materials in that edge effects of air interfaces or that of surrounding media, a.k.a. via walls, need to be taken into account. In microelectronics, Cu interconnects, damascenes, and vias are dimensionally restricted by the neighboring Si. Voids still can form at triple junctions in the center of these devices, however, as dimensions, such as linewidths (the width of interconnect lines), become smaller, less voids are typically formed at the center of these lines and most void nucleation sites are expected to be limited to the interface between the Cu and external

materials (edges) [44]. As interconnect linewidths reduce resulting in smaller Cu grains, one might expect that the Cu film's microstructure is more likely to take on bamboo-like grain morphologies, where the grains span the full width of the interconnect. Triple junctions are usually sparse in these structures, and voids are typically limited to nucleation at the intersection of grain boundaries and the Cu/diffusion barrier interface [44]. Here, high stresses (~ 160MPa), due to high temperature (723 K) heat treatments, has been shown to cause delamination of the Cu and has resulted in interfacial void formation in damascenes [37]. Furthermore, stress-induced voids have been observed at the interface of thermo-compression Cu bonded wafers and void size has been shown to be directly correlated with bonding temperature (typically ~ 300-400 °C) [45]. Bonding temperatures are typically much higher than in-service temperatures seen in consumer electronics, where operating temperatures are expected to stay under 100 °C. An exception may be found in extreme applications, such as aerospace and military conditions [46].

Stresses observed in Cu through-silicon vias (TSV) have been quantified through x-ray micro-diffraction [28-30,47]. Budiman *et al.* found high deviatoric shear stresses (~145 MPa) and hydrostatic tensile stresses (~165 MPa) in the Cu-TSVs after a 200°C 1 hr. anneal [30]. Thermo-mechanical stresses like these, can result in the formation of voids in TSVs and an overall reduction in tensile stresses in the Cu as demonstrated by Shin et al. [28].

2.2.2 Void Growth

The growth of nucleated voids has been observed in Cu, following heat

treatments [32]. The two primary mechanisms of void growth in Cu are through vacancy diffusion and dislocation emission. Vacancy diffusion is the dominating mechanism in Cu, which endures strain rates between 10^{-5} s^{-1} and 10^{8} s^{-1}, while dislocation emission is dominant at higher strain rates [34,48]. Vacancy diffusion along grain boundaries as a method of void growth has been observed in many studies [33,35,39]. Since this is a diffusion-based process, it is both time and temperature dependent. Voids located adjacent to these diffusion pathways are capable of coalescing as they come in contact from their growth along grain boundaries [33,34,49]. Specific Cu grain crystallographic orientations have been shown to influence control over void growth, since grain boundary diffusion is necessary for vacancy mobility. Strongly textured films contain far more tilt boundaries than twist boundaries, which are more susceptible to grain boundary diffusion of vacancies [43]. Thus, void growth may occur more readily in randomly textured Cu as opposed to strong textured Cu microstructures.

Voids can also grow by emitting dislocations from their surfaces into the surrounding grains [38]. Lubarda *et al.* did an extensive study on void growth by dislocation emission [48]. As mentioned earlier, this dislocation process occurs at strain rates above ~10^{8} s^{-1}. Void growth by dislocation emission can be broken down into two types, prismatic and shear loop emission. As shown by the illustration in Figure 2.4, both occur at 45° from the void centers. Prismatic loop emission transpires as a section of a spherical void is extruded outward from the void center, increasing the volume of the void. While dislocation emission occurs normal to the void's center in prismatic loop emission, shear loop emission occurs

by emitting a dislocation along the slip plane in which the spherical void is sectioned. The void then expands in a shear-like manner along the slip plane. Smaller voids require more stress for dislocation emission compared to larger voids, thus void growth through dislocation emission is size dependent [48]. Larger voids on the other hand, grow preferentially along grain boundaries due to partial dislocation emission from grain boundaries in close proximity to voids [49].

As noted previously, twins and their boundaries can play a beneficial microstructural role in the Cu of IC applications. Twin boundaries can impede dislocation emission and ultimately void growth [50]. Furthermore, twin boundaries spacing can limit the growth of these voids by blocking the migration of dislocations [51].

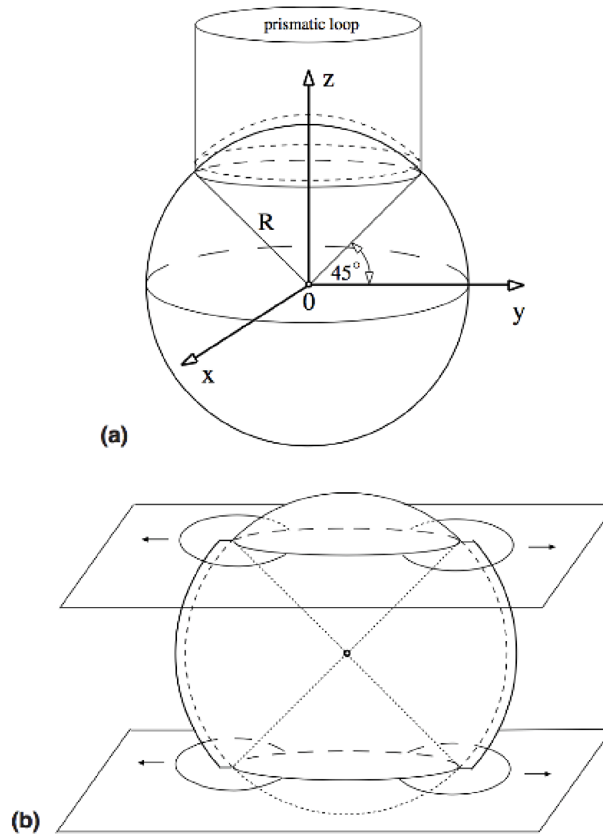

Figure 2.4: Depiction of (a) prismatic loop emission and (b) shear loop emission mechanisms of void growth by dislocation emission, taken from [48]**.**

2.2.3 Void-Induced Material Property Changes

The nucleation and growth of voids in Cu may have a negative impact on its material properties and ultimate device performance. The electrical resistance of the Cu is not considerably affected by voids as compared to cracks in the film microstructure; this tendency is usually found unless the void spans the width of a Cu interconnect and forces the signal to propagate through the metallization layer [16,52]. On the other hand, radio frequency signal scattering has been observed as a result of void clustering or concentrations (on the order of 200 to 1000 nm in size) in Cu [14,53,54]. Molecular dynamic simulations have shown the effect voids have on Cu's mechanical properties. Larger void sizes and volume fractions lower

the yield strength and elastic modulus of Cu [49,55]. Simulations indicate that voids nucleate at grain boundary/void interfaces and from the surfaces of voids in the direction of the maximum resolved shear stress [49]. Although twin boundaries are thought of as mechanical strengthening tools, voids located at twin boundaries can actually result in much lower yield strengths (~40-55% reduction) depending on void size within the system [49]. Lastly, one might expect the influence of such defects to be adverse to a metal's mechanical properties. In metals, the presence of voids has been attributed to lower ductility and toughness [56].

2.3 Electrodeposition

2.3.1 Electrodeposition Basics

Electrochemical Deposition, also known as electrodeposition or electroplating, is an electrolytic process which utilizes the oxidation and reduction of metal ions to deposit said metal onto a surface. The process is used to deposit Cu interconnects in microelectronics since it's inexpensive and can yield high deposition rates. A metal anode and conductive cathode is placed in an electrolyte, often containing the metal to be deposited. Once a current is applied to the system, the oxidation of the metal takes place at the anode and reduction occurs at the interface between the electrolyte and cathode to form the deposited film. In the case of copper, the metal loses two electrons at the anode interface and oxidizes to Cu^{2+} at the cathode as shown in the reaction below [1]:

$$\mathrm{Cu} \leftrightharpoons \mathrm{Cu}^{2+} + 2e^- \quad \text{(Eq. 2.1)}$$

A conventional Cu electrodeposition bath contains copper sulfate ($CuSO_4$) and sulfuric acid (H_2SO_4). The $CuSO_4$ contains the Cu, which ionizes and is transferred

to the cathode. If an inert anode, such as platinum, is used, the $CuSO_4$ concentration needs to be carefully monitored, however, in the case of a soluble anode, the Cu ions will be replenished by the Cu anode. The H_2SO_4 increases the conductivity of the solution and the uniformity of deposition. Chloride ions (Cl^-) are added to the bath in the form of hydrochloric acid (HCl) to reduce anode polarization [57]. The Cl^- also serves as a bridge for some organic additives to the cathode surface [7,57], which will be discussed later in the Chapter.

2.3.2 Pulsed Electrodeposition

Unlike conventional direct current (DC) electrodeposition, pulse electrodeposition (PED) periodically pulses the current during deposition. Figure 2.5 displays a typical pulse electrodeposition square pulse wave. Peak current density (PCD or J_p) is achieved in the pulse on-times (t_{on}) and the current is switched off during the off-times (t_{off}). The average current density (ACD or J_a) can be calculated through the following equation:

$$J_a = J_p \times D \quad \text{(Eq. 2.2)}$$

,where the D is the duty cycle and duty cycle is characterized by:

$$D = \frac{t_{on}}{t_{on}+t_{off}} \quad \text{(Eq. 2.3)}$$

When the current is flowing, a diffusion layer is formed at the cathode/electrolyte interface. In this region, the metal ion concentration is depleted compared to the bulk electrolyte. The off-times in pulse electrodeposition dissipate this region, allowing a more uniform metal ion distribution in the bath [58]. The result is more dense deposits and higher throwing power, or more uniform deposits [59]. While

DC electrodeposition is faster and has the highest theoretical current efficiency, PED grants superior control over the deposition process. On and off-times can be altered to change the pulse's duty cycle and frequency.

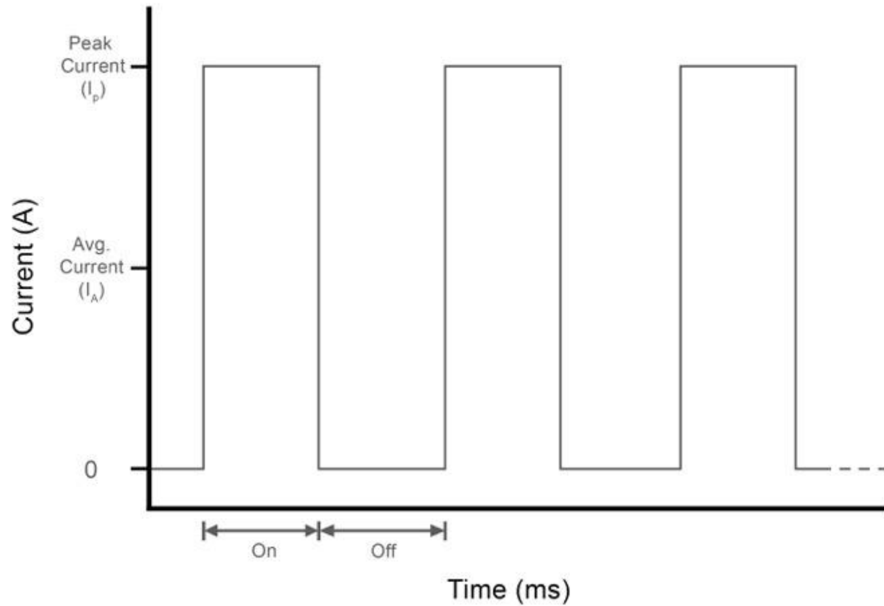

Figure 2.5: A typical PED pulse wave, labelled with the pulse parameters.

2.3.3 Advanced Geometry Filling

Blanket film deposition is fairly straight forward and offers few 'boundaries' beyond the film's surface to impact or impede film growth. Conversely, the filling of Cu into advanced geometries, such as trenches, damascenes, and vias is a complex process, that can yield many defects. Deposition parameters can largely affect the formation of seams and voids in these devices. Slower deposition rates are typically found to produce films with lower void densities in trenches. This can be achieved through lower current densities [60,61] and choosing the optimum off-time for the PED process' pulse cycle [62]. The optimum off-time has been found

to be dependent on trench height and diffusivity of the copper ions [62]. The traditional filling of these trenches, from the sidewalls to their centers, can result in non-uniform deposition and trapped air in the trenches as shown in Figure 2.6. Bottom-up filling, also known as super-filling or super-conformal filling, is less susceptible to void formation than this conventional deposition method [61,63-65]. This can be achieved through selective PED chemistries, which has also been shown to dictate the resistance to void formation in TSVs [66,67].

Bath additives, such as polyethylene glycol (PEG), bis(3-sulfopropyl) disulfide (SPS), and janus-green-b (JGB), have been shown to improve quality of the PED fill in Cu structures, yielding films with lower quantities of voids [60,68]. These three organic additives are frequently used in the filling of features and each serve a purpose in affecting the local deposition rate of the Cu. Suppressors, like PEG, inhibit the growth of copper on macro-steps of feature sidewalls and openings [7,69]. PEG forms complexes with the Cu^{2+} in the presence of Cl^- at the cathode surface, which results in the inhibition of Cu adatoms [12,70,71]. Accelerators are typically sulfur-based organics such as SPS, that act as a catalyst for Cu deposition into the features due to the postulated formation of cuprous thiolate [12,72]. Accelerators are often referred to as brighteners for the way they change the physical appearance of depositions. The last type of organic additive used in copper plating solutions is the leveler. The leveler is typically an organic dye that contains nitrogen, such as JGB, and acts as an inhibitor similar to the suppressors. The leveler functions to prevent overfill bumps above the features by inhibiting high current density deposition areas [7]. Such a reduction in overfill

reduces the time required for subsequent, post-fill planarization. The PEG, SPS, and JGB molecules are illustrated in Figure 2.7 and their expected surface contribution on the cathode is shown in Figure 2.8.

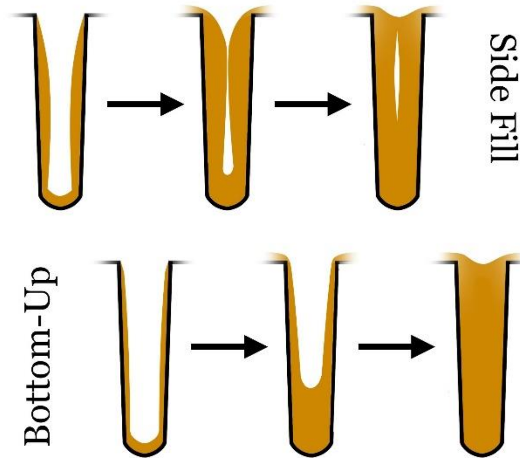

Figure 2.6: Illustration of voids and seams forming during deposition as well as defect-free bottom-up filling, taken from ref [15]**.**

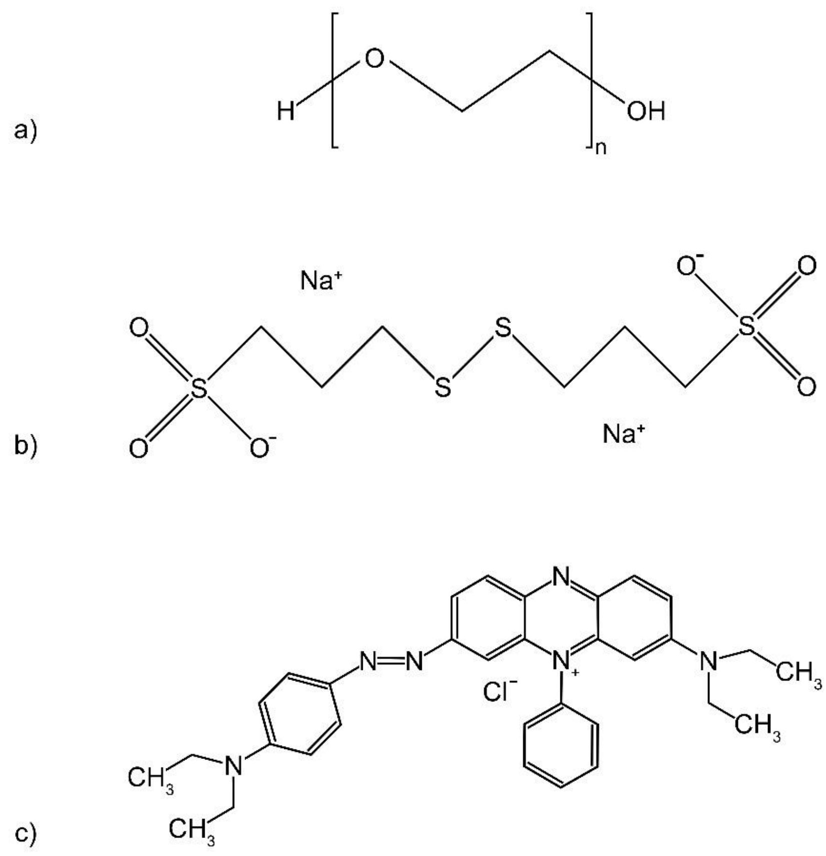

Figure 2.7: The chemical makeup of PEG (a), SPS (b), and JGB (c).

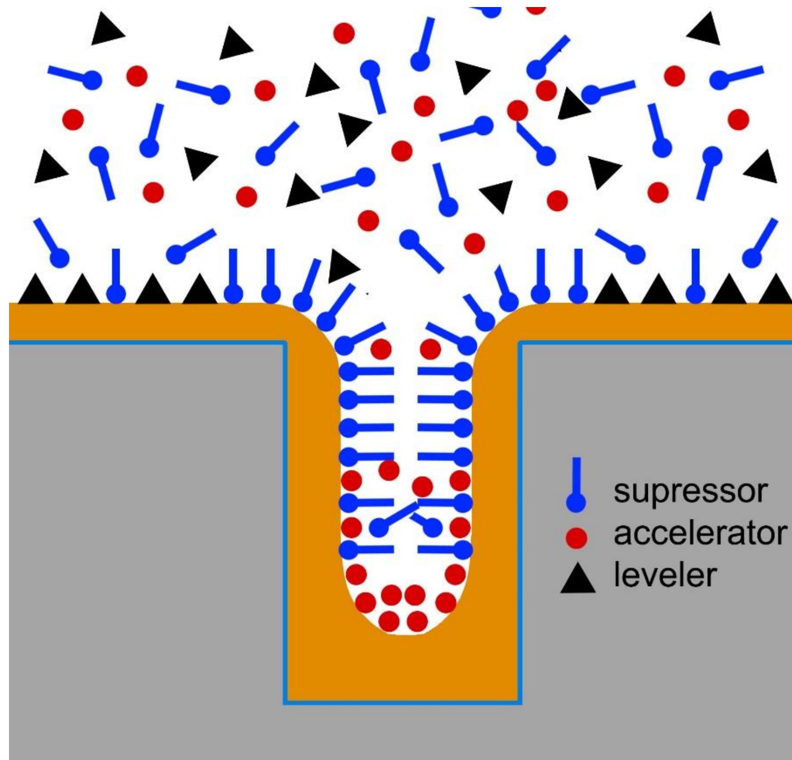

Figure 2.8: The theorized location of the suppressor, accelerator, and leveler organic additives on a Cu cathode containing advanced features.

Several models for the mechanism of bottom-up filling have been proposed and validated experimentally. The most widely accepted model has been proposed by Moffat et al., called the curvature-enhanced-accelerator coverage (CEAC) model [72-75]. Key assumptions in this model include the consumption of accelerator is minimal and surface coverage of the accelerator is directly proportional to the local deposition rate [72]. The filling of advanced features is thought to be controlled by the competition for surface sites between the accelerator and suppressor [76,77]. The CEAC model describes the mechanism for accelerator coverage as being dependent on the curvature of the surface within the features. This curvature changes as the filling process progresses, which explains the conformal filling at the initial stages of deposition and the overfill

bumps that occur once filling is completed [72,77,78].

2.4 Copper Microstructure

The final copper (Cu) film microstructure which results from the selected deposition method, specific experimental processing conditions, and bath/additive chemistries used, can dictate the electrical and mechanical properties of the Cu material and, ultimately, final device performance. As discussed previously, the Cu microstructure may hold the key to more reliable microelectronic interconnects. In this section we will discuss the benefits of certain Cu microstructures for microelectronic interconnects and what is known about using the electrodeposition process to tune it.

2.4.1 Desired Microstructure for Microelectronics

2.4.1.1 Grain Size

Grain boundary strengthening is the refinement of a material's microstructure, specifically the use of grain size, to improve its strength. The Hall-Petch relationship shown in equation 2.4 [79] displays how yield stress is altered by a material's grain size;

$$\sigma_y = \sigma_i + \frac{k_y}{\sqrt{d}} \qquad \text{(Eq. 2.4)}$$

where σ_y is the yield stress, σ_i is the flow stress or onset of dislocation motion, k_y is a material dependent strength constant, and d is the average grain size of the material. Since grain boundaries prevent the glide of dislocations, materials with smaller grain sizes have higher yield strength due to their larger grain boundary

area. As a slip bands intersect with obstructions like grain boundaries, the dislocations can pile up creating stress concentrations. This gives rise to a stress source in an adjacent grain, which will allow slip until another obstacle is reached [79,80]. This process is illustrated in Figure 2.9.

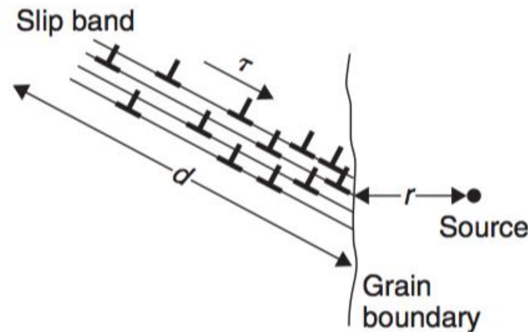

Figure 2.9: Diagram of dislocation pile up creating sources in neighboring grains, taken from [79]**.**

However, increasing the grain boundary area by grain size refining comes at a cost. Smaller grain sizes require electrons to pass through more grain boundaries and these boundaries scatter electrons. Thus, more grain boundary area can significantly increase resistivity in Cu films and interconnects [81-86].

2.4.1.2 Crystallographic Orientation of the Copper film

Further evidence that tuning Cu's microstructure may be beneficial for the reliability of microelectronic interconnects, is Cu's orientation-dependent material properties. Copper is elastically anisotropic, meaning its elastic modulus is dependent on the crystallographic direction. Larger elastic moduli would reduce the strain imparted on the material from the thermo-mechanical stresses created in the Cu. Since copper has a large elastic modulus in the <111> direction (~150

GPa compared to ~100 GPa in the <100> direction [87,88]), having a (111) Cu texture perpendicular to the interconnect interfaces would theoretically be the least susceptible to stress-induced defects in the Cu and increase the device's overall reliability.

Prior work has shown that Cu blanket films can be deposited with (111) and (110) textures [89-92]. This resulting film texture is dependent on several known factors. The substrate plays an important role in determining the Cu orientations and plated Cu tends to mimic the texture of seed layer as the adatoms build atop one another [89,93-95]. Typically, Cu films with smaller thicknesses are preferentially (111)-oriented, while larger thickness films have greater (110) orientations present due to the difference in grain growth mechanisms [96,97]. The surface energy and interfacial energy has a more prevalent role in thin film grain growth compared to bulk, since a larger percentage of grains are affected by the surfaces, especially in columnar microstructures. These energies are dependent on grain orientations. To minimize the surface/interfacial energy of the films, growth in grains that have an orientation of lower surface energies dominate and cause preferential orientations in the material [98-101]. Grains of (111) orientation typically have lower surface energies and thus dominate in surface/interfacial energy driven grain growth [102,103]. The evolution of grain orientation in films is quite complex, since the surface/interfacial energy-driven grain growth competes with strain energy density-driven grain growth in films. Zielinski *et al.* found a deposition temperature dependence of abnormal grain growth, which can determine the dominating driving force. Higher deposition temperatures result in

lower yield stresses in the films and leave less room for strain energy build up, thus abnormal grain growth is driven by interfacial/surface energy with a higher area of (111) oriented grains. At lower deposition temperatures (100) oriented grains are favored from the elastic anisotropy of Cu creating strain energy density differentials [102]. Furthermore, (100), (110), and (511) oriented grains have been shown to have lower strain energy densities and the preferential grains for growth during strain energy density driven grain growth [99,101,103,104]. Post-deposition heat treatments can transform highly (111)-dominated Cu microstructures to these strain energy density-favored orientations [103], and high temperature anneals (above 300 °C) have resulted in grain growth of (100) oriented grains to minimize overall strain energy densities in Cu that contains many nanometer sized twins (nano-twinned Cu) [101,105].

In work by Anderoglu et al., highly twinned films were shown to have (111) preferentially oriented microstructures, which were very thermally stable [105], since twin boundaries are low energy boundaries and require more temperature/energy to cause boundary migration [106]. Like films, (111)-oriented Cu has also been achieved in smaller aspect ratio damascenes and trenches [107-109], however, only randomly oriented Cu has been filled into high aspect ratio features, such as TSVs [14,19,28,110,111]. This behavior is studied in depth in this effort, investigating the role of bath chemistry (additives) on the microstructure of both blanket and low aspect Cu structures.

2.4.1.3 Twinning

Copper has the ability to twin, especially after annealing, but deformation

twins may also form when a sufficient mechanical load is imparted. In either instance, these twins are noted repeatedly in this introduction as beneficial for the resulting Cu properties and its ability to cope with stress. Recently, there has been a resurgence of work on nano-twinned Cu for its excellent mechanical strength and low resistivity, which may lend itself to applications in microelectronics [17,18].

Twins are two grains that have mirrored atomic structures across a common boundary, known as a twin boundary (TB). Twin boundaries (TB) are specific types of high angle grain boundaries. A coherent twin occurs when the twin plane and TB are superimposed, meaning atoms line up across the boundary as shown in Figure 2.10a. In an FCC metal like Cu, coherent twins are {111} grains that have been twisted 60° or 180° about the <111> direction. To achieve a coherent twin with pure tilt, a tilt angle of 70.53° about the <110> is necessary [41,112]. Due to this atomic alignment, coherent twin boundaries have much lower energy than boundaries of incoherent twins, twins that have an angle, ϕ, of offset between the twin plane and TB. An illustration of incoherent twins is shown in Figure 2.10b. Specifically, coherent twin boundaries in Cu have an energy of ~21 mJ/m^2, much lower than that of incoherent twin boundaries and high angle grain boundaries, ~498 mJ/m^2 and ~623 mJ/m^2 respectively [41,42].

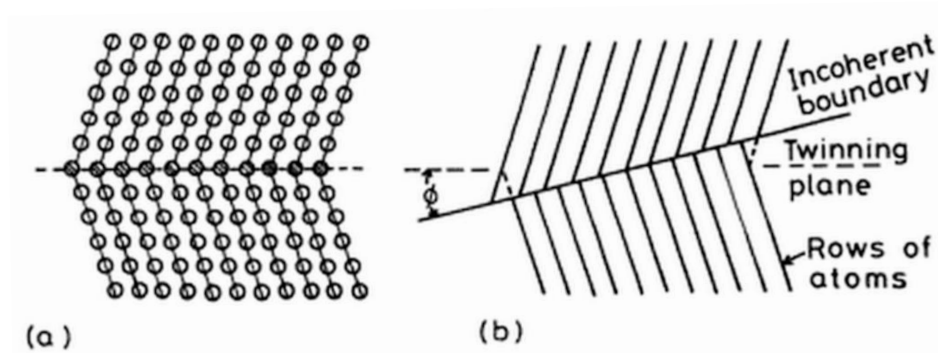

Figure 2.10: An illustration of the difference between coherent twins (a) and incoherent twins (b), taken from [41].

Twin boundary's effect on grain growth is very dependent on which types of twins (coherent or incoherent) are prominent in the microstructure. Coherent TB are low energy boundaries, making them much more thermally stable and resistant to grain growth than incoherent TB [105,106]. Nano-twinned Cu films have been shown to exhibit grain size retention up to 800 °C [106]; such microstructure features have also been shown to slow down grain boundary and triple junction migration rates [113]. On the other hand, incoherent TB have much higher mobility due to their higher interfacial energy (~480 erg/cm^2 [114]) over coherent TBs (~21 erg.cm^2 [115]) [116].

Like grain boundaries, twin boundaries also contribute to the Hall-Petch relationship as they too prevent the movement of dislocations. Thus, microstructures that contain coherent twin boundaries have high deformation stability and increased yield strength [17,18,50,88,117-120]. The tensile strength of nano-twinned Cu is an order of magnitude higher than coarse grained copper [17]. Lu *et al.* found that decreasing the twin spacing increases the ultimate tensile strength of the Cu, however decreases the ductility [18]. Nano-twinned Cu,

possessing an average twin spacing of 15 nm, showed the highest yield strength (~ 900 MPa), with smaller spacings dropping the yield strength below that of ultrafine grained Cu [18]. Highly nano-twinned Cu has much improved hardness values (between 2.4 and 1.6 GPa) over bulk Cu (between 1 and 1.2 GPa) [121]. Furthermore, nano-twinned Cu retained their hardness values much better than ultra fine grained Cu after fatigue stresses up to 450 MPa [118]. Twin boundaries also emit dislocations creating higher ductility of the Cu along with the improved strength [119]. Smaller twin spacing not only means higher twin density for improved strength, but also prevents many dislocations from building up stress in the twin boundaries and thus a larger stresses are required for dislocations to form in adjacent grains/twins and continued slip to occur [122,123]. The pile up, tangle, and creation of dislocation walls have been observed to form tilt boundaries and create new grains in Cu [124-126].

While nano-twinned Cu has superior mechanical properties, the large amount of TBs do not appear to be detrimental to electrical properties. For instance, nano-twinned copper had similar values for electrical conductivity and resistivity as bulk, coarse grained copper [17,121]. The high grain boundary area in ultrafine grained Cu resulted in an electrical conductivity two orders of magnitude larger than that of nano-twinned and bulk Cu [17]. The reason for this behavior is the low electrical resistivity coefficient of coherent twin boundaries, an order of magnitude lower than that seen for high angle grain boundaries [127].

Coherent twin boundaries have such low interfacial energy that defects are not likely to occur as readily compared to triple junctions [128]. Voids grow through

a dislocation emission mechanism. Molecular dynamic simulations have been performed on these systems and it was found that twin boundaries hinder the movement of partial dislocations and the emission from the void surface; this has been shown to result in slowed or hindered void growth [50,51]. Due to the buildup of stresses at void surfaces, molecular dynamic models also predict twin bands to form at void surfaces [49].

Electromigration (EM) is another important performance limiting phenomenon in ICs. EM is the diffusion of atoms in a material due to electron flow from an applied current. A material's ability to resist electromigration is important in microelectronics, since this mass transport often leads to void formation (see Figure 2.11). Generally speaking, Cu is more resistant to EM as compared to Al [129]. The activation energy for electromigration in Cu line structures is between 0.6 eV and 1.1 eV [130,131], while Al and Al-Cu alloys ranges from 0.5 eV to 0.8 eV [129,132]. Voids often nucleate at grain boundaries and grain boundary/interface junctions in Cu interconnect lines [130,131,133] from stresses that occur due to a variation in atomic fluxes [52,133,134]. EM diffusivities have been found to be orientation-dependent; (111) Cu orientations have been shown to demonstrate high EM resistance and longer EM lifetimes [134]. Cu interconnects with a large amount of {111} coherent twin boundaries have improved EM resistance, since these twin boundaries/grain boundary junctions are thought to slow down the diffusion of vacancies and Cu atoms [135,136].

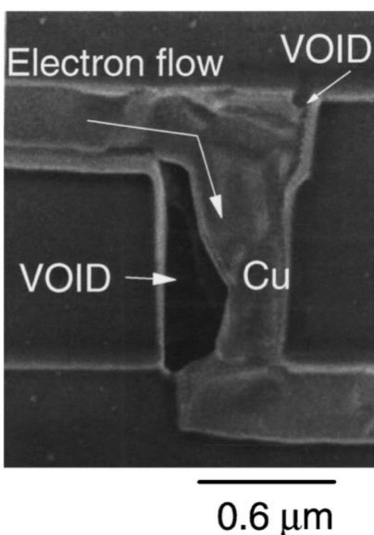

Figure 2.11: A void that formed in a Cu interconnect and is restricting the flow of electrons, taken from [129].

Once voids nucleate, their growth is driven by surface and grain boundary diffusion of Cu atoms [131]. Linigier *et al.* found void sizes increased linearly over time during EM and the void growth rate exhibited Arrhenius behavior in Cu [131]. Additionally, voids often grow directionally along interconnect paths by consuming grains, a process that can be hindered by grain boundaries as well as clusters of fine grains [52,131,133]. Once voids become large enough to force current to flow through the liner material, the electrical properties begin to diminish; specifically, increases in resistance have been observed when this occurs [129].

2.4.2 Electrodeposition Parameters and the Effect on Cu film Microstructure

Substantial control of Cu plating is achieved through a variety of pulse electrodeposition (PED) parameters. PED bath parameters, such as temperature, stir rate, and composition, have been shown to change the microstructure of Cu

deposits [137,138]. The peak current density (PCD) has been extensively studied and has a large impact on the deposited Cu microstructure. Increasing the PCD produces smaller grain sizes from higher cathodic over-potential, which causes faster nucleation rates [90,91]. These lower grain sizes have been shown to result in smaller surface roughness as well [91]. Furthermore, Cui *et al.* found a decreased Cu texture-dependence on the seed layer/substrate for films deposited at high current densities [89]. Using a large PCD also reduces the twin spacing, resulting in higher twin densities; however, Hsiang *et al.* found there to be an optimum PCD value (80 mA/cm^2) which produces the highest density of twins in microbumps [89,138].

The filling of advanced features (trenches, vias) can also be affected by the current density. There are optimum current densities for bottom up or super-filling of features. Current builds up at the opening of features and can change the filling profile, which results in void formation [61]. Higher deposition rates and PCD typically leads to larger void sizes in advanced features [10]. The pulse on and off times during PED have been found to affect filling profile as well, but their effect on twin density is perhaps the most significant. Xu *et al.* studied the effects of pulse parameters on stress and hypothesized that stress builds during the pulse on-times. It has been suggested that the nano-twins are then formed during the off-times to relax these stresses [135,139,140]. While many PED parameters have been studied to identify their influence on the resulting Cu microstructure, pulse parameters, such as frequency and duty cycle, have garnered little attention from the scientific community. Furthermore, twinning has not been a large focus of

many of these investigations. As will be discussed in the next chapter, these considerations went into the decision of film process parameters chosen for use in this study.

2.4.3 Microstructural Impact from Organic Bath Additives

Organic additives (OAs) are added to a PED bath to achieve defect-free filling through bottom-up depositions. However, the influence of OAs on the resulting Cu microstructure has not been systematically or extensively studied. Changes from columnar to bulk-like microstructures have been seen in metal films containing inhibitors [141]. Furthermore, coarse Cu grains were found in deposits with only Cl- and PEG additives to the bath. The addition of SPS and JGB to the bath have been shown to create finer grained structures [142]. There are several possible reasons for this alteration in the structure. These additives, along with other impurities, may hinder grain growth in a process known as Zener pinning. Pinning and prevention of grain boundary mobility occurs as the boundaries attempt to move passed these impurities. Boundaries are broken as they move through the particle and must reform upon exiting, creating a drag and requiring more energy to do so; hence, these particles counteract the movement of boundaries. The impurities within a material can prevent some grain boundaries from moving while others are able to move freely without the extra resistance from Zener pinning. However, impurities have been shown to move toward the surface and interface of the films, alleviating pinning and relieving grain growth stagnation [84].

Zener pinning was also found to be slightly dependent on orientation since grain boundary energy varies [143]. Low angle grain boundaries are more susceptible to pinning while high angle grain boundaries appear to be unaffected by particle interaction, due to their low energy and high elasticity [144]. Furthermore, brightener addition to the PED bath has been found to reduce the degree of recrystallization during room temperature self-annealing that occurs in Cu resulting in smaller grain sizes [145-147]. Finer grain structures are also created due to changes in cathodic over-potential. The addition of inhibitors creates a larger over-potential, which lowers activation energy for nucleation, promotes higher nucleation rates, and results in fine grained structures [137,142,148,149].

Changes in thermomechanical behavior have also been seen in Cu deposited using PED baths with organic additive chemistries [67]. Some variations in Cu orientation have been noted in the literature with the addition of organic additives (especially PEG) to PED baths [8,147,150], but a comprehensive analysis is yet to be conducted. This dissertation will supplement and extend existing studies on the role of additives in Cu films by expanding the understanding of the effects organic additives in PED and what role additives play in the resulting Cu microstructure.

CHAPTER THREE:

PULSED ELECTRODEPOSITION OF COPPER FILMS

In this Chapter, pulse electrodeposition parameters were studied for their impact on Cu blanket films properties. Pulse electrodeposition benefits from higher throwing power, density, and improved control (with added pulse parameters) over conventional direct current electroplating. Pulse current has been widely studied as a film processing variable based on its effects on the resulting Cu film microstructure, while the effects of pulse wave times (on-time, off-time, duty cycle, and frequency) have been largely ignored.

3.1 Motivation and Goals

The goal of this study is to identify the effects of square pulse wave duty cycle and frequency on Cu blanket film microstructure and stress state. Blanket films were chosen as a starting point for this effort instead of advanced geometries to ensure the capabilities are accessible and identify optimal pulse electrodeposition parameters before moving on to advanced geometry filling. As one might expect, advanced geometries require more sophisticated and numerous process variables. Understanding the effects of these parameters provides a baseline for future studies. Furthermore, the literature largely focuses on the *surface microstructure* of Cu films. While this is useful, this study is specifically interested in three dimensional (3D) microstructure variation and aims to provide insights into cross-sectional properties. Our efforts will compare blanket film

attributes to those seen in Cu deposited into trenches, geometries more constrained than in simple 2D films. This delineation and focus will allow for easier comparison to advanced geometry microstructures discussed in future sections.

It is also believed that highly twinned microstructures can be achieved through electrodeposition techniques and these microstructures provide better reliability for microelectronic interconnects [18,105,135]. As discussed in chapter 2, twinning is desirable in this application and pulse electrodeposition (PED) provides a pathway for tunable Cu microstructures and properties. The major findings of this study on blanket film deposition conditions and the resulting impact on Cu film microstructure have been reported in a paper resulting from our work [151].

3.2 Experimental Procedure

This section describes the experimental conditions used to fabrication and test Cu films. The first segment (3.2.1) describes the wafers used in the study, as well as the pretreatments conducted prior to the Cu pulse electrodeposition shown in the section 3.2.2. The characterization techniques for roughness and residual stress were also included in this section. Lastly, the techniques used to evaluate microstructure are described in section 3.2.3.

3.2.1 Sample Preparation

200 mm Si wafers pre-coated with 550 nm tetraethylorthosilicate (TEOS), 50 nm tantalum (Ta), and 100 nm copper (Cu) seed layers (as illustrated in Figure

3.1) were purchased from SKW Associates Inc. (www.testwafer.com, Santa Clara, CA). The wafers were stored in nitrogen atmosphere with desiccant to prevent oxidation of the Cu surface. Prior to handling the wafers were coated in s1813 photoresist to prevent scratching during dicing. The wafers were diced into 20 mm by 20 mm samples using a precision dicing saw (Kulicke & Soffa 982-6 Plus). The photoresist was removed using acetone, ethanol, and isopropanol and treated with a 200:1 mL solution of deionized H_2O: NH_4OH [152] to rid the surface of organic contamination the day of deposition.

Figure 3.1: An illustration of SKW Associates Inc. blanket wafer cross-section prior to deposition.

3.2.2 Pulsed Electrodeposition (PED)

The copper was electrodeposited using a two electrode galvanostatic system with the current pulses supplied by a Dynatronix DuP power supply. A 25x25x2 mm^3 Puratronic 99.999% copper sheet was used as the anode during depositions and the samples were attached to the cathode using a modified alligator clip (shown in Figure 3.2). The wafer samples were submerged in a typical acid-based electrolyte bath containing 200 g/L $CuSO_4 \cdot 5H_2O$, 50 g/L H_2SO_4 (ACS grade), and 50 mg/L HCl (ACS grade). Prior to depositions, the bath was degassed at ~7000 Pa with 99.999% ultra-high purity nitrogen from Air Liquide for

30 minutes. A 200 rpm bath stir rate was maintained during depositions and all depositions were conducted at room temperature in ambient atmosphere. Following the depositions, the samples were annealed at 150 °C for 1 hour under a 4% H_2 / 96% N_2 forming gas [153]. A post-deposition anneal was carried out to create a stable Cu microstructure, since Cu recrystallizes at room temperature. Such an anneal was found to prevent significant time-dependent microstructural changes through electron and ion microstructural imaging. An illustration of the PED and annealing processes are shown in Figure 3.3.

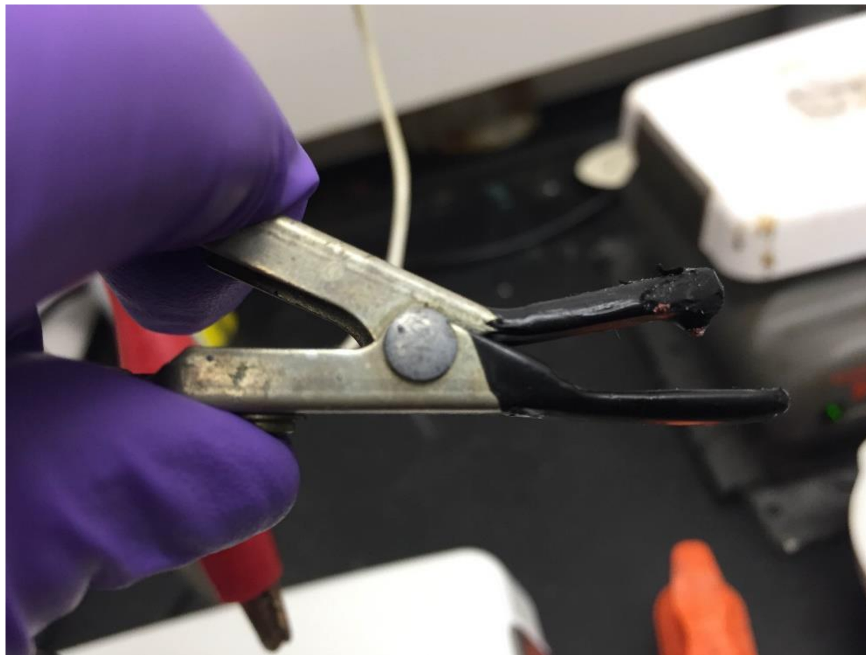

Figure 3.2: A modified alligator clip used as the cathode in the electrodeposition of the blanket films. It contains an insulated mouth with a single point metal contact.

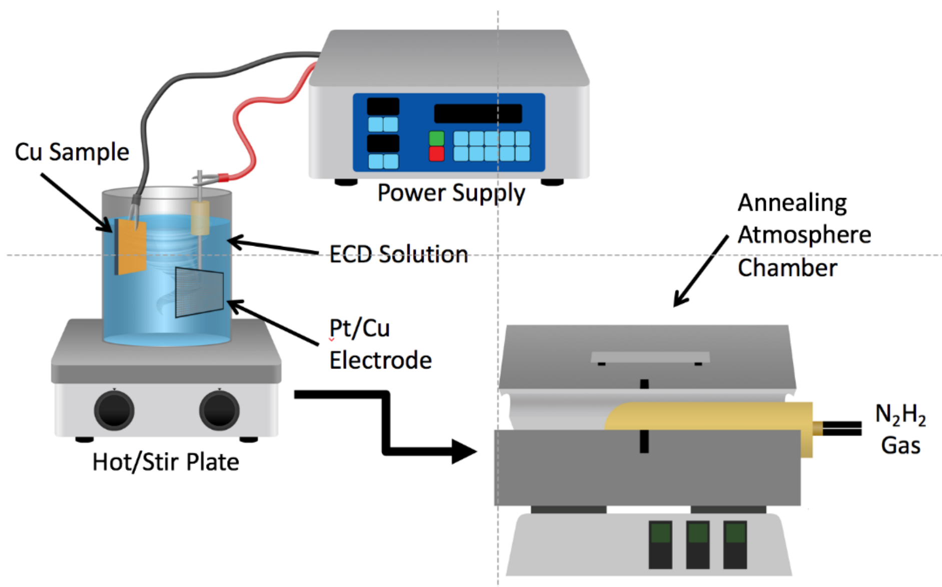

Figure 3.3: An Illustration of the pulse electrodeposition setup and annealing furnace.

The PED pulse parameters were based on those found by Hsiao *et al.* to produce highly textured copper with a large amount of nano-twins in electrodeposited microbumps [138]. In the present effort, films were formed using an 80 mA/cm^2 peak current density (PCD). The duty cycle and frequency of the pulse waves were varied systematically to study the effects of pulse parameters on the depositions physical and microstructural properties. Nine pulse parameter sets were used in this study, including duty cycles of 0.05, 0.1, and 0.25 and frequencies of 1 Hz, 50 Hz, and 100 Hz as shown in Table 3.1.

Table 3.1: The nine pulse parameter conditions used to electrodeposit the Cu films.

PED Condition #	Pulse Signature			
	On-Time [ms]	Off-Time [ms]	Frequency [Hz]	Duty Cycle
1	50	950	1	0.05
2	100	900	1	0.1
3	250	750	1	0.25
4	1	19	50	0.05
5	2	18	50	0.1
6	5	15	50	0.25
7	0.5	9.5	100	0.05
8	1	9	100	0.1
9	2.5	7.5	100	0.25

Target film thicknesses of 3000 ± 300 nm were verified by focused ion beam (FIB) cross-sectional milling and imaging using a Zeiss Crossbeam dual scanning electron microscope (SEM)/FIB or FEI 200 TEM FIB at the University of Central Florida's (UCF) Materials Characterization Facility (MCF). This film thickness was chosen as it represented the same length scale as Cu deposited onto TSV sidewalls. An example of a Cu film cross-section is shown in Figure 3.4.

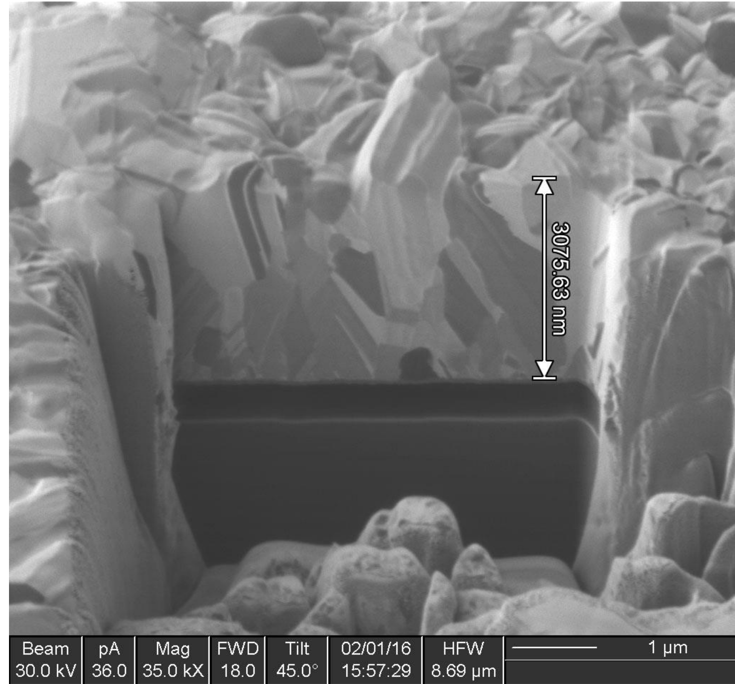

Figure 3.4: An ion beam image of a film cross-section, prepared using MCF's FEI 200 TEM FIB.

The resulting copper films' surface RMS roughness and residual stress were measured with the Zygo New View 8300 white light interferometer. Residual stress was approximated by the Stoney formula below [154]:

$$\boldsymbol{\sigma} = \frac{\mathbf{E_s t_s^2}}{\mathbf{6t_f(1-\upsilon_s)}}\left(\frac{\mathbf{1}}{\mathbf{R}} - \frac{\mathbf{1}}{\mathbf{R_0}}\right) \quad \text{(Eq. 3.1)}$$

where $\mathbf{E_s}$ and $\boldsymbol{\upsilon}_\mathbf{s}$ are the elastic modulus and Poisson ratio of the substrate respectively, $\mathbf{t_s}$ and $\mathbf{t_f}$ are the thicknesses of the substrate and the film respectively, and $\mathbf{R}$ and $\mathbf{R_0}$ are the radius of curvatures of film post and pre-deposition respectively. The Stoney formula uses the change in radius of curvature to determine the relative amount of stress introduced in the films. It assumes a uniform film thickness and a stress-free initial state of the sample. Each sample was mapped with the interferometer and the radius of curvature of the samples was measured in four directions (x, y, xy1, and xy2) as indicated in Figure

3.5.

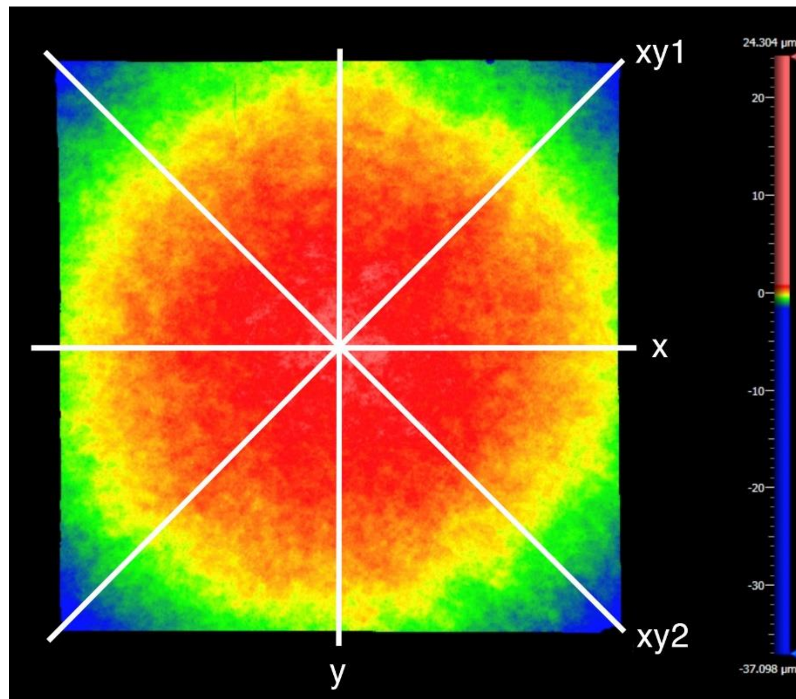

Figure 3.5: Radius of curvature measurements were taken along the four directions (x,y,xy1, and xy2) shown here.

3.2.3 Microstructural Evaluation

The surface grain orientation of the copper films was measured using x-ray diffraction (XRD) through use of the Panalytical X'Pert^3 MRD x-ray diffractometer. The instrument uses a Cu alpha source with a wavelength of ~1.54056 Å. The cradle in the XRD unit allowed three axes of rotation (omega, chi, and phi) for pole figures to be constructed and rocking curves to be conducted. A typical gonio curve for the Cu films is shown in Figure 3.6. Peaks of interest included the Cu (111), (200), (220), and (311) between 0° and 95° 2θ with several Si substrate peaks appearing in the scans. The texture coefficients (TC) were calculated using the following equation,

$$\mathrm{TC} = \frac{\mathrm{I_{hkl}}/\mathrm{I^0_{hkl}}}{(1/\mathrm{n})\sum \mathrm{I_{hkl}}/\mathrm{I^0_{hkl}}} \quad \text{(Eq. 3.2)}$$

where $\mathrm{I_{hkl}}$ is the intensity of the Cu peak of interest, $\mathrm{I^0_{hkl}}$ is the intensity of the peak in a randomly oriented Cu sample, and n is the number of total peaks of interest. The $\mathrm{I^0_{hkl}}$ used were from a standard in the Panalytical Highscore software database and are shown in Table 3.2.

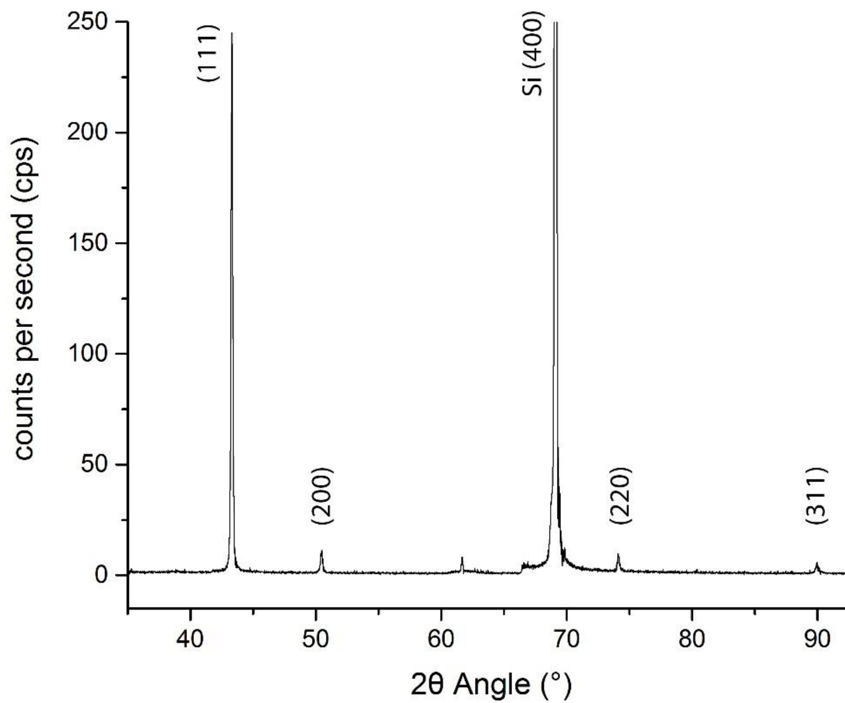

Figure 3.6: An XRD gonio scan of a Cu film, which contains four Cu peaks and at least one major Si substrate peak.

Table 3.2: The (111), (200), (220), and (311) Cu XRD peak locations and intensities of a randomly oriented Cu sample taken from the International Centre for Diffraction Database (ICDD) code: 03-065-9743. The intensities are used to calculate the texture coefficient for the Cu films.

Cu Peak	(111)	(200)	(220)	(311)
Peak 2θ Location	~43.2668°	~50.4058°	~74.1189°	~89.9018°
Normalized Peak Intensity	100%	42.5%	17.1%	15.5%

Electron backscattering diffraction (EBSD) was used to analyze the cross-sectional microstructure of the Cu films. A protocol, developed from our previous studies was adopted [15]. First, a cover glass was attached to the surface of the films using Loctite 460 epoxy to prevent scratching of the surface and delamination of the films during grinding. Cross-sections of the samples were ground using an Allied High Tech Techprep polishing system with diamond lapping paper in descending order of grit size (15 μm to 1 μm). The surfaces were finished by polishing with a 0.05 μm alumina slurry on a low nap, porous polyurethane polishing cloth. The cover glass was then removed using acetone to dissolve the epoxy.

The Clemson University Electron Microscopy Laboratory's Hitachi NB-5000 dual beam SEM/FIB was used to finalize the cross-sections with FIB milling down to 30 nA. The surface quality of the cross-sections were then sufficient for EBSD on the lab's Hitachi SU-6600 SEM with an Oxford EBSD detector. An EBSD step size of approximately 15 nm was used to analyze thousands of grains per deposition parameter set. The maps obtained by EBSD are shown in Figure 3.7. The Cu orientation was observed using the inverse pole figures and maps in the normal, transverse, and rolling directions were generated. Grain boundary maps identified the high angle grain boundaries (>15° misorientation), low angle grain

boundaries (<15° misorientation), and coherent twins (60° rotation about the {111}). The inverse pole figures show the degree of preferential orientation in the studied area and indicate the multiples of uniform density for the Cu orientations.

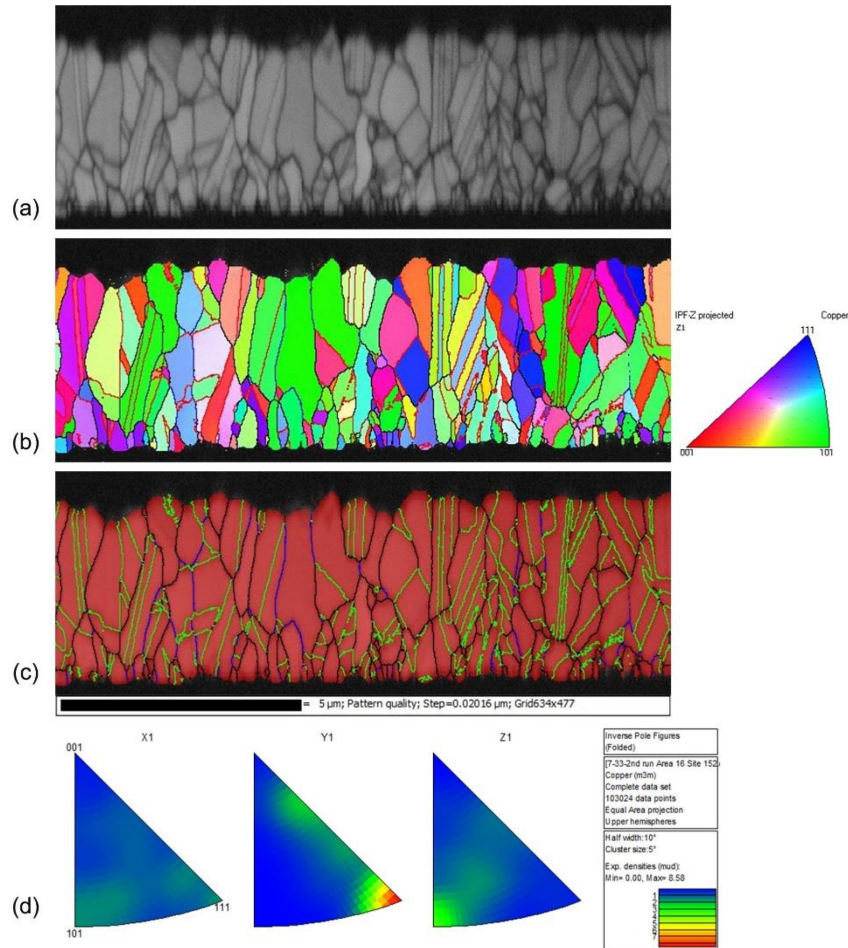

Figure 3.7: The types of EBSD maps used to evaluate the cross-sectional microstructure of the Cu films: (a) band contrast map, (b) inverse pole figure map, (c) grain boundary map, and (d) inverse pole figure.

3.3 Results and Discussion

The experimental methods from section 3.2 were carried out and the resulting measurements are disclosed in this section. The blanket films deposited

with various pulse parameters were evaluated for their microstructural and stress state. The results are discussed in detail, herein.

3.3.1 Grain Morphology of Blanket Cu Films

The cross-sectional microstructure of the Cu films were observed from the EBSD data collected for all nine deposition parameters. Figure 3.7 shows the band contrast map for the cross-section of PED #5. The map represents the grain morphology of all the films evaluated. Instead of a columnar structure, a common morphology of Cu films, all films had a bulk-like microstructure. The histogram for nine deposition conditions, shown in Figure 3.8, reveals the large distribution of grain sizes in the films. All films contained a large amount of smaller grains with diameters between 200 nm and 300 nm. Most of these small grains were located at the substrate/film interface, while larger grains were located toward the surface of the films. It is believed that the Cu seed layer plays a major role in determining the initial grain sizes of the film, but its influence dissipates as film growth continues and the resulting film thickness increases. Since the seed layer is only 100 nm thick, its grain size is assumed to be the same order of magnitude, due to limitations from surface and interfacial energies [100]. As the films were deposited and adatoms built atop one another, the grains became less restricted by the film thicknesses. The grain size contribution to overall cross-sectional area was also plotted in Figure 3.9 and shows an equal representation from small and large grains to the film area with the exception of grains larger than 2000 nm. Further analysis was done on these grains and is plotted in Figure 3.10 to assess

differences in the area fraction of large grains (>2000 nm). In films deposited with higher pulse frequencies and lower duty cycles, the data show that grains with a size >2000 nm diameter made up a much larger contribution of the overall film grain distribution. It is believed that the shorter on-times decrease the number of nuclei that form and longer off-times allow more time for the recrystallization to occur. The final product is larger surface grains as compared to the initially smaller grains found near the seed layer. A similar affect is seen with increasing pulse current densities, where the smaller grains are produced in Cu films [90,137].

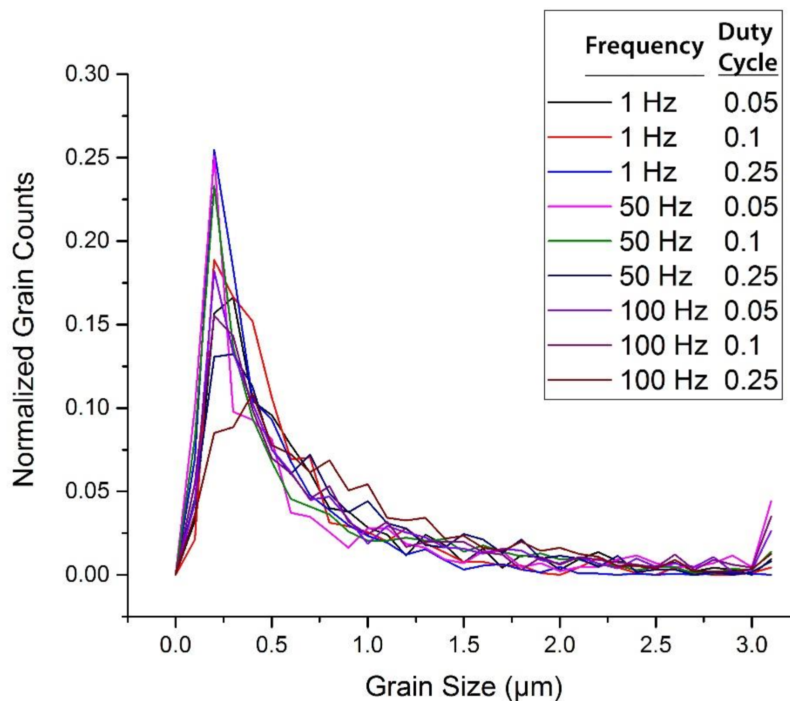

Figure 3.8: The cross-sectional grain size histogram for the nine deposition pulse conditions.

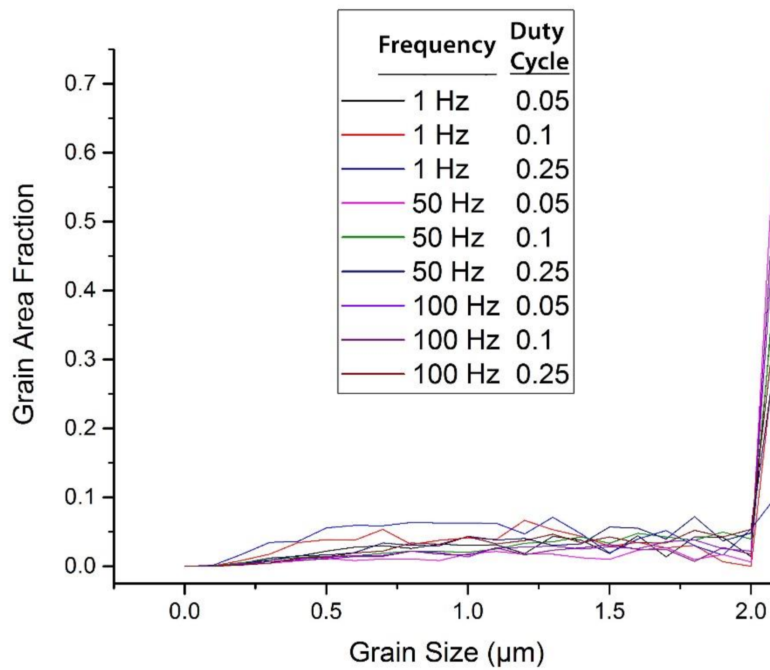

Figure 3.9: The area fraction taken up by different sized grains for each pulse deposition condition.

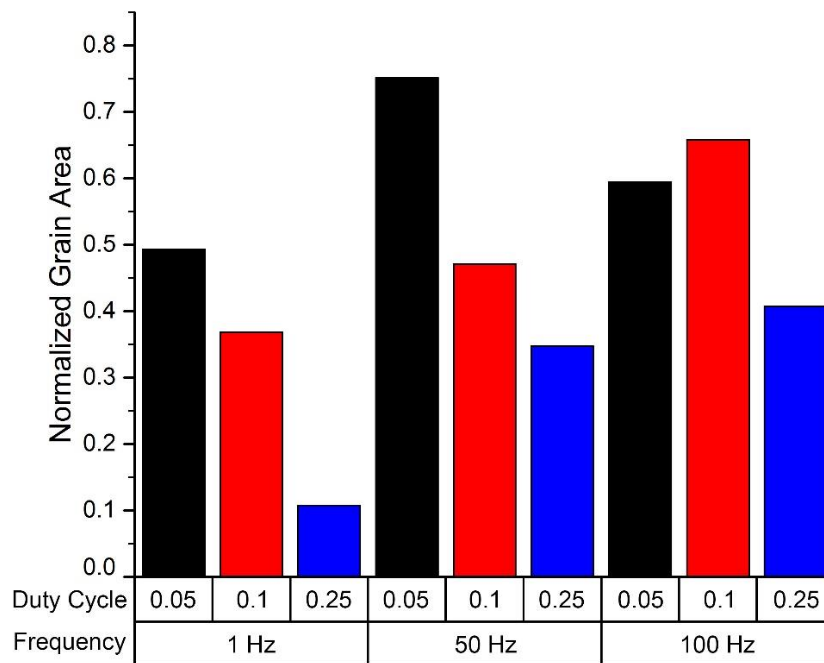

Figure 3.10: The cross-sectional area occupied by large grains (>2 μm diameter) for the nine deposition pulse parameters.

The film's surface morphology was also investigated through the use of surface roughness measurements. Surface grooves can have a large impact on surface energy driven grain growth as grain boundaries become pinned by these grooves [104,155-157]. Larger grains typically manifest themselves in higher RMS surface roughness values, while small grains commonly have smooth(er) surfaces. Figure 3.11 shows the RMS roughness for the deposited films in this study. As expected, the larger surface grains in higher frequency deposited films resulted in higher roughness values. The significant increase in roughness at the 0.25 duty cycle deposited films can be attributed to the fast deposition rate (~ 250 nm/min compared to ~50 nm/min and ~100 nm/min for 0.05 and 0.1 duty cycle, respectively) for these samples. It would be undesirable if films of such attributes were to be duplicated in via structures; they will lead to voids. Interestingly, the larger grain sizes would reduce the electrical resistance of the via fill because of minimized grain boundary density.

In conclusion, the grain morphology was impacted by the Cu seed layer. Grain sizes increased from the seed layer to the surface of the blanket Cu films. Lastly, shorter on-times for higher frequencies and lower duty cycles resulted in more large grains due to the decreased nucleation rates.

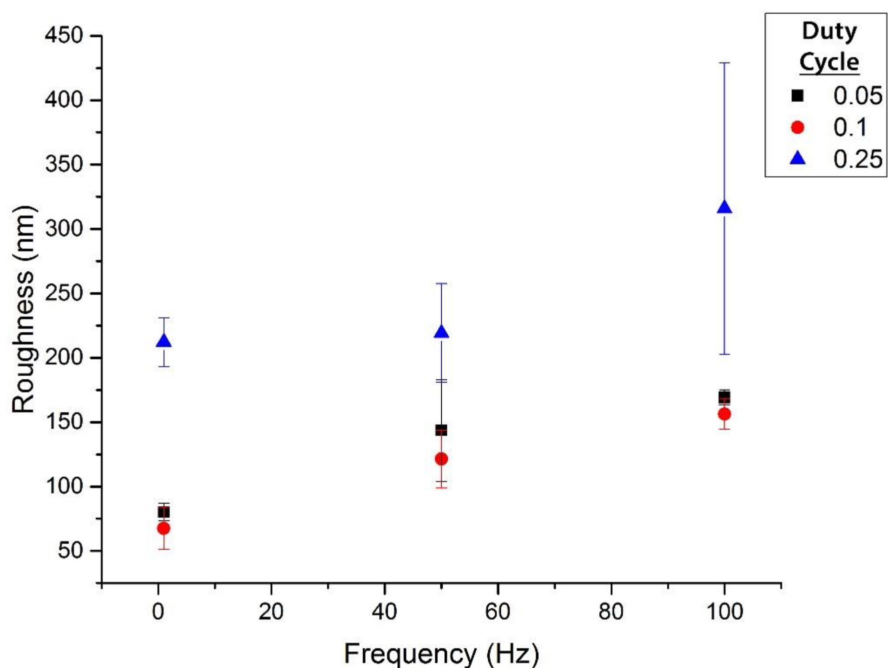

Figure 3.11: A graph showing the increase in Cu RMS surface roughness with frequency of the pulse for the three duty cycles used during deposition.

3.3.2 Texture of Cu Films

The inverse pole figure maps, shown in Figure 3.12, indicate a high degree of (111) oriented grains normal to the film surface in all the blanket film samples evaluated. This is especially true for grains near the copper-substrate interface. On the other hand, the in-plane grain directions appear to be randomly oriented. As noted earlier, the seed layer can have a major impact on the resulting microstructure [89,95,100], an XRD rocking curve was conducted on the Cu seed layer before deposition. The x-ray's penetration depth greatly exceeds the seed layer thickness (~100 nm), thus it is more beneficial to use a rocking curve to identify preferential orientation than a traditional 2θ scan. A rocking curve keeps the 2θ fixed at the orientation of interest's peak intensity and rotates the sample in

the chi or omega direction. The (111) Cu peak is located at approximately 43.2668° 2θ. The resulting chi rocking curve is plotted in Figure 3.13. The relatively sharp peak at 0° chi indicates and confirms a (111) preferential orientation in the Cu seed layer normal to the surface as expected.

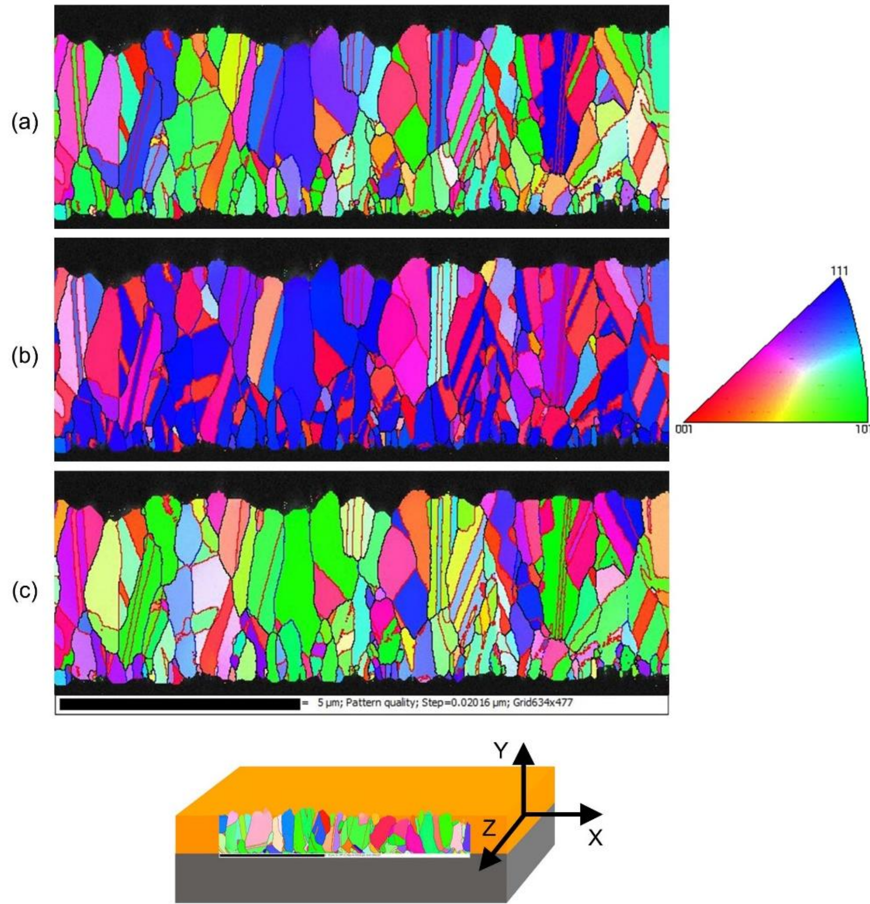

Figure 3.12: The (a) surface normal and (b)/(c) in-plane inverse pole figure maps for the PED #5 Cu film cross-section.

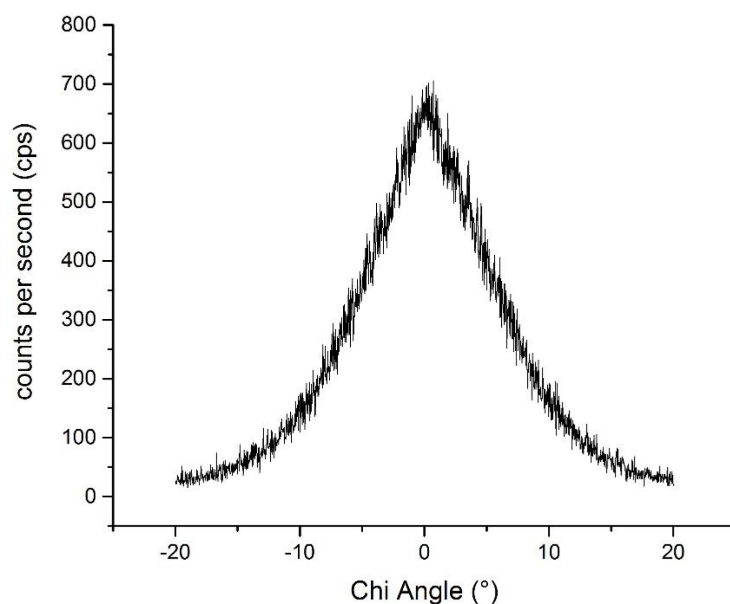

Figure 3.13: The XRD chi rocking curve illustrates the preferential (111) orientation normal to the surface of the Cu seed layer prior to deposition.

The texture coefficient (TC) was also calculated on films from XRD measurements to quantify their orientations. Figure 3.14 shows the variation in (111), (200), and (311) texture coefficient with pulse on-time during deposition. Although many copper films analyzed in literature studies have been found to be highly (110) oriented [90,96,97], the (220) peak did not appear in most film measurements within this study. The maximum texture coefficient for these samples was four due to the four Cu peaks in the 2θ scan. All Cu films evaluated were highly (111) textured regardless of processing conditions, but the degree of preferential orientation decreased with increasing on-time. In the case of increasing on-time samples, resulting orientations in blanket films were replaced by (200) and (311) oriented grains as evident from the increase in their texture coefficients with longer on-times. According to work by C. Thompson, grain growth

for (111) oriented grains is driven by surface/interface energy minimization in FCC metal films [98]. Strain energy minimization drives (110), (100) and (511) oriented grain growth [98,102] enhancing the prevalence of these orientations, as seen here. Since stresses have been found to build up during the on-time of pulse electrodeposition [140], the increased stress in the films with longer on-times may be activating additional (200) and (311) grain growth in our films. This can be clarified by examining post-deposition stress in the blanket films. The stress findings from this study will be discussed at length in the next section.

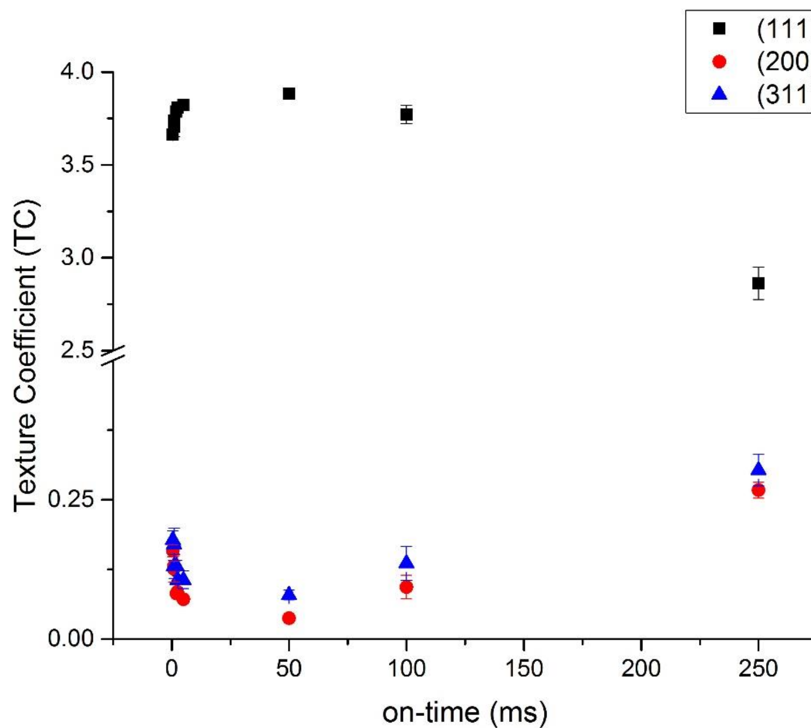

Figure 3.14: The change in (111), (200), and (311) texture coefficient with varying deposition pulse on-times. Error bars, which are not visible, are within the size of the data point.

To validate and understand the mechanism responsible for the variation in

texture with on-time, the (111) multiple of uniform density (MUD) was recorded from the cross-sectional EBSD measurements. The MUD gives insight into the degree of preferential orientation in the area measured. An MUD of one represents a randomly oriented specimen, while larger numbers indicate more texture. The MUD results are shown in Figure 3.15, where a similar trend to the texture coefficient is seen. The large error bars produced from this measurement are a result of the very localized area (~3 x 12 μm) that is measured by EBSD. A single grain can have a profound impact on the MUD of the measured area. However, the texture coefficient from XRD examines a much larger area (~15 x 15 mm).

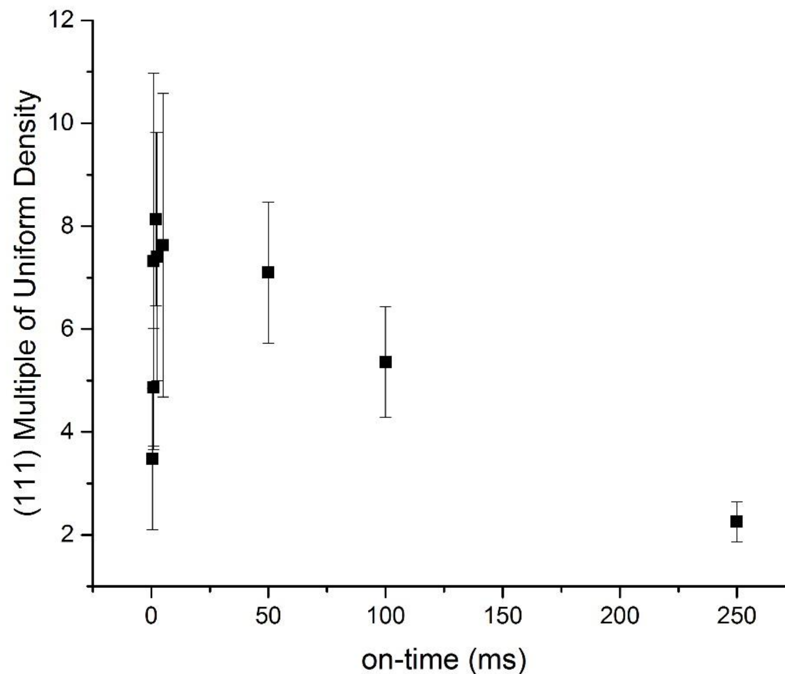

Figure 3.15: The (111) multiple of uniform density (MUD) for the Cu film cross-sections as the pulse on-time is changed.

3.3.3 Residual Stress in Cu Films

Alongside the biaxial residual stress measurements estimated from the radius of curvature method (Stoney formula), discussed in section 3.2.2, direct measurement of residual stress level in films was also attempted using the XRD. Here, the $\sin^2\psi$ residual stress measurements which utilizes the d-spacing strain were used to calculate the stress in the sample. The measurements yielded no repeatable findings as a linear correlation was unable to be made between the epsilon (the d-spacing strain) and $\sin^2\psi$, as shown in Figure 3.16. There are two possible reasons for this. The stress may be too low to be detected by the instrument (<150 MPa) or a stress gradient is present in the films restricting measurement of a repeatable level of stress.

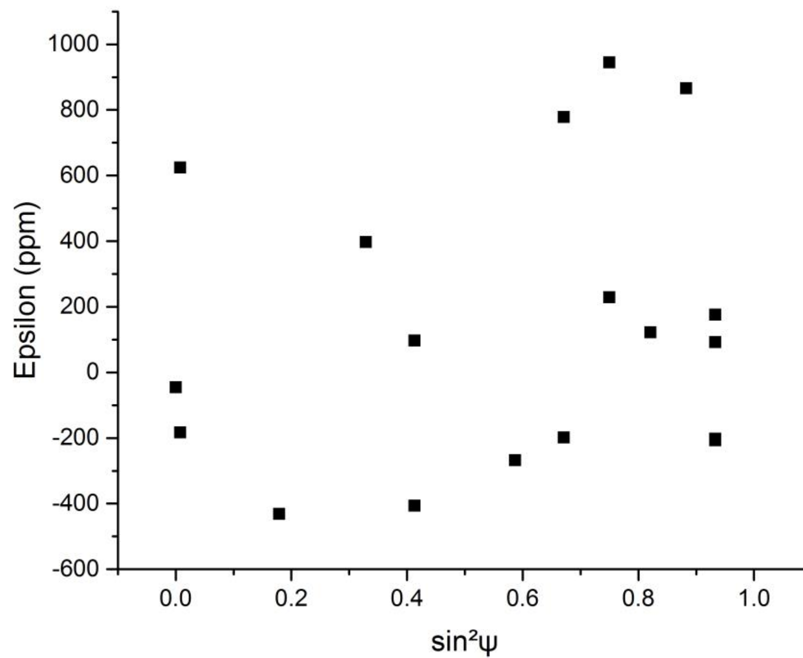

Figure 3.16: An XRD residual stress measurement of a Cu blanket film using the $\sin^2\psi$ method. The points represent individual measurements, thus the error is not shown.

Since, the XRD stress measurements did not produce any repeatable data, the biaxial residual stresses measurements of blanket films processed in this portion of our study were conducted using the radius of curvature method (section 3.2.2). The radius of curvature for all blanket Cu films was symmetrical as shown in Figure 3.5. The wafer's concave shape indicated residual tensile stresses in the film. Higher biaxial stresses were found in Cu films deposited at lower frequencies (Figure 3.17), but no trends were seen with respect to duty cycle. D. Xu *et al.* found, in his studies of Cu films, that stresses develop during the on-time and relax during pulse off-times of Cu deposition [139,140]. The buildup of these stresses are more rapid than the relaxation that occurs due to recrystallization and results in net residual stress following the deposition. Therefore, the on-time has more impact on the final stress state in the films and thus is likely the reason for larger stresses in Cu films deposited at lower frequencies.

The relationship between on-time and biaxial stress as quantified in our study is shown in Figure 3.18 and confirms this theory. Longer on-times produce more residual stresses in the Cu films, however stresses also form due to the mismatch in thermal expansion coefficients (CTE) between the Cu film and substrate during cooling. A low temperature anneal (150 °C for 1 hour under forming gas) was required to prevent self-annealing and stabilize the microstructure, without significantly affecting the stress in the films [153,158]. The high current during these on-times creates nuclei at a fast rate, increasing the stresses in the films. However, the residual stresses appear to level off when pulse

on-times become increasingly large (above 100 ms in this case). Once the surface is saturated with nuclei from long on-times, the stress reaches a maximum value. Lastly, these larger stresses produced by longer on-times appear to impact Cu texture in the films, with larger on-times producing less (111)-oriented grains and more (200) and (311)-oriented grains.

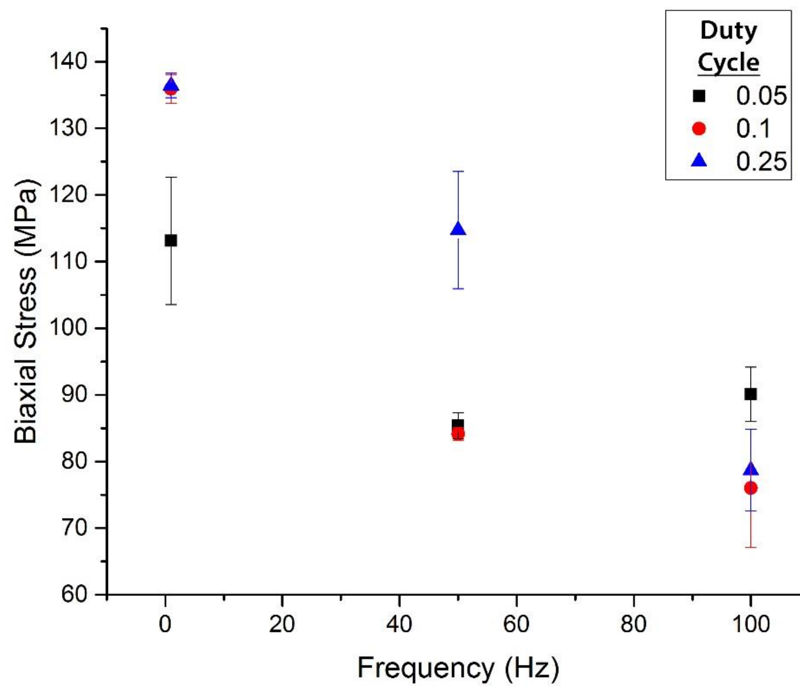

Figure 3.17: The biaxial residual stress in Cu films with various pulse frequencies and duty cycles.

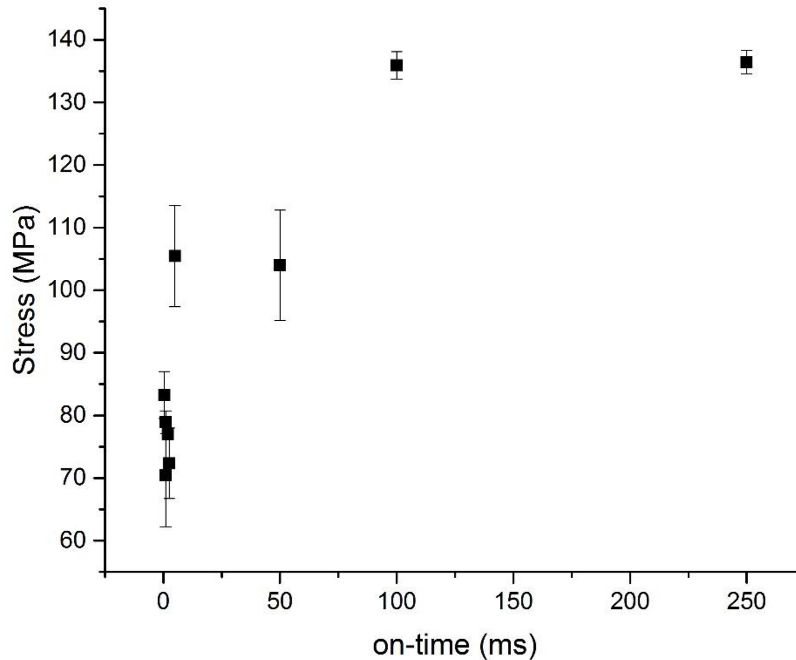

Figure 3.18: A graph showing the increase of residual stress in Cu films with longer on-times.

To evaluate the presence and formation of twins in the films, EBSD band contrast and boundary maps were used to identify and count the twins. The sum of the twins was then normalized by the number of grains examined to establish the twin density. This twin density measurement was conducted to determine the probability of a given grain containing a twin.

Smaller biaxial residual stresses were found in films with high twin concentrations (Figure 3.19), demonstrating the thermal stability and mechanical strength of twins in metals as observed in previous studies on Cu [18,105,159,160]. As noted repeatedly in the prior chapters, twins often form to relieve stresses in these systems. It is believed that nano-twins form in Cu films during off-time recrystallization to relieve the stresses that occur during the on-time

[139,140]. Thus, longer off-times would theoretically produce more twins; however, no correlation was found between the off-times and twin density within the films in the present study. The lower stress with larger twin densities shown in Figure 3.19 illustrate the high degree of recrystallization that occurred in these films. On the other hand, higher twin densities have been found in Cu with larger grain sizes [90,161]. As shown in Figure 3.20, the twin density increases with the area occupied by large grains (in this analysis, grains >2 μm in size) in the films produced in our study. This increase is especially apparent in films deposited with higher pulse frequencies (50 Hz and 100 Hz), as indicated by the average values (x's) in Figure 3.20. These high pulse frequencies deviate more from DC electroplating and the quicker pulses allow atoms to rearrange and twins to form during the off-times more frequently.

In conclusion, the twins create thermally stable microstructures, yielding lower stresses. Films with larger grains contained more twins, reducing the grain boundary area and creating microstructures that are potentially beneficial to Cu reliability.

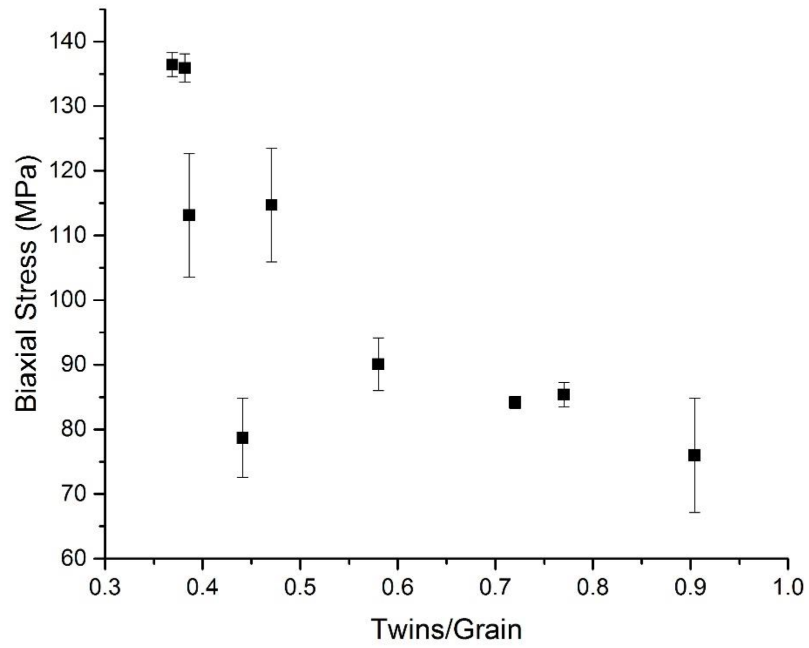

Figure 3.19: A plot illustrating the lower residual stresses are correlated to increased twin densities in Cu films. Error bars represent standard deviation of the points.

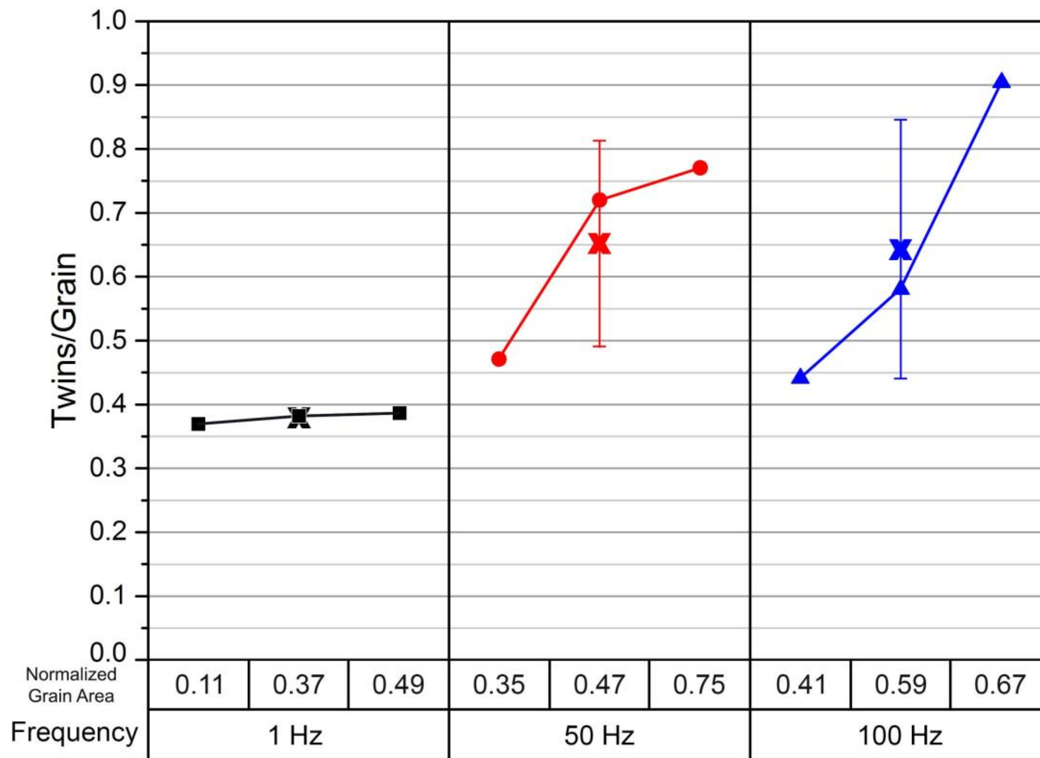

Figure 3.20: The relationship between twin density and grain area of large grains (> 2 μm) in Cu films deposited at various pulse frequencies. The x's indicate the average twin density for each frequency and are shown with their error (standard deviation).

3.4 Conclusions

Blanket Cu films were pulse electrodeposited using various pulse duty cycles and frequencies. The film microstructures were evaluated using x-ray diffraction and electron backscattering diffraction. All films evaluated contained a 'bulk-like' structure, with smaller grains at the substrate/film interface and larger grains toward the films' surface. The films were also highly (111) textured normal to the surface, due to the influence from the seed layer. The degree of (111) preferential orientation was found to depend on the pulse on-time during deposition. It is believed that the increased biaxial residual stresses, measured

from the wafer curvature technique, contributed to an increased growth of (200) and (311)-oriented grains. Films with larger twin densities also had lower residual stresses. This observation is consistent with the notion that the strain-relaxed nano-twinned Cu can be energetically more stable than the strained fcc Cu [139]. Furthermore, the twin formation, hence stress generation and relaxation, was also found to be less dependent on pulse off-times than previously expected, based on prior literature observations. Instead, more twins were found in films that contained larger grains. This observation is expected to be beneficial to stress reduction and reliability, without having a significant impact on electrical performance in microelectronic interconnects. The 50 Hz, 0.1 duty cycle parameters used to deposit the Cu, resulted in a high degree of (111) film texture, high twin density, low stress, and mid-ranged grain size, making these deposition conditions suitable for the next step in our microstructural evaluation, depositing Cu into trenches, which is discussed in Chapter 4.

CHAPTER FOUR:
ADVANCED GEOMETRY DEPOSITIONS

Based on the key conclusions from the blanket film study in Chapter 3, this chapter aims to further understand the role of deposition parameters on resulting film microstructure by focusing on the impact of organic additives on the filling and microstructure of Cu trenches. Through the study of these low aspect ratio features, we can gain a better understanding of the fundamental mechanisms that dictate the Cu microstructure in these confined areas and begin to predict what bath chemistries may influence in more commercially-relevant geometries, such as in high aspect ratio through-silicon vias (TSV).

4.1 Motivation and Goals

The results from Chapter 3 indicated that the PED #5 pulsed electrodeposition (PED) conditions produced the optimal microstructural features for theoretically highly reliable Cu interconnects, including highly texture Cu with large twin densities, low stresses, and coarse grains. Thus, PED #5 deposition parameters (50 Hz, 0.1 duty cycle) were used to deposit Cu into low aspect ratio trenches that are discussed in this Chapter. To reiterate, the objective of the study is to investigate the effects of organic additive concentration in the electrodeposition bath on the microstructure of Cu features that approach the spatial constraint seen in TSVs. Additionally, as discussed in section 2.3.3, the role of additives used to control the filling behavior of Cu in such non-blanket

applications, has been evaluated in the literature for their influence on filling, but not their resulting microstructural properties. Specifically, we investigate the quantity of additives and their impact on the desirable attributes of Cu orientation, twin density, void formation and grain size.

As introduced in section 2.3.3, organic additives are typically used in Cu electrodeposition baths to increase throwing power (the capability to deposit uniform thicknesses onto complex topographies) of the deposits and reduce voids that result from conformal or sub-conformal filling profiles. Although these additives are necessary, especially in the filling of high aspect ratio features, their impact on microstructure has not been extensively studied and are not well understood. Correlating the type of additive, its function and role on microstructure formation and corresponding film properties forms a core section of this chapter.

Literature has shown that some additives lead to a decrease in film grain size for several reasons, including pinning and changes to cathodic overpotential during the electrodeposition process [137,142,143,146-148]; additionally, additives, such as janus green b, have been shown to cause selective growth of certain Cu grain orientations [162]. Even so, many studies have focused on the *surface* microstructure of Cu interconnect lines, which can only be comprehensive if the grains have bamboo-like structures across the entire cross-section of the features of interest [107,108,147]. This chapter will concentrate on the *cross-sectional* (bulk) microstructure of 250 nm wide Cu film trenches and the influence of organic additives on the residual stresses, roughness, crystallite size, texture, and twin density of the Cu. Comparison to features observed in blanket films

discussed in Chapter 3, will be highlighted in a further discussion highlighting the impact on trench size, in Chapter 5.

4.2 Experimental Procedure

The methods used for conducting this study are discussed in this section. This section begins with a description of the samples being studied and move on to the stress and roughness measurements, before specifying the cross-sectioning protocol used to perform microstructural analysis on the trenches.

4.2.1 Copper Trench Depositions

Si wafers with unfilled trenches were also supplied by SKW Associates Inc., Santa Clara, CA. These 200 mm diameter wafers contained dies, 20 mm by 20 mm in size, which were diced using the Kulicke & Soffa 982-6 Plus. Each die contained 500 nm deep trenches with trench widths varying from 180 nm to 100 µm as seen in the die blueprint in Figure 4.1. The cross-sectional illustration in Figure 4.1 (at right) shows the various layers of plasma enhanced tetraethylorthosilicate (PETEOS), Si_3N_4, Ta, and Cu seed above the Si wafer surface. An identical PED pretreatment protocol as was used on the blanket film wafers was used on these 'trench-containing' wafers to keep the process as uniform as possible.

Figure 4.1: The layout of the trench samples provided by SKW Associates Inc. (left) and an illustration of the multi-material cross-section of the wafers (right).

An identical PED setup to the blanket Cu film depositions was used to fill trenches. A peak current density of 80 mA/cm^2, 200 rpm solution stir rate, and room temperature bath were kept consistent with the blanket film depositions. An on-time of 2 ms and off-time of 18 ms (50 Hz; 0.1 duty cycle) was used as part of the pulsed electrodeposition process, since it was determined from the blanket film depositions that these parameters produced a high twin count, low stress, and mid-sized grain microstructure; all of which are beneficial for microelectronic applications. The bath constituents and their concentrations also remained the same (200 g/L $CuSO_4{\cdot}5H_2O$, 50 g/L H_2SO_4, and 50 mg/L HCl). Prior to degassing, various amounts of 8000 molecular weight polyethylene glycol (PEG), bis-(sodium sulfopropyl)-disulfide (SPS), and janus green b (JGB) were added to the electrolyte bath. The PEG (CAS:25322-68-3) and JGB (CAS:2869-83-2) were obtained from Alfa Aesar, while SPS (CAS:27206-35-5) was provided by Carbosynth LTD. These organic additives are typically used to deposit Cu into trenches,

damascenes, and high aspect ratio through-silicon vias (TSV) with limited defects [60,163,164]. Table 4.1 shows the experimental matrix with all concentrations of the organic additives used in this study. Additive mixture of 200 mg/L PEG, 5 mg/L SPS, and 10 mg/L JGB was chosen as a baseline formulation as it was known to afford defect-free fillings [60,163,164]. While the precise 'recipe' of the fractions of these additives used in industry production environments is proprietary, in this study the concentration of each organic additive was varied independently within this baseline concentration level to evaluate their respective contribution to filling, physical properties, and resulting Cu microstructure.

Table 4.1: The organic additive concentrations used in the pulse electrodeposition baths for Cu trench filling.

PED Condition #	Organic Additives (mg/L)			JGB/SPS Ratio
	PEG	SPS	JGB	
1	0	0	0	N/A
2	200	5	0	0
3	200	50	10	0.2
4	200	20	10	0.5
5	200	5	5	1
6	200	5	10	2
7	200	5	50	10
8	200	5	100	20
9	100	5	10	2
10	500	5	10	2
11	500	5	100	20
12	200	0	0	N/A
13	0	200	0	N/A
14	0	0	200	N/A

4.2.2 Physical Property Measurements

Samples were inspected visually following processing for their appearance,

and post-processing attributes were measured. Roughness and biaxial stress were measured using experimental procedures similar to those used for the blanket films with the Zygo New View 8300 White Light Interferometer (WLI). Roughness was measured in the same (1 mm by 15 mm) area on each sample, where trenches would not interfere with the measurements. The trench layout of the samples prevents absolute values of stress from being calculated using the Stoney formula, however, relative stress from sample to sample was still obtained through Equation 4.1.

$$\boldsymbol{\sigma} = \left(\frac{\mathbf{1}}{\mathbf{R}} - \frac{\mathbf{1}}{\mathbf{R_0}}\right) \boldsymbol{t_f^{-1}} \qquad \text{(Eq. 4.1)}$$

where $\mathbf{R}$ and $\mathbf{R_0}$ are the radius of curvature of the sample after and before deposition respectively and $\boldsymbol{t_f}$ represents the thickness of the Cu above the trenches. The Si wafer's material properties were removed from the Stoney formula and the Cu layer's thickness (t_f) was used to normalize the measurements from sample to sample. Since all wafer samples used in this portion of the study had the same layout, relative stress measurements can still be made by comparing the radius of curvature from sample to sample. However, the advanced geometry and multi-material wafers used in this study make it difficult to obtain actual stress values. Hence, reported stress for trench studies are relative.

4.2.3 Cross-Sectioning Protocol

The filling efficiency for the 0.25, 1, 2, and 2.78 aspect ratio (depth/width) trenches, corresponding to the 500 nm deep and 2000 nm, 500 nm, 250 nm, and 180 nm wide trenches respectively, were evaluated using two methods. Table 4.2

shows the aspect ratios of interest and their corresponding dimensions. To determine the rate of deposition for the bottom, sidewall, and overfill of the trenches, the samples were placed in a cylindrical mold, filled with epoxy. Buehler Epothin epoxy was used for its low viscosity, which allowed the epoxy to conform to the surface morphology of the samples, and nickel was added to reduce charging in the SEM. The samples were placed under light vacuum to prevent air pockets and help the epoxy adhere to the surface of the samples. The post-cured cross-sections were ground to the approximate area of the trenches with the Allied High Tech Techprep polishing system using SiC paper (300 to 800 grit). The samples were then polished with reducing size diamond slurry suspensions (abrasive size from 9 um to 1 um) on a woven acetate cloth and finished with a 0.05 um alumina polish on a low nap, porous polyurethane polishing cloth. The resulting molds were imaged in the University of Central Florida (UCF) Material Characterization Facility's (MCF) Zeiss Ultra-55 FEG SEM to analyze the filling profiles of the trenches. It was later concluded upon microscopic analysis of the trench cross-sections that this fabrication method led to smearing of the copper into regions of voids created during the trench filling. This technique, however, was still used to determine the filling rates onto the trench sidewalls and base, but the trench voids were analyzed by cross-sectional milling and imaging with MCF's Zeiss Crossbeam dual SEM/FIB. Cross-sectional milling with the focused ion beam (FIB) could not be used to observe the filling profile since it caused redeposition of the Cu onto the trench sidewalls, giving a false filling profile image.

Table 4.2: The widths of the various aspect ratio trenches of interest in this study. All trenches are 500 nm deep.

Aspect Ratio (depth/width)	0.25	1	2	2.78
Trench Width	2000 nm	500 nm	250 nm	180 nm

4.2.4 Microstructural Evaluation

To evaluate the cross-sectional microstructure of the 1 and 2 aspect ratio Cu trenches (500 nm and 250 nm wide, respectively), two protocols were used depending on the size of the trenches. For the larger trench size (500 nm wide), the samples were cleaved across the trenches using a diamond scribe. Similar to the protocol used for the blanket films (described in section 3.2), the samples were then milled from the cleaved edge using North Carolina State University (NCSU) Analytical Instrumentation Facility's (AIF) FEI Quanta 3D FEG dual beam SEM/FIB and EBSD was conducted on the milled cross-section. The smaller trenches (250 nm wide) required transmission kikuchi diffraction (TKD), since TKD has higher spatial resolution than traditional EBSD [165]. An FIB liftout specimen from the 250 nm trenches was made and thinned to < 100 nm thickness to allow electron transmission. A representative FIB liftout specimen is shown in Figure 4.2, where the 250 nm trench cross-sections were ion beam polished and awaiting TKD.

To enable statistical analysis of trench features at least 10 trenches for each size were evaluated from each sample. While extremely time consuming, this number was chosen to represent all trenches of similar size on a given sample. Since the primary focus on this study is to determine the effect of *organic additives* on the Cu microstructure, only the 250 nm trenches were evaluated for this portion

of the study and are discussed in this chapter. Chapter 5 will focus on the differences between the two trench sizes where issues of trench size and film growth constraint are more precisely evaluated.

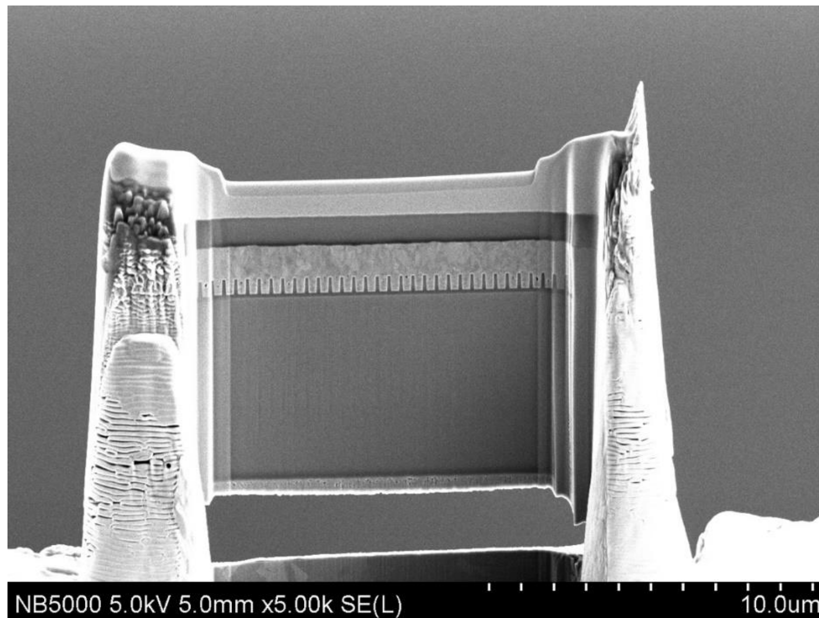

Figure 4.2: A liftout of the 250 nm trenches, which will be used for TKD.

4.3 Results and Discussion

This section includes the findings realized through measurement techniques and experimental procedures described in section 4.2. The relationship between organic additive concentration and trench filling profile, residual stress, surface roughness, and trench microstructure are presented and discussed.

4.3.1 Trench Filling

The filling profiles were examined using the grinding and polishing cross-

sectioning protocol defined in section 4.2.3. SEM micrographs of trench cross-sectional profiles are seen in Figure 4.3. The 0.25, 1, 2, and 2.78 aspect ratio trenches (dimensions shown in Table 4.2) were analyzed before deposition and 0.5 min, 1 min, 1.5 min, and 3.5 min into the deposition process. The 2 and 2.78 aspect ratios have smaller cross-sectional areas and filled much faster than the smaller aspect ratio (0.25 and 1) trenches. After 3.5 minutes of deposition, all four aspect ratio trenches were found to have filled completely. The filling profiles are relatively aligned with the curvature-enhanced-accelerator coverage (CEAC) model by Moffat et al. [72,73,75].

There were several interesting features of these structures that corresponded with the CEAC model and appeared to be impacted by the various additives. Firstly, one can observe that the accelerator (additive) takes time before becoming affective in servings its purpose, to induce bottom-up filling of the features. Between 1 min and 1.5 min, a jump in the thickness at the trench bottoms is apparent from Figure 4.4 for most of the baths containing organic additives, while the bath containing no organic additives has an almost constant deposition rate onto the base of the trenches. Figure 4.5 shows the trench cross-sections after 1 min of deposition into all four aspect ratios of interest and all organic additive concentrations studied. It is immediately apparent that the surface of the Cu was extremely rough for the depositions that contained no organic additives compared to Cu deposited with any amount of the three organic additive used in this study. The deposition was non-uniform, especially on the sidewalls, which can lead to trapped air and the formation of deposition voids in the center of the features.

Adding extra accelerator to the baths increased the filling rate as is evident by the 200/10/10 cross-sectional SEM images in Figure 4.5. Meanwhile, decreasing the PEG or JGB content in the bath increased the surface roughness of the depositions.

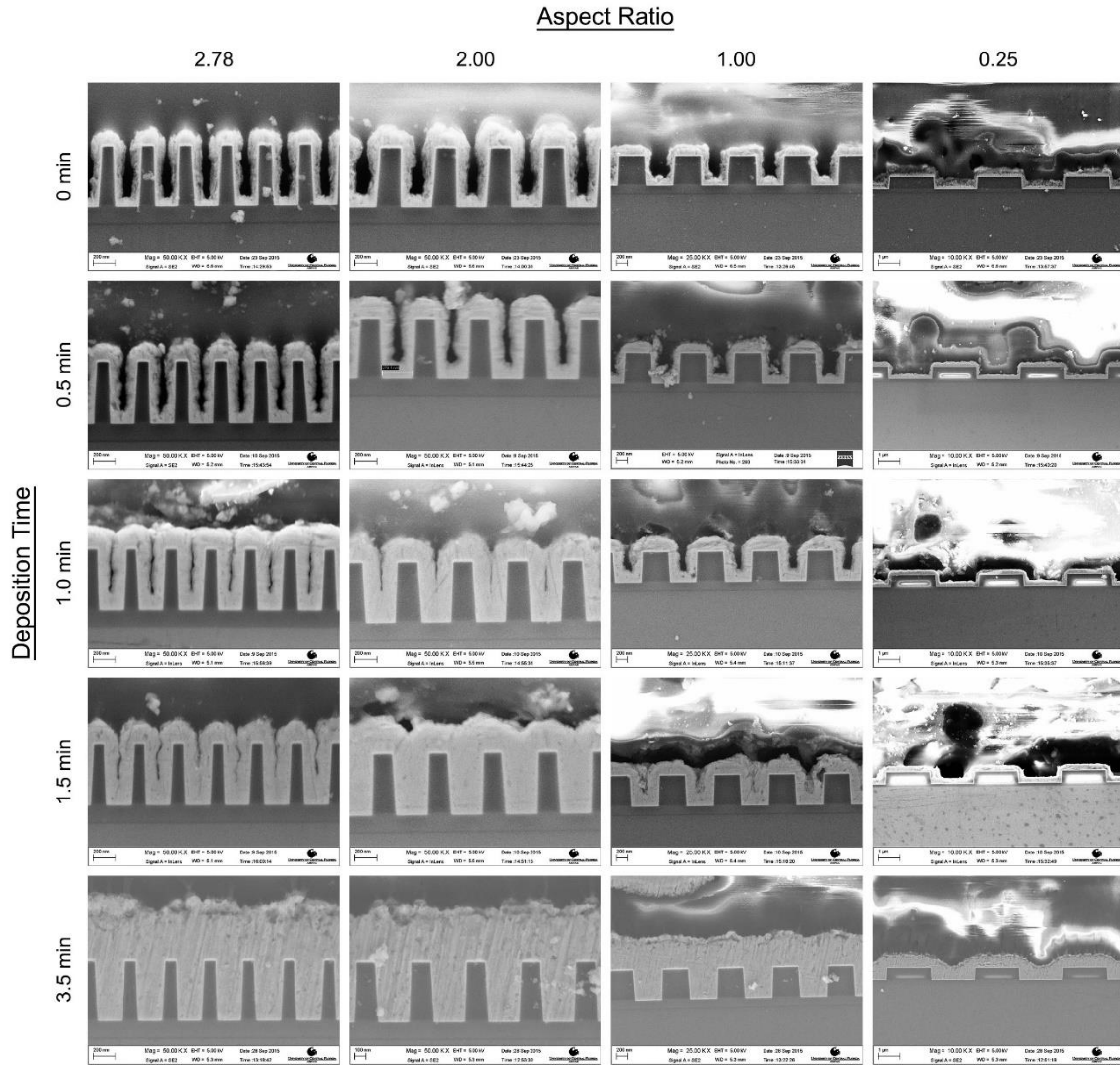

Figure 4.3: The progression of various aspect ratio trench filling over time of deposition.

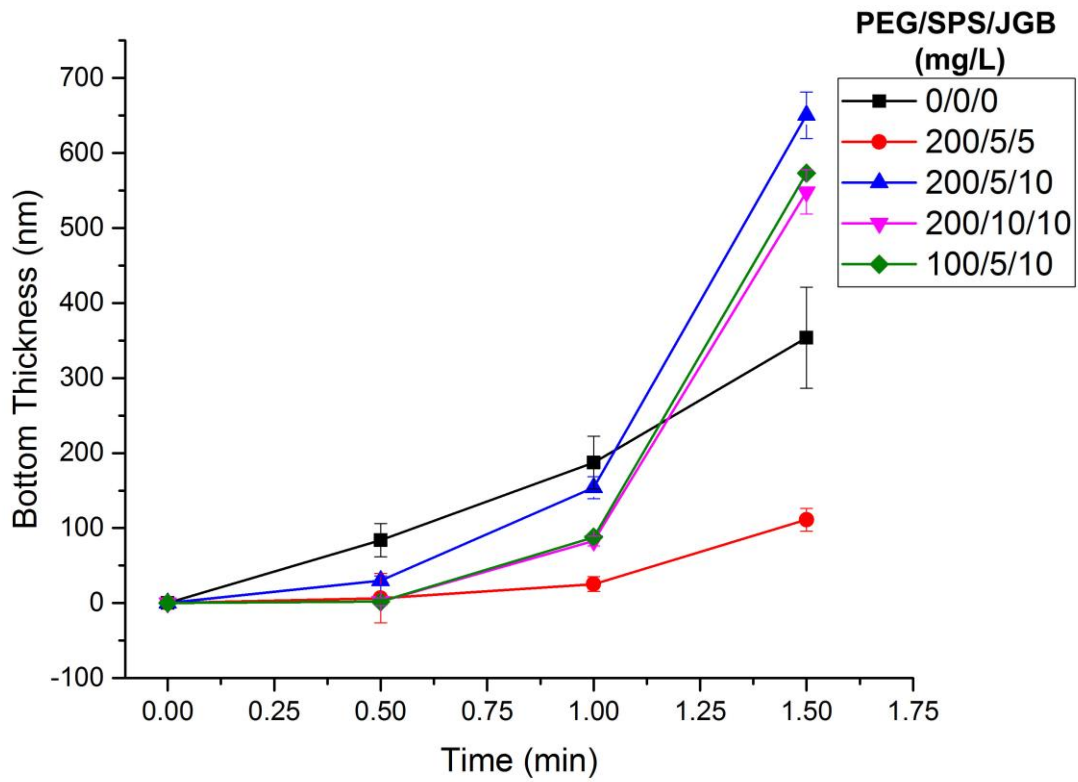

Figure 4.4: The Cu thickness at the trench base over time of the deposition for different organic additive concentrations used in the bath.

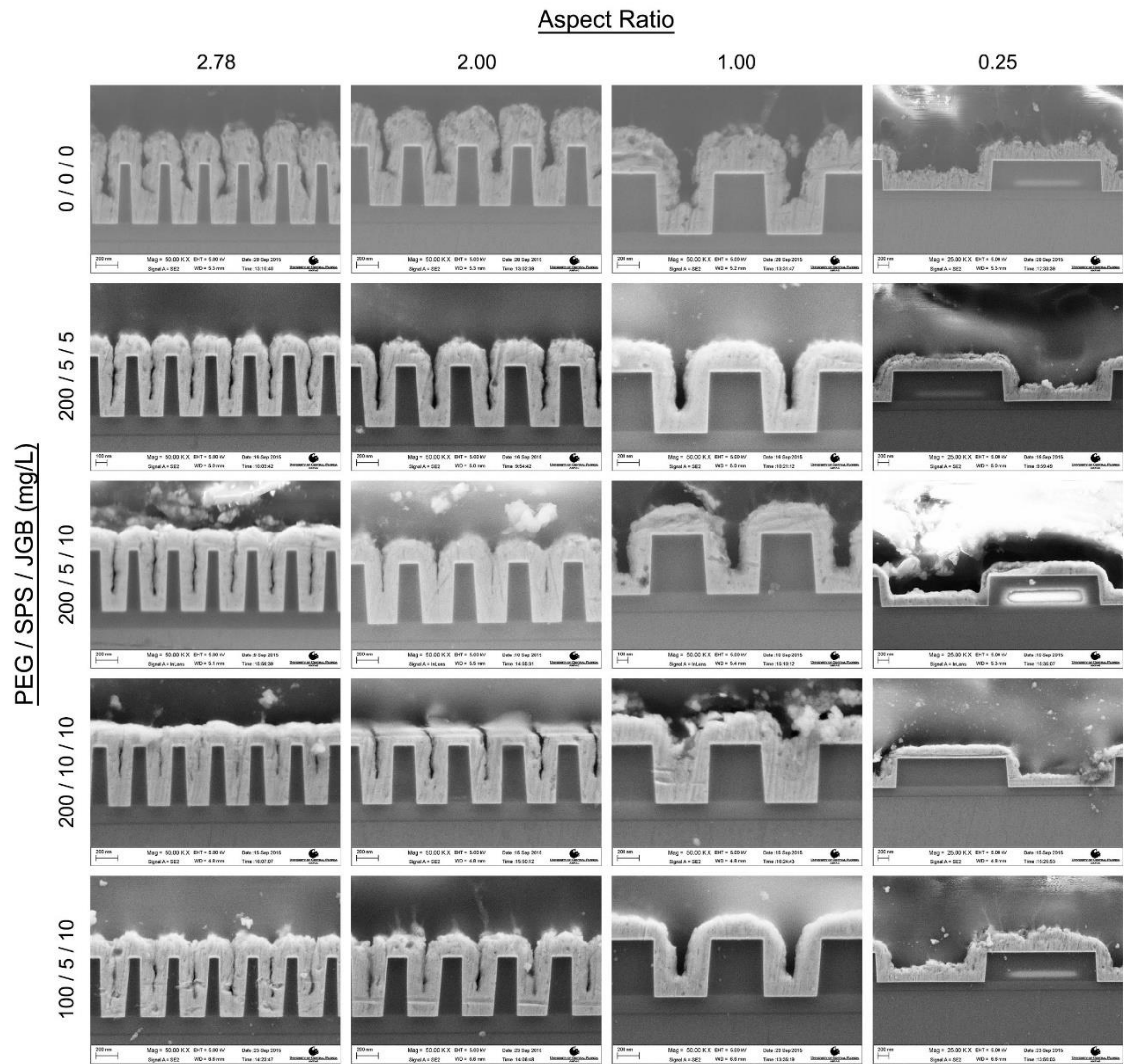

Figure 4.5: SEM micrographs of the trench cross-sections after 1 minute of Cu deposition. The four aspect ratios of trenches examined in the matrix are shown by the column heading and the organic additives concentrations (of each, in mg/L) added to the bath, are shown by the row.

Furthermore, after 3.5 min of filling, all features appeared to be completely filled and void-free, regardless of the organic additive content. Since deposition conditions and samples varied from the literature, it was thought that organic additives were not necessary to warrant defect free filling in these relatively low aspect ratio features. It was later discovered, through FIB milling for EBSD sample preparation, that most trenches actually did contain fill-related voids, due to

unexpected issues with the cross-sectioning protocol (smearing of Cu) discussed in section 4.2.3. The highest aspect ratio trenches (2.78) were the most susceptible trench geometries to fill voids and were evaluated for their void area with various organic additive concentrations. The presence of these voids, which ranged from pinhole like features, to seams, are clearly evident in the cross-sectional SEM micrographs of the trenches, shown in Figure 4.6. Here, all micrographs are sized to be comparable using the 500 nm scale-bar shown.

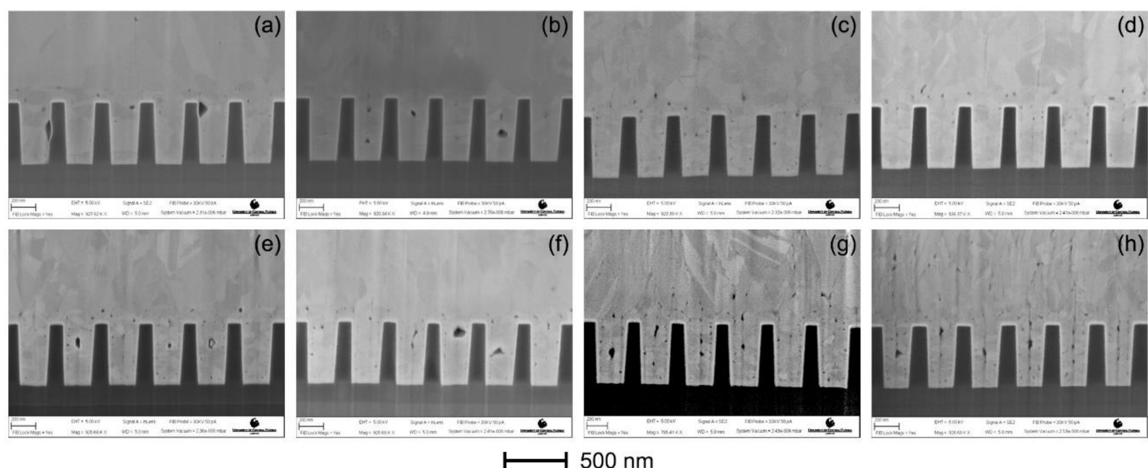

Figure 4.6: SEM micrographs for the 2.78 aspect ratio trench cross-sections deposited with PEG/SPS/JGB (mg/L) concentrations of (a) 0/0/0, (b) 200/5/0, (c) 200/50/10, (d) 200/20/10, (e) 200/5/5, (f) 200/5/10, (g) 200/5/50, and (h) 200/5/100. The images are in descending order of JGB/SPS ratio.

The three types of voids primarily observed in these trenches are more specifically illustrated in the micrograph of Figure 4.7 which more precisely highlights the typical location of each void type. Voids formed at the center of the trenches are typically found from subconformal or conformal filling profiles. Many voids were also seen at the interface between the Cu seed layer and the electrodeposited Cu. These voids may have occurred from oxidation of the Cu

seed layer prior to deposition. This issue is address in a subsequent discussion. Lastly, other voids were found at grain boundaries and triple junctions in the overfill of the trenches. Table 4.3 summarizes these findings quantitatively displaying the void area per trench for center voids, interfacial voids, and voids in other locations in trenches deposited with various organic additive concentrations.

It was important to correlate these void formation observations with the types of additives used and their concentration to obtain some indication as to how the additives were impacting the evolving microstructure during the trench filling process. To do this, we analyzed the void content with respect to individual organic additives as well as ratios between the additives, since additives may also influence one another's role when they co-exist in the deposition bath. Analysis showed that the total void area found in the cross-sections appears to increase with JGB/SPS ratio. The increase in SPS concentration of the baths produces less center voids, most likely due to the Cu's increased preference to grow from the base of the trenches.

However, increasing the JGB concentration seems to have the opposite effect. Center voids occupied a larger area in the trenches deposited with higher concentrations of JGB in the bath. Likewise, more voids and cracks were found along grain boundaries and triple junctions, especially at JGB concentrations of 50 mg/L and above. This finding suggests more stresses occurred during the deposition and annealing process that were later alleviated by void formation. This may be a result of JGB implantation into the Cu surface during deposition, acting as impurities in the system and preventing stress-relieving recrystallization from

occurring.

Interestingly, it was found that excluding the JGB from the electrodeposition bath almost completely eliminates interfacial and grain boundary voids. It is also curious to note that all organic additive concentrations produced *more* **center** voids than the trenches deposited *without any organics* in the bath. However, the **interfacial** voids in the 0/0/0 deposited trenches are large and often extend to the center of the trenches. It is believed that these voids were induced due to similar circumstances as center voids, but non-uniform deposition onto the trench sidewalls produced these off-center voids.

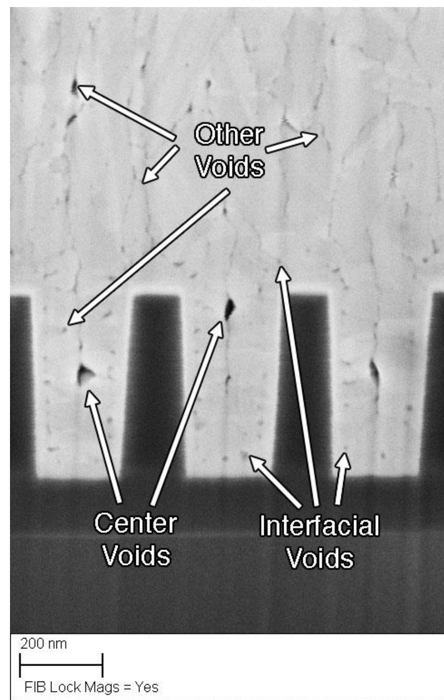

Figure 4.7: The three types of voids found in the Cu trench deposits, exemplified by the SEM cross-sectional image of the trenches deposited with 200/5/100 mg/L (PEG/SPS/JGB).

Table 4.3: The void area measurements for 2.78 aspect ratio trenches deposited with various organic additive concentrations.

Void Area per Trench (nm^2)								
PEG/SPS/ JGB (mg/L)	0/0/0	200/5/ 0	200/50/ 10	200/20/ 10	200/5/ 5	200/5/ 10	200/5/ 50	200/5/ 100
JGB/SPS	N/A	0	0.2	0.5	1	2	10	20
Center	102	1470	178	205	978	1485	1607	1736
Interfacial	1935	2	921	1140	890	1253	1076	1732
Other	43	0	133	403	0	223	1742	4948
Total	2080	1472	1232	1748	1868	2961	4425	8416

Dedicated sub-studies were conducted to determine if other electrodeposition parameters could be utilized to eliminate voids from the Cu trenches. Using higher peak current densities during Cu deposition is prone to producing center voids and seams in features [60]. Faster deposition rates close feature openings much faster and doesn't allow sufficient time for Cu ions to diffuse to the bottom of the features. Peak current densities of 5 mA/cm^2, 10 mA/cm^2, 20 mA/cm^2, and 80 mA/cm^2 were compared for their efficiencies in filling the 2.78 aspect ratio trenches. The bath used to deposit the features contained 200 mg/L of PEG, 5 mg/L of SPS, and 10 mg/L of JGB. The cross-sectional SEM micrographs and resulting void area are shown in Figure 4.8 and Table 4.4, respectively. The degree of sidewall voiding does not appear to change with the peak current density used during deposition and it is proposed that these voids are present due to contamination of the seed layer prior to deposition. One might expect the lower PCD used during deposition to result in less center voids due to the slower deposition rate. This was confirmed through the SEM cross-sectional observations in Figure 4.8 and void area measurements depicted in Table 4.4. However, lower PCD also increased the voids found along grain boundaries and

triple junctions in the Cu.

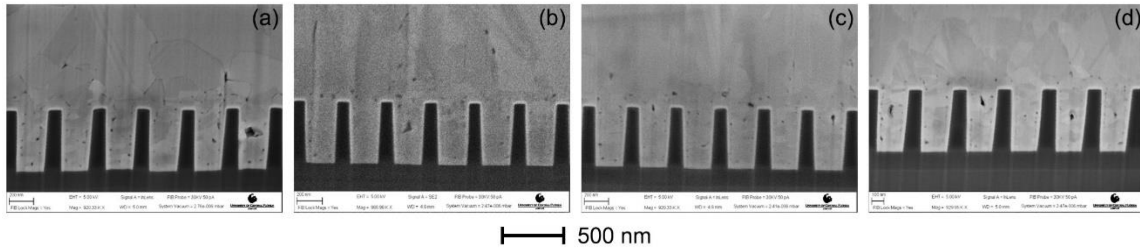

Figure 4.8: SEM images of FIB cross-sectioned 2.78 aspect ratio trenches deposited using a PCD of (a) 5 mA/cm^2, (b) 10 mA/cm^2, (c) 20 mA/cm^2, and (d) 80 mA/cm^2. All trenches were deposited using 200 mg/L PEG, 5 mg/L SPS, and 10 mg/L JGB.

Table 4.4: The void area measurements for the 2.78 aspect ratio trenches deposited with different peak current densities. All trenches were deposited using 200 mg/L PEG, 5 mg/L SPS, and 10 mg/L JGB.

Void Area per Trench (nm^2)				
Peak Current Density	5 mA/cm^2	10 mA/cm^2	20 mA/cm^2	80 mA/cm^2
Center	158	567	757	1103
Interfacial	1223	1184	2045	1249
Other	2813	1048	405	77
Total	4194	2798	3206	2429

It was our assumption that the sidewall voids occurred due to Cu seed layer oxidation after observing the cross-sectional micrographs. Therefore, several pretreatments were conducted on the samples prior to their deposition to reduce the sidewall void area. All samples shown until this point were pretreated with a 200:1 mL mixture of deionized water and ammonium hydroxide to rid the wafers of possible adventitious surface organic contamination. The surface pretreatments attempted for this sub-study included, samples without pretreatment (without NH_4OH), a 30 min anneal at 300 °C in a forming gas atmosphere (96% N_2 – 4% H), and etching for 2.5 s or 5 s with an aqueous ferric chloride ($FeCl_3$) etchant. These tests were conducted using an electrodeposition bath without organic additives due to their high sidewall void content. The cross-sectional SEM

micrographs of the 2.78 aspect ratio trenches using various pretreatments are displayed in Figure 4.9 and their subsequent void area measurements are shown in Table 4.5. For these void area measurements, the large sidewall voids were placed into the 'other' category to help distinguish between the interfacial voids that occur along the entire interface between the Cu seed layer and electrodeposited Cu. Only a few voids were observed at grain boundaries and triple junctions, so the 'other' category almost exclusively included these large voids (~100 nm in diameter) toward to top sidewalls of the trenches. None of the pretreatments utilized resulted in beneficial void area reduction in the trenches. The only pretreatment that appeared to have a significant impact on the resulting void area in the trenches, was the use of a "light" acid etch. Although a very diluted etchant (~25 $FeCl_3$ mg/mL) was used, it was found to create a rougher Cu seed layer surface, which resulted in larger amounts of voids in the trenches, and was thus discontinued.

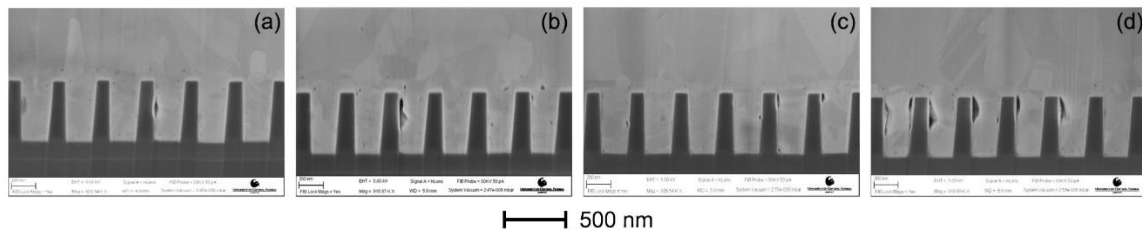

Figure 4.9: Cross-sections of the 2.78 aspect ratio trenches, where different pretreatments were used prior to Cu deposition: (a) Standard, (b) w/o NH_4OH, (c) heat treated 300 °C for 30 min, and (d) etched for 5s using a ferric chloride etchant. All trenches were deposited without organic additives.

Table 4.5: The void area measurements for the 2.78 aspect ratio trenches deposited with after various pretreatments. All trenches were deposited without organic additives.

Void Area per Trench (nm^2)				
Pretreatments	Standard	w/o NH_4OH	Annealed	5s Etch
Center	29	162	9	3
Interfacial	533	671	426	504
Other	1220	1391	1468	9669
Total	1783	2224	1903	10176

4.3.2 Impact of Additives on Resulting Cu Properties

In addition to the mechanical defects (voids) described above, this section discusses the impact of additives on other film properties. The residual stress and surface roughness of the Cu trench deposits were measured as the electrolyte bath compositions was varied. As discussed in section 4.2.2, the complex nature of the trench samples made it impossible to calculate the absolute stress values with the Stoney equation. However, by measuring the radius of curvature of the samples and normalizing by the thickness of the Cu deposit, *relative* stress values could be compared from sample to sample. Analysis of these relative stress levels, as a function of additive concentration allowed conclusions to be made as to their role in film stress. Since the trench blueprint of the samples is not symmetrical, it was expected that radius of curvature values would vary depending on the direction of the measurement. This is demonstrated in Figure 4.10, which shows a typical surface map of a trench sample after deposition. The average radius of curvature for all four directions (x, y, xy1, xy2) could not be utilized as it was for the blanket films. Stress measurements were compared side by side using the four directions for the radius of curvature measurements and are shown in Figure 4.11. Although individual directions used in the measurements produced different results, the trends remained intact with changing additive concentration. Thus,

only one direction was used consistently throughout the study. Similarly, RMS roughness measurements could not be taken in the center of the samples like for the blanket Cu films. Instead, the measurements were conducted in the same area on every sample, where no trenches were present.

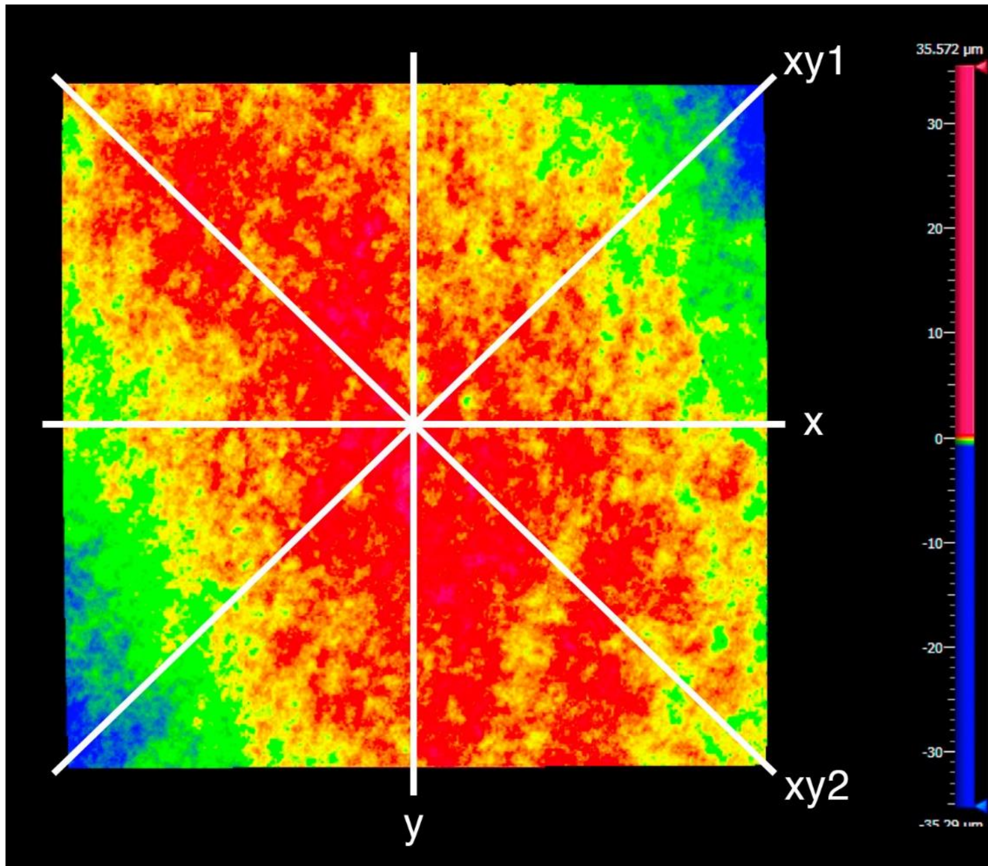

Figure 4.10: A surface map of a typical trench sample after deposition, where the red indicates area of increased height and blue represents depressed areas. This image shows the unsymmetrical nature for the radius of curvature due to the samples' blueprint.

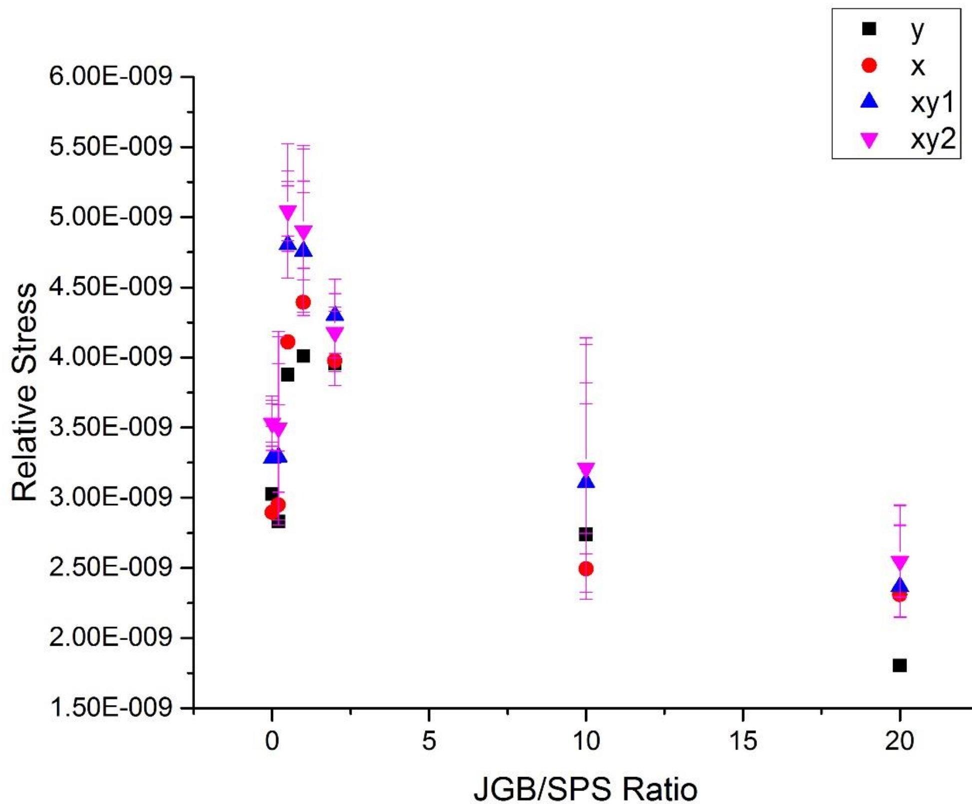

Figure 4.11: The relative stress in the four directions for radius of curvature measurements. Although the stress measurements differ with direction, the trends remain the same with changing JGB/SPS ratio. Error bars correspond to standard deviations of the measurements.

To assess the impact of individual organic additives on resulting Cu stress and roughness, samples were deposited with large amounts (200 mg/L) of each organic additive in the electrolyte. The results are shown in Table 4.6. The residual biaxial stress in the Cu slightly increases when PEG and SPS are added to the bath individually. On the other hand, the addition of JGB alleviated some of these stresses compared to the other individual additives as shown in Table 4.6.

Table 4.6: The relative stress and surface roughness measurements when only one organic additive is used in the electrodeposition bath of Cu.

Organic Additive	Relative Stress (a.u.)	RMS Roughness (nm)
None	3.28 ± 0.02	32.8 ± 2.4
200 mg/L PEG	4.11 ± 0.47	8.3 ± 0.6
200 mg/L SPS	4.09 ± 0.39	10.7 ± 0.7
200 mg/L JGB	1.62 ± 0.99	68.8 ± 13.9

It can be seen that the surface roughness of Cu deposits is reduced with the addition of PEG and SPS to the bath, and increased with the introduction of JGB. Reduced surface roughness suggested that smaller grains were present at the surface. This is expected to occur with the addition of all organic additives due to Zener pinning and the suppression of recrystallization from the accelerator (SPS) and reduced activation energy for nucleation from increased cathodic over-potential caused by the addition of inhibitors (PEG, JGB) [146-149]. The JGB does not follow this trend and may be creating larger grains in the Cu deposits. The JGB creates striations across the surface of the Cu deposits, which could be causing the significant increase in surface roughness.

The surface roughness and relative residual stresses were then analyzed for the Cu deposited with various organic additive concentrations when all three additives are present. As shown in Figure 4.12, the RMS surface roughness appears to decrease exponentially with increasing JGB/SPS ratio. The RMS roughness reaches a minimum of ~8 nm above a JGB/SPS ratio of 2. PEG concentrations of 100 mg/L, 200 mg/L, and 500 mg/L were also used and determined to have little to no impact on surface roughness of the Cu in the presence of the other two additives. The reduced roughness with increasing JGB/SPS ratio counters the observation seen in the individual study, where the

use of only JGB in the bath resulted in a rougher surface. The use of PEG and SPS simultaneously with the JGB may have counteracted the effect since the addition of PEG and SPS, individually, were shown to have lower roughnesses than the JGB. Furthermore, complex interactions between the organic additives may have also played a role. These results show that JGB and SPS concentrations are the main drivers in the bath for material property changes in the Cu.

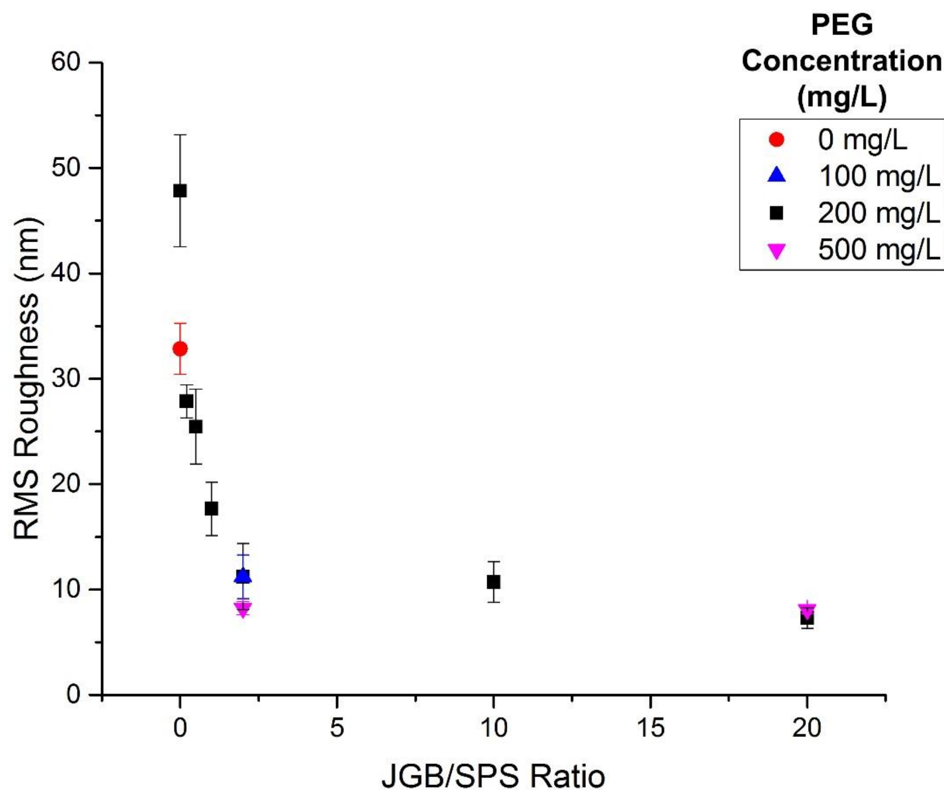

Figure 4.12: The RMS surface roughness with changing JGB/SPS concentration ratio in the bath and various PEG concentrations.

A similar trend is seen in the relative stresses as a function of JGB/SPS

ratio, shown in Figure 4.13. PEG concentration has a negligible effect on the stresses, while the JGB/SPS ratio scales inversely with the stress. These Cu systems are prone to voids, which act as a stress relieving mechanism [32,139]. When the total void area measurements from section 4.3.1 are plotted alongside these relative stress measurements (Figure 4.14), a strong correlation can be drawn between the two. Samples that contained a larger amount of voids, had lower residual stresses as the stresses were unable to build up in the most vulnerable areas (triple junctions, grain boundaries, and other interfaces).

This finding is consistent with the observation also made in the pulse current density (PCD) study. The relative stress, void area, and surface roughness of these samples are shown in Table 4.7. The samples deposited with lower PCD had lower residual stresses as a result of the increased void area in the Cu. Furthermore, lower current densities produced much rougher Cu surfaces. An order of magnitude difference is observed between the 80 mA/cm^2 and 5 mA/cm^2 deposited samples in Table 4.7. Again, this higher roughness is an indication of larger grain sizes at the surface. Lui *et al.* and many other studies have shown that higher PCD result in smaller grain sizes due to faster nucleation rates [90,91].

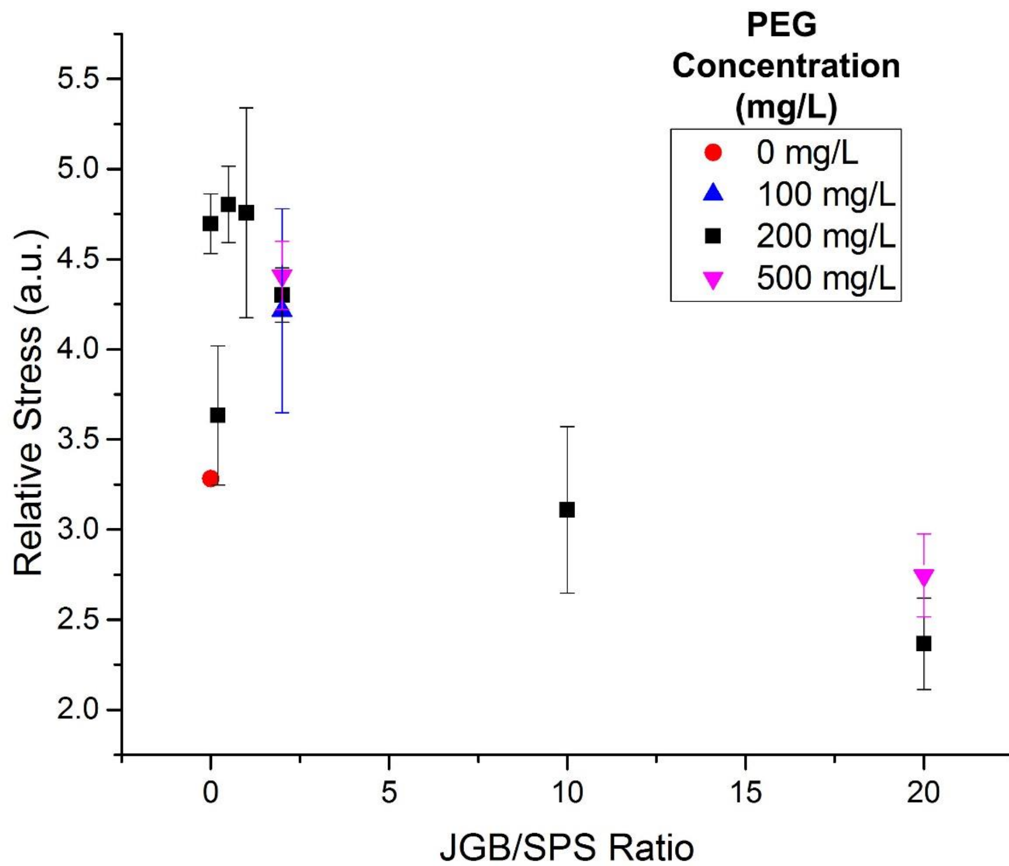

Figure 4.13: The relative stress as a function of JGB/SPS concentration ratio in the bath and various PEG concentrations. A change in y-axis by one arbitrary unit equates to ~10-15 MPa of stress.

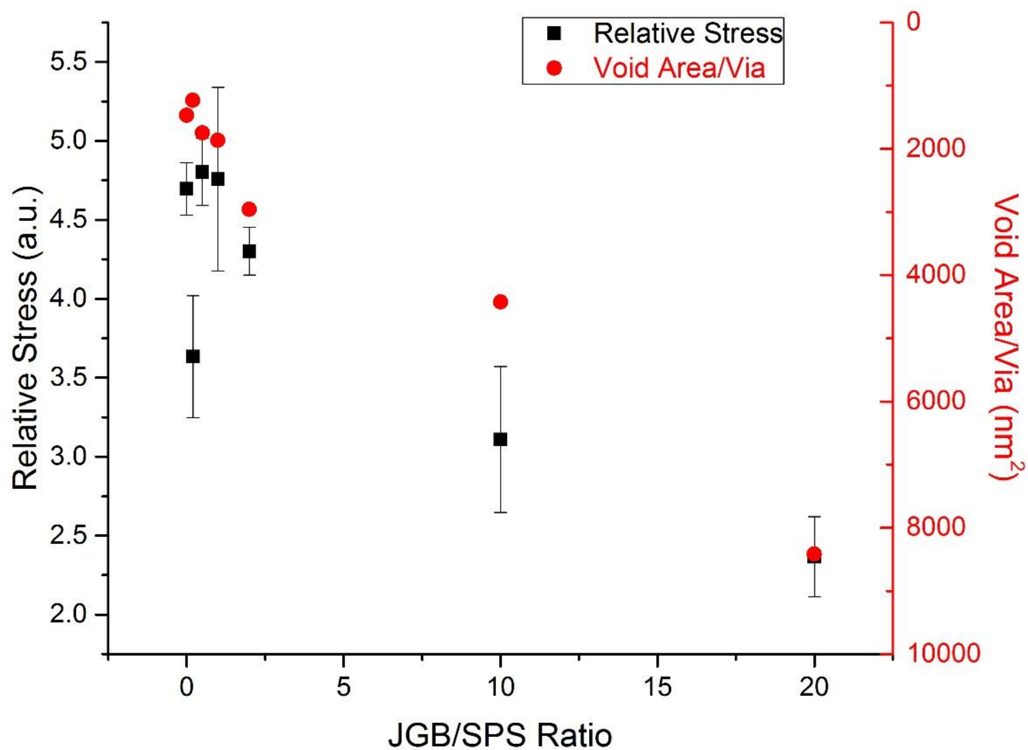

Figure 4.14: The relative stress and void area per trench plotted side by side with respect to JGB/SPS ratio. A change in y-axis by one arbitrary unit equates to ~10-15 MPa of stress.

Table 4.7: The relative stress, surface roughness, and void area measurements in Cu deposited with various peak current densities.

Peak Current Density (mA/cm^2)	Relative Stress (a.u.)	RMS Roughness (nm)	Void Area/Trench (nm^2)
5	N/A	211.1 ± 17.2	4194
10	2.63	28.4 ± 10.3	2798
20	4.31	14.4 ± 2.0	3206
80	7.90	11.2 ± 3.1	2429

4.3.3 Copper Trench Microstructure

To determine the effects of the organic additives and the resulting stress on the Cu microstructure, x-ray diffraction and cross-sectional electron backscattering diffraction or transmission Kikuchi diffraction were conducted on the samples. The

texture of the Cu seed layer on these trench samples was analyzed using a chi rocking curve, similar to protocol used in the blanket film study. Figure 4.15 shows the (111) rocking curve of the seed layer in the trench samples compared to the blanket film samples. While both sample types display a (111) texture of the samples normal to their surface, the narrower and higher intensity peak of the trench samples shows a higher degree of (111) orientation in the seed layer. Therefore, highly preferential Cu orientations in the trenches are expected. The texture coefficients of the Cu deposited with varying organic additive concentrations, from Figure 4.16, confirm this. Like the stress and roughness data, the (111) texture of copper decreases with increasing JGB/SPS ratio. The PEG concentration, similarly, has little effect on the texture coefficients, except at the highest JGB/SPS ratio. The Cu deposited without any organic additives in the bath is shown by the red data point in Figure 4.16. The (200), (220), and (311) peaks were indistinguishable in these sample, thus the (111) texture coefficient was the maximum achievable for these sample (TC = 4) and the Cu microstructure in these samples had little to no variation in Cu orientation. All samples exhibited large degrees of (111) texture, however, Figure 4.17 shows the increase in (311) texture coefficient as the (111) decreases with the larger JGB/SPS ratio in the electrolyte. This change in microstructure could be a result of the different mechanisms of grain growth between the (111) and (311) discussed in section 3.3.2; however, unlike the findings on blanket films in Chapter 3, the larger stresses do not appear to be the mechanism for the lower degree of preferential orientation observed here. TKD was required for a closer look into these microstructural variations and is

discussed later in this section.

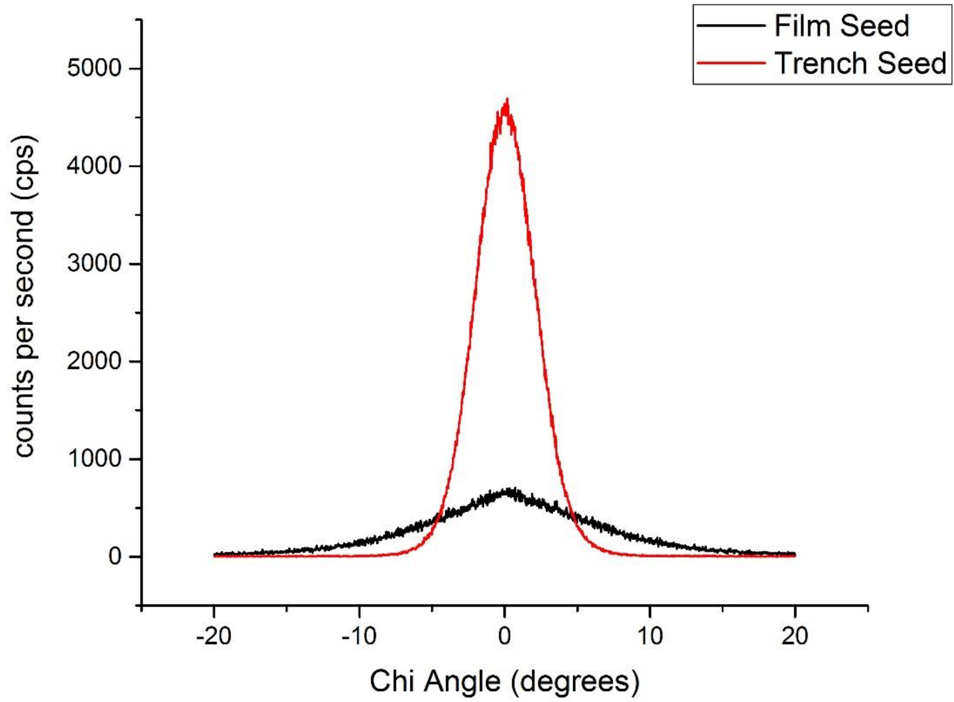

Figure 4.15: Chi rocking curve of the film and trench sample Cu seed layers prior to deposition illustrating degree of (111) preferential orientation is higher for the trench Cu seed layer over the film Cu seed layer.

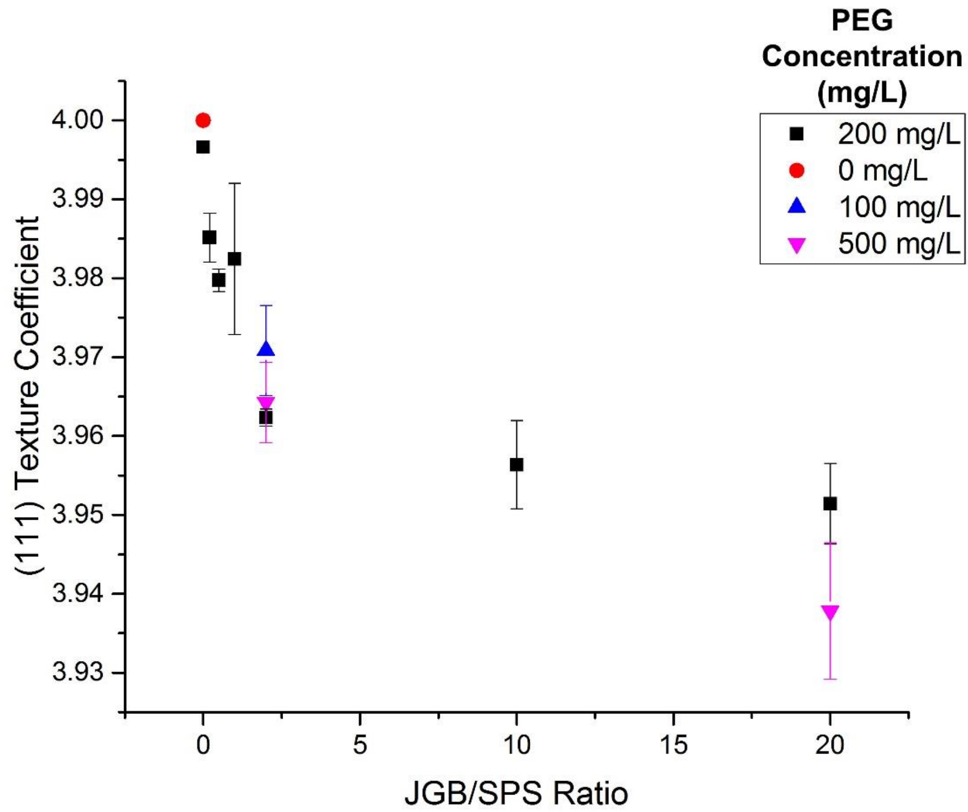

Figure 4.16: A plot of the Cu (111) texture coefficient as the organic additive concentrations in the electrodeposition bath were changed.

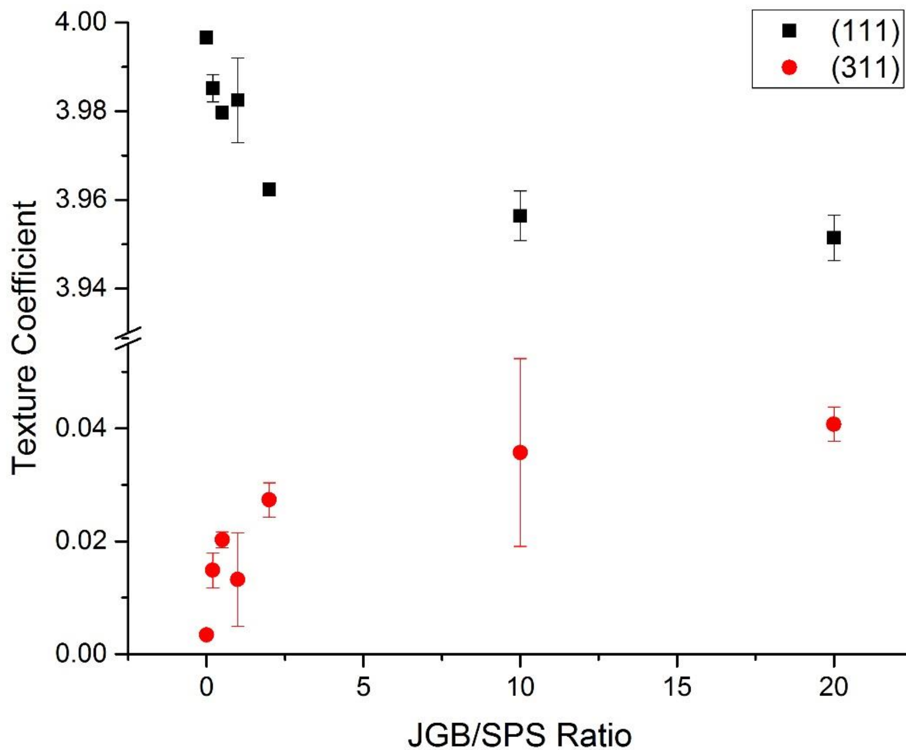

Figure 4.17: The change in texture coefficient for the (111) and (311) orientations with various JGB/SPS ratio in the bath used to deposit the Cu.

The microstructure of the 250 nm wide trenches with an aspect ratio of 2 were analyzed using TKD. Here, the goal was to observe changes in the Cu trench cross-sectional microstructure due to the changes in organic additive concentrations used to deposit the Cu and relate these microstructural features to the acquired stress measurements from section 4.3.2 and XRD texture measurements from earlier in this section. The samples deposited without organic additives were examined as well as three organic additive concentration combinations with different JGB/SPS ratios. These concentrations included the 200/20/10, 200/5/10, and 200/5/100 samples with JGB/SPS ratios of 0.5, 2, and

20 respectively. The band contrast maps for the cross-sections of each 250 nm trench are shown in Figure 4.18. The trenches that were deposited without any organic additives have much larger grains than those that did contain organic additives in the electrolytic bath. However, this observation is not reflected in the average grain diameters, shown in Table 4.8. Instead, Table 4.8 also shows that grains larger than 200 nm make up a majority of the trench area in the deposits without organic additives. Trenches that were filled with baths containing organic additives showed much smaller area percentages of these large grains, indicating an inhibition of grain growth or change in the nucleation rate as discussed in section 4.3.2.

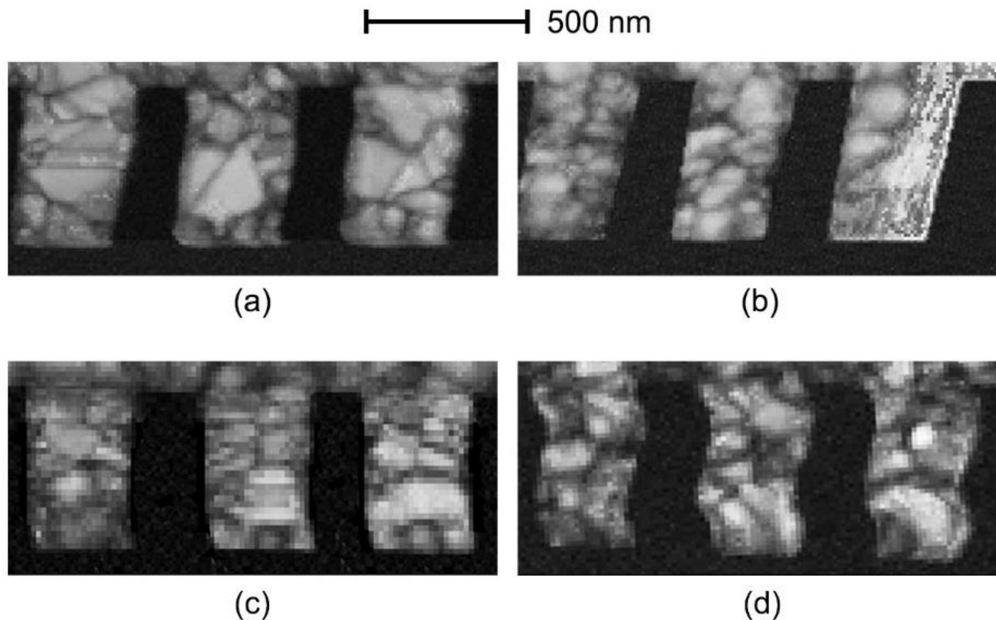

Figure 4.18: The band contrast maps of the 250 nm wide trenches (aspect ratio: 2) for the (a) 0/0/0, (b) 200/20/10, (c) 200/5/10, and (d) 200/5/100 samples. The images are in descending order of JGB/SPS ratio.

Table 4.8: The average grain size and percentage of microstructural area consumed by the large grains in the Cu deposited with various organic additive concentrations. The standard deviations are shown for the grain diameter measurements.

PEG/SPS/JGB (mg/L)	JGB/SPS Ratio	Average Grain Diameter (nm)	>200 nm Grain Area%
0/0/0	N/A	123 ± 92	65%
200/20/10	0.5	110 ± 55	27%
200/5/10	2	111 ± 45	23%
200/5/100	20	121 ± 61	38%

The inverse pole figure maps in Figure 4.19 show a similar result to that found in the XRD texture coefficients. The maps indicate a large number of (111)-oriented grains, normal to the sample surface, especially in the map of the non-organic additive deposited Cu trenches.

Once organics are used in the bath to deposit these trenches, the degree of (111) texture was seen to reduce and other grain orientations were found to become more prevalent. Leveler additives, such as JGB, have been shown to inhibit (111) and (100) orientations, while leaving (101) orientations uninhibited [162]. The non-(111)-oriented grains in this study were typically located at the top of the trenches or near their openings. It was found that the bottom of the trenches almost exclusively contained (111)-oriented grains normal to the sample's surface due to seed layer influences.

The inverse pole figure maps in all three directions (transverse, longitudinal, and normal) are shown in Figure 4.20 for the 0/0/0 trenches and 200/5/100 trenches. In evaluating the sequence of growth in this study, it was found that when grains grew from the sidewalls, they tend to be (101)-oriented normal to the sample surface. In the transverse direction of the trenches, this is a (111) orientation, signifying the sidewalls of the trenches are also (111) textured normal to their surface.

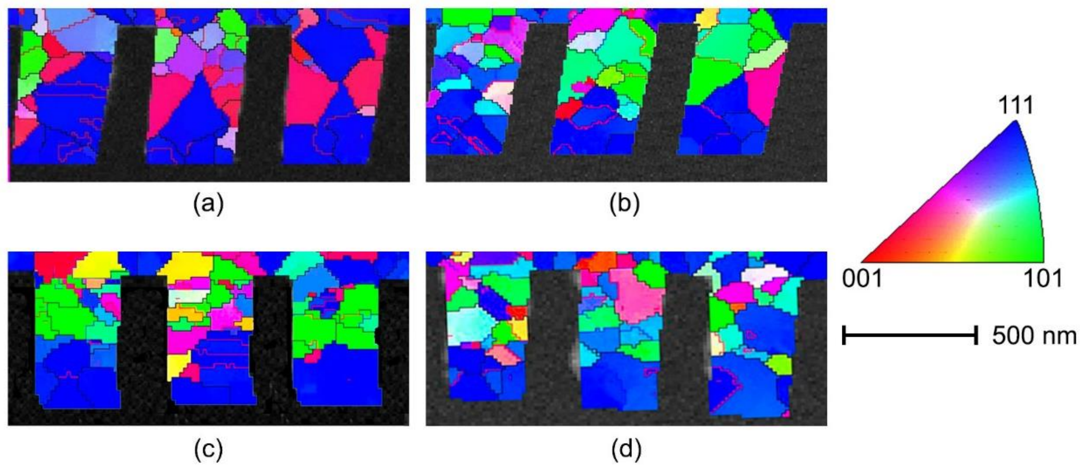

Figure 4.19: The inverse pole figure maps, normal to the sample surface, of the 250 nm wide trenches (aspect ratio: 2) for the (a) 0/0/0, (b) 200/20/10, (c) 200/5/10, and (d) 200/5/100 samples. The images are in descending order of JGB/SPS ratio.

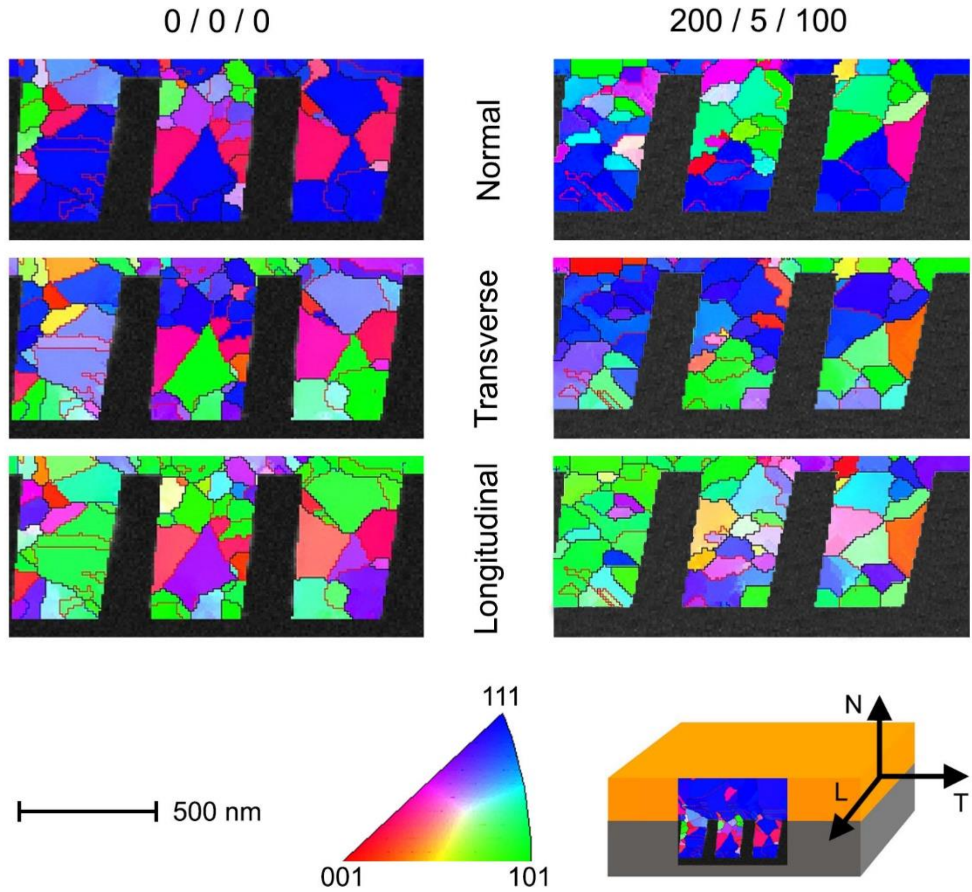

Figure 4.20: The inverse pole figure maps of the 250 nm wide trench cross-sections in the normal, transverse and longitudinal directions for the PEG/SPS/JGB (mg/L) concentrations of 0/0/0 and 200/5/100.

The amount of twinning in the trenches was measured as the number of twins per grain and twins per unit area, as illustrated in Table 4.9. Both measurements show a larger amount of twins present in the trenches when the baths contained no organic additives. Since the grain size was large in the trenches that were deposited without organic additives, the twins/grain measurement was much higher than for the other samples examined. Furthermore, the dominant stress relieving mechanism in this system clearly appears to be void formation. Increased void area in trenches filled with the use

of organic additives have created lower stresses in these areas and lower driving force for twin formation during recrystallization. The larger grained samples also appear to have more twins, similar to observations made for the blanket Cu films.

Table 4.9: The amount of twins in the microstructure of the Cu trenches filled using different organic additive concentrations.

PEG/SPS/JGB (mg/L)	JGB/SPS Ratio	Twins/Grain	Twins/μm^2
0/0/0	N/A	0.74	40.2
200/20/10	0.5	0.39	33.5
200/5/10	2	0.39	35.2
200/5/100	20	0.30	21.4

To determine if the residual impurities in the deposited Cu from the organic additives may have contributed to the decrease in grain size with the addition of the organics in the bath, the organics in the deposited Cu were measured with thermogravimetric analysis (TGA) and surface-enhanced Raman spectroscopy (SERS). Both metrology did not yield conclusive results on the residual organic contamination; the TGA was not sensitive enough to observe the burn off of the organics in the Cu, and Au-Pd was sputtered onto the Cu surface for SERS, but the organics were still not detected.

Some information was obtained from cesium (Cs) secondary ion mass spectrometry (SIMS) was conducted on the Cu deposits. A baseline spectrum was obtained on a Cu sample that was deposited without organic additives. Then, the Cu that was deposited with 200 mg/L of each organic additive was analyzed to determine, the peaks of interest, which would be good indicators of the individual additives. The PEG did not have any distinguishable peaks, however, it was determined that the $Cs^{2+}S$ adduct peak at 298 mass/charge (m/z) was a good indicator for sulfur contamination from the SPS, and the $Cs^{2+}CN$ adduct peak at

292 m/z is a good indicator of the JGB additive. The 200/20/10, 200/5/10, and 200/5/100 were also analyzed and are shown in Figure 4.21. The intensity of the CN and S peaks appear to scale well with concentration in the bath, however, the S peak falls below detection limit at the low concentrations used (< 20 mg/L). These results suggest that the Cu deposits had residual contaminants from the organic additives, which could be inhibiting grain growth and causing the finer Cu microstructures.

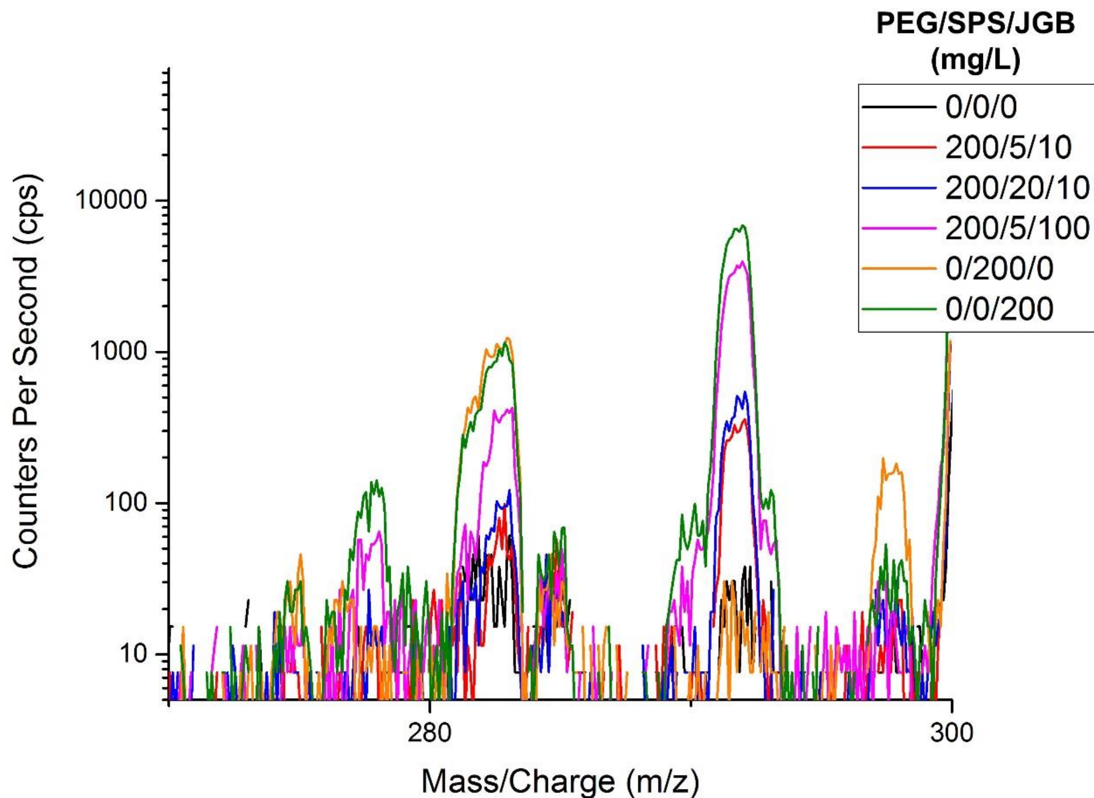

Figure 4.21: The SIMS spectra revealing the amount of residual SPS and JGB left in the Cu after deposition.

4.4 Conclusions

The effect of organic additive concentration in the bath during pulsed electrodeposition was studied for Cu trench samples. Here, the bath deposition parameters optimized for blanket film deposition were utilized with bath chemistries modified with additives meant to affect the filling process of the trench, during deposition. Specific copper film properties evaluated as function of additive type and concentration included filling profiles, surface roughness, biaxial residual stress, and the resulting Cu microstructure in 250 nm wide and 500 nm deep trenches.

The filling profile was observed through cross-sectional analysis agreed reasonably well with the CEAC model for Cu filling. While a limited response was seen with the addition of PEG to the bath, it was determined that the JGB/SPS ratio was the controlling factor in many property changes for the Cu. The biaxial residual stress appeared to decrease with increasing JGB/SPS ratio. This was attributed to the increase in void area found in the cross-sections of the trenches with increasing JGB/SPS ratio. These observations suggest that the JGB/SPS additives interfered with the so-called bottom-up fill of nanometer-scale features. Thus, the diffusion-limited mass transfer of additives, and the variation in adsorption rate of additives, assumptions implicit in the CEAC model, may not be valid at least under the pulsed electroplating experimental conditions used in this work. Factors such as the activity of reduced species, additives flux, adsorption and movement on the cathode surface under the pulsed conditions may be contributing to the observed deviation from the CEAC model, and deserve further

examination [166].

The microstructure of the copper was analyzed using x-ray diffraction and transmission Kikuchi diffraction. Similar to the blanket films, the Cu seed layer contributed to the (111) texture found in all samples examined. The texture, however, did appear to diminish with increasing JGB/SPS ratio. The cross-sectional TKD revealed a large difference between the trenches filled with and without organic additives. Smaller grain sizes were observed in the Cu that utilized organic additives, likely from the residual organics found in the Cu. The TKD also confirmed texture results from the XRD. The (111)-oriented Cu grains were observed at the trench bases and with the addition of organics to the bath, other grain orientations were appeared at the trench openings due to sidewall contributions.

Lastly, higher twin densities were observed in samples which had larger residual stresses, since the fill voids were the dominant stress-relieving mechanisms in these systems. The microstructural findings here, are carried over to the next chapter, where the impact of constraint on the microstructure will be discussed.

CHAPTER FIVE:
GEOMETRIC CONSTRAINTS OF DEPOSITS

While the scope of this dissertation does not include the specific examination of through-silicon vias (TSVs), studying the microstructural differences between Cu of varying degrees of geometric constraint (such as seen through comparison of higher aspect ratio trenches) can help extend our understanding as to how the microstructural characteristics evolve in these higher aspect ratio features. This chapter will utilize findings from previous chapters as well as independent experimental data to focus on the microstructural response of Cu observed in structures which employ different degrees of geometric constraint.

5.1 Motivation and Objectives

To set the stage for this analysis, we considered blanket films to be under little to no constraint during growth as their growth is bound only by the seed layer and the top of the film's interface with the environment. Alternatively, Cu grown in trenches are additionally confined by the surrounding trench/substrate sidewalls as well as the underlying base. Furthermore, trenches with higher aspect ratios (with a narrower trench width to trench depth) are additionally confined as the trench floor area is small as compared to the sidewall area that participates in the Cu film deposition.

Here, two different trench widths (aspect ratios) are investigated to allow us to draw conclusions on how increasing constraint on film formation, impacts

microstructure. We have chosen the 250 nm and 500 nm wide trenches (aspect ratio (AR) of 2 and 1 respectively) and each will be evaluated in this chapter. Ideally, one might expect that the more constrained Cu dimensions may have larger stresses due to the CTE mismatch between the Cu and surrounding layers which have a larger interfacial area to trench area ratio, in higher aspect ratio trenches. More confined areas offer limited growth potential, thus small grains are expected in higher constrained regions. These hypotheses are examined in the following section.

5.2 Results and Discussion

This section shows the comparison between Cu microstructures under varying levels of constraint. First, the blanket films and trench overfills are compared. The microstructures of the various aspect ratio trenches are then observed to anticipate the microstructural behavior of high aspect ratio features.

5.2.1 Blanket Films vs. Trench Overfill

The overfill, or overburden, is the excess Cu layer above the trenches, which is deposited after the features have been filled. This layer is shown in Figure 5.1. While this layer is traditionally polished away through chemical mechanical polishing (CMP) processes to allow flat layers to be aligned during chip bonding, the microstructure of this layer gives us an impression of growth behavior in Cu that is constrained similarly to the blanket Cu films. Unfortunately, the blanket film microstructures were not evaluated with the addition of organics to the

electrodeposition bath. For the trench study in the previous chapter, the overfill was disregarded during our analysis. This section will compare the blanket films and overfill above the 250 and 500 nm wide trenches deposited without organic additives to determine if the overfill's microstructural features epitomize that of the blanket films, since blanket Cu films were not deposited with organic additives. The blanket film microstructures were only evaluated up to thicknesses comparable to the overfill thicknesses from the trenched samples.

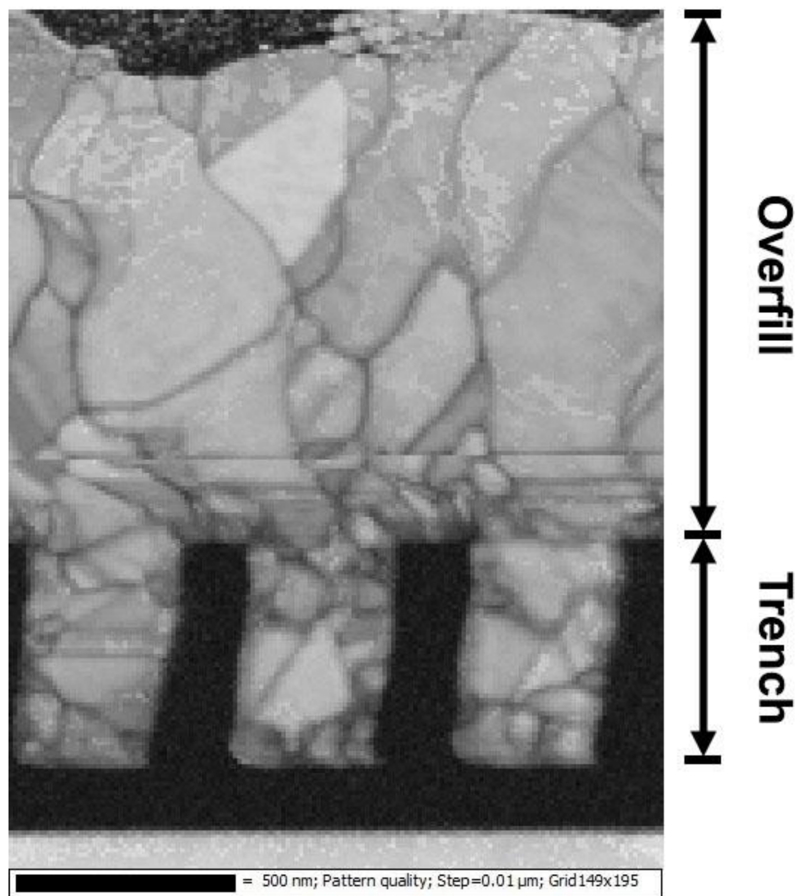

Figure 5.1: A cross-sectional band contrast map of the 250 nm wide trenches, with labelled overfill and trench regions.

As mentioned in Chapters 3 and 4, EBSD and TKD were used to evaluate the Cu blanket film and trenched sample microstructures. The same tools have been employed to assess the Cu grain morphology, texture, and twinning as in prior chapters. The inverse pole figure maps in the direction normal to the sample surfaces are shown in Figure 5.2. Regardless of constraint, all samples exhibited a high degree of (111) texture, however, some effects from the underlying Cu microstructure in the trenches are apparent at the bottom of the overfill IPF maps. The XRD texture coefficients shown in Table 5.1 are further indication of the preferential orientation. While the (111) TC of the trenched samples is much higher than the blanket films, this can be attributed to the more textured Cu seed layers shown in Figure 4.15 of the previous Chapter. Furthermore, the larger thickness of the Cu blanket films (approximately 3x that of the overfill layer) may have contributed to the lower texture coefficient. As the film became thicker, it became less influenced by the Cu seed layer and most non-(111) oriented grains were found closer to the sample surface. If the blanket film was thinner, the results would have been comparable.

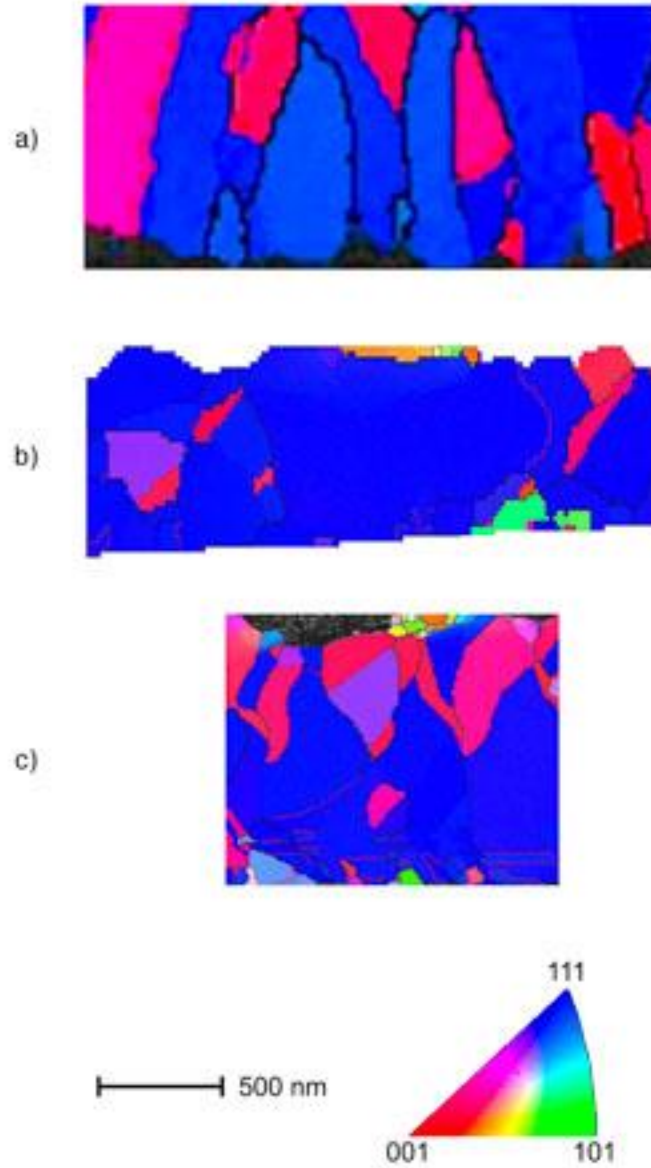

Figure 5.2: The cross-sectional inverse pole figure maps (normal to the sample surface) of the (a) blanket Cu film, (b) 500 nm trench overfill, and (c) 250 nm trench overfill. All samples shown were deposited without organic additives under the same conditions.

Table 5.1: The microstructural characteristics of the blanket films and overfill above the 250 nm and 500 nm wide trenches.

Region	(111) Texture Coefficient	Average Grain Size (nm)	Twins/μm^2
Blanket Films	3.79	382 ± 243	4.26
500 nm Overfill	4	311 ± 260	4.4
250 nm Overfill	4	249 ± 348	7.41

Table 5.1 also displays the average grain diameter of the blanket film and the overfill of the 250 and 500 nm wide trenches. Although the measurements indicate a higher average grain size in the blanket films, the large standard deviations from the wide distribution of grain sizes make the differences inconclusive. The grain size distributions, shown in Figure 5.3, illustrate the influence from the underlying Cu trench sizes on the grain size of the Cu overfill. A larger amount of smaller grains were found in the 250 nm trench overfill than the 500 nm trench overfill. The blanket films and 500 nm overfill grain size distributions are very similar. Both show a large amount of 200 nm diameter grains.

The 500 nm and blanket film twin densities (Table 5.1) were also similar, while the 250 nm trench overfill contained a larger degree of twinning. Twins were mostly located at the bottom of the 250 nm trench overfill, near the trench openings. Higher stresses are expected in those areas, which would have resulted in the increased twin propensity in those regions.

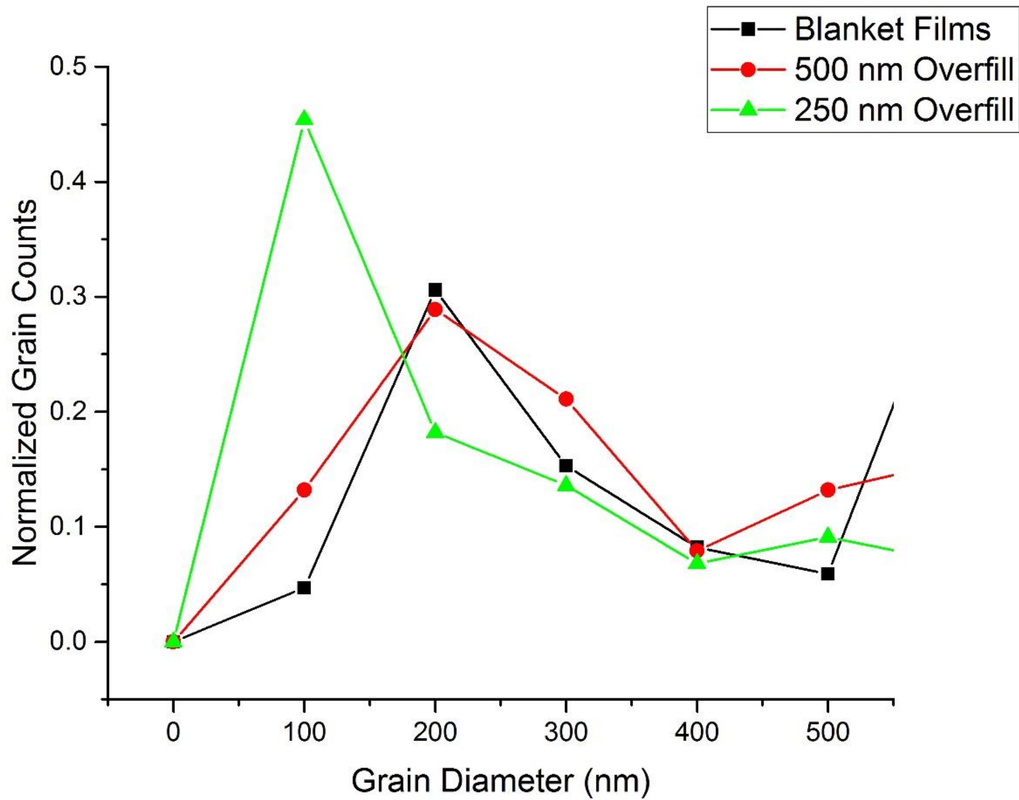

Figure 5.3: Comparison of the grain size histogram for the blanket films and overfill above the 250 nm and 500 nm wide trenches. Error bars are not present due to sample limitations.

The microstructural features analyzed here, show the impact of trench microstructure on the overfill region. The 500 nm trenches are less constrained and expected to have a more comparable microstructure to the blanket films than the 250 nm trench overfill. The 500 nm trench overfill was more representative of the Cu blanket films with similar grain sizes, texture, and twin densities.

5.2.2 The Influence of Geometric Constraint

As noted above, the cross-sectional microstructures of the trench regions and overfill regions were analyzed separately, using EBSD and TKD to determine

the influence from geometric constraints. The overfill regions were considered the least constrained areas and the constraint increased with increasing aspect ratio. Thus, the 250 nm trenches were treated as higher constrained regions compared to the 500 nm trenches.

The 250 nm and 500 nm trench grain size distributions are shown in Figures 5.4 and 5.5 respectively. Most grains were approximately 100 nm in diameter for the 250 nm trenches. The distribution of the 500 nm trenches shifted to higher grain sizes or the peak widened, indicating a larger distribution of grain sizes and possibly larger grains than in the 250 nm trenches. This is expected since the confined space of the 250 nm trenches does not give the grains the freedom to grow as much as the 500 nm wide trenches. When the grains are less confined in the overfill regions, they are allowed to grow even larger. Many grains shown in Figure 5.2 were larger than the maximum possible grain size within the trenches (500 nm) and some spanned the entire thickness of the overfill. Meanwhile, the largest grains inside the trenches were located at the base of the trenches, as shown in Figure 5.6, and are thought to have formed before additives were able to diffuse to the surface and have a large impact on the areas. Another possible scenario which would have yielded this result is that the accelerator preferentially grew the grains at the base of the trenches while the suppressor and leveler inhibited the growth from the sidewalls.

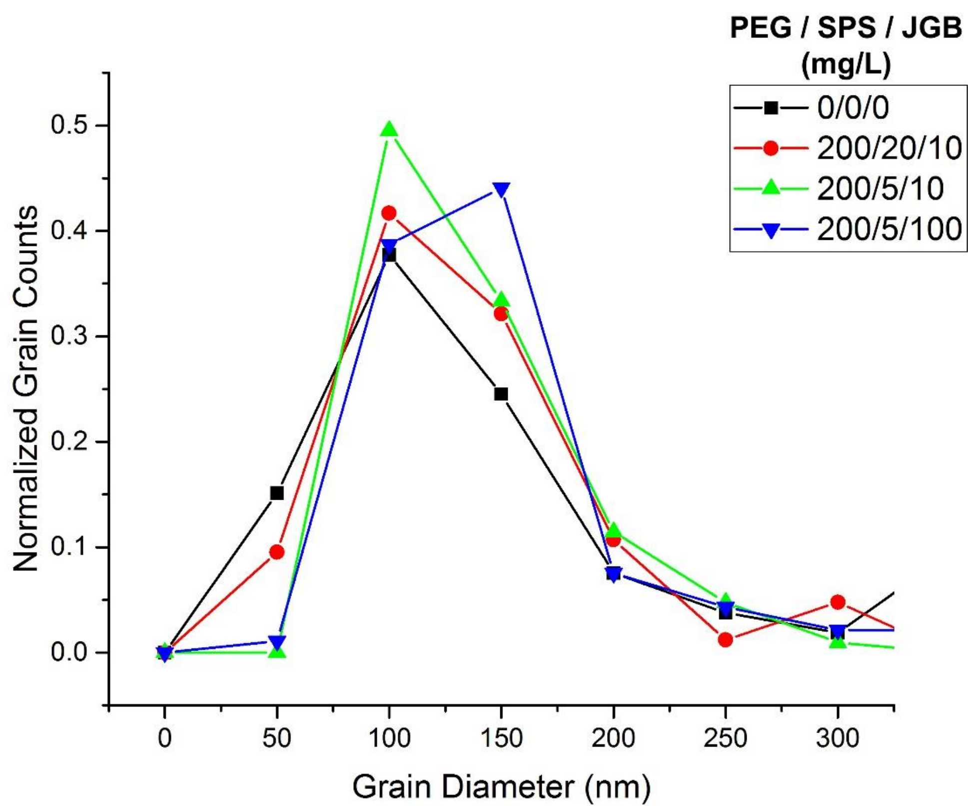

Figure 5.4: Grain size histogram of the 250 nm wide trench microstructure deposited with various bath additive concentrations.

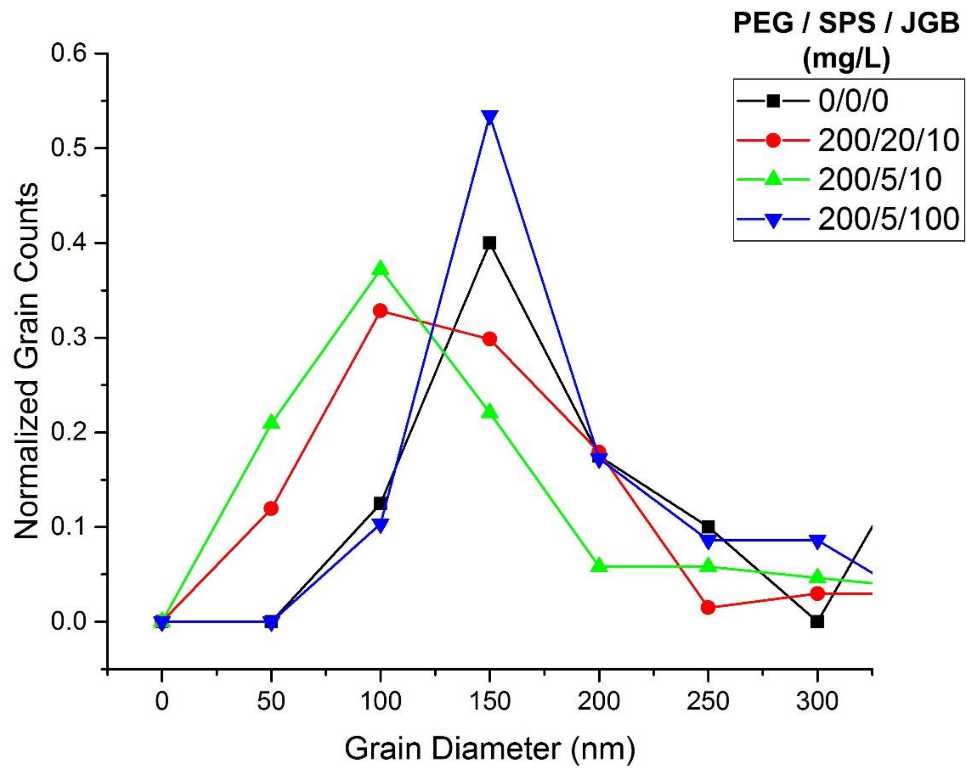

Figure 5.5: Grain size histogram of the 500 nm wide trench microstructure deposited with various bath additive concentrations.

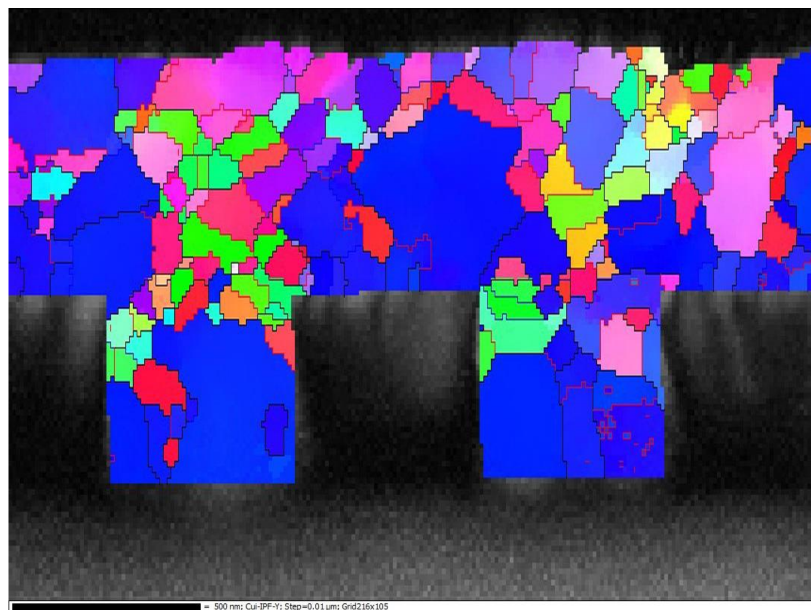

Figure 5.6: The cross-sectional IPF map normal to the sample surface for the 200/20/10 sample. This map shows the grain sizes at the bottom of trenches compared to other areas.

The inverse pole figure maps (normal to the sample surface) are shown in Figure 5.7 for the various regions of constraint. As discussed in Chapter 4 the (111) texture originates from the Cu seed layer and thus is seen growing from surface parallel to the Surface (trench base). This includes bottom of the trenches as well as the pitch between trenches in the overfill. Both aspect ratio trenches and overfill regions exhibit a strong suppression of the (111)-oriented grain contribution with the addition of organics to the bath and is consistent with observations from Wu *et al*. [162]. The smaller grains grown from the trench sidewalls also effect the overfill above and is clearly a result of the organic additives in the bath. The sidewalls appear to have a less significant contribution to the grain structure in the 500 nm trenches compared to the 250 nm trenches as shown in Figure 5.7. The (111)-oriented grains at the trench base are allowed to grow much more and consume a much larger percentage of the trench area in the 500 nm trenches, resulting in the larger multiple of uniform densities for the 500 nm trenches in Table 5.2. In the case of extremely high aspect ratio features, such as 10:1 TSVs, the base contribution is expected to be almost nonexistent, while the sidewall contribution would be overwhelming. This explains the inability to deposit high aspect ratios with preferentially oriented Cu grains to date [14,15,67,110,167].

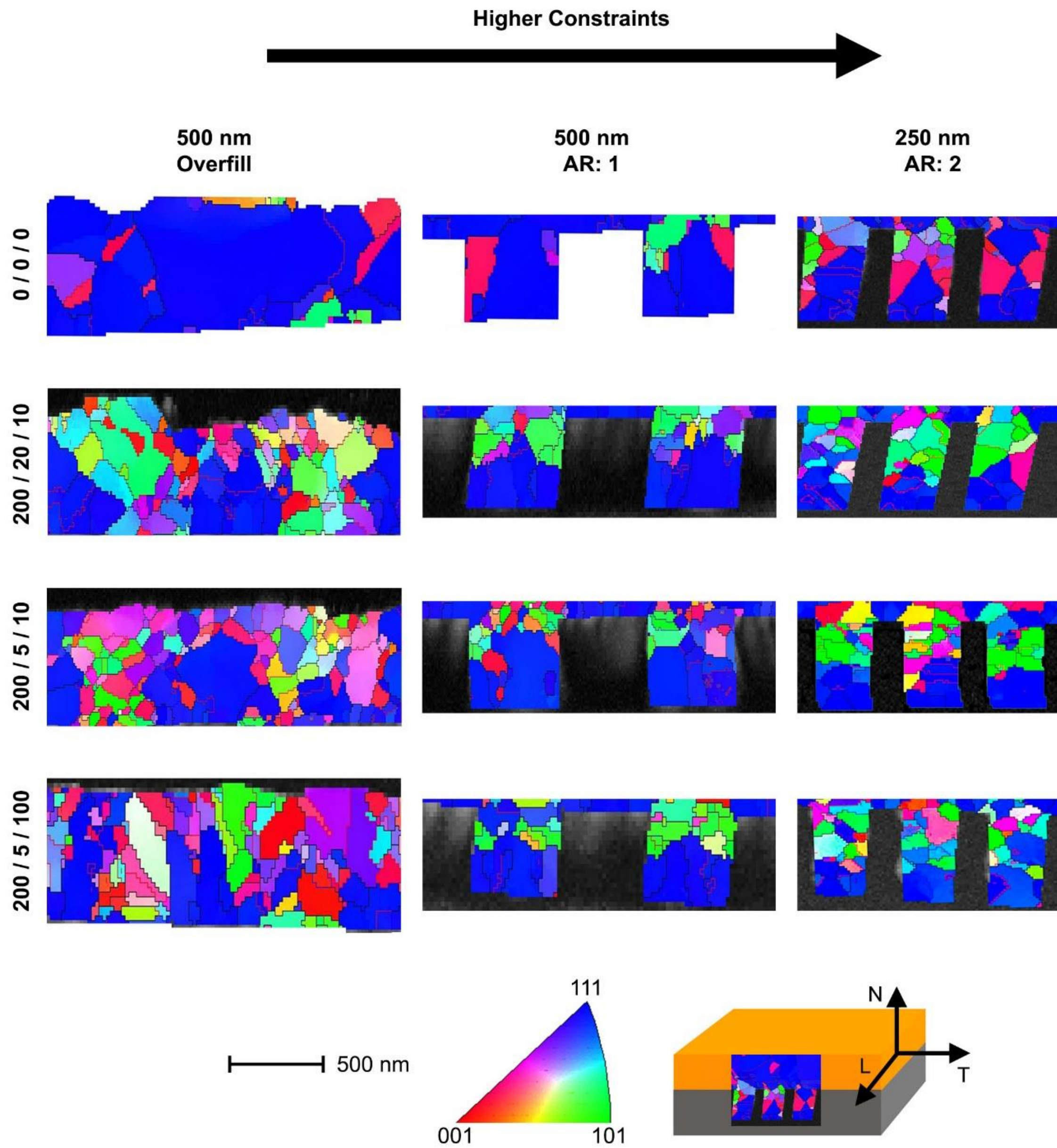

Figure 5.7: The cross-sectional inverse pole figure maps in the direction normal to the sample surface for the regions under various geometric constraint and deposited with different organic additive concentrations in the electrodeposition bath.

Table 5.2: The multiple of uniform density inside the 250 nm and 500 nm wide trenches, deposited with various organic additive bath concentrations.

	Multiple of Uniform Density (MUD)	
PEG/SPS/JGB (mg/L)	250 nm Trenches	500 nm Trenches
0 / 0 / 0	25 ± 5	30 ± 1
200 / 20 / 10	10 ± 2	23 ± 3
200 / 5 / 10	15 ± 3	14 ± 2
200 / 5 / 100	6 ± N/A	20 ± 2

The EBSD and TKD data was also used to map the relative strain in the samples (shown in Figure 5.8). By analyzing minute changes in local orientation of the crystal lattice within a grain from its average orientation the strain can be estimated. Low amounts of strain are indicated by blue and red shows areas of higher strain. Unfortunately, this method only allows for analysis of *relative* strain and comparing sample to sample can be difficult. Figure 5.8 shows the strain component maps between the 250 nm and 500 nm trenches deposited without organic additives and with PEG 200 mg/L, SPS 20 mg/L, and JGB 10 mg/L. Large strains were expected to occur at the interface between the Cu and the substrate, however, this was generally not the case. The trenches that were deposited without organic additives were the only samples to have a majority of the larger strains located inside the trenches. This is especially evident in the 0/0/0 250 nm trench illustration in Figure 5.8. Samples that used organic additives for the depositions contained their largest strains in areas where clusters of smaller grains were present. There are several reasons believed to account for these trends. Higher stresses were seen in the samples deposited without organic additives and from Chapter 4, it was discovered that these stresses were inversely proportional to total void area and samples that contained organic additives had larger void areas. A majority of these voids were located inside the trenches and act as stress relieving mechanisms. Therefore, lower strains in the samples that contain organic additives is expected. High strains can occur for many reasons. The clusters of small grains have a higher grain boundary area than other regions in the samples.

Dislocation pile ups at the boundaries could be causing these strain concentrations. Lastly, the elastically anisotropic nature of Cu may be contributing to the strain concentrations in these locations. Intrinsic stress has been found to accumulate at triple junctions and grain boundaries, where the grain orientations are different due to their contrasting elastic constants [168].

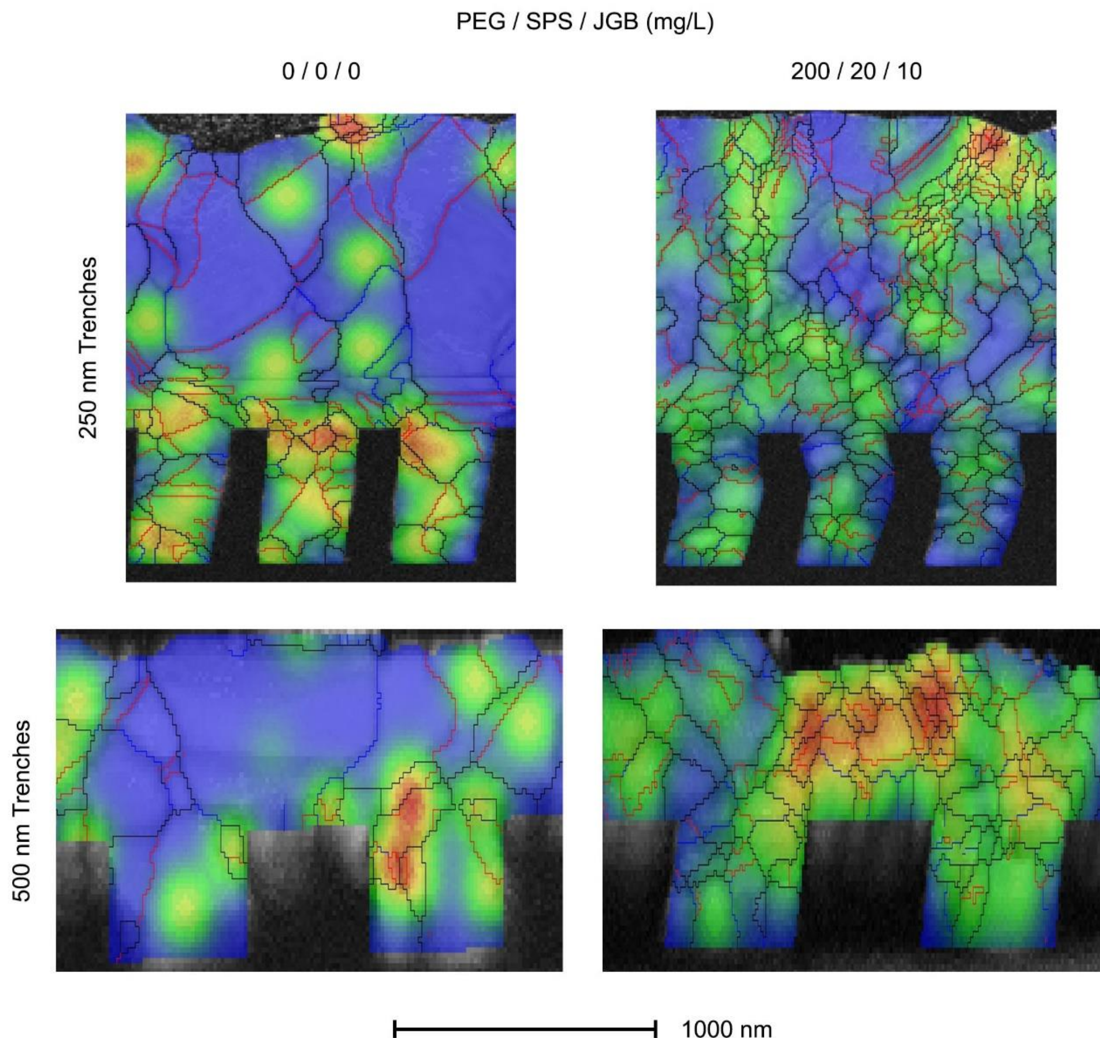

Figure 5.8: The strain component maps for the 0/0/0 and 200/20/10 deposited trenches (250 nm and 500 nm). Blue indicates smaller strains, while red represents larger strains.

High twin densities are anticipated in areas of increasing constraint, since

the stresses are expected to scale with geometrical constraints, however, findings from the strain component maps don't necessarily match the predicted regions of elevated stress. The twin densities are shown in Table 5.3 and were measured by counting the twins per unit area in each of the desired regions. Higher twin densities were found in the non-organic additive deposited trenches compared to their corresponding overfill. However, once organic additives were utilized in the depositions, more twins were observed in the overfill than the trenches. Again, this is thought to be a result of the increased void area within the trenches in these deposits. The large increase in twin density of the overfill in the presence of organic additives could be due to grain-boundary pinning by adsorbed organic molecules [169]. The adsorbed additives act as defects during the deposition, disturbing the lattice formation and creating more twins. The higher aspect ratio 250 nm trenches (and higher constrained regions) were found to contain more twins than the 500 nm trenches for all chemistries used.

Table 5.3: The twin density of the 250 nm and 500 nm trenches and overfill of each, deposited with different organic additive bath concentrations.

PEG/SPS/JGB (mg/L)	Twins/μm^2			
	250 nm		500 nm	
	Trenches	Overfill	Trenches	Overfill
0 / 0 / 0	40	7	11	4
200 / 20 / 10	33	54	32	52
200 / 5 / 10	35	25	23	44
200 / 5 / 100	21	22	17	25

5.3 Conclusions

EBSD and TKD were used to compare the cross-sectional microstructure of the Cu blanket films and trench overfill layers for their similar degree of constraint. The overfill above the 500 nm trenches was determined to be the most

comparable to the Cu blanket films due to the lower contribution from the underlying trench grains. The 500 nm overfill and blanket films exhibited similar grain morphologies and twin densities.

The 250 nm and 500 nm trench microstructures were also studied for their various level of constraint. As expected, the grain size scaled inversely with degree of confinement. The overfill layers contained the largest grains, with the 500 nm trenches and 250 nm trenches following, respectively. The sidewall grains contributed to the smaller amount of (111) preferential orientation in the 250 nm trenches compared to the 500 nm trenches. Furthermore, stresses appeared to be larger in the smaller trenches, resulting in higher twin densities. High strain concentrations were also found in clusters of small grains.

With these findings taken into account, high aspect ratio features, such as TSVs are speculated to be extremely influenced by the sidewalls, since the surface area of the sidewalls is much greater than the base, especially compared to the low aspect ratio trenches observed in this study. Sidewall seed layer texture, therefore, becomes exceedingly important, suggesting epitaxial deposition during the copper deposition. We believe by eliminating sidewall seed layers completely or modifying / optimizing the texture of the copper seed layer [170], as demonstrated in several studies [65,171], Cu depositions in high aspect ratio geometries will result in larger, more preferentially oriented microstructures, with the added benefit of guaranteed void-free fillings. Lastly, this study suggests that high aspect ratio features will contain large amounts of twins, which are expected to be beneficial to thermal stability of the structure.

CHAPTER SIX:
CONCLUSIONS AND FUTURE WORK

Three-dimensional integrated circuits have become an attractive avenue to circumvent the slowing of Moore's law. With the increasing popularity of these devices, interconnects have become the primary bottleneck for better performance. Cu interconnects are susceptible to thermo-mechanical reliability issues due to the mismatch in material properties between the Cu and the surrounding insulating layers. Recent investigations have suggested that highly twinned and textured Cu microstructures may hold the key to reducing stresses and creating stable Cu interconnects. By understanding the role and inter-relationships of Cu deposition conditions, chemical additives (routinely used to enhance deposition uniformity in complex structures), and the extent of spatial constraint on the formation of such microstructural features (twins, stress, orientation, and void content) in deposited Cu, we may predict the microstructural properties of higher aspect ratio features, such as those currently deployed in microelectronic applications. How such processing and processing-related microstructural features are related, formed the core of the present study.

The goal of this dissertation was to evaluate the effects of the pulse electrodeposition parameters on the Cu microstructure and determined the microstructure's response to varying levels of constraint. The electrodeposition pulse parameters and electrolyte organic additive concentrations were studied for their effect on the cross-sectional microstructure of blanket Cu films and Cu-filled

trenches. Specifically, the following objectives were investigated:

1. Evaluate the impact of pulse electrodeposition duty cycle and frequency on the copper microstructure and link these microstructural characteristics to the biaxial residual stress and surface roughness.
2. Analyze the effect of organic additive concentration in the electrodeposition bath on the processes ability to fill 500 nm deep trenches with aspect ratios varying from 0.25 to 2.78.
3. Correlate the influence of the organic additive concentration on the deposited trench microstructures and stress state.
4. Determine the significance of geometric constraints on the Cu microstructure by investigating trenches of varying size and less confined Cu areas.

6.1 Summary of Conclusions

Cu was deposited onto predesigned wafers using a two electrode pulse electrodeposition setup with a typical acid-based electrolyte. The pulse electrodeposition frequency and duty cycle were varied for the deposition of Cu blanket films to study the effects of pulse parameters on the resulting Cu film's stress state and microstructure (grain size, orientation, and twin density). An optimal combination of these pulse parameters was determined and used in the deposition of trenched samples. Blanket films of Cu, with uniform and repeatable physical attributes were produced without additives and served as a baseline for further experiments on more constrained, trench structures. Film quality, as

defined by large grain size, high twin density, low stress, and high texture, was found to be highest with a deposition pulse rate of 50 Hz and duty cycle of 0.1 in additive-free films.

Using baseline blanket film deposition conditions as a basis for evaluating the role of organic additives, the Cu trench quality was investigated. It was found that the addition of PEG, SPS, and JGB organic additive concentrations in the electrodeposition bath influenced the resulting Cu trench microstructures. Firstly, it was determined that varying ratios of the additives impacted the texture of the Cu trenches. White light interferometric assessment of biaxial residual stress and surface roughness showed that additives impacted the resulting Cu films by lowering the stress and roughness of the trenched samples. The role of additives on higher constrained Cu trenches (as compared to blanket films) showed that PEG had little impact, while SPS and JGB influenced the grain morphology and texture.

The literature-referenced behavior of each additive was evaluated and compared to films prepared in this study by examining blanket film and trench microstructure with a variety of tools to ascertain how the additives impacted Cu microstructure and properties. The trench filling profiles were evaluated by grinding and polishing or FIB milling trench cross-sections. X-ray diffraction provided insight into the texture of the Cu, while cross-sectional microstructure was evaluated though electron backscattering diffraction or transmission kikuchi diffraction of the blanket films and the 250 nm and 500 nm wide trenches. Key findings from these studies indicated differences in grain size, texture, and twinning

between the lower constraint 500 nm trenches, and more highly constrained 250 nm trenches.

Key findings from XRD and EBSD showed that Cu blanket films contained a 'bulk-like' structure with smaller grains residing at the Cu seed/film interface and larger grains were found at the surface of the films. The films were found to be highly (111) textured due to preferential orientation of the Cu seed layer, however the degree of (111) orientation decreased with increasing pulse on-time used in the deposition. The change in texture was attributed to increased biaxial residual stresses in these films, which activated the strain reduction mechanism that drives (100) and (311) grain growth. Higher twin densities were found in films that contained lower stresses, exhibiting the thermal and mechanical stability of twins in the Cu microstructure.

The filling of Cu trenches was influenced greatly by the organic additive concentrations in the electrolytic bath and fill profiles were in general agreement with the Curvature Enhanced Accelerator Coverage (CEAC) model. However, trenches still contained many fill voids. The lower stresses were associated with the increased void area in the trenches. The introduction of organics into the electrolyte bath, resulted in finer microstructures and lower (111) textures, possibly due to adsorbed organic molecules at grain boundaries that prevent the further grain growth. Cu growth from the sidewalls contributed greatly to the change in orientation in the trenches. Void density from insufficient copper filling was found to be the dominant stress relieving mechanism in these systems as opposed to twin formation. Although small scale studies have shown some changes in the

microstructure of Cu with organic additives, a detailed account, like this one, has not been reported to date.

To determine how these microstructural effects would scale with larger aspect ratio features, the Cu microstructure was examined under different degrees of constraints. As expected, a majority of the stresses were found in the trenches where voids were not as prevalent. It is also apparent that smaller trenches underwent greater levels of stress, due to the increased twin density found in the 250 nm compared to the 500 nm wide trenches. Greater levels of stress may also have occurred from the smaller grain sizes due to more confined area of the 250 nm trenches. Effects from the sidewall were also more dominant in the smaller trenches, as the (111) texture of the Cu was not as extensive as in the larger trenches.

6.2 Contribution and Impact

This work shows the capability of using the pulse electrodeposition technique to effectively control the Cu microstructure and will act as a template for others to create desired microstructures in blanket films and Cu trenches. Most of the literature has focused on the microstructural effects from pulse current density of pulse electrodeposition and the effect of organic additive concentration on the filling process of advanced features. This dissertation extends the current knowledge in the field. Specifically, this dissertation is a comprehensive study of the effects of pulse times on the Cu microstructure as well as a detailed account of the organic additive's influence on Cu low aspect ratio trench microstructure,

both of which have not been studied in detail in the literature.

The key conclusions from this dissertation include:

- Higher pulse frequency and lower duty cycle produced coarser grained Cu blanket film microstructures due to lower nucleation rates and more time for recrystallization during the on and off-times respectively.
- The (111) texture decreased in Cu blanket films with increasing stress from longer pulse electrodeposition on-times. The energy minimization mechanism, which determines the preferential growth of certain Cu orientations, changed with the increased stress.
- Highly twinned Cu microstructures were found in films that had lower biaxial residual stresses due to the large extent of recrystallization.
- The introduction of organic additives to the electrodeposition bath created finer microstructures with lower (111) textures, due to increasing sidewall contribution. Sidewall contribution became more prominent in more constrained aspect ratio trenches.
- Void density from insufficient copper filling was found to be the dominant stress relieving mechanism in these systems as opposed to twin formation; however, larger stresses in more confined trenches created higher twin densities.

While the correlation between pulse on-time and residual stress has been recorded in the literature, the twin densities have not been taken into account and provide a more complete understanding of the pulse parameters effects on Cu

microstructure, and how the material's behavior changes on a global scale (stress). Larger residual biaxial stresses were observed in Cu films that were deposited with longer on-times. These stresses level out in depositions that more closely replicate DC electroplating (>100 ms on-times).

Yet another distinguishing contribution from this dissertation is the impact of the interaction between organic additives, higher confinement, and the copper seed sidewall texture on the final microstructure in Cu trenches. These findings have not been illustrated in the literature to date. Furthermore, the fill voids ability to lower residual stress in Cu is a unique attribute of this study.

6.3 Future Work

Although this work included the microstructural analysis of several aspect ratio features, the next step would be to investigate the microstructure of high aspect ratio TSVs. The effects of organic additive concentration may be much more pronounced in TSVs and could vary dramatically in these delicate structures. The theory suggested in Chapter 5 that high aspect ratio features filled solely from the bottom would contain large grain sizes and texture needs to be investigated. Further work is needed to study the material property response to the varying microstructures documented in this work and would allow a definitive answer to the most beneficial microstructural characteristics for these features with microelectronic applications in mind. The electrical properties and mechanical properties would be of interest, as well as electromigration testing. Lastly,

synchrotron x-ray microdiffraction could be utilized to achieve a more detailed residual stress analysis of the trenche.

REFERENCES

1. A. Pratt, 'Overview of the Use of Copper Interconnects in the Semiconductor Industry,' *Adv Energy Ind* (2004).

2. M. M. Waldrop, 'The chips are down for Moore's law,' *Nature News*, 530 [7589] 144 (2016).

3. J. D. Meindl, 'Beyond Moore's Law: the interconnect era,' *Computing in Science & Engineering*, 5 [1] 20-24 (2003).

4. S. F. Al-Sarawi, D. Abbott and P. D. Franzon, 'A review of 3-D packaging technology,' *Components, Packaging, and Manufacturing Technology, Part B: Advanced Packaging, IEEE Transactions on*, 21 [1] 2-14 (1998).

5. J. A. Davis, R. Venkatesan, A. Kaloyeros, M. Beylansky, S. J. Souri, K. Banerjee, K. C. Saraswat, A. Rahman, R. Reif and J. D. Meindl, 'Interconnect limits on gigascale integration (GSI) in the 21st century,' *Proceedings of the IEEE*, 89 [3] 305-324 (2001).

6. 'International Technology Roadmap for Semiconductors 2.0, Interconnect,' (2015). Retrieved from http://www.itrs2.net/.

7. M. Hasegawa, Y. Negishi, T. Nakanishi and T. Osaka, 'Effects of additives on copper electrodeposition in submicrometer trenches,' *J. Electrochem. Soc.*, 152 [4] C221-C228 (2005).

8. R. Manu and S. Jayakrishnan, 'Influence of polymer additive molecular weight on surface and microstructural characteristics of electrodeposited copper,' *Bull. Mater. Sci.*, 34 [2] 347-356 (2011).

9. K. Kondo, T. Matsumoto and K. Watanabe, 'Role of Additives for Copper Damascene Electrodeposition: Experimental Study on Inhibition and Acceleration Effects,' *Journal of The Electrochemical Society*, 151 [4] C250-C255 (2004).

10. M. Georgiadou and D. Veyret, 'Optimization of trench filling during copper electrodeposition by additives and pulse plating,' *Proc. Inst. Mech. Eng. Pt. B: J. Eng. Manuf.*, 217 [6] 857-863 (2003).

11. J. Tang, Q. Zhu, Y. Zhang, X. Zhang, J. Guo and J. Shang, 'Copper Bottom-up Filling for Through Silicon Via (TSV) Using Single JGB Additive,' *ECS Electrochemistry Letters*, 4 [9] D28-D30 (2015).

12. P. M. Vereecken, R. A. Binstead, H. Deligianni and P. C. Andricacos, 'The chemistry of additives in damascene copper plating,' *IBM Journal of Research and Development*, 49 [1] 3-18 (2005).

13. C. Okoro, M. Gonzalez, B. Vandevelde, B. Swinnen, G. Eneman, P. Verheyen, E. Beyne and D. Vandepitte, 'Prediction of the Influence of Induced Stresses in Silicon on CMOS Performance in a Cu-Through-Via Interconnect Technology,' *Thermal, Mechanical and Multi-Physics Simulation Experiments in Microelectronics and Micro-Systems, 2007. EuroSime 2007. International Conference on* 1-7 (2007).

14. J. Marro, C. Okoro, Y. Obeng and K. Richardson, 'Defect and microstructural evolution in thermally cycled Cu through-silicon vias,' *Microelectronics Reliability*, 54 [11] 2586-2593 (2014).

15. J. Marro, 'Thermo-mechanical effects of thermal cycled copper through-silicon vias,' *ProQuest Dissertations and Theses* (2013).

16. C. Okoro, J. W. Lau, F. Golshany, K. Hummler and Y. S. Obeng, 'A Detailed Failure Analysis Examination of the Effect of Thermal Cycling on Cu TSV Reliability,' *Electron Devices, IEEE Transactions on*, 61 [1] 15-22 (2014).

17. L. Lu, Y. Shen, X. Chen, L. Qian and K. Lu, 'Ultrahigh strength and high electrical conductivity in copper,' *Science*, 304 [5669] 422-426 (2004).

18. L. Lu, X. Chen, X. Huang and K. Lu, 'Revealing the Maximum Strength in Nanotwinned Copper,' *Science*, 323 [5914] 607-610 (2009).

19. J. B. Marro, C. A. Okoro, Y. S. Obeng, K. A. Richardson and K. Chamma, 'Temperature Dependence of Defect Evolution and Distribution in Thermally Cycled Cu-TSVs,' *ECS Transactions*, 61 [2] 177-184 (2014).

20. C. Okoro and Y. S. Obeng, 'Effect of thermal cycling on the signal integrity and morphology of TSV isolation liner- SiO2,' *Interconnect Technology Conference (IITC), 2012 IEEE International* 1-3 (2012).

21. P. Kumar, I. Dutta and M. S. Bakir, 'Interfacial Effects During Thermal Cycling of Cu-Filled Through-Silicon Vias (TSV),' *Journal of Electronic Materials*, 41 [2] 322-335 (2012).

22. G. E. Moore, 'Cramming More Components Onto Integrated Circuits,' *Proceedings of the IEEE*, 86 [1] 82-85 (1998).

23. R. Borkar, M. Bohr and S. Jourdan, 'Advancing Moore's Law —The Road to 14 nm,' (2014). Retrieved from http://www.intel.com/.

24. A. W. Topol, D. C. L. Tulipe, L. Shi, D. J. Frank, K. Bernstein, S. E. Steen, A. Kumar, G. U. Singco, A. M. Young, K. W. Guarini and M. Ieong, 'Three-dimensional integrated circuits,' *IBM Journal of Research and Development*, 50 [4.5] 491-506 (2006).

25. J. H. Lau, 'Overview and outlook of through-silicon via (TSV) and 3D integrations,' *Microelectronics International*, 28 [2] 8-22 (2011).

26. M. Koyanagi, '3D integration technology and reliability,' *Reliability Physics Symposium (IRPS), 2011 IEEE International* 3F.1.1-3F.1.7 (2011).

27. J. Czochralski, 'A new method of measuring the speed of cristilation in metals.' *ZEITSCHRIFT FUR PHYSIKALISCHE CHEMIE-STOCHIOMETRIE UND VERWANDTSCHAFTSLEHRE*, 92 [2] 219-221 (1917).

28. H. Shin, B. Kim, J. Kim, S. Hwang, A. Budiman, H. Son, K. Byun, N. Tamura, M. Kunz, D. Kim and Y. Joo, 'Microstructure Evolution and Defect Formation in Cu Through-Silicon Vias (TSVs) During Thermal Annealing,' *Journal of Electronic Materials*, 41 [4] 712-719 (2012).

29. C. Okoro, L. E. Levine, R. Xu, K. Hummler and Y. S. Obeng, 'Nondestructive Measurement of the Residual Stresses in Copper Through-Silicon Vias Using Synchrotron-Based Microbeam X-Ray Diffraction,' *Electron Devices, IEEE Transactions on*, PP [99] 1-1 (2014).

30. A. S. Budiman, H. A. S. Shin, B. J. Kim, S. H. Hwang, H. Y. Son, M. S. Suh, Q. H. Chung, K. Y. Byun, N. Tamura, M. Kunz and Y. C. Joo, 'Measurement of stresses in Cu and Si around through-silicon via by synchrotron X-ray microdiffraction for 3-dimensional integrated circuits,' *Microelectronics Reliability*, 52 [3] 530-533 (2012).

31. W. S. Kwon, D. T. Alastair, K. H. Teo, S. Gao, T. Ueda, T. Ishigaki, K. T. Kang and W. S. Yoo, 'Stress evolution in surrounding silicon of Cu-filled through-silicon via undergoing thermal annealing by multiwavelength micro-Raman spectroscopy,' *Applied Physics Letters*, 98 [23] 232106-232106-3 (2011).

32. L. W. Kong, J. R. Lloyd, K. B. Yeap, E. Zschech, A. Rudack, M. Liehr and A. Diebold, 'Applying x-ray microscopy and finite element modeling to identify the mechanism of stress-assisted void growth in through-silicon vias,' *J. Appl. Phys.*, 110 [5] 053502 (2011).

33. R. Page and J. R. Weertman, 'HVEM observations of grain boundary voids in high purity copper,' *Acta Metallurgica*, 29 [3] 527-535 (1981).

34. R. E. Rudd and J. F. Belak, 'Void nucleation and associated plasticity in dynamic fracture of polycrystalline copper: an atomistic simulation,' *Computational materials science*, 24 [1] 148-153 (2002).

35. A. Sekiguchi, J. Koike, S. Kamiya, M. Saka and K. Maruyama, 'Void formation by thermal stress concentration at twin interfaces in Cu thin films,' *Appl. Phys. Lett.*, 79 [9] 1264-1266 (2001).

36. A. Sekiguchi, J. Koike and K. Maruyama, 'Microstructural influences on stress migration in electroplated Cu metallization,' *Appl. Phys. Lett.*, 83 [10] 1962-1964 (2003).

37. A. Sekiguchi, J. Koike and K. Maruyama, 'Formation of slit-like voids at trench corners of damascene Cu interconnects,' *Materials Transactions*, 43 [7] 1633-1637 (2002).

38. J. Belak, 'Molecular dynamics simulation of high strain-rate void nucleation and growth in copper,' *The tenth American Physical Society topical conference on shock compression of condensed matter*, 429 [1] 211-214 (1998).

39. M. Butron-Guillen, J. Cabanas-Moreno and J. Weertman, 'Fatigue cavitation and relative grain orientations in pure copper,' *Scripta Metallurgica et Materialia*, 24 [6] 991-996 (1990).

40. A. Cuitino and M. Ortiz, 'Ductile fracture by vacancy condensation in fcc single crystals,' *Acta materialia*, 44 [2] 427-436 (1996).

41. D. A. Porter and K. E. Easterling, 'Phase Transformations in Metals and Alloys, (Revised Reprint)'. CRC press 1992.

42. L. E. Murr, 'Interfacial phenomena in metals and alloys'. Addison-Wesley Publishing Company, United States, 1975.

43. J. A. Nucci, R. R. Keller, J. E. Sanchez and Y. Shacham-Diamand, 'Local crystallographic texture and voiding in passivated copper interconnects,' *Appl. Phys. Lett.*, 69 [26] 4017-4019 (1996).

44. J. A. Nucci, Y. Shacham-Diamand and J. E. Sanchez, 'Effects of linewidth, microstructure, and grain growth on voiding in passivated copper lines,' *Appl. Phys. Lett.*, 66 [26] 3585-3587 (1995).

45. C. Tan, R. Reif, N. Theodore and S. Pozder, 'Observation of interfacial void formation in bonded copper layers,' *Appl. Phys. Lett.*, 87 [20] 201909-201909-3 (2005).

46. D. Eaton, N. Durrant, S. Huber, R. Blish and N. Lycoudes, 'Knowledge-Based Reliability Qualification Testing of Silicon Devices,' *Austin, Texas, Sematech* (2000).

47. C. Okoro, L. E. Levine, R. Xu, J. Z. Tischler, W. Liu, O. Kirillov, K. Hummler and Y. S. Obeng, 'X-ray micro-beam diffraction determination of full stress tensors in Cu TSVs,' *IEEE 63rd Electronic Components and Technology Conference* 648-652 (2013).

48. V. A. Lubarda, M. S. Schneider, D. H. Kalantar, B. A. Remington and M. A. Meyers, 'Void growth by dislocation emission,' *Acta Materialia*, 52 [6] 1397-1408 (2004).

49. E. Lin, L. Niu, H. Shi and Z. Duan, 'Molecular dynamics study on the nano-void growth and coalescence at grain boundary,' *Science China Physics, Mechanics and Astronomy*, 55 [1] 86-93 (2012).

50. L. Zhang, H. Zhou and S. Qu, 'Blocking effect of twin boundaries on partial dislocation emission from void surfaces,' *Nanoscale research letters*, 7 [1] 1-8 (2012).

51. S. Zhang, J. Zhou, L. Wang, Y. Wang and S. Dong, 'Effect of twin boundaries on nanovoid growth based on dislocation emission,' *Materials Science and Engineering: A*, 582 29-35 (2013).

52. M. Meyer, M. Herrmann, E. Langer and E. Zschech, 'In situ SEM observation of electromigration phenomena in fully embedded copper interconnect structures,' *Microelectronic Engineering*, 64 [1] 375-382 (2002).

53. Joohee Kim, Jonghyun Cho, Jun So Pak, Joungho Kim, Jong-Min Yook and Jun Chul Kim, 'High-frequency through-silicon Via (TSV) failure analysis,' *Electrical Performance of Electronic Packaging and Systems (EPEPS), 2011 IEEE 20th Conference on* 243-246 (2011).

54. C. Okoro, P. Kabos, J. Obrzut, K. Hummler and Y. S. Obeng, 'Accelerated Stress Test Assessment of Through-Silicon Via Using RF Signals,' *Electron Devices, IEEE Transactions on*, 60 [6] 2015-2021 (2013).

55. K. Zhao, C. Chen, Y. Shen and T. Lu, 'Molecular dynamics study on the nano-void growth in face-centered cubic single crystal copper,' *Computational Materials Science*, 46 [3] 749-754 (2009).

56. G. Green and J. Knott, 'The initiation and propagation of ductile fracture in low strength steels,' *Journal of Engineering Materials and Technology*, 98 [1] 37-46 (1976).

57. J. W. Dini and D. D. Synder, 'Chapter 2: Electrodeposition of Copper'; pp. 33 in Modern Electroplating. Edited by M. Schlesinger and M. Paunovic (Eds.). Wiley, Hoboken, NJ, USA, 2011.

58. M. S. Chandrasekar and M. Pushpavanam, 'Pulse and pulse reverse plating—Conceptual, advantages and applications,' *Electrochim. Acta*, 53 [8] 3313-3322 (2008).

59. G. Devaraj and S. Seshadri, 'Pulsed electrodeposition of copper,' *Plating and surface finishing*, 79 [8] 72-78 (1992).

60. Myung-Won Jung, Young-Sik Song, Tae-Hong Yim and Jae-Ho Lee, 'Evaluation of additives and current mode on copper via filling,' *Electronic Components and Technology Conference (ECTC), 2011 IEEE 61st* 1908-1912 (2011).

61. B. Kim, C. Sharbono, T. Ritzdorf and D. Schmauch, 'Factors affecting copper filling process within high aspect ratio deep vias for 3D chip stacking,' *Electronic Components and Technology Conference, 2006. Proceedings. 56th* 6 pp. (2006).

62. S. S. West, G. Winther and D. J. Jensen, 'Analysis of Orientation Relations Between Deformed Grains and Recrystallization Nuclei,' *Metallurgical and Materials Transactions A*, 42 [5] 1400-1408 (2011).

63. T. P. Moffat and D. Josell, 'Extreme Bottom-Up Superfilling of Through-Silicon-Vias by Damascene Processing: Suppressor Disruption, Positive Feedback and Turing Patterns,' *Journal of The Electrochemical Society*, 159 [4] D208-D216 (2012).

64. D. Wheeler, T. Moffat and D. Josell, 'Spatial-Temporal Modeling of Extreme Bottom-up Filling of Through-Silicon-Vias,' *J. Electrochem. Soc.*, 160 [12] D3260-D3265 (2013).

65. C. Song, Z. Wang and L. Liu, 'Bottom-up copper electroplating using transfer wafers for fabrication of high aspect-ratio through-silicon-vias,' *Microelectronic Engineering*, 87 [3] 510-513 (2010).

66. P. C. Andricacos, C. Uzoh, J. O. Dukovic, J. Horkans and H. Deligianni, 'Damascene copper electroplating for chip interconnections,' *IBM Journal of Research and Development*, 42 [5] 567-574 (1998).

67. C. Okoro, R. Labie, K. Vanstreels, A. Franquet, M. Gonzalez, B. Vandevelde, E. Beyne, D. Vandepitte and B. Verlinden, 'Impact of the electrodeposition chemistry used for TSV filling on the microstructural and thermo-mechanical response of Cu,' *Journal of Materials Science*, 46 [11] 3868-3882 (2011).

68. P. Taephaisitphongse, Y. Cao and A. C. West, 'Electrochemical and fill studies of a multicomponent additive package for copper deposition,' *J. Electrochem. Soc.*, 148 [7] C492-C497 (2001).

69. K. Kondo, N. Yamakawa, Z. Tanaka and K. Hayashi, 'Copper damascene electrodeposition and additives,' *J Electroanal Chem*, 559 [0] 137-142 (2003).

70. M. Yokoi, S. Konishi and T. Hayashi, 'Adsorption behavior of polyoxyethyleneglycole on the copper surface in an acid copper sulfate bath,' *Denki Kagaku oyobi Kogyo Butsuri Kagaku*, 52 [4] 218-223 (1984).

71. K. R. Hebert, S. Adhikari and J. E. Houser, 'Chemical mechanism of suppression of copper electrodeposition by poly (ethylene glycol),' *J. Electrochem. Soc.*, 152 [5] C324-C329 (2005).

72. T. P. Moffat, D. Wheeler, M. D. Edelstein and D. Josell, 'Superconformal film growth: Mechanism and quantification,' *IBM Journal of Research and Development*, 49 [1] 19-36 (2005).

73. D. Josell, D. Wheeler, W. Huber, J. Bonevich and T. Moffat, 'A simple equation for predicting superconformal electrodeposition in submicrometer trenches,' *J. Electrochem. Soc.*, 148 [12] C767-C773 (2001).

74. D. Wheeler, D. Josell and T. Moffat, 'Modeling superconformal electrodeposition using the level set method,' *J. Electrochem. Soc.*, 150 [5] C302-C310 (2003).

75. T. P. Moffat, D. Wheeler, W. H. Huber and D. Josell, 'Superconformal Electrodeposition of Copper,' *Electrochemical and Solid-State Letters*, 4 [4] C26-C29 (2001).

76. T. P. Moffat, D. Wheeler and D. Josell, 'Electrodeposition of Copper in the SPS-PEG-Cl Additive System: I. Kinetic Measurements: Influence of SPS,' *Journal of The Electrochemical Society*, 151 [4] C262-C271 (2004).

77. Y. H. Im, M. O. Bloomfield, S. Sen and T. S. Cale, 'Modeling pattern density dependent bump formation in copper electrochemical deposition,' *Electrochemical and solid-state letters*, 6 [3] C42-C46 (2003).

78. D. Josell, D. Wheeler, W. H. Huber and T. P. Moffat, 'Superconformal Electrodeposition in Submicron Features,' *Phys. Rev. Lett.*, 87 [1] 016102 (2001).

79. R. E. Smallman and A. Ngan, 'Physical metallurgy and advanced materials'. Butterworth-Heinemann 2011.

80. E. J. Mittemeijer, 'Fundamentals of materials science: the microstructure–property relationship using metals as model systems'. Springer 2010.

81. C. Su and X. Su, 'Impact of grain size and grain size distribution on the resistivity of metal nanocrystalline systems,' *Computational Materials Science*, 108, Part A 62-65 (2015).

82. M. Treger, C. Witt, C. Cabral, C. Murray, J. Jordan-Sweet, R. Rosenberg, E. Eisenbraun and I. C. Noyan, 'Characterization of room temperature recrystallization kinetics in electroplated copper thin films with concurrent x-ray diffraction and electrical resistivity measurements,' *J. Appl. Phys.*, 113 [21] (2013).

83. T. Sun, B. Yao, A. Warren, V. Kumar, K. Barmak and K. R. Coffey, 'Resistivity Size Effect in Encapsulated Cu Thin Films,' *Interconnect Technology Conference, 2008. IITC 2008. International* 141-143 (2008).

84. Rui Huang, W. Robl, H. Ceric, T. Detzel and G. Dehm, 'Stress, Sheet Resistance, and Microstructure Evolution of Electroplated Cu Films During Self-Annealing,' *Device and Materials Reliability, IEEE Transactions on*, 10 [1] 47-54 (2010).

85. L. H. Qian, Q. H. Lu, W. J. Kong and K. Lu, 'Electrical resistivity of fully-relaxed grain boundaries in nanocrystalline Cu,' *Scr. Mater.*, 50 [11] 1407-1411 (2004).

86. W. Wu, S. Brongersma, M. Van Hove and K. Maex, 'Influence of surface and grain-boundary scattering on the resistivity of copper in reduced dimensions,' *Appl. Phys. Lett.*, 84 [15] 2838-2840 (2004).

87. Y. Xiang, X. Chen and J. J. Vlassak, 'The mechanical properties of electroplated Cu thin films measured by means of the bulge test technique,' *MRS Proceedings*, 695 L4. 9.1 (2001).

88. Y. Xiang, T. Y. Tsui and J. J. Vlassak, 'The mechanical properties of freestanding electroplated Cu thin films,' *J. Mater. Res.*, 21 [06] 1607-1618 (2006).

89. B. Z. Cui, K. Han, Y. Xin, D. R. Waryoba and A. L. Mbaruku, 'Highly textured and twinned Cu films fabricated by pulsed electrodeposition,' *Acta Materialia*, 55 [13] 4429-4438 (2007).

90. Guan-Tai Lui and Delphic Chen,and Jui, 'EBSD characterization of twinned copper using pulsed electrodeposition,' *J. Phys. D*, 42 [21] 215410 (2009).

91. L. Zeng, S. Xu, J. Tan, L. Zhang, W. Zhang, L. Wang and X. Qu, 'Copper pulse plating on Ru/TaSiN barrier,' *8th International Conference onSolid-State and Integrated Circuit Technology. ICSICT.* 345-347 (2006).

92. X. Zhang, K. Tu, Z. Chen, Y. Tan, C. C. Wong, S. G. Mhaisalkar, X. Li, C. H. Tung and C. Cheng, 'Pulse electroplating of copper film: a study of process and microstructure,' *Journal of nanoscience and nanotechnology*, 8 [5] 2568-2574 (2008).

93. J. Li and Y. Shacham-Diamand, 'On the Texture of Electroless Copper Films on Epitaxial Cu Seed Layers Grown on Si (100) and Si (111) Substrates,' *Journal of The Electrochemical Society*, 139 [4] L37-L39 (1992).

94. T. Hara, K. Sakata and Y. Yoshida, 'Control of the (111) orientation in copper interconnection layer,' *Electrochemical and solid-state letters*, 5 [3] C41-C43 (2002).

95. Y. Pan, Y. Liu, T. Wang and X. Lu, 'Effect of a Cu seed layer on electroplated Cu film,' *Microelectronic Engineering*, 105 [0] 18-24 (2013).

96. Y. W. Lin, J. C. Kuo, K. T. Lui and D. Chen, 'Effect of plating current density and frequency on the crystallographic texture of electrodeposited copper,' *Materials Science Forum*, 638 2841-2845 (2010).

97. B. Hong, C. Jiang and X. Wang, 'Influence of complexing agents on texture formation of electrodeposited copper,' *Surface and Coatings Technology*, 201 [16–17] 7449-7452 (2007).

98. C. V. Thompson, 'Texture evolution during grain growth in polycrystalline films,' *Scripta Metallurgica et Materialia*, 28 [2] 167-172 (1993).

99. C. V. Thompson and R. Carel, 'Stress and grain growth in thin films,' *J. Mech. Phys. Solids*, 44 [5] 657-673 (1996).

100. C. V. Thompson, 'Grain-Growth in Thin-Films,' *Annu. Rev. Mater. Sci.*, 20 245-268 (1990).

101. K. Mirpuri, H. Wendrock, S. Menzel, K. Wetzig and J. Szpunar, 'Texture evolution in Copper film at high temperature studied in situ by electron back-scatter diffraction,' *Thin Solid Films*, 496 [2] 703-717 (2006).

102. E. M. Zielinski, R. P. Vinci and J. C. Bravman, 'Effects of barrier layer and annealing on abnormal grain growth in copper thin films,' *J. Appl. Phys.*, 76 [8] 4516-4523 (1994).

103. J. Zhang, K. Xu and J. He, 'Effects of Grain Orientation on Preferred Abnormal Grain Growth in Copper Films on Silicon Substrates,' *J. Mater. Sci. Lett.*, 18 [6] 471-473 (1999).

104. K. Barmak, E. Eggeling, D. Kinderlehrer, R. Sharp, S. Ta'asan, A. D. Rollett and K. R. Coffey, 'Grain growth and the puzzle of its stagnation in thin films: The curious tale of a tail and an ear,' *Progress in Materials Science*, 58 [7] 987-1055 (2013).

105. Y. Zhao, T. A. Furnish, M. E. Kassner and A. M. Hodge, 'Thermal stability of highly nanotwinned copper: The role of grain boundaries and texture,' *J. Mater. Res.*, 27 [24] 3049-3057 (2012).

106. O. Anderoglu, A. Misra, H. Wang and X. Zhang, 'Thermal stability of sputtered Cu films with nanoscale growth twins,' *J. Appl. Phys.*, 103 [9] (2008).

107. J. Y. Cho, K. Mirpuri, D. N. Lee, J. K. An and J. A. Szpunar, 'Texture investigation of copper interconnects with a different line width,' *J Electron Mater*, 34 [1] 53-61 (2005).

108. P. R. Besser, E. Zschech, W. Blum, D. Winter, R. Ortega, S. Rose, M. Herrick, M. Gall, S. Thrasher, M. Tiner, B. Baker, G. Braeckelmann, L. Zhao, C. Simpson, C. Capasso, H. Kawasaki and E. Weitzman, 'Microstructural characterization of inlaid copper interconnect lines,' *J Electron Mater*, 30 [4] 320-330 (2001).

109. C. Lingk, M. Gross and W. Brown, 'X-ray diffraction pole figure evidence for (111) sidewall texture of electroplated Cu in submicron damascene trenches,' *Appl. Phys. Lett.*, 74 [5] 682-684 (1999).

110. C. Okoro, K. Vanstreels, R. Labie, O. Lühn, B. Vandevelde, B. Verlinden and D. Vandepitte, 'Influence of annealing conditions on the mechanical and microstructural behavior of electroplated Cu-TSV,' *J Micromech Microengineering*, 20 [4] 045032 (2010).

111. A. Heryanto, W. N. Putra, A. Trigg, S. Gao, W. S. Kwon, F. X. Che, X. F. Ang, J. Wei, R. I Made, C. L. Gan and K. L. Pey, 'Effect of Copper TSV Annealing on Via Protrusion for TSV Wafer Fabrication,' *Journal of Electronic Materials*, 41 [9] 2533-2542 (2012).

112. J. Brown and N. Ghoniem, 'Structure and motion of junctions between coherent and incoherent twin boundaries in copper,' *Acta Materialia*, 57 [15] 4454-4462 (2009).

113. C. Saldana, T. Murthy, M. Shankar, E. Stach and S. Chandrasekar, 'Stabilizing nanostructured materials by coherent nanotwins and their grain boundary triple junction drag,' *Appl. Phys. Lett.*, 94 [2] 021910 (2009).

114. R. L. Fullman, 'Interfacial Free Energy of Coherent Twin Boundaries in Copper,' *J. Appl. Phys.*, 22 [4] 448-455 (1951).

115. R. L. Fullman, 'Crystallography and Interfacial Free Energy of Noncoherent Twin Boundaries in Copper,' *J. Appl. Phys.*, 22 [4] 456-460 (1951).

116. J. Brons, J. Hardwick, H. Padilla II, K. Hattar, G. Thompson and B. Boyce, 'The role of copper twin boundaries in cryogenic indentation-induced grain growth,' *Materials Science and Engineering: A*, 592 182-188 (2014).

117. J. Wang, N. Li, O. Anderoglu, X. Zhang, A. Misra, J. Y. Huang and J. P. Hirth, 'Detwinning mechanisms for growth twins in face-centered cubic metals,' *Acta Materialia*, 58 [6] 2262-2270 (2010).

118. C. J. Shute, B. D. Myers, S. Xie, S. -. Li, T. W. Barbee Jr., A. M. Hodge and J. R. Weertman, 'Detwinning, damage and crack initiation during cyclic loading of Cu samples containing aligned nanotwins,' *Acta Materialia*, 59 [11] 4569-4577 (2011).

119. K. Lu, L. Lu and S. Suresh, 'Strengthening materials by engineering coherent internal boundaries at the nanoscale,' *Science*, 324 [5925] 349-352 (2009).

120. N. Li, J. Wang, A. Misra, X. Zhang, J. Huang and J. Hirth, 'Twinning dislocation multiplication at a coherent twin boundary,' *Acta Materialia*, 59 [15] 5989-5996 (2011).

121. X. Meng-Burany, 'Analysis of Electroplated Films Using Dual-Beam FIB/SEM and TEM Techniques,' *Modern Electroplating, Fifth Edition* 637-663 (2010).

122. Y. Shen, L. Lu, Q. Lu, Z. Jin and K. Lu, 'Tensile properties of copper with nano-scale twins,' *Scr. Mater.*, 52 [10] 989-994 (2005).

123. X. Zhang, A. Misra, H. Wang, T. Shen, M. Nastasi, T. Mitchell, J. Hirth, R. Hoagland and J. Embury, 'Enhanced hardening in Cu/330 stainless steel multilayers by nanoscale twinning,' *Acta Materialia*, 52 [4] 995-1002 (2004).

124. K. Wang, N. Tao, G. Liu, J. Lu and K. Lu, 'Plastic strain-induced grain refinement at the nanometer scale in copper,' *Acta Materialia*, 54 [19] 5281-5291 (2006).

125. G. Wang, Z. Jiang, J. Lian and Q. Jiang, 'The grain refinement mechanism of electrodeposited copper,' *J. Mater. Res.*, 24 [10] 3226-3236 (2009).

126. B. Chalmers, J. W. Christian and T. B. Massalski, 'Grain-boundary sliding,' *Progress in Materials Science*, 16 179-217 (1972).

127. O. Anderoglu, A. Misra, F. Ronning, H. Wang and X. Zhang, 'Significant enhancement of the strength-to-resistivity ratio by nanotwins in epitaxial Cu films,' *J. Appl. Phys.*, 106 [2] 024313-024311; 024313-9 (2009).

128. L. Li, P. Zhang, Z. Zhang and Z. Zhang, 'Effect of crystallographic orientation and grain boundary character on fatigue cracking behaviors of coaxial copper bicrystals,' *Acta Materialia*, 61 [2] 425-438 (2013).

129. R. Rosenberg, D. Edelstein, C. Hu and K. Rodbell, 'Copper metallization for high performance silicon technology,' *Annual review of materials science*, 30 [1] 229-262 (2000).

130. N. McCusker, H. Gamble and B. Armstrong, 'Surface electromigration in copper interconnects,' *Microelectronics Reliability*, 40 [1] 69-76 (2000).

131. E. Liniger, L. Gignac, C. Hu and S. Kaldor, 'In situ study of void growth kinetics in electroplated Cu lines,' *J. Appl. Phys.*, 92 [4] 1803-1810 (2002).

132. O. Kononenko, V. Matveev and D. Field, 'The energy of activation of electromigration in aluminum conductors tested by the drift-velocity method,' *Russian Microelectronics*, 29 [5] 316-323 (2000).

133. M. Meyer, M. Grafe, H. Engelmann, E. Langer and E. Zschech, 'Investigation of the influence of the local microstructure of copper interconnects on void formation and evolution during electromigration testing,' *Eighth International Workshop on Stress-Induced Phenomena in Metallization*, 817 [1] 175-184 (2006).

134. Z. Choi, R. Mönig and C. V. Thompson, 'Dependence of the electromigration flux on the crystallographic orientations of different grains in polycrystalline copper interconnects,' *Appl. Phys. Lett.*, 90 [24] (2007).

135. D. Xu, V. Sriram, V. Ozolins, J. Yang, K. N. Tu, G. R. Stafford, C. Beauchamp, I. Zienert, H. Geisler, P. Hofmann and E. Zschech, 'Nanotwin formation and its physical properties and effect on reliability of copper interconnects,' *Microelectronic Engineering*, 85 [10] 2155-2158 (2008).

136. K. Chen, W. Wu, C. Liao, L. Chen and K. N. Tu, 'Observation of Atomic Diffusion at Twin-Modified Grain Boundaries in Copper,' *Science*, 321 [5892] 1066-1069 (2008).

137. H. Natter and R. Hempelmann, 'Nanocrystalline Copper by Pulsed Electrodeposition: The Effects of Organic Additives, Bath Temperature, and pH,' *J. Phys. Chem.*, 100 [50] 19525-19532 (1996).

138. H. Hsiao, C. Liu, H. Lin, T. Liu, C. Lu, Y. Huang, C. Chen and K. N. Tu, 'Unidirectional Growth of Microbumps on (111)-Oriented and Nanotwinned Copper,' *Science*, 336 [6084] 1007-1010 (2012).

139. D. Xu, W. L. Kwan, K. Chen, X. Zhang, V. Ozoliņš and K. Tu, 'Nanotwin formation in copper thin films by stress/strain relaxation in pulse electrodeposition,' *Appl. Phys. Lett.*, 91 [25] 254105 (2007).

140. D. Xu, V. Sriram, V. Ozolins, J. Yang, K. Tu, G. R. Stafford and C. Beauchamp, 'In situ measurements of stress evolution for nanotwin formation during pulse electrodeposition of copper,' *J. Appl. Phys.*, 105 [2] 023521 (2009).

141. R. Winand, 'Electrodeposition of metals and alloys—new results and perspectives,' *Electrochim. Acta*, 39 [8] 1091-1105 (1994).

142. J. J. Kelly, C. Tian and A. C. West, 'Leveling and Microstructural Effects of Additives for Copper Electrodeposition,' *Journal of The Electrochemical Society*, 146 [7] 2540-2545 (1999).

143. F. J. Humphreys and M. G. Ardakani, 'Grain boundary migration and Zener pinning in particle-containing copper crystals,' *Acta Materialia*, 44 [7] 2717-2727 (1996).

144. C. J. Tweed, B. Ralph and N. Hansen, 'The pinning by particles of low and high angle grain boundaries during grain growth,' *Acta Metallurgica*, 32 [9] 1407-1414 (1984).

145. M. Abrahams, S. Rao, C. Buiocchi and L. Trager, 'Decorated boundaries observed in copper electrodeposits,' *J. Electrochem. Soc.*, 133 [9] 1786-1791 (1986).

146. S. Lagrange, S. Brongersma, M. Judelewicz, A. Saerens, I. Vervoort, E. Richard, R. Palmans and K. Maex, 'Self-annealing characterization of electroplated copper films,' *Microelectronic Engineering*, 50 [1] 449-457 (2000).

147. J. Neuner, I. Zienert, A. Peeva, A. Preuße, P. Kücher and J. W. Bartha, 'Microstructure in copper interconnects–Influence of plating additive concentration,' *Microelectronic Engineering*, 87 [3] 254-257 (2010).

148. G. Fabricius, K. Kontturi and G. Sundholm, 'Influence of thiourea on the nucleation of copper from acid sulphate solutions,' *Electrochim. Acta*, 39 [16] 2353-2357 (1994).

149. X. Feng, W. Luo, M. Li and S. Wang, 'Effect of leveler on microstructure and stress of electroplated copper for TSV application,' *3rd IEEE CPMT Symposium Japan* (2013).

150. S. Ko, J. Lin, Y. Wang and C. Wan, 'Effect of the molecular weight of polyethylene glycol as single additive in copper deposition for interconnect metallization,' *Thin Solid Films*, 516 [15] 5046-5051 (2008).

151. J. Marro, T. Darroudi, C. Okoro, Y. Obeng and K. Richardson, 'The Influence of Pulsed Electroplating Frequency and Duty Cycle on Copper Film Microstructure and Stress State,' *Thin Solid Films* (submitted 2016).

152. J. J. Kim and S. Kim, 'Optimized surface pretreatments for copper electroplating,' *Appl. Surf. Sci.*, 183 [3] 311-318 (2001).

153. S. H. Kang, Y. S. Obeng, M. A. Decker, M. Oh, S. M. Merchant, S. K. Karthikeyan, C. S. Seet and A. S. Oates, 'Effect of annealing on the surface microstructural evolution and the electromigration reliability of electroplated Cu films,' *J Electron Mater*, 30 [12] 1506-1512 (2001).

154. G. G. Stoney, 'The tension of metallic films deposited by electrolysis,' *Proceedings of the Royal Society of London.Series A, Containing Papers of a Mathematical and Physical Character*, 82 [553] 172-175 (1909).

155. W. W. Mullins, 'The effect of thermal grooving on grain boundary motion,' *Acta Metallurgica*, 6 [6] 414-427 (1958).

156. W. W. Mullins, 'Theory of Thermal Grooving,' *J. Appl. Phys.*, 28 [3] 333-339 (1957).

157. H. J. Frost, 'Microstructural evolution in thin films,' *Mater Charact*, 32 [4] 257-273 (1994).

158. A. Sikder, A. Kumar, P. Shukla, P. Zantye and M. Sanganaria, 'Effect of multistep annealing on mechanical and surface properties of electroplated Cu thin films,' *J Electron Mater*, 32 [10] 1028-1033 (2003).

159. H. Li, C. Zhu, S. Tian, G. Xu and L. Luo, 'Thermomechanical behavior of nanotwinned copper interconnection line in wafer level packaging and the influence on wafer warpage,' *Electronic Components and Technology Conference (ECTC) IEEE 65th* 1228-1233 (2015).

160. X. Zhang and A. Misra, 'Superior thermal stability of coherent twin boundaries in nanotwinned metals,' *Scr. Mater.*, 66 [11] 860-865 (2012).

161. Q. Yu, Z. Shan, J. Li, X. Huang, L. Xiao, J. Sun and E. Ma, 'Strong crystal size effect on deformation twinning,' *Nature*, 463 [7279] 335-338 (2010).

162. C. Wu, X. Feng, H. Cao, H. Ling, M. Li and D. Mao, 'The effect of different TSV electroplating levelers on the copper residual stress,' *Electronic Packaging Technology and High Density Packaging (ICEPT-HDP), 2012 13th International Conference on* 430-433 (2012).

163. S. Armini, Z. El-Mekki, K. Vandersmissen, H. Philipsen, S. Rodet, M. Honore, A. Radisic, Y. Civale, E. Beyne and L. Leunissen, 'Void-Free Filling of HAR TSVs Using a Wet Alkaline Cu Seed on CVD Co as a Replacement for PVD Cu Seed,' *Journal of The Electrochemical Society*, 158 [2] H160-H165 (2011).

164. Sang-Soo Noh, Eun-Hey Choi, Yong-Hyuk Lee, Hyun-jin Ju, Sa-Kyun Rha, Boung-ju Lee, Dong-Kyu Kim and Youn-Seoung Lee, 'Optimization of Cu electrodeposition parameters for Through Silicon Via (TSV),' *Physical and Failure Analysis of Integrated Circuits (IPFA), 2011 18th IEEE International Symposium on the* 1-4 (2011).

165. R. R. KELLER and R. H. GEISS, 'Transmission EBSD from 10 nm domains in a scanning electron microscope,' *J. Microsc.*, 245 [3] 245-251 (2012).

166. A. Pohjoranta and R. Tenno, 'A method for microvia-fill process modeling in a Cu plating system with additives,' *J. Electrochem. Soc.*, 154 [10] D502-D509 (2007).

167. H. Kadota, R. Kanno, M. Ito and J. Onuki, 'Texture and Grain Size Investigation in the Copper Plated Through-Silicon via for Three-Dimensional Chip Stacking Using Electron Backscattering Diffraction,' *Electrochemical and Solid-State Letters*, 14 [5] D48-D51 (2011).

168. C. R. Chen, S. X. Li, J. L. Wen and W. P. Jia, 'Finite element analysis about effects of stiffness distribution on stresses and elastic strain energy near the triple junction in a tricrystal,' *Materials Science and Engineering: A*, 282 [1–2] 170-176 (2000).

169. V. A. Vas'ko, I. Tabakovic, S. C. Riemer and M. T. Kief, 'Effect of organic additives on structure, resistivity, and room-temperature recrystallization of electrodeposited copper,' *Microelectronic Engineering*, 75 [1] 71-77 (2004).

170. Z. Li and R. G. Gordon, 'Thin, continuous, and conformal copper films by reduction of atomic layer deposited copper nitride,' *Chemical Vapor Deposition*, 12 [7] 435-441 (2006).

171. Q. Zhu, A. Toda, Y. Zhang, T. Itoh and R. Maeda, 'High-speed copper filling within high aspect ratio through holes in polymer substrates,' *Int.J.Electrochem.Sci*, 8 [8] 10568-10577 (2013).

APPENDICES

Appendix A:

Pulse Electrodeposition EBSD Maps

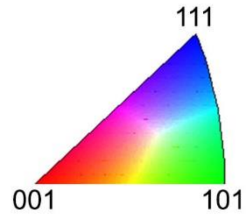

Figure A1: The inverse pole figure legend for all figures in Appendix A.

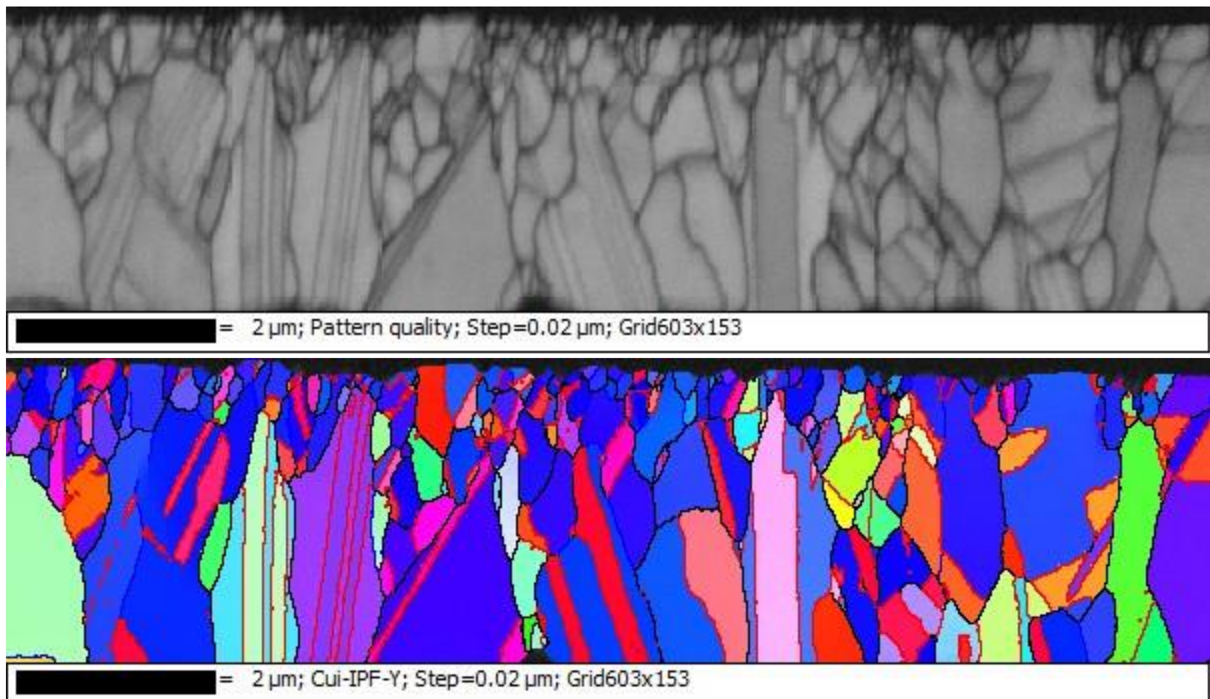

Figure A2: The band contrast map (top) and inverse pole figure map (bottom) normal to the sample surface for the cross-section of a Cu blanket film, deposited under the PED #1 conditions (frequency: 1 Hz; duty cycle: 0.05).

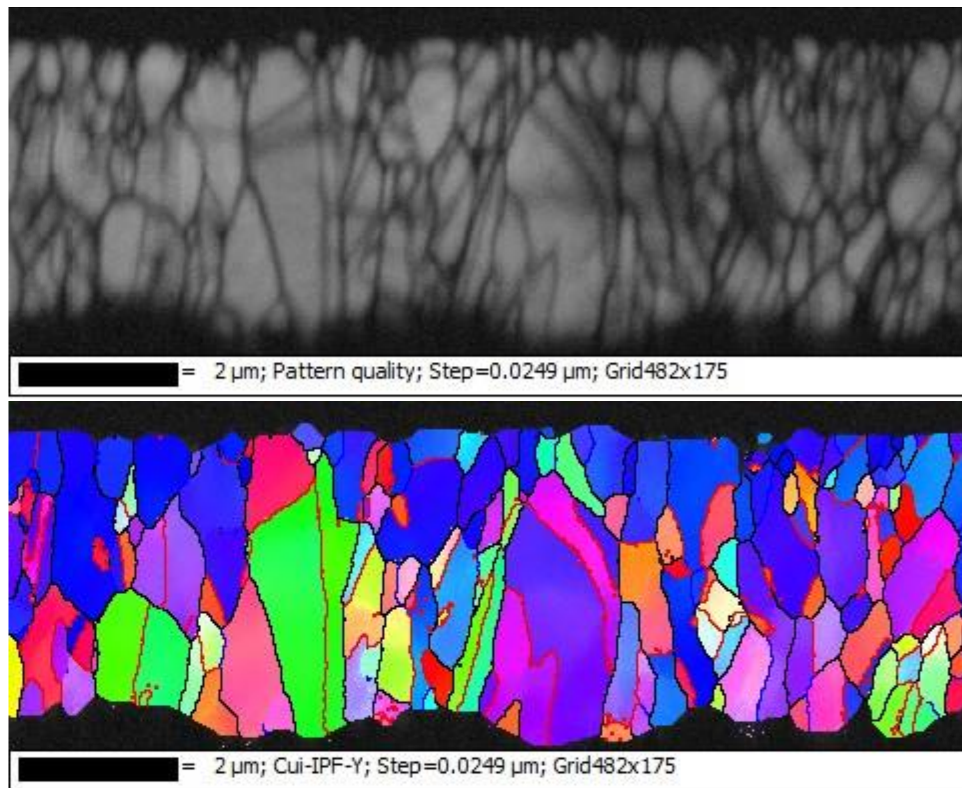

Figure A3: The band contrast map (top) and inverse pole figure map (bottom) normal to the sample surface for the cross-section of a Cu blanket film, deposited under the PED #2 conditions (frequency: 1 Hz; duty cycle: 0.1).

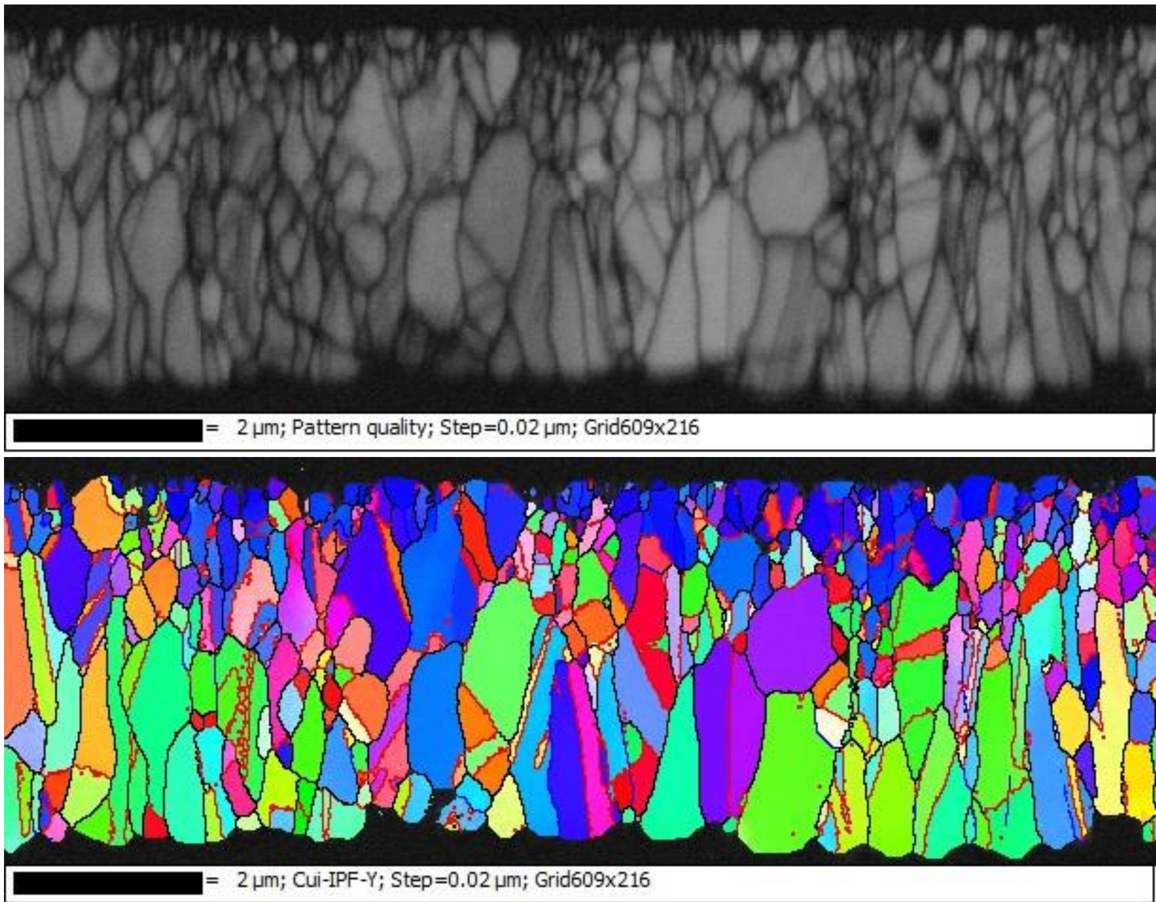

Figure A4: The band contrast map (top) and inverse pole figure map (bottom) normal to the sample surface for the cross-section of a Cu blanket film, deposited under the PED #3 conditions (frequency: 1 Hz; duty cycle: 0.25).

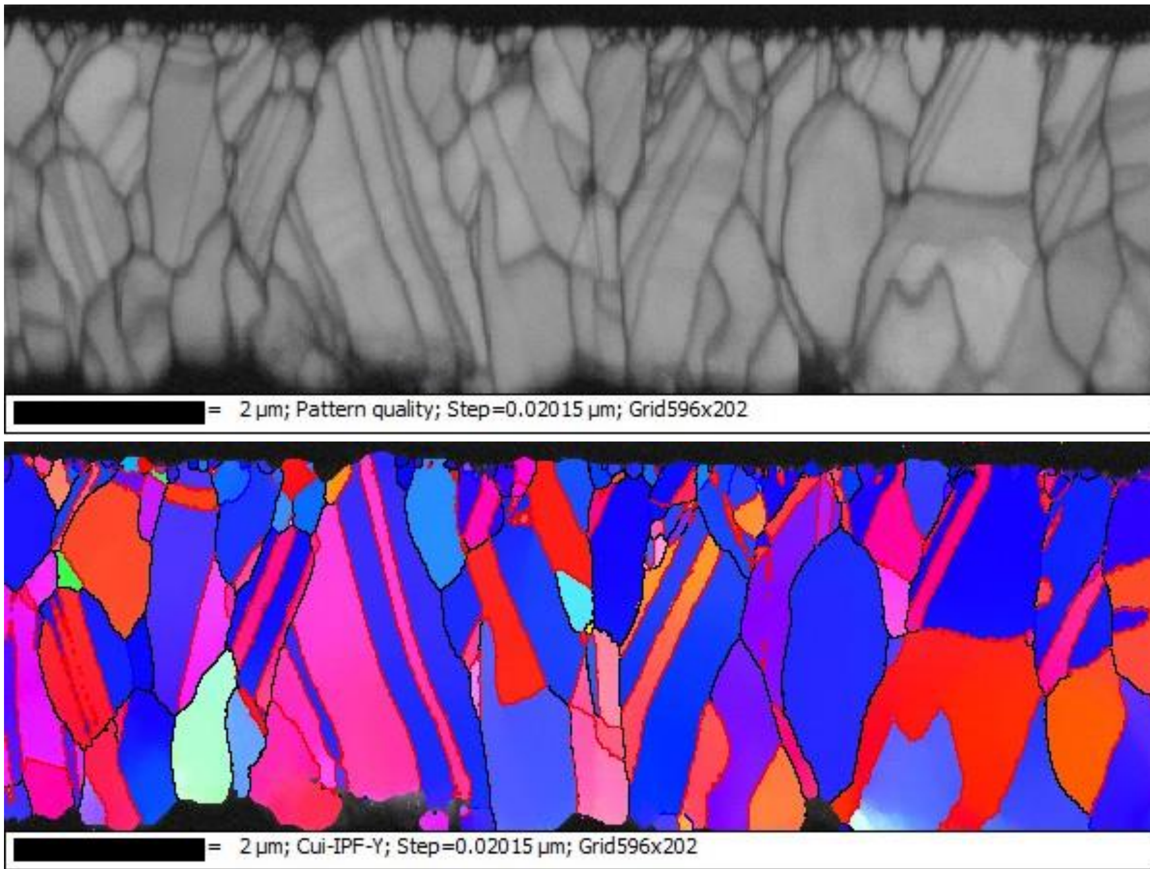

Figure A5: The band contrast map (top) and inverse pole figure map (bottom) normal to the sample surface for the cross-section of a Cu blanket film, deposited under the PED #4 conditions (frequency: 50 Hz; duty cycle: 0.05).

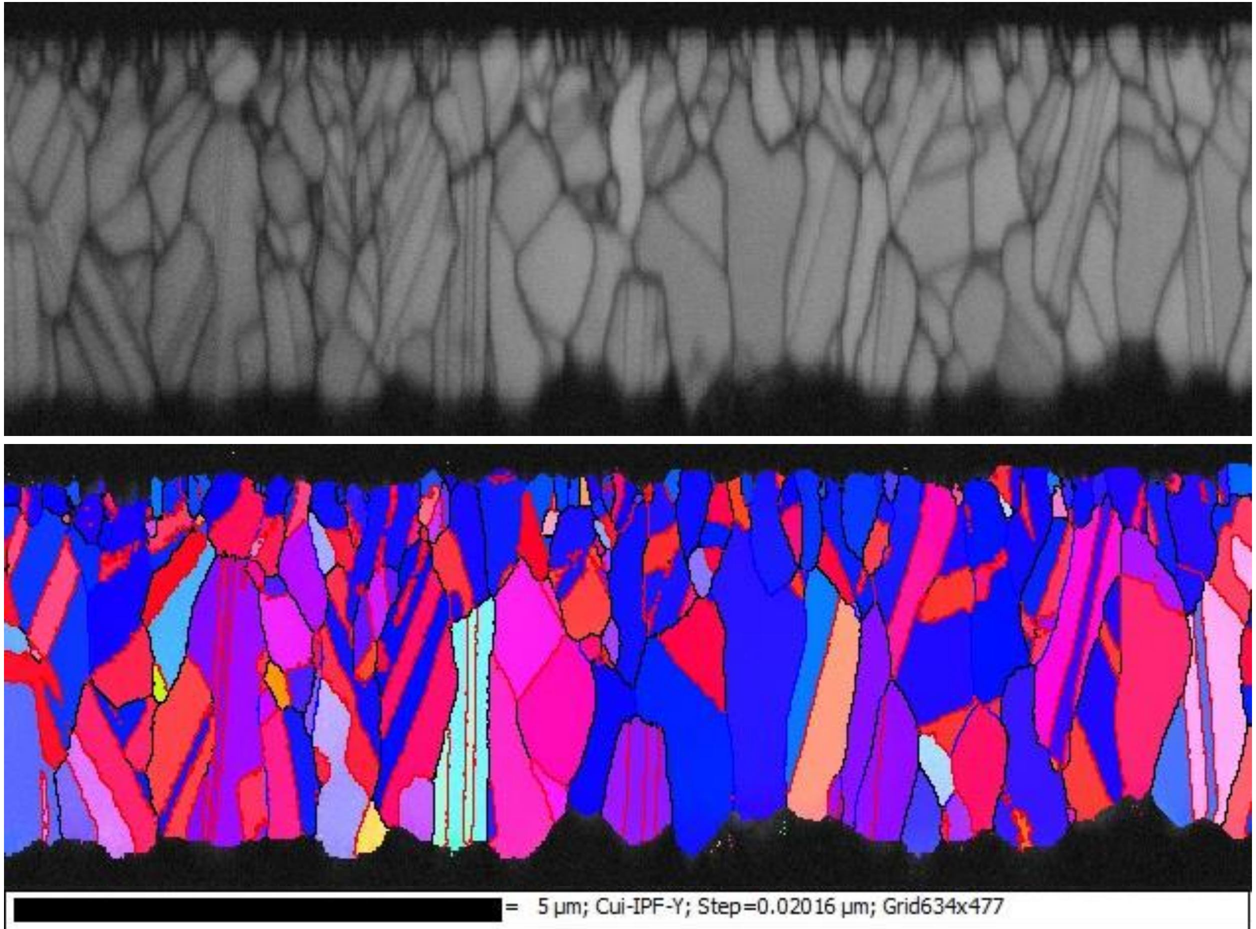

Figure A6: The band contrast map (top) and inverse pole figure map (bottom) normal to the sample surface for the cross-section of a Cu blanket film, deposited under the PED #5 conditions (frequency: 50 Hz; duty cycle: 0.1).

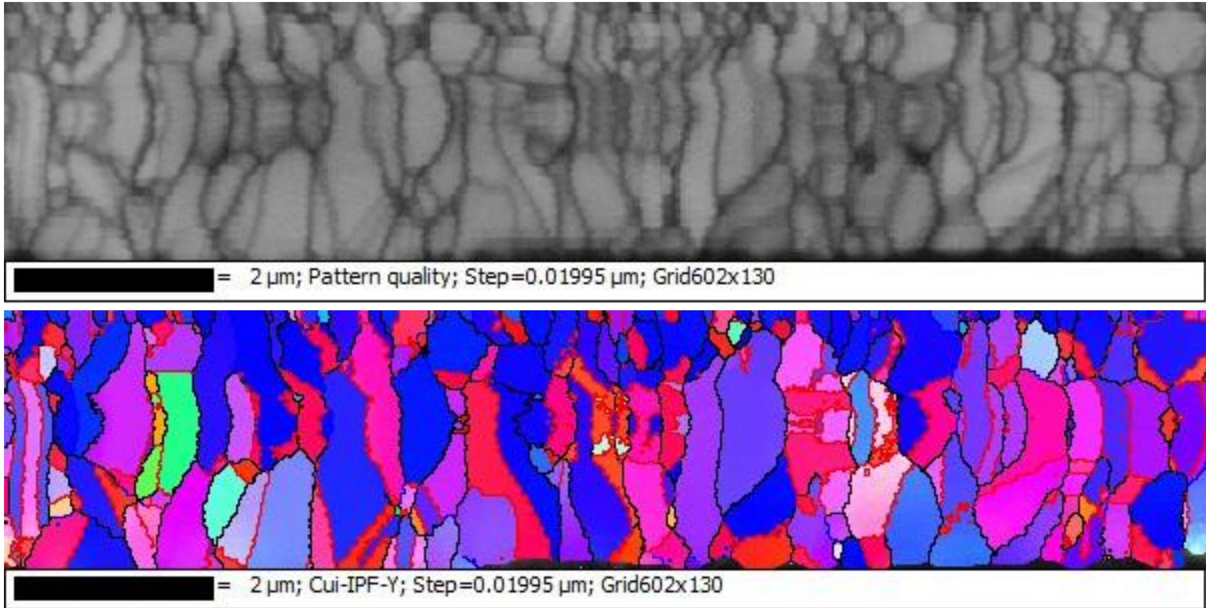

Figure A7: The band contrast map (top) and inverse pole figure map (bottom) normal to the sample surface for the cross-section of a Cu blanket film, deposited under the PED #6 conditions (frequency: 50 Hz; duty cycle: 0.25).

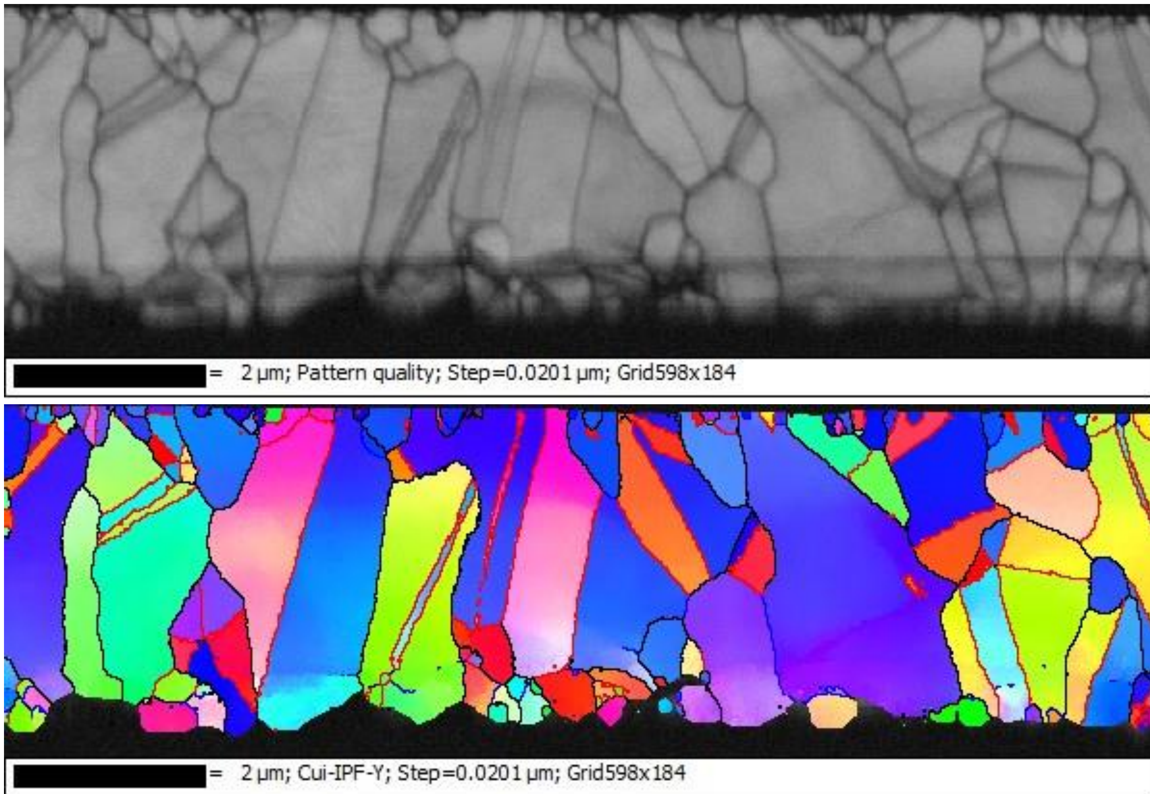

Figure A8: The band contrast map (top) and inverse pole figure map (bottom) normal to the sample surface for the cross-section of a Cu blanket film, deposited under the PED #7 conditions (frequency: 100 Hz; duty cycle: 0.05).

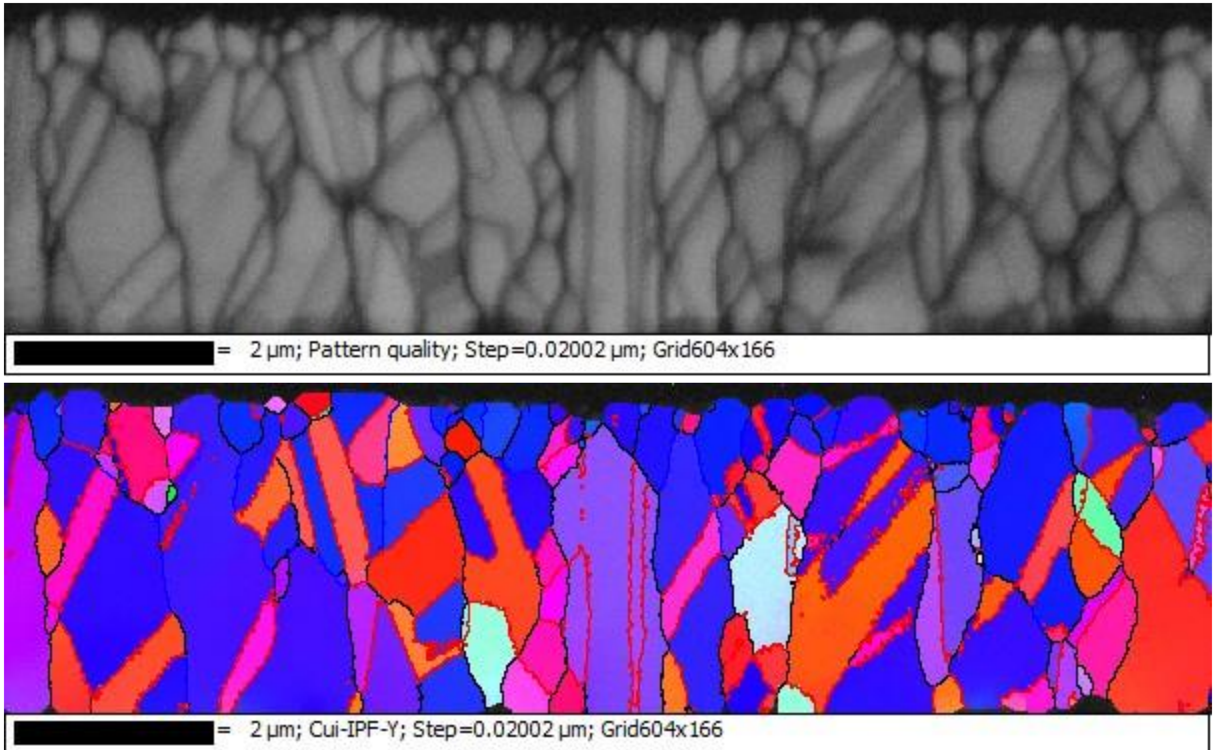

Figure A9: The band contrast map (top) and inverse pole figure map (bottom) normal to the sample surface for the cross-section of a Cu blanket film, deposited under the PED #8 conditions (frequency: 100 Hz; duty cycle: 0.1).

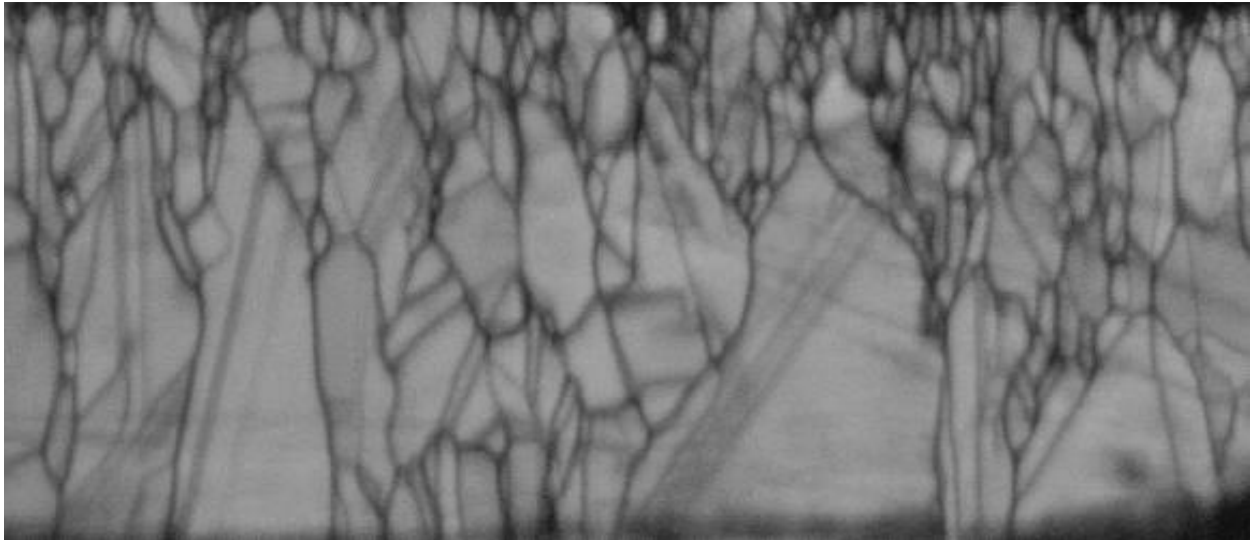

=2 µm; Pattern quality; Step=0.02 µm; Grid580x251

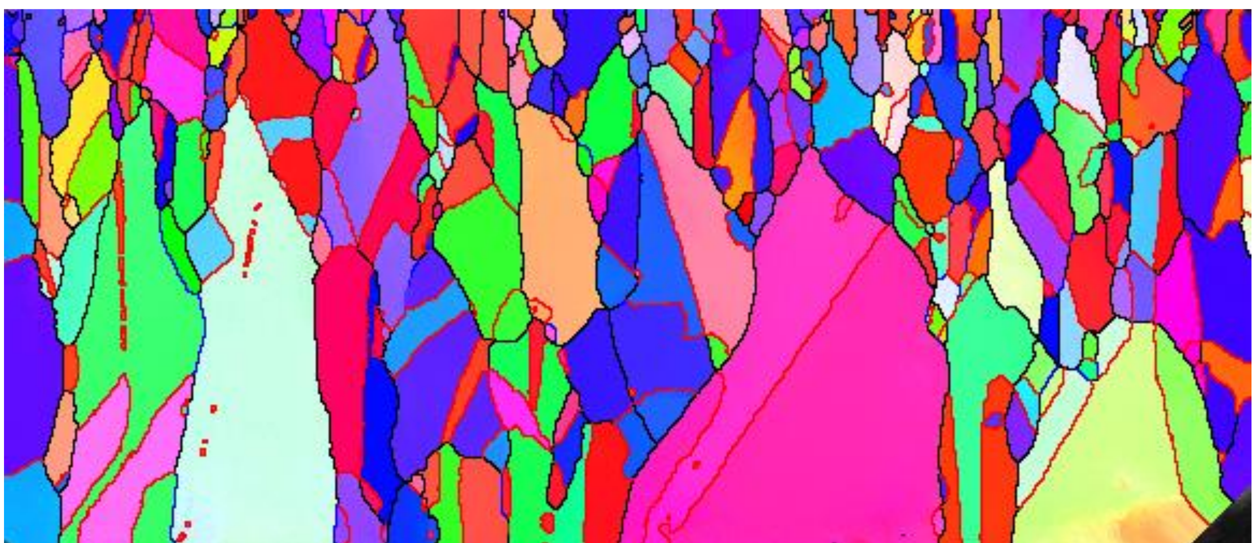

=2 µm; Cu- IPF-Z; Step=0.02 µm; Grid580x251

Figure A10: The band contrast map (top) and inverse pole figure map (bottom) normal to the sample surface for the cross-section of a Cu blanket film, deposited under the PED #9 conditions (frequency: 100 Hz; duty cycle: 0.25).

Appendix B:

Trench Pretreatment and PCD

Table B1: Material properties (stress, roughness, and texture coefficient) with various pretreatments used on trench samples. Stress and surface roughness were measured with the WLI and the (111) texture coefficient was calculated from XRD measurements.

Sample Pretreatment	Relative Stress (a.u.)	RMS Roughness (nm)	(111) Texture Coefficient (a.u.)
Normal	3.82	33.2 ± 0.7	3.99945
w/o NH_4OH	3.19	33.1 ± 1.0	3.99913
30 min @ 300 °C	1.87	29.9 ± 0.1	3.99945
2.5 s etch	2.92	36.3 ± 0.8	3.99928
5 s etch	2.38	42.4 ± 11.2	3.99937

Table B2: The (111) texture coefficient, calculated from XRD measurements, for trench samples deposited with various peak current densities.

Peak Current Density (mA/cm^2)	(111) Texture Coefficient (a.u.)
5	3.99945
10	3.99913
20	3.99945
80	3.99928

Appendix C:

Alternative Organic Additive Impurity Measurements

Thermogravimetric analysis (TGA) was attempted as an alternative method for measuring the impurity content created by the organic additives becoming embedded into the Cu during deposition. Figure C1 shows the individual organic additive powders (PEG, SPS, and JGB) weight decay with increasing temperature. From this map it was determined that a significant weight loss occurs for the PEG at ~220 °C, SPS at ~280 °C, and the JGB slowly lost weight over time. The 200/5/10 Cu sample was delaminated from the substrate and analyzed with the TGA in Figure C2. While there is a weight loss achieved at lower temperatures (<150 °C), the graph does not show a significant weight loss change at the designated areas for PEG or SPS degradation (220 °C and 280 °C). The jump at approximately 150 °C is believed to be caused by vibrations in the room. Although the chamber was purged with Ar, the Cu still began to oxidize at approximately 350 °C, as indicated by the increase in weight.

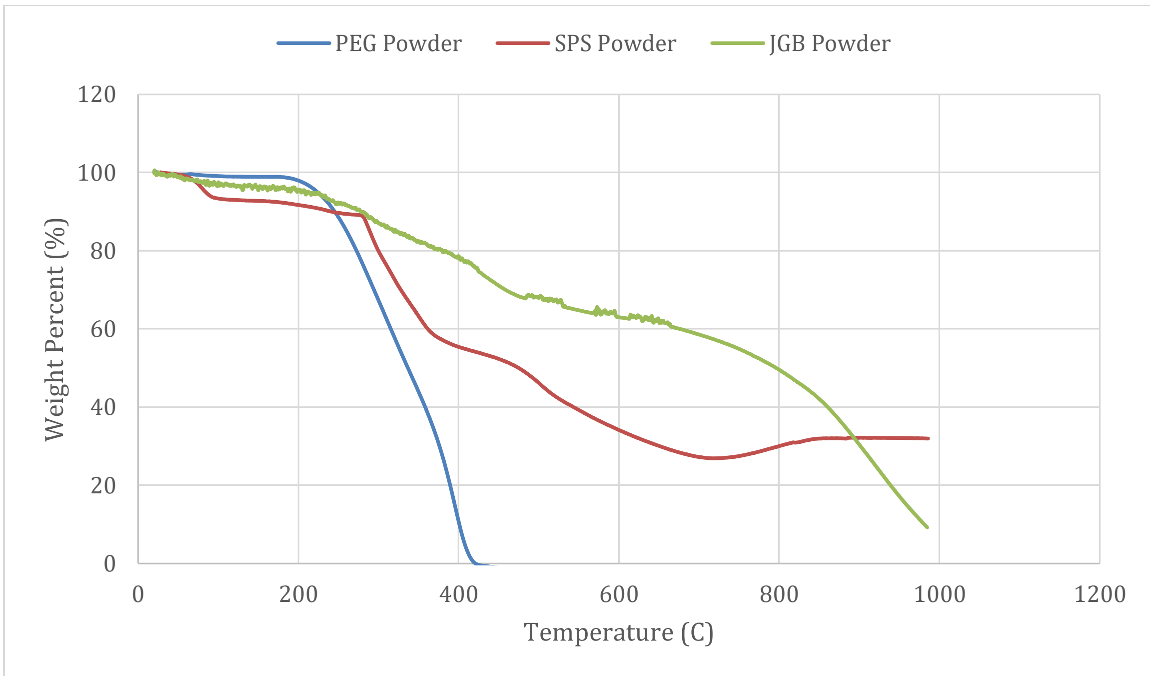

Figure C1: The weight loss with temperature measured by thermogravimetric analysis of the individual PEG, SPS, and JGB organic additive powders.

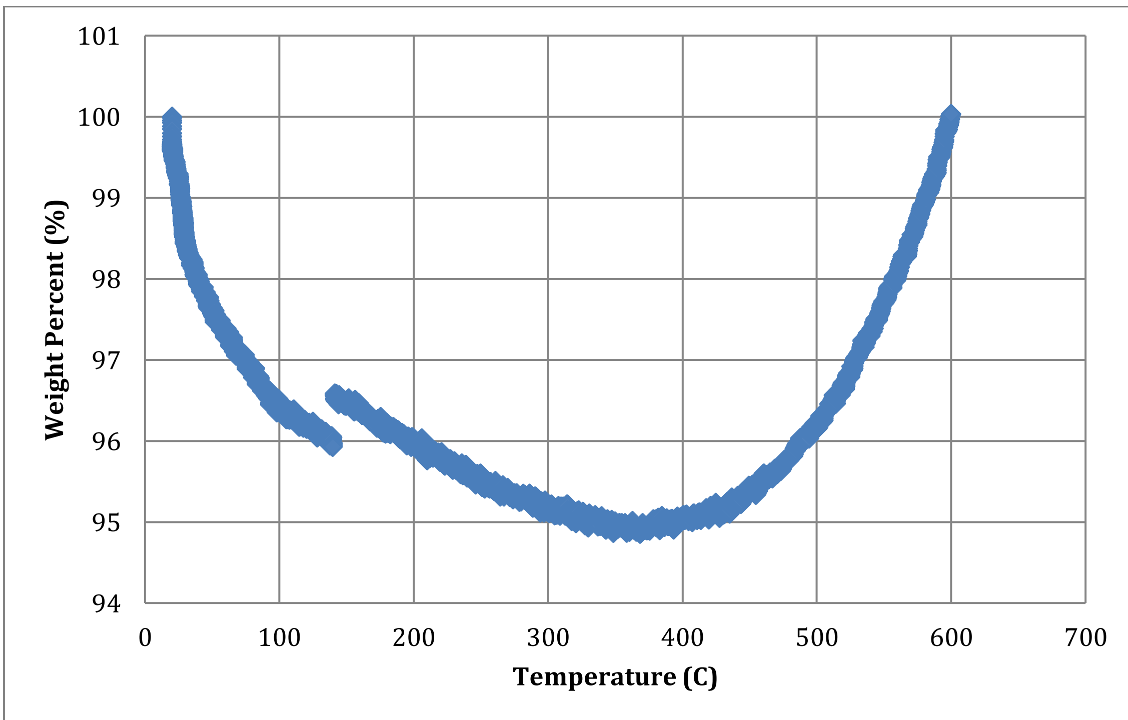

Figure C2: The weight loss from TGA of the 200/5/10 mg/L (PEG/SPS/JGB) to determine if this method was sensitive enough to measure a weight change from the small amount of organics used in the Cu.

Appendix D:

Review on Voids in Copper

The byproduct of stress buildup in a material is typically the formation of voids. Voids are areas or pockets of missing material, which form to relieve stresses by distributing them over a larger area [1,2]. The multi-material system, associated with microelectronics, does not lend itself to defect-free devices. The mismatch in coefficient of thermal expansion (CTE) between copper (Cu) interconnects and silicon (Si) wafers is 16.7 ppm/°C and 2.3 ppm/°C respectively [3]. The variation of expansion rates between the two materials upon exposure to heat results in the formation of stresses, not only in the Cu, but also the surrounding Si [1,4-7]. Temperature fluctuations in electronic chips occur during processing, environmental conditions, and during use, as current flow can produce Joule heating in the Cu interconnects. Furthermore, electromigration (EM), or the mass transport of Cu atoms during current flow, is also a concern for void formation and growth. The phenomena of void nucleation and growth in Cu will be discussed in detail throughout this overview, as well as the affects these voids have on Cu's material properties.

Void Nucleation

Stress-Induced Nucleation

As mentioned earlier, voids form as a mechanism of stress relief [1,2]. Thus, areas of high stress concentrations are prone to void nucleation, most commonly at interfaces, triple junctions, and grain boundaries in the Cu's

microstructure [8-13]. Upon heating, the elastic anisotropy of Cu grains result in stress at interfaces, where the crystallographic orientations are significantly different [10]. Furthermore, grain boundaries provide a diffusion path for vacancies to migrate, coalesce, and become voids [11,14,15]. While voids frequently nucleate at twin/grain boundary junctions [10], voids are less likely to form at {111} coherent twin interfaces compared to incoherent twin boundaries, such as {322} textured twins, and high angle grain boundaries. This can be attributed to the significantly lower interfacial energy and grain boundary diffusivity of coherent twins [11,14]. Coherent twin boundary energy in Cu is estimated at 21 mJ/m^2 in contrast to the 498 mJ/m^2 of incoherent grain boundaries and 623 mJ/m^2 grain boundary energy of high angle grain boundaries [16,17]. This was further exemplified by the findings of Nucci *et al.*, who observed less voids in strongly textured <111> Cu films than in randomly oriented or weakly textured Cu films [18]

Creep and fatigue can both induce void nucleation in Cu; however, fatigue produces a much quicker void nucleation rate [8]. Void nucleation is strain rate dependent. Thus, larger strain rates result in the nucleation of more voids and a decrease in void spacing in monocrystalline Cu [13].

Void Formation in Microelectronics

Nucleation of voids in microelectronics differs from bulk materials in that edge effects are taken into account. In microelectronics, Cu interconnects, damascenes, and vias are dimensionally restricted. Voids still form at triple junctions in the center of these devices, however, as dimensions, such as

linewidths of interconnects, become smaller, less voids are formed at the center of these lines and most void nucleation sites are limited to the interface between the Cu and external materials (edges) [19]. As the interconnect linewidths become smaller, the Cu's microstructure is more likely to take on bamboo-like grains, where the grains span the width of the interconnect. Triple junctions are sparse in these structures, and voids are limited to nucleation at the intersection of grain boundaries and the Cu/diffusion barrier interface [19]. High stresses, due to high temperature (723 K) heat treatments, causes delamination of the Cu and interfacial void formation in damascenes [12]. Furthermore, stress-induced voids have been observed at the interface of thermocompression Cu bonded wafers and void size correlated with bonding temperature [20].

Stresses in Cu through-silicon vias (TSV) have been quantified through x-ray micro-diffraction [1,4-6]. Budiman *et al.* found high deviatoric shear stresses (~145 MPa) and hydrostatic tensile stresses (~165 MPa) in the Cu-TSVs after a 200°C 1 hr. anneal [6]. Thermo-mechanical stresses, like these, can result in the formation of voids in TSVs and a reduction in tensile stresses in the Cu as demonstrated by Shin *et al.* [1].

Deposition-Induced Formation

The filling of Cu into damascene and TSV trenches is typically conducted by electro-chemical deposition (ECD). Deposition parameters can largely affect the formation of seams and voids in these devices (see Figure D1). The traditional filling of these trenches, from the sidewalls to their centers, can result in non-

uniform deposition and trapped air in the trenches. Bottom-up filling, also known as superfilling or super-conformal, is less susceptible to void formation than this conventional deposition method [21-24]. This can be achieved through selective ECD chemistries, which as also been shown to dictate the resistance to void formation in TSVs from thermal cycling stresses [25,26]. Bath additives, such as Janus Green B (JGB) and bis(3-sulfopropyl) disulfide (SPS), have been shown to improve quality of the ECD fill with lower quantities of voids [27,28] . Furthermore, slower deposition rates also produce lower void yields in trenches. This can be achieved through lower current densities [23,28] and choosing the optimum off-time during pulsed ECD [29]. The off-time is dependent on trench height and diffusivity of the copper ions [29].

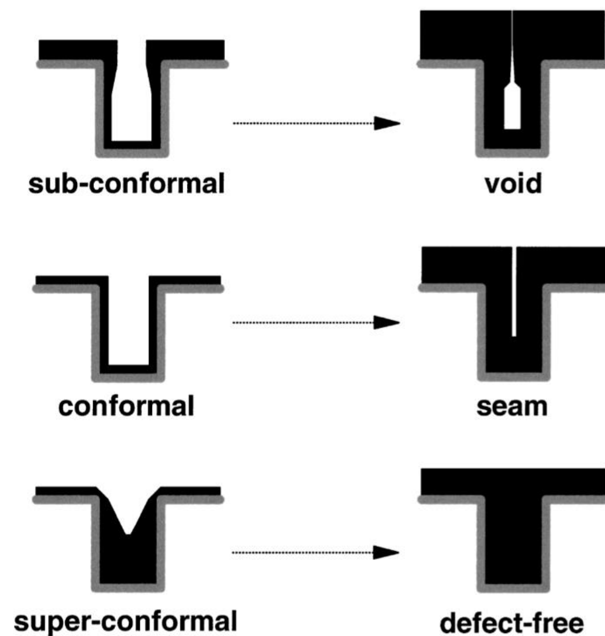

Figure D1: Illustration of voids and seams forming during deposition as well as defect-free bottom-up filling, taken from [30].

Electromigration-Induced Nucleation

Electromigration (EM) is the diffusion of atoms in a material due to electron flow from an applied current. A material's ability to resist electromigration is important in microelectronics, since this mass transport often leads to void formation (see Figure D2), and is one advantage Cu has over its predecessor, Al [30]. The activation energy for electromigration in Cu is 0.6 eV to 1.1 eV [31,32]. Voids often nucleate at grain boundaries and grain boundary/interface junctions in Cu interconnect lines [31-33] from stresses that occur due to a variation in atomic fluxes [33-35]. EM diffusivities are orientation dependent. For instance, (111) Cu orientations have been shown to demonstrate high EM resistance and longer EM lifetimes [35]. Cu interconnects with a large amount of {111} coherent twin boundaries have improved EM resistance, since these twin boundaries/grain boundary junctions are thought to slow down the diffusion of vacancies and Cu atoms [36,37].

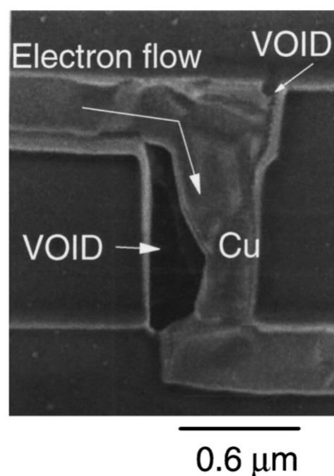

Figure D2: A void that formed in a Cu interconnect and is restricting the flow of electrons, taken from [30].

Once voids nucleate, their growth is driven by surface and grain boundary diffusion of Cu atoms [32]. Linigier *et al.* found void sizes increased linearly over time during EM and the void growth rate exhibited Arrhenius behavior in Cu [32]. Additionally, voids often grow directionally along interconnect paths by consuming grains, a process that can be hindered by grain boundaries as well as clusters of fine grains [32-34]. Once voids become large enough to force current to flow through the liner material, the electrical properties begin to diminish; specifically, increases in resistance have been observed [30].

Void Growth

The growth of nucleated voids has been observed in Cu, following heat treatments [2]. The two primary mechanisms of void growth in Cu are vacancy diffusion and dislocation emission. Vacancy diffusion is the dominating mechanism in Cu, which endure strain rates between 10^{-5} s^{-1} and 10^{8} s^{-1}, while dislocation emission is dominant at higher strain rates [9,38]. Both will be discussed in detail throughout this section.

Vacancy Diffusion

Vacancy diffusion along grain boundaries as a method of void growth has observed in many studies [8,10,14]. Since this is a diffusion-based process, it is time and temperature dependent. Voids located nearby are capable of coalescing as they come in contact from their growth along grain boundaries [8,9,39]. Cu

orientations have some control over void growth since grain boundary diffusion is necessary for vacancy mobility. Strongly textured films contain far more tilt boundaries than twist boundaries, which are more susceptible to grain boundary diffusion of vacancies [18]. Thus, void growth may occur more readily in randomly textured Cu as opposed to strong textured Cu.

Dislocation Emission

Voids can also grow by emitting dislocations from their surfaces into the surrounding grains [13]. Lubarda *et al.* did an extensive study on void growth by dislocation emission [38]. As mentioned earlier, this process occurs at strain rates above ~10^8 s^{-1}. Void growth by dislocation emission can be broken down into two types, primastic and shear loop emission. As shown by the illustration in Figure D3, both occur at 45° from the void centers. Prismatic loop emission transpires as a section of a spherical void is extruded outward from the void center, increasing the volume of the void. While dislocation emission occurs normal to the void's center in prismatic loop emission, shear loop emission occurs by emitting a dislocation along the slip plane in which the spherical void is sectioned. The void then expands in a shear like manner along the slip plane. Smaller voids require more stress for dislocation emission compared to larger voids, thus void growth through dislocation emission is size dependent [38]. Larger voids on the other hand, grow preferentially along grain boundaries due to partial dislocation emission from grain boundaries in close proximity to voids [39]. Twin boundaries can impede dislocation emission and ultimately void growth [40]. Furthermore, twin

boundaries spacing can limit the growth of these voids by blocking the dislocations [41].

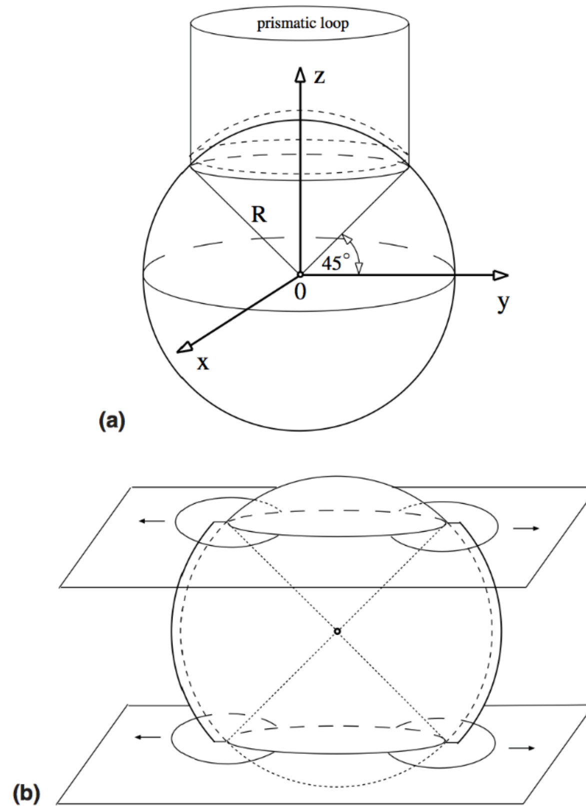

Figure D3: Depiction of (a) prismatic loop emission and (b) shear loop emission mechanisms of void growth by dislocation emission, taken from [38].

Void-Induced Material Property Changes

The nucleation and growth of voids in Cu may have a negative impact on its material properties. Two important material property categories (electrical and mechanical) for microelectronic applications will be discussed in the following section.

Electrical Properties

As mentioned in an earlier section, the electrical resistance of the Cu is not considerably affected by voids, unlike cracks, unless the void spans the width of a Cu interconnect and forces the signal to propagate through the metallization layer [34,42]. On the other hand, radio frequency signal scattering has been observed as a result of void concentrations in Cu [43-45].

Mechanical Properties (Strength)

Molecular dynamic simulations have demonstrated the effect voids have on Cu's mechanical properties. Larger void sizes and volume fractions lower the yield strength and elastic modulus of Cu [39,46]. Simulations indicate that voids nucleate at grain boundary/void interfaces and from the surfaces of voids in the direction of the maximum resolved shear stress [39]. Although twin boundaries are thought of as mechanical strengthening tools, voids located at twin boundaries actually result in much lower yield strengths of the system [39]. Lastly, the presence of voids has been attributed to lower ductility and toughness of metals [47]. Overall, twins are detrimental to Cu's mechanical properties.

Conclusion

This paper discusses in depth void nucleation, growth, and effects on material properties in Cu, with an emphasis on microelectronic applications. Voids form in Cu due to stresses, inadequate filling techniques and parameters, and vulnerability to electromigration. The voids are than allowed to grow through

vacancy diffusion along grain boundaries at lower strain rates and dislocation emission from the voids' surfaces at high strain rates. Voids in Cu negatively impact the electrical properties, via signal scattering, and mechanical properties, with reduced yield strength and young's modulus. Thus, the reduction of voids in Cu for microelectronics will greatly improve their reliability and performance.

References

1. H. Shin, B. Kim, J. Kim, S. Hwang, A. Budiman, H. Son, K. Byun, N. Tamura, M. Kunz, D. Kim and Y. Joo, 'Microstructure Evolution and Defect Formation in Cu Through-Silicon Vias (TSVs) During Thermal Annealing,' *Journal of Electronic Materials*, 41 [4] 712-719 (2012).

2. L. W. Kong, J. R. Lloyd, K. B. Yeap, E. Zschech, A. Rudack, M. Liehr and A. Diebold, 'Applying x-ray microscopy and finite element modeling to identify the mechanism of stress-assisted void growth in through-silicon vias,' *J. Appl. Phys.*, 110 [5] 053502 (2011).

3. C. Okoro, M. Gonzalez, B. Vandevelde, B. Swinnen, G. Eneman, P. Verheyen, E. Beyne and D. Vandepitte, 'Prediction of the Influence of Induced Stresses in Silicon on CMOS Performance in a Cu-Through-Via Interconnect Technology,' *Thermal, Mechanical and Multi-Physics Simulation Experiments in Microelectronics and Micro-Systems, 2007. EuroSime 2007. International Conference on* 1-7 (2007).

4. C. Okoro, L. E. Levine, R. Xu, J. Z. Tischler, W. Liu, O. Kirillov, K. Hummler and Y. S. Obeng, 'X-ray micro-beam diffraction determination of full stress tensors in Cu TSVs,' *IEEE 63rd Electronic Components and Technology Conference* 648-652 (2013).

5. C. Okoro, L. E. Levine, R. Xu, K. Hummler and Y. S. Obeng, 'Nondestructive Measurement of the Residual Stresses in Copper Through-Silicon Vias Using Synchrotron-Based Microbeam X-Ray Diffraction,' *Electron Devices, IEEE Transactions on*, PP [99] 1-1 (2014).

6. A. S. Budiman, H. -. -. Shin, B. -. Kim, S. -. Hwang, H. -. Son, M. -. Suh, Q. -. Chung, K. -. Byun, N. Tamura, M. Kunz and Y. -. Joo, 'Measurement of stresses in Cu and Si around through-silicon via by synchrotron X-ray microdiffraction for 3-dimensional integrated circuits,' *Microelectronics Reliability*, 52 [3] 530-533 (2012).

7. W. S. Kwon, D. T. Alastair, K. H. Teo, S. Gao, T. Ueda, T. Ishigaki, K. T. Kang and W. S. Yoo, 'Stress evolution in surrounding silicon of Cu-filled through-silicon via undergoing thermal annealing by multiwavelength micro-Raman spectroscopy,' *Applied Physics Letters*, 98 [23] 232106-232106-3 (2011).

8. R. Page and J. R. Weertman, 'HVEM observations of grain boundary voids in high purity copper,' *Acta Metallurgica*, 29 [3] 527-535 (1981).

9. R. E. Rudd and J. F. Belak, 'Void nucleation and associated plasticity in dynamic fracture of polycrystalline copper: an atomistic simulation,' *Computational materials science*, 24 [1] 148-153 (2002).

10. A. Sekiguchi, J. Koike, S. Kamiya, M. Saka and K. Maruyama, 'Void formation by thermal stress concentration at twin interfaces in Cu thin films,' *Appl. Phys. Lett.*, 79 [9] 1264-1266 (2001).

11. A. Sekiguchi, J. Koike and K. Maruyama, 'Microstructural influences on stress migration in electroplated Cu metallization,' *Appl. Phys. Lett.*, 83 [10] 1962-1964 (2003).

12. A. Sekiguchi, J. Koike and K. Maruyama, 'Formation of slit-like voids at trench corners of damascene Cu interconnects,' *Materials Transactions*, 43 [7] 1633-1637 (2002).

13. J. Belak, 'Molecular dynamics simulation of high strain-rate void nucleation and growth in copper,' *The tenth American Physical Society topical conference on shock compression of condensed matter*, 429 [1] 211-214 (1998).

14. M. Butron-Guillen, J. Cabanas-Moreno and J. Weertman, 'Fatigue cavitation and relative grain orientations in pure copper,' *Scripta Metallurgica et Materialia*, 24 [6] 991-996 (1990).

15. A. Cuitino and M. Ortiz, 'Ductile fracture by vacancy condensation in fcc single crystals,' *Acta materialia*, 44 [2] 427-436 (1996).

16. D. A. Porter and K. E. Easterling, 'Phase Transformations in Metals and Alloys, (Revised Reprint)'. CRC press 1992.

17. L. E. Murr, 'Interfacial phenomena in metals and alloys'. Addison-Wesley Publishing Company, United States, 1975.

18. J. A. Nucci, R. R. Keller, J. E. Sanchez and Y. Shacham- Diamand, 'Local crystallographic texture and voiding in passivated copper interconnects,' *Appl. Phys. Lett.*, 69 [26] 4017-4019 (1996).

19. J. A. Nucci, Y. Shacham- Diamand and J. E. Sanchez, 'Effects of linewidth, microstructure, and grain growth on voiding in passivated copper lines,' *Appl. Phys. Lett.*, 66 [26] 3585-3587 (1995).

20. C. Tan, R. Reif, N. Theodore and S. Pozder, 'Observation of interfacial void formation in bonded copper layers,' *Appl. Phys. Lett.*, 87 [20] 201909-201909-3 (2005).

21. T. P. Moffat and D. Josell, 'Extreme Bottom-Up Superfilling of Through-Silicon-Vias by Damascene Processing: Suppressor Disruption, Positive Feedback and Turing Patterns,' *Journal of The Electrochemical Society*, 159 [4] D208-D216 (2012).

22. D. Wheeler, T. Moffat and D. Josell, 'Spatial-Temporal Modeling of Extreme Bottom-up Filling of Through-Silicon-Vias,' *J. Electrochem. Soc.*, 160 [12] D3260-D3265 (2013).

23. B. Kim, C. Sharbono, T. Ritzdorf and D. Schmauch, 'Factors affecting copper filling process within high aspect ratio deep vias for 3D chip stacking,' *Electronic Components and Technology Conference, 2006. Proceedings. 56th* 6 pp. (2006).

24. C. Song, Z. Wang and L. Liu, 'Bottom-up copper electroplating using transfer wafers for fabrication of high aspect-ratio through-silicon-vias,' *Microelectronic Engineering*, 87 [3] 510-513 (2010).

25. P. C. Andricacos, C. Uzoh, J. O. Dukovic, J. Horkans and H. Deligianni, 'Damascene copper electroplating for chip interconnections,' *IBM Journal of Research and Development*, 42 [5] 567-574 (1998).

26. C. Okoro, R. Labie, K. Vanstreels, A. Franquet, M. Gonzalez, B. Vandevelde, E. Beyne, D. Vandepitte and B. Verlinden, 'Impact of the electrodeposition chemistry used for TSV filling on the microstructural and thermo-mechanical response of Cu,' *Journal of Materials Science*, 46 [11] 3868-3882 (2011).

27. P. Taephaisitphongse, Y. Cao and A. C. West, 'Electrochemical and fill studies of a multicomponent additive package for copper deposition,' *J. Electrochem. Soc.*, 148 [7] C492-C497 (2001).

28. Myung-Won Jung, Young-Sik Song, Tae-Hong Yim and Jae-Ho Lee, 'Evaluation of additives and current mode on copper via filling,' *Electronic Components and Technology Conference (ECTC), 2011 IEEE 61st* 1908-1912 (2011).

29. S. S. West, G. Winther and D. J. Jensen, 'Analysis of Orientation Relations Between Deformed Grains and Recrystallization Nuclei,' *Metallurgical and Materials Transactions A*, 42 [5] 1400-1408 (2011).

30. R. Rosenberg, D. Edelstein, C. Hu and K. Rodbell, 'Copper metallization for high performance silicon technology,' *Annual review of materials science*, 30 [1] 229-262 (2000).

31. N. McCusker, H. Gamble and B. Armstrong, 'Surface electromigration in copper interconnects,' *Microelectronics Reliability*, 40 [1] 69-76 (2000).

32. E. Liniger, L. Gignac, C. Hu and S. Kaldor, 'In situ study of void growth kinetics in electroplated Cu lines,' *J. Appl. Phys.*, 92 [4] 1803-1810 (2002).

33. M. Meyer, M. Grafe, H. Engelmann, E. Langer and E. Zschech, 'Investigation of the influence of the local microstructure of copper interconnects on void formation and evolution during electromigration testing,' *Eighth International Workshop on Stress-Induced Phenomena in Metallization*, 817 [1] 175-184 (2006).

34. M. Meyer, M. Herrmann, E. Langer and E. Zschech, 'In situ SEM observation of electromigration phenomena in fully embedded copper interconnect structures,' *Microelectronic Engineering*, 64 [1] 375-382 (2002).

35. Z. Choi, R. Mönig and C. V. Thompson, 'Dependence of the electromigration flux on the crystallographic orientations of different grains in polycrystalline copper interconnects,' *Appl. Phys. Lett.*, 90 [24] (2007).

36. D. Xu, V. Sriram, V. Ozolins, J. Yang, K. N. Tu, G. R. Stafford, C. Beauchamp, I. Zienert, H. Geisler, P. Hofmann and E. Zschech, 'Nanotwin formation and its physical properties and effect on reliability of copper interconnects,' *Microelectronic Engineering*, 85 [10] 2155-2158 (2008).

37. K. Chen, W. Wu, C. Liao, L. Chen and K. N. Tu, 'Observation of Atomic Diffusion at Twin-Modified Grain Boundaries in Copper,' *Science*, 321 [5892] 1066-1069 (2008).

38. V. A. Lubarda, M. S. Schneider, D. H. Kalantar, B. A. Remington and M. A. Meyers, 'Void growth by dislocation emission,' *Acta Materialia*, 52 [6] 1397-1408 (2004).

39. E. Lin, L. Niu, H. Shi and Z. Duan, 'Molecular dynamics study on the nano-void growth and coalescence at grain boundary,' *Science China Physics, Mechanics and Astronomy*, 55 [1] 86-93 (2012).

40. L. Zhang, H. Zhou and S. Qu, 'Blocking effect of twin boundaries on partial dislocation emission from void surfaces,' *Nanoscale research letters*, 7 [1] 1-8 (2012).

41. S. Zhang, J. Zhou, L. Wang, Y. Wang and S. Dong, 'Effect of twin boundaries on nanovoid growth based on dislocation emission,' *Materials Science and Engineering: A*, 582 29-35 (2013).

42. C. Okoro, J. W. Lau, F. Golshany, K. Hummler and Y. S. Obeng, 'A Detailed Failure Analysis Examination of the Effect of Thermal Cycling on Cu TSV Reliability,' *Electron Devices, IEEE Transactions on*, 61 [1] 15-22 (2014).

43. Joohee Kim, Jonghyun Cho, Jun So Pak, Joungho Kim, Jong-Min Yook and Jun Chul Kim, 'High-frequency through-silicon Via (TSV) failure analysis,' *Electrical Performance of Electronic Packaging and Systems (EPEPS), 2011 IEEE 20th Conference on* 243-246 (2011).

44. C. Okoro, P. Kabos, J. Obrzut, K. Hummler and Y. S. Obeng, 'Accelerated Stress Test Assessment of Through-Silicon Via Using RF Signals,' *Electron Devices, IEEE Transactions on*, 60 [6] 2015-2021 (2013).

45. J. Marro, C. Okoro, Y. Obeng and K. Richardson, 'Defect and microstructural evolution in thermally cycled Cu through-silicon vias,' *Microelectronics Reliability* [0].

46. K. Zhao, C. Chen, Y. Shen and T. Lu, 'Molecular dynamics study on the nano-void growth in face-centered cubic single crystal copper,' *Computational Materials Science*, 46 [3] 749-754 (2009).

47. G. Green and J. Knott, 'The initiation and propagation of ductile fracture in low strength steels,' *Journal of Engineering Materials and Technology*, 98 [1] 37-46 (1976).

Appendix E:

Review on the Deformation of Copper

Plastic deformation is a major property of metals. Their ability to deform is utilized in many applications. The deformation of Cu and metals in general is discussed in detail throughout this paper. Dislocations and their contribution to plastic deformation are also reviewed, along with creep and fatigue of materials.

Elastic vs. Plastic Deformation

Elastic deformation is a reversible deformation in which bonds in the material are bent and deformed, but not broken. It is the region of stress-strain linear relationship as seen in uniaxial tensile tests (Figure E1). Strain that occurs in this region is not permanent.

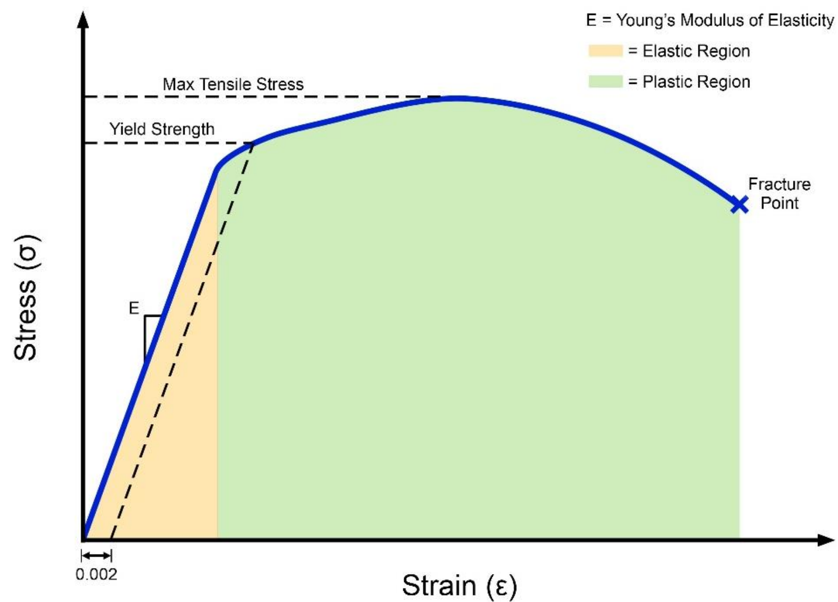

Figure E1: Stress-strain curve demonstrating the areas of elastic and plastic deformation.

Anything beyond the elastic deformation region is known as plastic deformation. Plastic deformation is an irreversible, permanent deformation. Bonds break and atoms move in the material during this type of deformation. During plastic deformation, slip and twinning occur. Slip is a uniform shift of atoms along a slip plane when a shear stress is applied. On the other hand, twinning is the rotation of atoms about a twin plane. Both processes are illustrated in Figure E2.

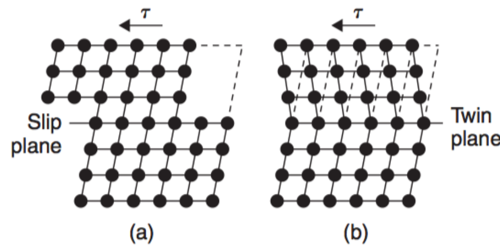

Figure E2: Plastic deformation occurs through slip (a) and twinning (b), taken from [1].

Face centered cubic (FCC) metals, such as copper, have 12 slip systems (sets of slip directions and planes) [1,2]. Slip occurs once the critical resolved shear stress (CRSS) has been surpassed in the slip direction along a slip plane. The CRSS is calculated through the following equation [2];

$$\tau_{CRSS} = \sigma \cos\varphi \cos\theta \qquad \text{(Eq. E1)}$$

where σ is an applied tensile stress, φ is the angle between the slip direction and applied stress, and θ is the angle separating the normal of the slip plane and the applied stress. These terms may be more easily understood from the illustration in Figure E3.

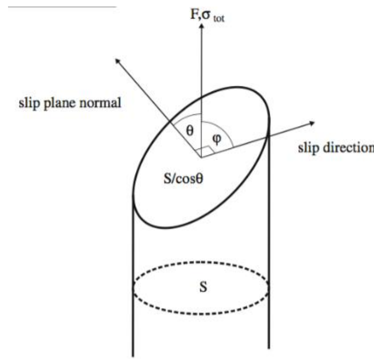

Figure E3: A slip system and its components, taken from [2].

Slip typically occurs in the direction and plane of the highest atomic packing, for FCC metals, like Cu, this is in the {111} planes along the <110> directions [1]. These slip systems occur through dislocation motion, which will be discussed in a later section.

While slip occurs at lower shear stresses, twinning is prominent in the higher shear stress regime [1]. Twins form due to stacking faults. In FCC metals, the ideal atomic packing sequence is ABCABCABC; however, a stacking fault occurs as the sequence is deserted. The sequence can then occur in reverse order until another inconsistency is generated. Twinning occurs by the movement of partial dislocations and these dislocations often form at the ends of stacking faults [1,2]. At high strain rates (~10^3/s) finely spaced twin lamellae structures are formed and the twin density has been shown to scale with strain rate [3,4].

Dislocations

Dislocations are two-dimensional or line defects in a material's atomic structure. There are two basic types of dislocations, edge and screw. Edge dislocations are defects where half a plane of atoms are "missing." Screw

dislocations are similar to skewing or shearing a half of a block of atoms. Both are visualized in Figure E4.

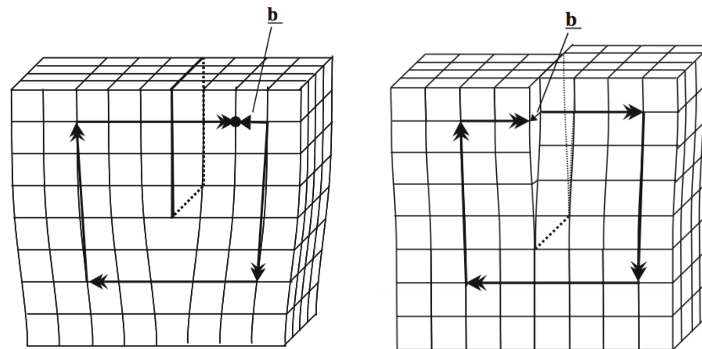

Figure E4: An edge dislocation (left) and screw dislocation (right), taken from [2].

In FCC metals with low stacking fault energies, such as Cu, dislocations often divide into two partial dislocations [1,5]. Since FCC metals have {111} slip planes, this is where dislocations typically reside and move [1]. Cu often contains geometrically necessary dislocations (GND) or excess dislocations, which help retain the shape or geometry of a material from anisotropic straining or plastic deformation [6]. The density of GNDs increase with plastic deformation and are typically located near grain boundaries instead of at the grain cores. Triple junctions are areas of high GND densities as well since stress build up is common in these areas. Furthermore, a higher GND density has been found at lower strains in smaller grains compared to larger grains [7].

Sources

Dislocation generation occurs from a few mechanisms. A Frank-Read source occurs as a dislocation line is pinned on either end. As a shear stress is

applied, the dislocation line begins to bow out. If the stress surpasses a critical shear stress the dislocation will loop around its pinned points. At this point, pure edge character is exhibited in several areas of the loop. Two edge dislocation characters, which have opposite signs are attracted to one another and finally annihilate creating a dislocation loop and leaving behind the original pinned dislocation line. This process may then repeat creating more dislocations [2]. Cross-slip is another source for dislocations but does not occur as readily in low stacking fault metals like Cu. It relies on a Frank-Read dislocation source and the cross-slip of screw dislocations onto numerous slip planes, connected by jogs, to generate new dislocations [1].

High dislocation densities have been observed in areas surrounding clusters of cavities and isolated creep induced voids [8]. The emission of dislocations as a mechanism of void growth at high strain rates (> ~10^9/s) may be the contributing factor here [9-12]. Furthermore, dislocation sources are typically found in or around grain boundaries. If the boundaries contain excess dislocations, they emit partial dislocation loops into the grains, where part of the loop remains in the grain boundary, where the dislocation will seek other dislocations to annihilate [13,14].

Movement

As mentioned earlier, plastic deformation is dependent on dislocation motion in the material and the movement of these dislocations causes stress relaxation in the system [15]. Thus, the mobility of dislocations is important to

better understand the stresses in materials and extent of plastic deformation due to these stresses. In single crystal Cu, dislocations must first be unlocked from their annealed position to move. A critical stress is necessary to unlock these dislocations and this marks the onset of plastic deformation [16]. Once dislocation movement is initiated, their velocity is influenced by the applied stress. Higher stresses translate to faster moving dislocations [17]. Furthermore, edge dislocations generally move much faster than screw dislocations [1]. Molecular dynamic simulations have also shown that dislocation velocity can determine the stacking fault widths [18].

Dislocation movement often leads to the annihilation if two dislocations of opposite signs come in contact [5]. This has been observed during recovery, in which dislocations meet in grain boundaries or sub-boundaries and annihilate [19]. Edge and screw dislocations do no annihilate using the same method. Once edge dislocations on the same slip plane have glided to one another, climb is required for annihilation to occur. Meanwhile, the cross-slip of two opposite signed screw dislocations is necessary for their annihilation [5,20].

Glide, Climb, and Cross-Slip

There are three basic means by which dislocations move about the atomic structure of a material (glide, climb, and cross-slip). Glide is the ability for a dislocation to move along a slip or glide plane from shear stresses. Climb, on the other hand, is the movement of the dislocation perpendicular to the glide plane. It requires the movement of a point defect (vacancy) [5]. Climb does not occur as

readily or fast in low stacking fault energy materials which can result in it being the rate limiting factor for some processes as will be discussed in the next section [21]. The last dislocation movement method is cross-slip. Cross-slip is the ability of a dislocation, particularly screw dislocations, to shift from one slip plane to another.

Grain Boundary Sliding

While the plastic deformation of polycrystalline Cu with grains coarser than 10 nm is dislocation mobility dependent, grain boundary sliding is the dominant mechanism with grains smaller than 10 nm [22]. Sliding, however, still occurs in larger grain sized materials. Grain boundary sliding is directed by the dislocation climb into grain boundaries from the dislocation pile-ups [23-25]. It is for this reason that sliding is grain boundary diffusion dependent. Dislocations often annihilate one another when traveling along the grain boundaries [1,2]. The stresses built up due to the pile-up of dislocations at the grain boundaries and triple junctions can lead to void formation in these areas [26].

Strengthening of Cu (Dislocation Interactions)

Typically, there are several strengthening mechanism in materials; most notable are work hardening, grain boundary strengthening, precipitate hardening, and solid solution strengthening. The focus of this paper is on pure Cu and since precipitate and solid solution strengthening do not fall in the scope of this paper, they will not be discussed. The strengthening of a material is its resistance to plastic deformation, which means higher activation stresses are required to cause

dislocation motion [1]. Equation E2 [1] clearly shows that strain rate is governed by the velocity of dislocations in a material;

$$\gamma = \rho b v \qquad \text{(Eq. E2)}$$

where γ is the strain rate, ρ is the number of dislocations, b is the change in length, and v is the velocity of the mobile dislocations.

Work Hardening

Work hardening is a strengthening mechanism in which plastic deformation is used to form a higher dislocation density in the material. These dislocations interact and can hinder each other from moving [1,16]. Thus, dislocation density improves yields stress by increasing the threshold stress for dislocation mobility (flow stress) [27]. This increase in flow stress is illustrated in equation E3 [1];

$$\tau = \frac{\alpha \mu b}{l} \qquad \text{(Eq. E3)}$$

where τ is the flow stress, α is a constant dictated by the Poisson ratio of the material, μ is the shear modulus, b is the burgers vector, and l is the average distance between two dislocations.

There are three distinct stages of work hardening (shown in Figure E5). First, dislocations are allowed to glide freely creating a slow rate of work hardening. The second stage is a rapid increase in work hardening rate due to dislocation pile-ups forming stresses. The work hardening rate then slows in the third and final stage of work hardening. This is the result of dislocation annihilation due to cross-slip [1].

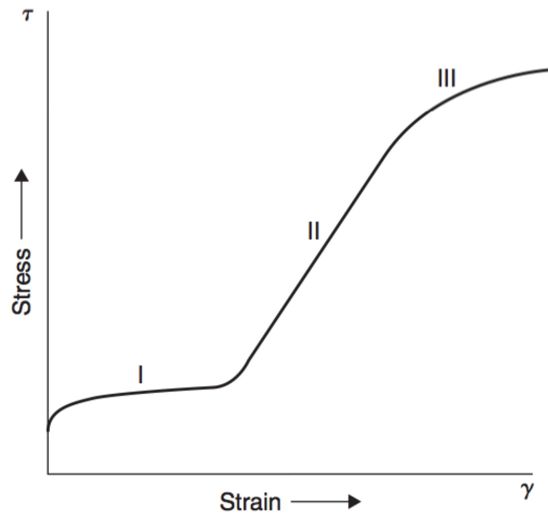

Figure E5: The three regimes of work hardening, taken from [1].

Experimentally, the interaction of dislocations in room temperature fatigued single crystal copper has been proven to prevent strain. The spread of clustered dislocations improves the resistance to strain-induced effects (deformation) [28]. When dislocations collide they can become entangled and produce walls or boundaries inside grains [8]. Wang *et al.* also documented this at low strain rates in Cu. They found "dislocation cells" or clusters between 200 nm and 1 μm in size formed, which later transformed into dislocation walls and became low angle grain boundaries, creating new grains [4].

Grain Boundary Strengthening

Grain boundary strengthening is the refinement of a material's microstructure, specifically grain size, to improve its strength. The Hall-Petch relationship shown in equation E4 [1] displays how yield stress is altered by a material's grain size;

$$\sigma_y = \sigma_i + \frac{k_y}{\sqrt{d}} \quad \text{(Eq. E4)}$$

where σ_y is the yield stress, σ_i is the flow stress or onset of dislocation motion, k_y is a material dependent strength constant, and d is the average grain size of the material. Since grain boundaries prevent the glide of dislocations, materials with smaller grain sizes have higher yield strength due to their larger grain boundary area. As a slip bands intersect with obstructions, like grain boundaries, the dislocations pile up creating stress concentrations, giving rise to a source in an adjacent grain, which will allow slip until another obstacle is reached [1,2]. This process is illustrated in Figure E6.

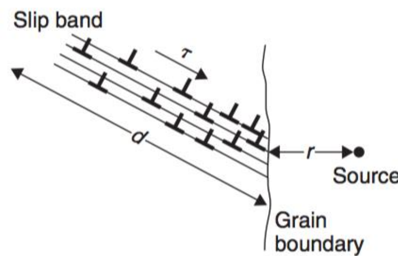

Figure E6: Diagram of dislocation pile up creating sources in neighboring grains, taken from [1].

Like grain boundaries, twin boundaries also contribute to the Hall-Petch relationship as they too prevent the movement of dislocations. Thus, coherent twin boundaries have high deformation stability and increased yield strength [10,29-35]. Furthermore, twin boundaries also emit dislocations creating higher ductility of the Cu along with the improved strength [32]. Smaller twin spacing not only means higher twin density for improved strength, but also prevents many dislocations from building up stress in the twin boundaries and thus a larger stress

is required for dislocations to form in adjacent grains/twins and continue slip [36,37]. The pile up, tangle, and creation of dislocation walls have been observed to form tilt boundaries and create new grains in Cu as shown in Figure E7 [4,25,38].

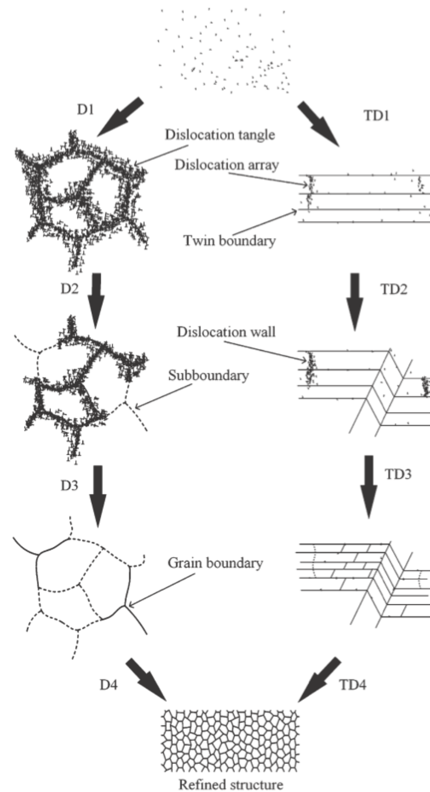

Figure E7: The process of dislocation arrangements creating sub-boundaries, grain boundaries, and new grains, taken from [38].

Creep

Creep is time-dependent plastic deformation, which occurs below the yield stress of the material and at elevated temperatures (typically above, but not limited to 0.4 T_m) [2]. There are two particular types of creep, Nabarro-Herring and Coble. Nabarro-Herring creep is the diffusion of atoms via bulk diffusion. Thus, this diffusion takes place in the grain cores. Coble creep occurs by grain boundary diffusion of atoms. Creep can also arise from glide and climb of dislocations in

what is known as power-law creep [24]. Climb is the primary mechanism here as climb allows dislocations to dodge and circumvent obstructions in the structure [1]. Deformation mechanism maps, such as the one for Cu in Figure E8, provide means for visualizing the temperatures and stresses at which the different deformation mechanisms occur in a material. The deformation map shows that Nabarro-Herring creep occurs at higher temperatures than Coble creep [1]. Furthermore, power law creep takes place at higher sheer stresses. Cai *et al.* studied creep in cold rolled Cu at $0.22T_m$ to $0.24T_m$, where T_m is the melting temperature of Cu (~1085 °C). Coble creep was the primary creep mechanism at these temperatures, with creep rate increasing with temperature, and the activation for creep was in the range of 0.72 eV to 0.82 eV [23,39]. This creep activation energy was found to increase linearly with stresses from temperatures between ~$0.46T_m$ to ~$0.72T_m$ [40].

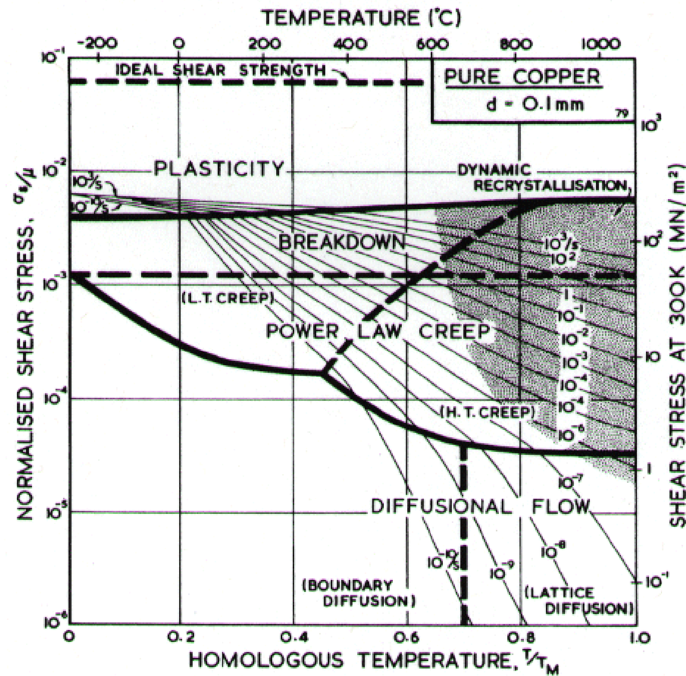

Figure E8: The deformation mechanism map for Cu, taken from [41].

Fatigue

Fatigue is plastic deformation due to the cyclic loading below yield stress of a material. Fatigue occurs in stages. Dislocations, first pile up and work hardening of the material occurs, followed by persistent slip band (PSB) formation, which then grow and become susceptible to crack formation and propagation within the bands [1]. Temperature apparently plays a large role in fatigue as a material's resistance to fatigue lowers at higher temperatures [1]. Materials are often prone to crack initiation in the slip bands during fatigue [42,43]. Fatigue has also been found to influence the microstructure of Cu. Detwinning has occurred in some nano-twinned Cu that have undergone fatigue stresses of 450 MPa [30]. Furthermore, grain orientation changes have also been observed due to fatigue plastic deformation [44].

Conclusions

Plastic deformation in Cu was discussed in detail throughout this paper. Plastic deformation is closely tied to dislocations and their movement. Frank-Read along with other dislocation sources create high dislocation densities during plastic deformation, which lead to strengthening mechanisms, such as work hardening and grain boundary strengthening. These strengthening mechanisms occur through the impediment of dislocation motion. Lastly, specific plastic deformation instances (creep and fatigue) were briefly discussed.

References

1. R. E. Smallman and A. Ngan, 'Physical metallurgy and advanced materials'. Butterworth-Heinemann 2011.

2. E. J. Mittemeijer, 'Fundamentals of materials science: the microstructure–property relationship using metals as model systems'. Springer 2010.

3. C. Saldana, T. Murthy, M. Shankar, E. Stach and S. Chandrasekar, 'Stabilizing nanostructured materials by coherent nanotwins and their grain boundary triple junction drag,' *Appl. Phys. Lett.*, 94 [2] 021910 (2009).

4. K. Wang, N. Tao, G. Liu, J. Lu and K. Lu, 'Plastic strain-induced grain refinement at the nanometer scale in copper,' *Acta Materialia*, 54 [19] 5281-5291 (2006).

5. T. Vegge and K. W. Jacobsen, 'Atomistic simulations of dislocation processes in copper,' *Journal of Physics: Condensed Matter*, 14 [11] 2929 (2002).

6. H. Gao and Y. Huang, 'Geometrically necessary dislocation and size-dependent plasticity,' *Scr. Mater.*, 48 [2] 113-118 (2003).

7. J. Jiang, T. B. Britton and A. J. Wilkinson, 'Evolution of dislocation density distributions in copper during tensile deformation,' *Acta Materialia*, 61 [19] 7227-7239 (2013).

8. R. Page and J. R. Weertman, 'HVEM observations of grain boundary voids in high purity copper,' *Acta Metallurgica*, 29 [3] 527-535 (1981).

9. E. Lin, L. Niu, H. Shi and Z. Duan, 'Molecular dynamics study on the nano-void growth and coalescence at grain boundary,' *Science China Physics, Mechanics and Astronomy*, 55 [1] 86-93 (2012).

10. L. Zhang, H. Zhou and S. Qu, 'Blocking effect of twin boundaries on partial dislocation emission from void surfaces,' *Nanoscale research letters*, 7 [1] 1-8 (2012).

11. V. A. Lubarda, M. S. Schneider, D. H. Kalantar, B. A. Remington and M. A. Meyers, 'Void growth by dislocation emission,' *Acta Materialia*, 52 [6] 1397-1408 (2004).

12. R. E. Rudd and J. F. Belak, 'Void nucleation and associated plasticity in dynamic fracture of polycrystalline copper: an atomistic simulation,' *Computational materials science*, 24 [1] 148-153 (2002).

13. J. C. Li, 'Mechanical grain growth in nanocrystalline copper,' *Phys. Rev. Lett.*, 96 [21] 215506 (2006).

14. M. A. Tschopp and D. L. McDowell, 'Grain boundary dislocation sources in nanocrystalline copper,' *Scr. Mater.*, 58 [4] 299-302 (2008).

15. R. Huang, D. Gan and P. S. Ho, 'Isothermal stress relaxation in electroplated Cu films. II. Kinetic modeling,' *J. Appl. Phys.*, 97 [10] (2005).

16. K. Marukawa, 'Dislocation motion in copper single crystals,' *Journal of the Physical Society of Japan*, 22 [2] 499-510 (1967).

17. W. F. Greenman, T. Vreeland Jr and D. S. Wood, 'Dislocation Mobility in Copper,' *J. Appl. Phys.*, 38 [9] 3595-3603 (1967).

18. H. Tsuzuki, P. S. Branicio and J. P. Rino, 'Molecular dynamics simulation of fast dislocations in copper,' *Acta Materialia*, 57 [6] 1843-1855 (2009).

19. M. J. Luton, R. A. Petkovic and J. J. Jonas, 'Kinetics of recovery and recrystallization in polycrystalline copper,' *Acta Metallurgica*, 28 [6] 729-743 (1980).

20. J. W. Steeds, 'Dislocation Arrangement in Copper Single Crystals as a Function of Strain,' *Proceedings of the Royal Society of London.Series A, Mathematical and Physical Sciences*, 292 [1430] 343-373 (1966).

21. R. W. Cahn, 'Chapter 28 - Recovery and Recrystallization'; pp. 2399-2500 in Physical Metallurgy (Fourth Edition). Edited by R. W. Cahn and P. Haasen (Eds.). North-Holland, Oxford, 1996.

22. J. Schiøtz, 'Atomic-scale modeling of plastic deformation of nanocrystalline copper,' *Scr. Mater.*, 51 [8] 837-841 (2004).

23. B. Cai, Q. P. Kong, P. Cui, L. Lu and K. Lu, 'Creep behavior of cold-rolled nanocrystalline pure copper,' *Scr. Mater.*, 45 [12] 1407-1413 (2001).

24. M. E. Kassner, 'Fundamentals of creep in metals and alloys'. Elsevier 2008.

25. B. Chalmers, J. W. Christian and T. B. Massalski, 'Grain-boundary sliding,' *Progress in Materials Science*, 16 179-217 (1972).

26. L. Wang, J. Zhou, S. Zhang, Y. Liu and S. Dong, 'Effects of accommodated grain boundary sliding on triple junction nanovoid nucleation in nanocrystalline materials,' *Mech. Mater.*, 71 [0] 10-20 (2014).

27. M. Hordon, 'Dislocation density and flow stress of copper,' *Acta Metallurgica*, 10 [11] 999-1005 (1962).

28. J. Dralla and J. Bilello, 'Mechanical Hysteresis and Dislocation- Dislocation Interactions in Copper Crystals,' *J. Appl. Phys.*, 41 [6] 2340-2347 (1970).

29. J. Wang, N. Li, O. Anderoglu, X. Zhang, A. Misra, J. Y. Huang and J. P. Hirth, 'Detwinning mechanisms for growth twins in face-centered cubic metals,' *Acta Materialia*, 58 [6] 2262-2270 (2010).

30. C. J. Shute, B. D. Myers, S. Xie, S. -. Li, T. W. Barbee Jr., A. M. Hodge and J. R. Weertman, 'Detwinning, damage and crack initiation during cyclic loading of Cu samples containing aligned nanotwins,' *Acta Materialia*, 59 [11] 4569-4577 (2011).

31. L. Lu, X. Chen, X. Huang and K. Lu, 'Revealing the Maximum Strength in Nanotwinned Copper,' *Science*, 323 [5914] 607-610 (2009).

32. K. Lu, L. Lu and S. Suresh, 'Strengthening materials by engineering coherent internal boundaries at the nanoscale,' *Science*, 324 [5925] 349-352 (2009).

33. Y. Xiang, T. Y. Tsui and J. J. Vlassak, 'The mechanical properties of freestanding electroplated Cu thin films,' *J. Mater. Res.*, 21 [06] 1607-1618 (2006).

34. N. Li, J. Wang, A. Misra, X. Zhang, J. Huang and J. Hirth, 'Twinning dislocation multiplication at a coherent twin boundary,' *Acta Materialia*, 59 [15] 5989-5996 (2011).

35. L. Lu, Y. Shen, X. Chen, L. Qian and K. Lu, 'Ultrahigh strength and high electrical conductivity in copper,' *Science*, 304 [5669] 422-426 (2004).

36. Y. Shen, L. Lu, Q. Lu, Z. Jin and K. Lu, 'Tensile properties of copper with nano-scale twins,' *Scr. Mater.*, 52 [10] 989-994 (2005).

37. X. Zhang, A. Misra, H. Wang, T. Shen, M. Nastasi, T. Mitchell, J. Hirth, R. Hoagland and J. Embury, 'Enhanced hardening in Cu/330 stainless steel multilayers by nanoscale twinning,' *Acta Materialia*, 52 [4] 995-1002 (2004).

38. G. Wang, Z. Jiang, J. Lian and Q. Jiang, 'The grain refinement mechanism of electrodeposited copper,' *J. Mater. Res.*, 24 [10] 3226-3236 (2009).

39. B. Cai, Q. P. Kong, L. Lu and K. Lu, 'Low temperature creep of nanocrystalline pure copper,' *Materials Science and Engineering: A*, 286 [1] 188-192 (2000).

40. S. V. Raj and T. G. Langdon, 'Creep behavior of copper at intermediate temperatures—I. Mechanical characteristics,' *Acta Metallurgica*, 37 [3] 843-852 (1989).

41. H. J. Frost and M. F. Ashby, 'Deformation mechanism maps: the plasticity and creep of metals and ceramics'. Pergamon press 1982.

42. L. Li, P. Zhang, Z. Zhang and Z. Zhang, 'Effect of crystallographic orientation and grain boundary character on fatigue cracking behaviors of coaxial copper bicrystals,' *Acta Materialia*, 61 [2] 425-438 (2013).

43. Z. Zhang, Z. Wang and Z. Sun, 'Evolution and microstructural characteristics of deformation bands in fatigued copper single crystals,' *Acta materialia*, 49 [15] 2875-2886 (2001).

44. A. Mishra, B. K. Kad, F. Gregori and M. A. Meyers, 'Microstructural evolution in copper subjected to severe plastic deformation: Experiments and analysis,' *Acta Materialia*, 55 [1] 13-28 (2007).

Appendix F:

Review of Copper Twinning

Twins are grains that mirror one another in a material's microstructure. Copper (Cu) has the ability to twin, especially after annealing, but deformation twins may also form given a sufficient mechanical load is imparted. Recently, there has been a resurgence of work on nano-twinned Cu for its excellent mechanical strength and low resistivity, which may lend itself to applications in microelectronics [1,2]. Characterizing twins within a material's microstructure can indicate how the microstructure will behave, predict material properties, and determine the mechanical history of the material. This review article will focus on twinning specifically in Cu and how twins affect the Cu's material properties as well as evolution of voids.

Coherent vs. Incoherent Twins

As mentioned earlier, twins are two grains that have mirrored atomic structures across a boundary, known as a twin boundary (TB). These TBs are specific types of high angle grain boundaries. A coherent twin occurs when the twin plane and TB are superimposed, meaning atoms line up across the boundary as shown in Figure F1a. In an FCC metal, like Cu, coherent twins are {111} grains that have been twisted 60° or 180° about the <111> direction. To achieve a coherent twin with pure tilt, a tilt angle of 70.53° about the <110> is necessary [3,4]. Due to this atomic alignment, coherent twin boundaries have much lower energy than boundaries of incoherent twins, twins that have an angle, ϕ, of offset between

the twin plane and TB. An illustration of incoherent twins is shown in Figure F1b. Specifically, coherent twin boundaries in Cu have an energy of ~21 mJ/m^2, much lower than that of incoherent twin boundaries and high angle grain boundaries, ~498 mJ/m^2 and ~623 mJ/m^2 respectively [3,5].

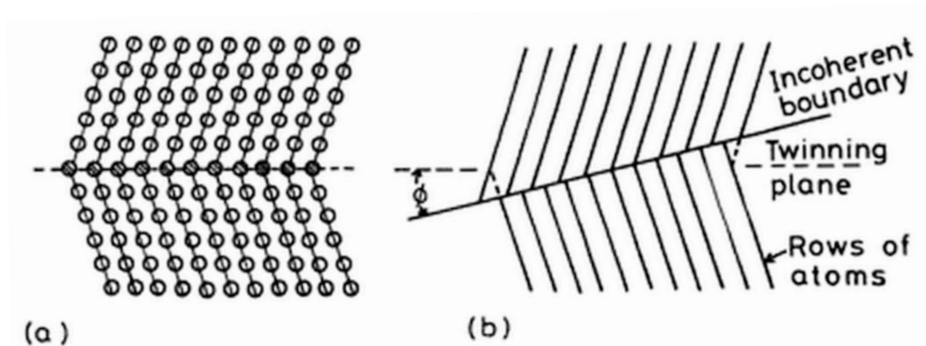

Figure F1: An illustration of the difference between coherent twins (a) and incoherent twins (b), taken from [3].

Twin Formation

Twins form from a deviation in stacking sequence. FCC materials have a continuous ABCABCABC stacking sequence, but once this sequence is abandoned, a TB is formed. The sequence then continues in reverse order until another error in the sequence is made, closing out the twin with a second TB [6,7]. Cu's low coherent TB energy, mentioned above, shows that twins can readily form [6]. There are two types of twins, those caused by mechanical stresses (deformation twins) and twins that form during grain coarsening (annealing twins). Both are discussed in detail in the following sections.

Deformation Twins

While twinning is not as prevalent in FCC metals, like Cu, due to its

competition with slip, it does occur at higher shear stresses [6]. The difference between the two processes are shown in Figure F2. Slip refers to the ability of an atomic structure to shift uniformly along a slip plane due to shear. On the other hand, twinning is the skewing of the atoms along a plane (boundary). The twinning mechanism is related to partial dislocation movement, which is why greater shear required for activation; however, decreasing the temperature during deformation increases the stress activation for slip and twinning will become favorable [6]. Li et al. proposed that deformation twins were not observed in nano-twinned Cu from nanoindention due to the highly structured coherent TBs, which contained a minimal amount of dislocations and thus lacked nucleation sites for twinning [8]. Yet, deformation twin formation has been observed in non-twinned copper at high strain rates (~10^3/s) [9]. Increasing the strain rate also caused more finely spaced twin lamella structures to form, resulting in higher twin densities [9,10].

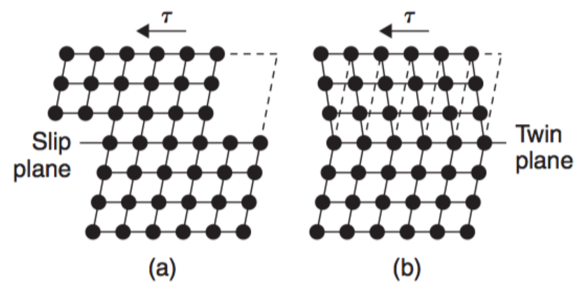

Figure F2: Comparison between slip (a) and twinning (b), taken from [6].

Annealing and Growth Twins

Unlike, deformation twins, annealing twins are quite common in FCC metals [6,11-13]. Cu is a low stacking fault energy material, which is prone to lamellar

twin formation [14,15]. One possible mechanism of annealing twin formation is shown in Figure F3. As grains grow and new grains come in contact, a twin can nucleate from a triple junction and lower the overall boundary energy between the three grains [6]. Miura et al. found a large majority (>80%) of grains nucleated at triple junctions during recrystallization of Cu were twins [16,17]. The formation of annealing twins have also been observed following the stagnation of grain growth during recrystallization, resulting in the resumption of grain coarsening [11].

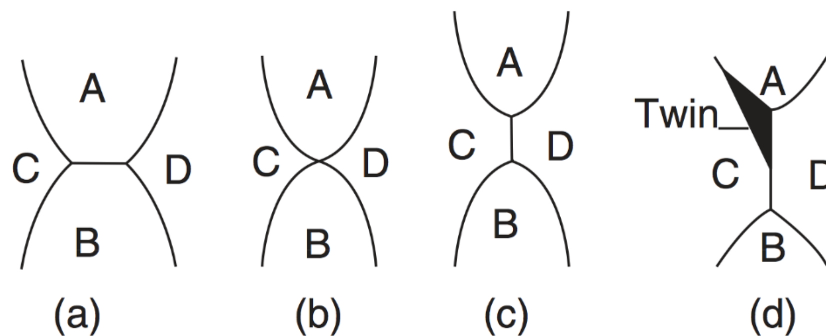

Figure F3: Proposed annealing twin nucleation process, taken from [6].

Furthermore, rapid grain growth promotes the formation of twins in Cu [18], since twins are thought to nucleate behind migrating grain boundaries [16,17,19]. Thus, increased twin fractions in Cu's microstructure have been observed by Lui et al. and Kohama et al. to scale with coarser grain sizes [18,20].

For pulsed electrochemically deposited Cu, the deposition parameters have shown some relationships to twinning. For example, higher peak current densities produce more densely packed lamellar structured twins with small thicknesses during deposition [21]. On the other hand, higher additive concentrations and

lower current densities have resulted in higher strains, resulting in increased amounts of growth twins and dislocations after deposition [22]. The higher additive concentration also lead to increased twinning of {111} and {112} oriented grains [22]. Meanwhile, in a different study by Lui et al. twins were also shown to prefer formation in grains of the <110> out of plane direction [20].

Annealing twins also may disappear at high temperatures (above 400C) once recrystallization [23] or even abnormal grain growth [24] is complete. This, along with the shortening of twins during annealing, has been attributed to the migration of incoherent TB, which migrate easily due to their high interfacial energy [23].

Effect on Material Properties

Nano-twinned Cu (shown in Figure F4) is becoming an attractive material for microelectronics since twin boundaries act like grain boundaries in hindering dislocation movement, yet don't interfere greatly with electron propagation. Furthermore, nano-twinned Cu has high thermal stability. The impact of twins on Cu's material properties, such as orientation, mechanical strength, and electrical properties will be discussed in this section.

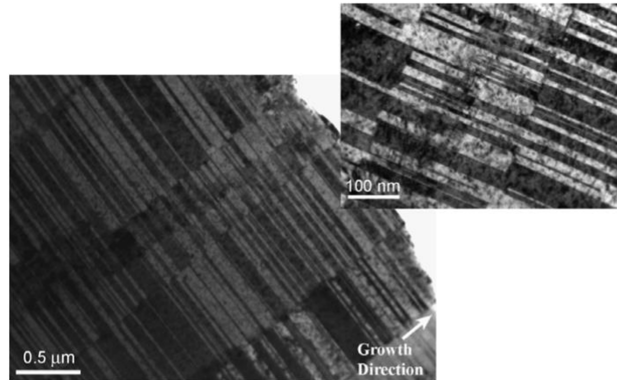

Figure F4: Example of nano-twinned Cu grains, taken from [25].

Recrystallization and Grain Growth

Twins don't build up stress or strain as readily as other types of grain boundaries. Since nucleation of recrystallized grains often occurs at triple junctions (see Figure F5), the presence of a twin boundary lowers the probability of nucleation occurring at that site [16]. Specifically, there is a 25% chance that a recrystallized Cu grain will nucleate at a triple junction containing a TB. This is much lower than the 40% probability of a grain nucleating without the presence of a TB [17].

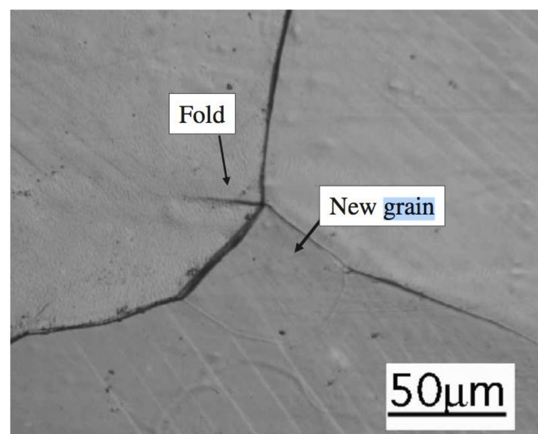

Figure F5: The formation of a recrystallized grain at a triple junction, taken from [16].

Twin boundary's effect on grain growth is very dependent on which types of

twins (coherent or incoherent) are prominent in the microstructure. Coherent TB are low energy boundaries, making them much more thermally stable than incoherent TB and resistant to grain growth [26,27]. Nano-twinned Cu have demonstrated grain size retention up to 800 °C [27] and can slow down grain boundary and triple junction migration rates [9]. On the other hand, incoherent TB have much higher mobility due to their higher interfacial energy (~480 erg/cm^2 [28]) over coherent TBs (~21 erg.cm^2 [29]) [30]. Thus, strain-induced grain growth has been observed in nantwinned copper from incoherent TB mobility and detwinning [30].

Lastly, Wang et al. observed a phenomenon where twin lamellar structures can lead to grain refinement in Cu microstructures [22]. When growth twins form simultaneously in perpendicular directions the paths of their boundaries will eventually intersect, creating a new grain. Alternatively, dislocations can pile up creating dislocation walls that lie perpendicular to the twin lamellae, also forming a new grain. In both cases, dislocations later become absorbed by the twin boundaries causing different energy distributions along the boundary and curvature of the boundaries. [22].

Orientation

There are two conflicting results when it comes to the affects of twinning on Cu texture. First, strong {111} textures have been observed in highly coherent twinned Cu, with lower amounts of coherent twins having a random texture [15,26]. However, there are studies that show multiple twinning results in randomly oriented

textures of Cu films from previously (111) textured films [22,31].

Mechanical Properties

The mechanical properties of Cu can be enhanced by introducing nano-twins, since TB, like grain boundaries, slow down the migration of dislocations. Highly nano-twinned Cu has much improved hardness values (between 2.4 and 1.6 GPa) over bulk Cu (between 1 and 1.2 GPa) [32]. Furthermore, nano-twinned Cu retained their hardness values much better than ultra fine grained Cu after fatigue stresses up to 450 MPa [25]. However, the high fatigue stresses were shown to cause some detwinning in the Cu [25].

The tensile strength of nano-twinned Cu is an order of magnitude higher than coarse grained copper [1]. Lu et al. found that increasing the twin spacing increases the ultimate tensile strength of the Cu, however decreases the ductility [2]. Nano-twinned Cu with an average twin spacing of 15 nm showed the highest yield strength, with smaller spacings dropping the yield strength below that of ultrafine grained Cu [2].

Electrical Properties

While nano-twinned Cu has superior mechanical properties, the large amount of TB do not appear to be too detrimental to electrical properties. For instance, nano-twinned copper had similar values for electrical conductivity and resistivity as bulk, coarse grained copper [1,32]. The high grain boundary area in ultrafine grained Cu resulted in an electrical conductivity two orders of magnitude

larger than that of nano-twinned and bulk Cu [1]. The reason for this behavior is the low electrical resistivity coefficient of coherent twin boundaries, an order of magnitude lower than high angle grain boundaries [33].

Electromigration

Electromigration is the atomic diffusion in a material caused by the momentum of electron flow. Void nucleation and growth from increased stress imparted during electromigration often leads to failure in Cu interconnects [34]. Nano-twinned Cu has been shown to have good electromigration resistance [35,36]. It is proposed that triple junctions between coherent twin boundaries and a grain boundaries slow down the Cu atomic diffusion during electromigration [35].

Effect on Voids

Voids are typically formed in Cu to dissipate stresses over larger areas [37]. They can act as scattering centers for electronic signal propagation and thus their behavior with respect to twinning is important [38]. Voids can nucleate at twin interfaces [37], especially incoherent {322} twin interfaces, which have high interfacial energies compared to {111} twins [39]. Furthermore, {322} twin boundaries are favorable diffusion paths for voids/vacancies [40]. On the other hand, coherent twin boundaries have such low interfacial energy that defects are not likely to occur as readily [41].

Voids grow through a dislocation emission mechanism. Molecular dynamic simulations have been performed on these systems and found that twin

boundaries hinder the movement of partial dislocations and the emission from the void surface, which could result in slowed or hindered void growth [42,43]. Due to the buildup of stresses at void surfaces, molecular dynamic models also predict twin bands to form at void surfaces [44]. While twins can provide areas for void nucleation, twins are thought to inhibit the growth of voids.

Conclusion

Twins are atomically mirrored grains. In copper, twins typically nucleate at triple junctions during recrystallization or grain growth. They can have a profound affect on the properties of Cu. Their high degree of thermal stability can impede grain growth, while helping to retain mechanical properties. Nano-twinned Cu meshes high mechanical strength, low electrical resistivity, and high electromigration resistance, making it a prime candidate for applications in microelectronics. Lastly, twins interfere with the dislocation emission of voids and may serve to hinder void growth.

References

1. L. Lu, Y. Shen, X. Chen, L. Qian and K. Lu, 'Ultrahigh strength and high electrical conductivity in copper,' *Science*, 304 [5669] 422-426 (2004).

2. L. Lu, X. Chen, X. Huang and K. Lu, 'Revealing the Maximum Strength in Nanotwinned Copper,' *Science*, 323 [5914] 607-610 (2009).

3. D. A. Porter and K. E. Easterling, 'Phase Transformations in Metals and Alloys, (Revised Reprint)'. CRC press 1992.

4. J. Brown and N. Ghoniem, 'Structure and motion of junctions between coherent and incoherent twin boundaries in copper,' *Acta Materialia*, 57 [15] 4454-4462 (2009).

5. L. E. Murr, 'Interfacial phenomena in metals and alloys'. Addison-Wesley Publishing Company, United States, 1975.

6. R. E. Smallman and A. Ngan, 'Physical metallurgy and advanced materials'. Butterworth-Heinemann 2011.

7. E. Mittemeijer, 'Recovery, Recrystallization and Grain Growth'; pp. 463-496. Springer Berlin Heidelberg 2011.

8. N. Li, J. Wang, A. Misra, X. Zhang, J. Huang and J. Hirth, 'Twinning dislocation multiplication at a coherent twin boundary,' *Acta Materialia*, 59 [15] 5989-5996 (2011).

9. C. Saldana, T. Murthy, M. Shankar, E. Stach and S. Chandrasekar, 'Stabilizing nanostructured materials by coherent nanotwins and their grain boundary triple junction drag,' *Appl. Phys. Lett.*, 94 [2] 021910 (2009).

10. K. Wang, N. Tao, G. Liu, J. Lu and K. Lu, 'Plastic strain-induced grain refinement at the nanometer scale in copper,' *Acta Materialia*, 54 [19] 5281-5291 (2006).

11. D. Field, L. Bradford, M. Nowell and T. Lillo, 'The role of annealing twins during recrystallization of Cu,' *Acta materialia*, 55 [12] 4233-4241 (2007).

12. W. G. Burgers, J. C. Meijs and T. J. Tiedema, 'Frequency of annealing twins in copper crystals grown by recrystallization,' *Acta Metallurgica*, 1 [1] 75-78 (1953).

13. H. Wendrock, W. Brueckner, M. Hecker, T. Koetter and H. Schloerb, 'Room temperature grain growth in electroplated copper thin films,' *Microelectronics Reliability*, 40 [8] 1301-1304 (2000).

14. J. Bystrzycki, K. Kurzydłowski and W. Przetakiewicz, 'On the geometry of twin boundaries and their contribution to the strengthening and recovery of FCC polycrystals,' *Materials Science and Engineering: A*, 225 [1] 188-195 (1997).

15. E. Shinada, T. Nagoshi, T. M. Chang and M. Sone, 'Crystallographic study on self-annealing of electroplated copper at room temperature,' *Materials Science in Semiconductor Processing*, 16 [3] 633-639 (2013).

16. H. Miura *, T. Sakai, S. Andiarwanto and J. J. Jonas, 'Nucleation of dynamic recrystallization at triple junctions in polycrystalline copper,' *Philosophical Magazine*, 85 [23] 2653-2669 (2005).

17. H. Miura, S. Andiarwanto, K. Sato and T. Sakai, 'Preferential dynamic nucleation at triple junction in copper tricrystal during high-temperature deformation,' *Materials Transactions*, 43 [3] 494-500 (2002).

18. K. Kohama, K. Ito, T. Matsumoto, Y. Shirai and M. Murakami, 'Role of Cu film texture in grain growth correlated with twin boundary formation,' *Acta Materialia*, 60 [2] 588-595 (2012).

19. S. Mahajan, C. Pande, M. Imam and B. Rath, 'Formation of annealing twins in fcc crystals,' *Acta materialia*, 45 [6] 2633-2638 (1997).

20. G. Lui, D. Chen and J. Kuo, 'EBSD characterization of twinned copper using pulsed electrodeposition,' *J. Phys. D*, 42 [21] 215410 (2009).

21. B. Cui, K. Han, Y. Xin, D. Waryoba and A. Mbaruku, 'Highly textured and twinned Cu films fabricated by pulsed electrodeposition,' *Acta materialia*, 55 [13] 4429-4438 (2007).

22. G. Wang, Z. Jiang, J. Lian and Q. Jiang, 'The grain refinement mechanism of electrodeposited copper,' *J. Mater. Res.*, 24 [10] 3226-3236 (2009).

23. F. Brisset, A. Helbert and T. Baudin, 'In Situ Electron Backscatter Diffraction Investigation of Recrystallization in a Copper Wire,' *Microscopy and Microanalysis*, 19 [04] 969-977 (2013).

24. J. Brons and G. Thompson, 'A comparison of grain boundary evolution during grain growth in fcc metals,' *Acta Materialia*, 61 [11] 3936-3944 (2013).

25. C. Shute, B. Myers, S. Xie, S. Li, T. Barbee Jr, A. Hodge and J. Weertman, 'Detwinning, damage and crack initiation during cyclic loading of Cu samples containing aligned nanotwins,' *Acta Materialia*, 59 [11] 4569-4577 (2011).

26. Y. Zhao, T. A. Furnish, M. E. Kassner and A. M. Hodge, 'Thermal stability of highly nanotwinned copper: The role of grain boundaries and texture,' *J. Mater. Res.*, 27 [24] 3049-3057 (2012).

27. O. Anderoglu, A. Misra, H. Wang and X. Zhang, 'Thermal stability of sputtered Cu films with nanoscale growth twins,' *J. Appl. Phys.*, 103 [9] 094322 (2008).

28. R. Fullman, 'Crystallography and Interfacial Free Energy of Noncoherent Twin Boundaries in Copper,' *J. Appl. Phys.*, 22 [4] 456-460 (1951).

29. R. Fullman, 'Interfacial Free Energy of Coherent Twin Boundaries in Copper,' *J. Appl. Phys.*, 22 [4] 448-455 (1951).

30. J. Brons, J. Hardwick, H. Padilla II, K. Hattar, G. Thompson and B. Boyce, 'The role of copper twin boundaries in cryogenic indentation-induced grain growth,' *Materials Science and Engineering: A*, 592 182-188 (2014).

31. M. Perez-Prado and J. Vlassak, 'Microstructural evolution in electroplated Cu thin films,' *Scr. Mater.*, 47 [12] 817-823 (2002).

32. X. Meng- Burany, 'Analysis of Electroplated Films Using Dual- Beam FIB/SEM and TEM Techniques,' *Modern Electroplating, Fifth Edition* 637-663 (2010).

33. O. Anderoglu, A. Misra, F. Ronning, H. Wang and X. Zhang, 'Significant enhancement of the strength-to-resistivity ratio by nanotwins in epitaxial Cu films,' *J. Appl. Phys.*, 106 [2] 024313 (2009).

34. Z. Choi, R. Mönig and C. V. Thompson, 'Dependence of the electromigration flux on the crystallographic orientations of different grains in polycrystalline copper interconnects,' *Appl. Phys. Lett.*, 90 [24] (2007).

35. K. Chen, W. Wu, C. Liao, L. Chen and K. N. Tu, 'Observation of Atomic Diffusion at Twin-Modified Grain Boundaries in Copper,' *Science*, 321 [5892] 1066-1069 (2008).

36. D. Xu, V. Sriram, V. Ozolins, J. Yang, K. N. Tu, G. R. Stafford, C. Beauchamp, I. Zienert, H. Geisler, P. Hofmann and E. Zschech, 'Nanotwin formation and its physical properties and effect on reliability of copper interconnects,' *Microelectronic Engineering*, 85 [10] 2155-2158 (2008).

37. H. Shin, B. Kim, J. Kim, S. Hwang, A. Budiman, H. Son, K. Byun, N. Tamura, M. Kunz, D. Kim and Y. Joo, 'Microstructure Evolution and Defect Formation in Cu Through-Silicon Vias (TSVs) During Thermal Annealing,' *Journal of Electronic Materials*, 41 [4] 712-719 (2012).

38. C. Okoro, P. Kabos, J. Obrzut, K. Hummler and Y. S. Obeng, 'Accelerated Stress Test Assessment of Through-Silicon Via Using RF Signals,' *Electron Devices, IEEE Transactions on*, 60 [6] 2015-2021 (2013).

39. A. Sekiguchi, J. Koike and K. Maruyama, 'Microstructural influences on stress migration in electroplated Cu metallization,' *Appl. Phys. Lett.*, 83 [10] 1962-1964 (2003).

40. A. Sekiguchi, J. Koike, S. Kamiya, M. Saka and K. Maruyama, 'Void formation by thermal stress concentration at twin interfaces in Cu thin films,' *Appl. Phys. Lett.*, 79 [9] 1264-1266 (2001).

41. L. Li, P. Zhang, Z. Zhang and Z. Zhang, 'Effect of crystallographic orientation and grain boundary character on fatigue cracking behaviors of coaxial copper bicrystals,' *Acta Materialia*, 61 [2] 425-438 (2013).

42. L. Zhang, H. Zhou and S. Qu, 'Blocking effect of twin boundaries on partial dislocation emission from void surfaces,' *Nanoscale research letters*, 7 [1] 1-8 (2012).

43. S. Zhang, J. Zhou, L. Wang, Y. Wang and S. Dong, 'Effect of twin boundaries on nanovoid growth based on dislocation emission,' *Materials Science and Engineering: A*, 582 29-35 (2013).

44. E. Lin, L. Niu, H. Shi and Z. Duan, 'Molecular dynamics study on the nano-void growth and coalescence at grain boundary,' *Science China Physics, Mechanics and Astronomy*, 55 [1] 86-93 (2012).

Appendix G:

Review of Copper Grain Growth

Copper (Cu) has been widely accepted as the material of choice for microelectronic interconnects since it replaced aluminum (Al) for its lower resistance [1]. Secondary processes, such as recovery, recrystallization, and grain growth, allow manipulation of the Cu microstructure, which has a significant impact on the metal's properties, such as electrical and mechanical properties. For instance, copper has lower resistivity and higher mechanical strength (hardness) as grain size decreases, since there is higher grain boundary area, which impedes electrons and dislocations from moving [2-5]. Recovery, recrystallization, and grain growth occur sequentially to minimize excess free energy in the system. The physical configuration of the material (bulk vs. thin film) can determine the grain coarsening behavior, while other material properties, such as grain orientations, impurity levels, and stress will also play a role in this process. This article will review the mechanisms of and circumstances that influence grain growth in copper.

Recovery

Recovery is the process of restoring a deformed material by dislocation movement, resulting reduction of overall free energy. Dislocation movement can occur by dislocation glide, or the shift of a dislocation along a slip plane, and dislocation climb, which is migration of the dislocation normal to the slip plane [6]. There are three primary driving forces for recovery. A reduction in the length of

curved dislocations will lower the energy of the dislocation. The absorption of vacancies during dislocation climb will decrease the overall system energy as well. Lastly is the reduction of strain energy via dislocation annihilation, incorporation into a grain boundary, or rearrangement of dislocations within a grain [6,7]. Annihilation of two dislocations, sharing a glide plane, can occur upon collision; if they are oppositely oriented [6,7]. Luton et al. discovered there are two distinct phases during recovery in copper. First is the migration of dislocations to sub-boundaries within a grain, followed by the annihilation of the dislocations [8]. Furthermore, recovery is thermally activated and rate dependent on temperature [9]. The degree of recovery also correlates to holding temperature and extent of strain in the material [8].

Recrystallization

Recovery is succeeded by recrystallization, the nucleation and growth of new grains in a deformed material's microstructure. Unlike recovery, recrystallization incorporates the migration of high angle grain boundaries, however, it too is driven by the relaxation of strain energy [7]. Thus, the amount of recrystallizations is dependent on temperature and strain imparted on the material [8]. Microstructural evolution due to recrystallization has a profound effect on material properties as will be discussed in the following sections.

Recrystallization Activation

For a material to undergo recrystallization, a sufficient amount of

deformation (or excess strain energy) must be exerted. The degree of deformation will influence the rate of recrystallization at a given temperature and time [10,11]. However, it doesn't take much to overcome the activation energy required for grain boundary motion in electroplated copper, as recrystallization has also been observed at room temperature only hours after deposition [2,5,12,13] and is suspected to occur during the deposition of copper [14]. Room temperature annealing is referred to as self-annealing. Deposition parameters, such as larger amounts of additives in the bath chemistry, higher current densities, and lower ECD temperatures, have been shown to affect the post-deposition on-set time for self-annealing [13]. Specifically, higher purity copper has demonstrated lower activation temperatures for recrystallization [9]. Impurity movement to the surface of Cu films have been thought to relieve pinning, a form of grain growth stagnation that will be discussed in further detail talked later in this paper. This depinning correlates to recrystallization first occurring near the surface and sides of the films and working their way down to the substrate [12,14,15]. Lastly, smaller grain sizes also result in lower temperatures for the onset of recrystallization [16-18] and grain sizes stabilize after approximately 48 hours following deposition of the films [19].

Recrystallization Nucleation and Growth

There are several processes that are thought to initiate recrystallization in materials. First is strain-induced grain boundary migration, which occurs due to the differing degree of deformation between grains of contrasting orientations. The variation in dislocation density between two grains can cause “bulging” of the grain

boundary if the release in energy is favored (see equation G1) [7],

$$\Delta E_{Strain} > \Delta E_{gb} \qquad \text{(Eq. G1)}$$

where ΔE_{Strain} refers to the discharge in strain energy and ΔE_{gb} indicates the changes in grain boundary energy due to the geometrical change in grain boundary. Recrystallization has shown dependence on grain boundary mobility in the copper microstructure [20].

Each grain in a metal's microstructure contain subgrains of slightly varying orientations. Subgrain size is also thought to initiate recrystallization, with the condition indicated by equation G2 [7],

$$R_{subgrain} > \frac{4}{3}\langle R_B\rangle\frac{\gamma}{\gamma_B} \qquad \text{(Eq. G2)}$$

where $R_{subgrain}$ is the radius of a subgrain in one grain, $\langle R_B\rangle$ is the average subgrain radius in an adjacent grain, γ is the interfacial energy per unit area of the boundary between the two grains, and γ_B is the subgrain boundary energy per unit area in the second grain. Thus, if there is a significantly larger subgrain along a high angle grain boundary compared to the size of the subgrains in the adjacent grain, recrystallization may be initiated [7].

The nucleation of recrystallized grains occurs in areas of high dislocation or strain concentrations [10]. In copper, nucleation has been readily observed at triple junctions, since triple junctions resist grain boundary sliding, causing strain buildup and the formation of folds, or "localized deformation zones" [21,22], and triple junction affected zones [23-25]. An example of this is depicted in Figure G1. Furthermore, nucleation at triple junctions are far less favorable if a twin is involved since twins don't build up stress/strain as readily as other grain boundaries [23].

The nucleation of new grains occurs continuously throughout recrystallization in copper by Jägle et al. [26]; however, recrystallization slows down as favorable (high energy grains) recrystallize, lowering their energy and decreasing the overall system strain energy [27]. The growth of recrystallized grains is driven by high angle grain boundaries, similar to grain growth, which will be discussed in a later section.

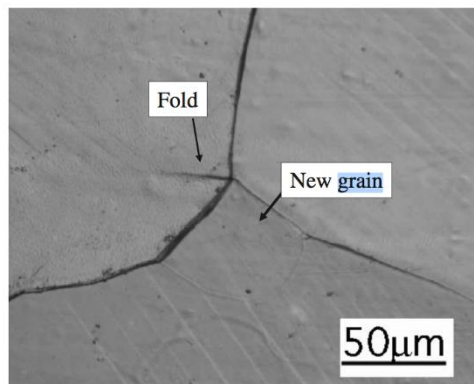

Figure G1: An SEM image of a recrystallized grain that formed at a triple junction in copper, taken from [28].

Resulting Copper Property Changes

During recrystallization, new grains are formed and grow resulting in an increased grain size over the previous microstructure as well as reduced electrical resistivity [29,30]. Annealing twin formation is also prevalent in the copper during recrystallization [31,32]. The twins form to unpin grains that become stagnated during recrystallization growth and allow further growth to take place [32]. Annealing twins have also been shown to decrease the (111) predominantly textured orientations in copper [33], however, contrasting observations by Va'sko et al. show intensified (111) and (200) textures after recrystallization [29,30].

Grain Growth

While recrystallization is the nucleation and growth of new grains in a deformed microstructure, grain growth is the further coarsening of the recrystallized grains. The main difference between these two processes is the driving forces. While recrystallization is driven by the reduction in strain energy due to deformation, grain growth is driven by the reduction in excess free energy in the system through minimization of grain boundary area. Both processes use high angle grain boundary migration as means for grain coarsening.

Driving force

Reducing Grain Boundary Area

Polycrystalline copper contains grain boundaries, or areas that separate grains and consist of disordered atoms as opposed to the structured atomic nature of the grains themselves. Grain boundaries (GB) are areas of high energy due to their non-crystalline nature where bonds aren't at equilibrium with their pr eferred (lowest energy) bond lengths and angles. Thus, the elimination or reduction in grain boundary area, through grain boundary migration, results in the reduction of overall system Gibb's energy (equation G3 [7]),

$$dG = d(\gamma_{gb} A) \quad \text{(Eq. G3)}$$

where G is Gibbs free energy, γ_{gb} is the grain boundary energy, and A is the grain boundary area.

Grain Boundary Curvature

The grain boundary's curvature is one driving force for grain boundary migration and can be used to predict movement of these boundaries. When a grain boundary takes the shortest path between two junctions (straight line) it has reduced its latitudinal area. An ideal triple junction, where all grain boundaries contribute equal surface tensions or grain boundary energies, has dihedral angles of 120°, thus is six-sided with straight boundaries [6]. Grains with more than six sides will likely have concave grain boundaries, while those with smaller than six sides will result in convex shaped grain boundaries as shown in Figure G2. This was represented in a formula (equation G4 [34]) developed by von Neumann who applied it to diffusive coarsening of soap foam [35] and later confirmed and slightly modified by Mullins to be implemented on grain coarsening [34,36]. The equation is now known as the von Neumann-Mullins equation shown below:

$$\frac{dA}{dt} = k(n-6) \qquad \text{(Eq. G4)}$$

where A is the area of the grain, t is time, k is a constant related to the grain boundary energy and mobility, and n is the number of sides for the grain. The curvature of the grain boundaries plays a large role in the velocity of these boundaries (see equation G5 [6]) and directionality of the movement;

$$v = M_B \gamma_{gb} \kappa \qquad \text{(Eq. G5)}$$

where v is the grain boundary velocity, M_B is the mobility of the boundary, γ_{gb} is the grain boundary energy, and κ is the curvature of the grain boundary. The pressure imparted on the grain boundaries due to this curvature drives the boundaries toward the center of their radius of curvature to achieve ideal, isotropic,

triple junctions discussed earlier. Thus, grains with less than six sides will become smaller, while grains with more than six sides will grow [6,36].

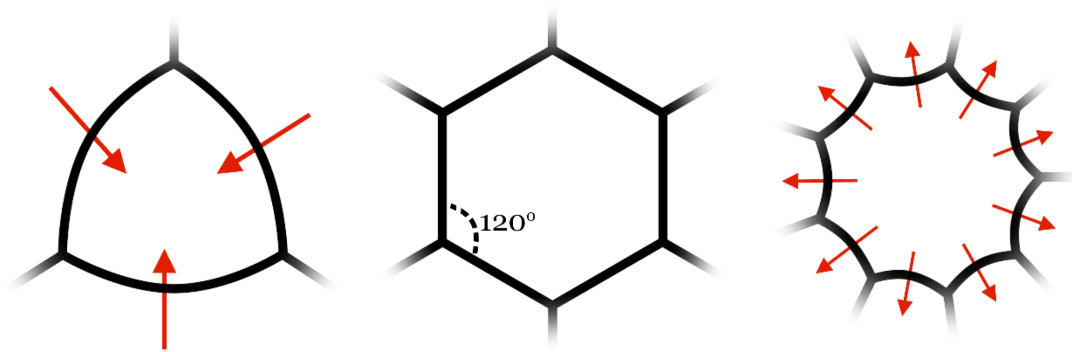

Figure G2: The preferred direction of boundary movement due to the number of grain sides.

Grain growth is a temperature and time dependent process as indicated by equation G6 [37],

$$\overline{r} - \overline{r_0} = \alpha_0 \exp\left(\frac{-Q}{kT}\right) t \qquad \text{(Eq. G6)}$$

where r is the final grain radius, r_0 is the initial grain radius, α_0 is a constant, Q is the grain boundary mobility activation energy, k is Boltzmann's constant, T is the temperature, and t is time. Increased grain sizes have been found in electrodeposited copper with higher annealing temperatures and longer annealing times [38].

Bulk Copper vs. Thin Film Copper

There is some debate as what constitutes a thin film compared to a bulk material. Typically a thin film is regarded as a much more constrained material than bulk and is said to be much smaller, but while some can designate a set

threshold thickness (1 μm) to thin films [39], it is not clear at what thickness we can truly define these types of materials. However, it is known that thin films can behave much differently than bulk materials, especially in their grain coarsening processes [37,39].

Bulk

Bulk materials typically exhibit normal grain growth, which was explained in earlier sections. A monomodal grain size distribution is common as most grains grow at similar rates. Furthermore, as discussed earlier, curvature-driven grain boundary movement leads to smaller grains shrinking and larger grains increasing in size [37,39,40].

Thin Film

Grain growth in thin films can differ greatly from that of bulk, depending on the microstructure of the film. There are two main types of microstructure (displayed in Figure G3) observed in thin films; one resembling bulk materials, where the grains sizes are smaller than the thickness of the film, and the other which contains columnar grains of larger grain sizes than the film's thickness [37,39]. The former typically exhibits normal grain growth, while the later is prone to abnormal grain growth. Abnormal grain growth refers to the growth of more favorable grains and commonly leads to bimodal grain size distributions [37]. This can result in a few large grains dominating the entire microstructure of the film. There are several key factors or inhibitors that can cause preferential grain growth

and will be discussed in the following section.

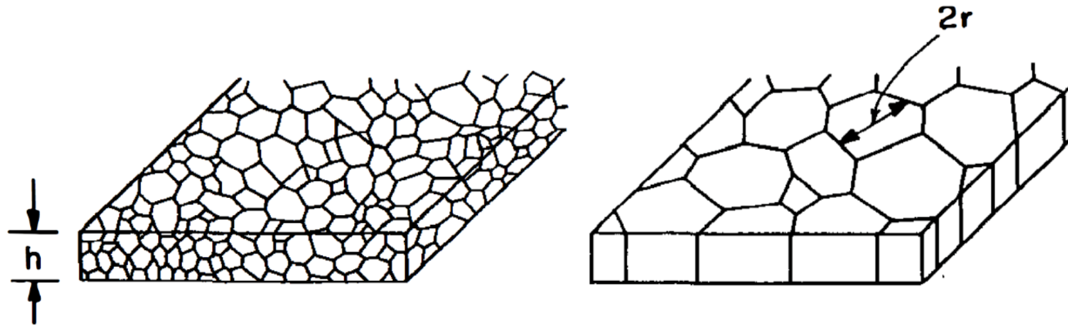

Figure G3: Two typical types of film microstructures; grain sizes are smaller than the film thickness (left) and columnar microstructure (right), where grains are large and span the thickness of the entire film, taken from [37].

Grain Growth Inhibitors

In many studies stagnation of grain growth has been observed in copper thin films with the maximum grain sizes reaching 2 to 3 times the film thickness [40-42]. The growth inhibitors listed prevent microstructural evolution and, in some cases, are the cause of selective grain growth in copper.

Zener Pinning

Many additives are used in the electro-chemical deposition process to increasing the deposition rate as well as enhance fill uniformity and quality [43,44]. These additives, along with other impurities, may hinder grain growth in what is known as Zener pinning. Pinning and prevention of grain boundary mobility occurs as the boundaries attempt to move passed these impurities. Boundaries are broken as they move through the particle and must reform upon exiting, creating a drag and requiring more energy to do so, thus these particles counteract the

movement of boundaries. The impurities within a material can prevent some grain boundaries from moving while others are able to move freely without the extra resistance from Zener pinning. However, impurities have been shown to move toward the surface and interface of the films, alleviating pinning and relieving grain growth stagnation [15]. Zener pinning was also found to be slightly dependent on orientation since grain boundary energy varies [45]. Low angle grain boundaries are more susceptible to pinning while high angle grain boundaries appear to be unaffected by particle interaction, due to their low energy and high elasticity [46].

Surface/Interfacial Energy vs. Strain Energy Density

The surface energy and interfacial energy has a more prevalent role in thin film grain growth compared to bulk, since a larger percentage of grains are affected by the surfaces, especially in columnar microstructures. These energies are dependent on grain orientations. To minimize the surface/interfacial energy of the films, growth in grains that have an orientation of lower surface energies dominate and cause preferential orientations in the material [37,39,47,48]. Grains of (111) orientation typically have lower surface energies and thus dominate in surface/interfacial energy driven grain growth [49,50]. The evolution of grain orientation in films is quite complex, since the surface/interfacial energy driven grain growth competes with strain energy density driven grain growth in films. Zielinski et al. found a deposition temperature dependence of abnormal grain growth, which can determine the dominating driving force. Higher deposition temperatures result in lower yield stresses in the films and leave less room for

strain energy build up, thus abnormal grain growth is driven by interfacial/surface energy with a higher area of (111) oriented grains. At lower deposition temperatures (100) oriented grains are favored from the elastic anisotropy of Cu creating strain energy density differentials [49]. Furthermore, (100), (110), and (511) oriented grains have been shown to have lower strain energy densities and the preferential grains for growth during strain energy density driven grain growth [39,41,48,50]. Post-deposition heat treatments can transform highly (111) dominated Cu microstructures to these strain energy density favored orientations [50] and high temperature anneals (above 300 °C) have resulted in grain growth of (100) oriented grains to minimize overall strain energy densities in nano-twinned Cu [48,51]. Highly twinned films caused (111) preferentially oriented microstructures, which were very stable thermally [51], since twin boundaries are low energy boundaries and require more temperature/energy to cause boundary migration [52].

When grain boundaries intersect with the film's surface, a thermal, or surface, groove forms as illustrated in Figure G4. Surface diffusion displaces material to equilibrate the surface energies of the two grains and grain boundary surface energy, which creates a triple junction-like structure [37,39-41,53,54]. The angle, given in equation G7 [40], of the groove demonstrates the amount of energy needed to unpin the boundary from groove,

$$\theta_0 = arcsin\left(\frac{\gamma_{gb}}{2\gamma_s}\right) \approx \frac{\gamma_{gb}}{2\gamma_s} \qquad \text{(Eq. G7)}$$

where θ_0 is the groove angle, γ_{gb} is the grain boundary energy, and γ_s is the surface energy. The critical curvature, κ_{crit}, for grain boundary unpinning can also

be calculated by equation G8 [40],

$$\kappa_{crit} = \frac{2\theta_0}{h} = \frac{\gamma_{gb}}{\gamma_s h} \quad \text{(Eq. G8)}$$

where h is the thickness of the film.

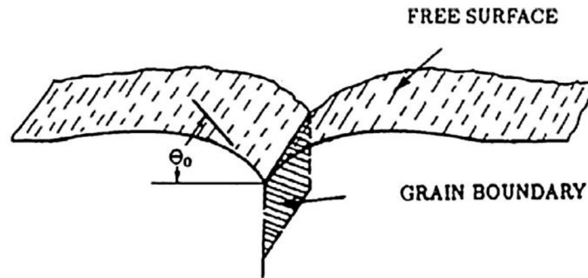

Figure G4: An illustration of a surface groove, taken from [41].

Grain Boundary Energy

Abnormal grain growth has also been observed in films where the grains are smaller than the film thickness. This is thought to occur from anisotropic grain boundary energies, due to larger distributions of dihedral triple junction angles in the films as a result of impurities in the grain boundaries [55]. The combination and distribution of low angle grain boundaries, which have low degrees of misorientation and low energy, with the high energy, high angle grain boundaries favors abnormal grain growth [7]. Boundaries tilted 40° about the <111> have the highest mobility in fcc materials, thus promoting {001}<100> preferential grain growth [56].

Conclusion

Grain growth is a process that occurs through grain boundary migration to minimize the excess free energy of grain boundaries by reducing their overall area

in the material. Normal grain growth occurs in most bulk copper and some thin film copper, while abnormal grain growth is the primary form of grain coarsening in copper thin films. Abnormal grain growth is spurred by the selective prevention of growth through impurity/groove pinning and preferential growth of favored grains from non-uniform surface/interfacial energies, strain energy densities, and grain boundary energies.

References

1. A. Pratt, 'Overview of the Use of Copper Interconnects in the Semiconductor Industry,' *Adv Energy Ind* (2004).

2. W. Dong, J. Zhang, J. Zheng and J. Sheng, 'Self-annealing of electrodeposited copper thin film during room temperature storage,' *Mater Lett*, 62 [10–11] 1589-1591 (2008).

3. S. Chang, J. Shieh, B. Dai, M. Feng and Y. Li, 'The Effect of Plating Current Densities on Self-Annealing Behaviors of Electroplated Copper Films,' *Journal of The Electrochemical Society*, 149 [9] G535-G538 (2002).

4. Rui Huang, W. Robl, H. Ceric, T. Detzel and G. Dehm, 'Stress, Sheet Resistance, and Microstructure Evolution of Electroplated Cu Films During Self-Annealing,' *Device and Materials Reliability, IEEE Transactions on*, 10 [1] 47-54 (2010).

5. H. Wendrock, W. Brückner, M. Hecker, T. G. Koetter and H. Schloerb, 'Room temperature grain growth in electroplated copper thin films,' *Microelectronics Reliability*, 40 [8–10] 1301-1304 (2000).

6. R. W. Balluffi, S. M. Allen and W. C. Carter, 'Kinetics of Materials'. John Wiley & Sons, Inc., Hoboken, New Jersey, 2005.

7. E. Mittemeijer, 'Recovery, Recrystallization and Grain Growth'; pp. 463-496. Springer Berlin Heidelberg 2011.

8. M. J. Luton, R. A. Petkovic and J. J. Jonas, 'Kinetics of recovery and recrystallization in polycrystalline copper,' *Acta Metallurgica*, 28 [6] 729-743 (1980).

9. L. M. Clarebrough, M. E. Hargreaves, D. Michell and G. W. West, 'The Determination of the Energy Stored in a Metal during Plastic Deformation,' *Proceedings of the Royal Society of London.Series A, Mathematical and Physical Sciences*, 215 [1123] 507-524 (1952).

10. R. W. Cahn, 'Chapter 28 - Recovery and Recrystallization'; pp. 2399-2500 in Physical Metallurgy (Fourth Edition). Edited by R. W. Cahn and P. Haasen (Eds.). North-Holland, Oxford, 1996.

11. N. Alshwawreh, M. Militzer and D. Bizzotto, 'Recrystallization of Electrodeposited Copper Thin Films During Annealing,' *J Electron Mater*, 39 [11] 2476-2482 (2010).

12. S. H. Brongersma, E. Richard, I. Vervoort, H. Bender, W. Vandervorst, S. Lagrange, G. Beyer and K. Maex, 'Two-step room temperature grain growth in electroplated copper,' *J. Appl. Phys.*, 86 [7] 3642-3645 (1999).

13. T. Ritzdorf, L. Chen, D. Fulton and C. Dundas, 'Comparative investigation of plating conditions on self-annealing of electrochemically deposited copper films,' *Interconnect Technology, 1999. IEEE International Conference* 287-289 (1999).

14. Jun Liu, Changqing Liu, P. P. Conway, Jun Zeng and Changhai Wang, 'Growth and recrystallization of electroplated copper columns,' *Electronic Packaging Technology & High Density Packaging, 2009. ICEPT-HDP '09. International Conference on* 695-700 (2009).

15. Rui Huang, W. Robl, H. Ceric, T. Detzel and G. Dehm, 'Stress, Sheet Resistance, and Microstructure Evolution of Electroplated Cu Films During Self-Annealing,' *Device and Materials Reliability, IEEE Transactions on*, 10 [1] 47-54 (2010).

16. M. H. Loretto and A. J. White, 'The influence of grain size on the energy stored in deformed copper,' *Acta Metallurgica*, 9 [5] 512-513 (1961).

17. L. M. Clarebrough, M. E. Hargreaves and M. H. Loretto, 'The influence of grain size on the stored energy and mechanical properties of copper,' *Acta Metallurgica*, 6 [12] 725-735 (1958).

18. A. J. Pedraza and M. J. Godbole, 'Recrystallization and mechanical properties of electroless copper. I,' *Scripta Metallurgica et Materialia*, 24 [7] 1185-1189 (1990).

19. K. Pantleon and M. A. J. Somers, 'Interpretation of microstructure evolution during self-annealing and thermal annealing of nanocrystalline electrodeposits—A comparative study,' *Materials Science and Engineering: A*, 528 [1] 65-71 (2010).

20. R. A. Vandermeer, D. J. Jensen and E. Woldt, 'Grain boundary mobility during recrystallization of copper,' *Metallurgical and Materials Transactions A*, 28 [3] 749-754 (1997).

21. S. Hashimoto, T. K. Fujii and S. Miura, 'Grain-boundary sliding and triple-point fold in aluminum tricrystals,' *Scripta Metallurgica*, 21 [2] 169-174 (1987).

22. A. V. Sisanbaev and R. Z. Valiev, 'The effect of triple junction type on grain-boundary sliding and accomodation in aluminium tricrystals,' *Acta Metallurgica et Materialia*, 40 [12] 3349-3356 (1992).

23. H. Miura *, T. Sakai, S. Andiarwanto and J. J. Jonas, 'Nucleation of dynamic recrystallization at triple junctions in polycrystalline copper,' *Philosophical Magazine*, 85 [23] 2653-2669 (2005).

24. H. Miura, S. Andiarwanto, K. Sato and T. Sakai, 'Preferential dynamic nucleation at triple junction in copper tricrystal during high-temperature deformation,' *Materials Transactions*, 43 [3] 494-500 (2002).

25. H. Miura, T. Sakai, H. Hamaji and J. J. Jonas, 'Preferential nucleation of dynamic recrystallization at triple junctions,' *Scr. Mater.*, 50 [1] 65-69 (2004).

26. E. Jägle and E. Mittemeijer, 'The Kinetics of and the Microstructure Induced by the Recrystallization of Copper,' *Metallurgical and Materials Transactions A*, 43 [4] 1117-1131 (2012).

27. E. Jägle and E. Mittemeijer, 'Interplay of Kinetics and Microstructure in the Recrystallization of Pure Copper: Comparing Mesoscopic Simulations and Experiments,' *Metallurgical and Materials Transactions A*, 43 [7] 2534-2551 (2012).

28. H. Miura *, T. Sakai, S. Andiarwanto and J. J. Jonas, 'Nucleation of dynamic recrystallization at triple junctions in polycrystalline copper,' *Philosophical Magazine*, 85 [23] 2653-2669 (2005).

29. V. Vas'Ko, I. Tabakovic and S. Riemer, 'Structure and room-temperature recrystallization of electrodeposited copper,' *Electrochemical and solid-state letters*, 6 [7] C100-C102 (2003).

30. V. A. Vas'ko, I. Tabakovic, S. C. Riemer and M. T. Kief, 'Effect of organic additives on structure, resistivity, and room-temperature recrystallization of electrodeposited copper,' *Microelectronic Engineering*, 75 [1] 71-77 (2004).

31. F. Brisset, A. Helbert and T. Baudin, '*In Situ*Electron Backscatter Diffraction Investigation of Recrystallization in a Copper Wire,' *Microscopy and Microanalysis*, 19 [04] 969-977 (2013).

32. D. P. Field, L. T. Bradford, M. M. Nowell and T. M. Lillo, 'The role of annealing twins during recrystallization of Cu,' *Acta Materialia*, 55 [12] 4233-4241 (2007).

33. C. Lingk, M. E. Gross and W. L. Brown, 'Texture development of blanket electroplated copper films,' *J. Appl. Phys.*, 87 [5] 2232-2236 (2000).

34. O. Hunderi and N. Ryum, 'A note on the von Neumann–Mullins equation,' *Scr. Mater.*, 53 [6] 719-722 (2005).

35. J. von Neumann, 'Metal interfaces,' *American Society for Metals, Cleveland*, 108 (1952).

36. W. W. Mullins, 'Two-Dimensional Motion of Idealized Grain Boundaries,' *J. Appl. Phys.*, 27 [8] 900-904 (1956).

37. C. Thompson, 'Grain-Growth in Thin-Films,' *Annu. Rev. Mater. Sci.*, 20 245-268 (1990).

38. C. H. Seah, S. Mridha and L. H. Chan, 'Annealing of copper electrodeposits,' *Journal of Vacuum Science & Technology A*, 17 [4] 1963-1967 (1999).

39. C. V. Thompson and R. Carel, 'Stress and grain growth in thin films,' *J. Mech. Phys. Solids*, 44 [5] 657-673 (1996).

40. H. J. Frost, 'Microstructural evolution in thin films,' *Mater Charact*, 32 [4] 257-273 (1994).

41. K. Barmak, E. Eggeling, D. Kinderlehrer, R. Sharp, S. Ta'asan, A. D. Rollett and K. R. Coffey, 'Grain growth and the puzzle of its stagnation in thin films: The curious tale of a tail and an ear,' *Progress in Materials Science*, 58 [7] 987-1055 (2013).

42. J. E. Palmer, C. V. Thompson and H. I. Smith, 'Grain growth and grain size distributions in thin germanium films,' *J. Appl. Phys.*, 62 [6] 2492-2497 (1987).

43. J. W. Dini and D. D. Synder, 'Chapter 2: Electrodeposition of Copper'; pp. 33 in Modern Electroplating. Edited by M. Schlesinger and M. Paunovic (Eds.). Wiley, Hoboken, NJ, USA, 2011.

44. K. Kondo, Y. Suzuki, T. Saito, N. Okamoto and M. Takauchi, 'High Speed Through Silicon Via Filling by Copper Electrodeposition,' *Electrochemical and Solid-State Letters*, 13 [5] D26-D28 (2010).

45. F. J. Humphreys and M. G. Ardakani, 'Grain boundary migration and Zener pinning in particle-containing copper crystals,' *Acta Materialia*, 44 [7] 2717-2727 (1996).

46. C. J. Tweed, B. Ralph and N. Hansen, 'The pinning by particles of low and high angle grain boundaries during grain growth,' *Acta Metallurgica*, 32 [9] 1407-1414 (1984).

47. C. V. Thompson, 'Texture evolution during grain growth in polycrystalline films,' *Scripta Metallurgica et Materialia*, 28 [2] 167-172 (1993).

48. K. Mirpuri, H. Wendrock, S. Menzel, K. Wetzig and J. Szpunar, 'Texture evolution in Copper film at high temperature studied in situ by electron back-scatter diffraction,' *Thin Solid Films*, 496 [2] 703-717 (2006).

49. E. M. Zielinski, R. P. Vinci and J. C. Bravman, 'Effects of barrier layer and annealing on abnormal grain growth in copper thin films,' *J. Appl. Phys.*, 76 [8] 4516-4523 (1994).

50. J. Zhang, K. Xu and J. He, 'Effects of Grain Orientation on Preferred Abnormal Grain Growth in Copper Films on Silicon Substrates,' *J. Mater. Sci. Lett.*, 18 [6] 471-473 (1999).

51. Y. Zhao, T. A. Furnish, M. E. Kassner and A. M. Hodge, 'Thermal stability of highly nanotwinned copper: The role of grain boundaries and texture,' *J. Mater. Res.*, 27 [24] 3049-3057 (2012).

52. O. Anderoglu, A. Misra, H. Wang and X. Zhang, 'Thermal stability of sputtered Cu films with nanoscale growth twins,' *J. Appl. Phys.*, 103 [9] (2008).

53. W. W. Mullins, 'Theory of Thermal Grooving,' *J. Appl. Phys.*, 28 [3] 333-339 (1957).

54. W. W. Mullins, 'The effect of thermal grooving on grain boundary motion,' *Acta Metallurgica*, 6 [6] 414-427 (1958).

55. J. Paik, Y. Park, M. Yoon, J. Lee and Y. Joo, 'Anisotropy of grain boundary energies as cause of abnormal grain growth in electroplated copper films,' *Scr. Mater.*, 48 [6] 683-688 (2003).

56. A. D. Rollett, 'Crystallographic texture change during grain growth,' *JOM*, 56 [4] 63-68 (2004).

Appendix H:

List of Publications and Presentations

Publications and Conference Proceedings:

- J. Marro, C. Okoro, Y. Obeng, and K. Richardson, 'The Impact of Organic Additives in Pulse Electrodeposition Bath on the Microstructure of Copper Trenches,' Manuscript in preparation (2016).
- J. Marro, T. Darroudi, C. Okoro, Y. Obeng, and K. Richardson, 'The Influence of Pulsed Electroplating Frequency and Duty Cycle on Copper Film Microstructure,' Thin Solid Films, Submitted/pending review (2016).
- J. Marro, C. Okoro, Y. Obeng and K. Richardson, 'Defect and microstructural evolution in thermally cycled Cu through-silicon vias,' Microelectronics Reliability, 54 [11] 2586-2593 (2014).
- J. Marro, C. Okoro, Y. Obeng, K. Richardson and K. Chamma, 'Temperature Dependence of Defect Evolution and Distribution in Thermally Cycled Cu-TSVs,' ECS Transactions, 61 [2] 177-184 (2014).
- J. Marro, 'Thermo-mechanical effects of thermal cycled copper through-silicon vias,' ProQuest Dissertations and Theses (2013).

Conference Posters and Presentation Abstracts:

- J. Marro, A. Kapat, T. Darroudi, C. Okoro, Y. Obeng, and K. Richardson, 'Microstructural Investigation of Pulse Electroplated Copper Trenches Deposited with Organic Additives,' oral presentation delivered at the 229th Electrochemical Society Annual Meeting (ECS), San Diego, CA, USA (2016).
- J. Marro, C. Okoro, Y. Obeng, and K. Richardson, 'Impact of Thermal History on Grain size and Grain size Distribution of Thermally Cycled Cu-TSVs,' Oral presentation delivered at the 225th Electrochemical Society Annual Meeting (ECS), Orlando, FL, USA (2014). Poster presentation delivered at the Glass & Optical Materials Division Annual Meeting (GOMD), Aachen, Germany (2014).
- J. Marro, C. Okoro, Y. Obeng, and K. Richardson, 'Temperature dependence of defect evolution and distribution in thermally cycled Cu-TSVs,' Oral presentation delivered at the Glass & Optical Materials Division Annual Meeting (GOMD), Aachen, Germany (2014).